Dissertation

(KUMULATIV)

Quantum Dynamics in Lattice Models of Interacting Spins and Fermions

---

Tjark HEITMANN

Contents

Publications

This cumulative dissertation is based on the publications [P1]-[P6].

[P1] <u>Tjark Heitmann</u> and Jürgen Schnack,
Combined Use of Translational and Spin-Rotational Invariance for Spin Systems,
Journal reference: Phys. Rev. B **99**, 134405 (2019)
DOI: 10.1103/PhysRevB.99.134405
Preprint: `arXiv:1902.02093`

[P2] <u>Tjark Heitmann</u>, Jonas Richter, Dennis Schubert, and Robin Steinigeweg,
Selected Applications of Typicality to Real-Time Dynamics of Quantum Many-Body Systems,
Journal reference: Z. Naturforsch. A **75**, 421 (2020) [Open Access]
DOI: 10.1515/zna-2020-0010
Preprint: `arXiv:2001.05289`

[P3] Jürgen Schnack, Johannes Richter, <u>Tjark Heitmann</u>, Jonas Richter, and Robin Steinigeweg,
Finite-Size Scaling of Typicality-Based Estimates,
Journal reference: Z. Naturforsch. A **75**, 465 (2020) [Open Access]
DOI: 10.1515/zna-2020-0031
Preprint: `arXiv:2002.00411`

[P4] <u>Tjark Heitmann</u>, Jonas Richter, Thomas Dahm, and Robin Steinigeweg,
Density Dynamics in the Mass-Imbalanced Hubbard Chain,
Journal reference: Phys. Rev. B **102**, 045137 (2020) [Open Access]
DOI: 10.1103/PhysRevB.102.045137
Preprint: `arXiv:2004.13604`

[P5] Jonas Richter, <u>Tjark Heitmann</u>, and Robin Steinigeweg,
Quantum Quench Dynamics in the Transverse-Field Ising Model:
A Numerical Expansion in Linked Rectangular Clusters,
Journal reference: SciPost Phys. **9**, 031 (2020) [Open Access]
DOI: 10.21468/SciPostPhys.9.3.031
Preprint: `arXiv:2005.03104`

[P6] <u>Tjark Heitmann</u>, Jonas Richter, Jochen Gemmer, and Robin Steinigeweg,
Nontrivial Damping of Quantum Many-Body Dynamics,
Journal reference: Phys. Rev. E **104**, 054145 (2021)
DOI: 10.1103/PhysRevE.104.054145
Preprint: `arXiv:2103.06646`

Publication [P7] was published during the PhD phase but is not related to the other publications [P1]-[P6] and hence not included in this dissertation.

*[P7] Julian Ehrens, Florian Gayk, Patrick Vorndamme, <u>Tjark Heitmann</u>, Niklas Biere, Dario Anselmetti, Xianghui Zhang, Armin Gölzhäuser, and Jürgen Schnack,
Theoretical Formation of Carbon Nanomembranes Under Realistic Conditions Using Classical Molecular Dynamics,
Journal reference: Phys. Rev. B **103**, 115416 (2021)
DOI: 10.1103/PhysRevB.103.115416
Preprint: `arXiv:2011.00880`

Quantum Dynamics in Lattice Models of Interacting Spins and Fermions

Tjark Heitmann

Fachbereich Physik, Universität Osnabrück, Barbarastr. 7, D-49076 Osnabrück, Germany

This cumulative dissertation is based on the publications [P1–P6], covering various aspects in theoretical studies of isolated quantum many-body systems. The transport and relaxation dynamics in quantum lattice models are studied with a particular focus on (i) the effect of a mass imbalance between different particles on their relaxation dynamics as well as (ii) the influence of generic perturbations on different reference dynamics. As for (i), the dynamics of two mutually interacting fermionic particle species on a lattice are investigated for different mass ratios between the two species [P4]. Numerical studies of density dynamics show that diffusive transport which is expected for small mass imbalances persists also for moderate imbalances and becomes anomalous for stronger imbalances. On the other hand, while transport is suppressed in the limit of infinite imbalance, i.e., if one particle species is immobile, this effective localization is shown to give way to anomalous diffusion as soon as the heavy particle species gains a finite mobility. Regarding (ii), the effect of perturbations on dynamics is investigated from the perspective of projection-operator techniques [P6]. As a main result, it is demonstrated that simple exponential damping, which is expected in the overwhelming majority of cases, may only occur for the density matrix in the interaction picture. Within this approach, this simple damping carries over to the time dependence of standard correlation functions only in certain cases. In particular, the possibility of nontrivial damping in physically relevant perturbation scenarios is discussed. A considerable portion of this work is concerned with the implementation of powerful numerical and (semi-)analytical tools to overcome the enhanced computational complexity in numerical studies of quantum many-body systems. This includes the concept of dynamical quantum typicality [P2, P3], numerical linked-cluster expansions [P5], and projection-operator techniques, as well as the combined use of available symmetries [P1].

CONTENTS

I. INTRODUCTION

A central objective in modern physics is to comprehensively understand the properties of isolated quantum many-body systems. Significant progress has been made in the past from both the experimental and the theoretical side, though many open questions concerning nonequilibrium transport and equilibration dynamics in closed quantum systems constitute an area of active, ongoing research [7–14]. A common yet puzzling observation in this context is that in many nonequilibrium settings, the quantum system relaxes to an equilibrium state that complies with the predictions of statistical mechanics. While the emergence of thermalization in isolated quantum systems is not easily reconcilable with the reversible nature of the unitary time evolution [11, 12], significant progress in its explanation has been made with the advent of new concepts like the eigenstate thermalization hypothesis (ETH) [15–17] and typicality of pure states [18–21]. The precise way in which a closed quantum system relaxes to equilibrium is of interest as well. Universal principles are particularly searched for as a means to describe a system's way to equilibrium regardless of specific microscopic details [7, 22, 23]. For example, a system might show diffusive transport on its way to equilibrium, which, again, is commonly observed in every-day macroscopic systems but not completely understood from the microscopic level [24].

There are known situations where transport is suppressed in certain quantum systems, which then fail to thermalize. For example, as first proposed by Anderson in 1958, noninteracting particles in one dimension instead localize in arbitrarily weak disorder potentials [25, 26]. It is widely believed that, given strong enough disorder, localization is also possible in interacting quantum systems, which is referred to as many-body localization (MBL) [27–30]. An increased interest in this context lays on the possibility of MBL in translationally invariant, i.e. disorder-free, systems [27, 31–43].

Another important question in the context of quantum many-body dynamics is how the dynamics of a given system are affected in presence of a perturbation [15, 44–48]. Here, a simple relation between perturbed and unperturbed dynamics, which (to some degree) universally holds true in different perturbation scenarios and different systems, is desirable. Based on random-matrix arguments and typicality, such a relation is indeed expected in the overwhelming majority of cases [46–48]. However, it remains unclear how frequent and under which conditions counterexamples to the typical behavior occur.

In general, theoretical studies of quantum many-body systems are very challenging, both analytically and numerically. Analytical solutions are typically impractical in strongly interacting quantum systems and, if at all feasible, restricted to specific models and use cases. On the other hand, numerical approaches, most notably full exact diagonalization (ED), are notoriously limited by the enhanced computational complexity that arises with the exponential growth of the Hilbert-space dimension with system size. This, in turn, prompted the development of sophisticated numerical techniques such as, e.g., the density-matrix renormalization group algorithm and other methods based on matrix product states [49, 50]. The numerical studies in this work mostly rely on the concept of quantum typicality [18–21, 51], in particular dynamical quantum typicality (DQT) [52, 53], which essentially employs randomly drawn pure states to accurately approximate ensemble averages. This is also closely related to other random-state based techniques [54–57]. The typicality concept proves particularly versatile in combination with other numerical and (semi-)analytical techniques, such as numerical linked-cluster expansions [58] or projection-operator techniques. In any case, an important factor in the efficient implementation of numerical methods is the utilization of available symmetries [59]. With this, the computational effort can be partitioned into smaller, manageable chunks, though the general symmetry adaption technique can potentially entail an additional layer of complexity if not implemented with appropriate care.

Based on the publications [P1–P6], this work studies transport and relaxation dynamics in quantum lattice models as well as methodological aspects in theoretical approaches to quantum many-body systems. First, the effect of a mass imbalance between different particles on their relaxation dynamics is studied in a setting comprising two mutually interacting fermionic particle species on a lattice [P4]. Numerical studies of density dynamics in that setting show that diffusive transport persists beyond the limit of small imbalances to moderate mass imbalances and becomes anomalous for stronger imbalances. On the other hand, while transport is suppressed in the limit of infinite mass imbalance, i.e., if one particle species is immobile, this effective localization is shown to give way to anomalous diffusion as soon as the heavy particle species gains a finite mobility.

Second, the influence of generic perturbations on different reference dynamics is investigated from the perspective of projection-operator techniques [P6]. As a main result, it is demonstrated that simple exponential damping, which is expected in the overwhelming majority of cases, may only occur for the density matrix in the interaction picture. Within this approach, this simple damping only carries over to the time dependence of standard correlation functions in certain cases. In particular, the possibility of nontrivial damping in physically relevant perturbation scenarios is discussed. A considerable portion of this work is concerned with the implementation of powerful numerical and (semi-)analytical tools to overcome the enhanced computational complexity in numerical studies of quantum many-body systems. This includes the concept of dynamical quantum typicality [P2, P3], numerical linked-cluster expansions [P5], and projection-operator techniques, as well as the combined use of available symmetries [P1].

4

This work is structured as follows: Section II provides the theoretical background that the publications [P1–P6] rely on, including the introduction of relevant quantum lattice models and different aspects in transport dynamics as well as an overview of the employed numerical and (semi-)analytical techniques. The main contents and results of the publications [P1–P6] are outlined in Sec. III and summarized in Sec. IV. Some unpublished results are included in App. A. While the list of references is restricted to a number of roughly 100 works for convenience, more relevant references can be found in the individual publications [P1–P6].

II. THEORETICAL BACKGROUND

This section provides an overview over the theoretical foundations that the publications [P1–P6] rely on. This includes the definitions of different quantum lattice models, (thermo-)dynamic quantum expectation values, and important quantities and physical aspects in connection with quantum transport. The section concludes with a brief description of the employed numerical and (semi-)analytical techniques.

A. Quantum Lattice Models

The works presented in this thesis study various versions of quantum lattice models, where the Hamilton operator $\mathcal{H}$ is composed of local terms h_r for each site r of the given lattice,

$$\mathcal{H} = \sum_r h_r \ . \tag{1}$$

Every h_r comprises the interaction terms that link site r to other (typically neighboring) sites r', using an appropriate convention (e.g., $r' > r$) to avoid duplicate terms in $\mathcal{H}$. The lattice geometries considered here include onedimensional chains, quasi-onedimensional ladders, and square lattices, which are sketched in Fig. 1. As will prove to be convenient later on, neighboring sites on different legs of a ladder are labeled with the same r and equipped with a secondary label, owing to the essentially onedimensional structure. In all cases, additional periodic boundary conditions may be applied, where opposite sites at the ends of the lattice are linked by interactions as well.

Given a system of L lattice sites, the Hilbert space $\mathbb{H}$ hosting all possible states of a quantum system is composed of the local Hilbert spaces $\mathbb{H}_r$ on each site via a tensor product,

$$\mathbb{H} = \bigotimes_{r=1}^{L} \mathbb{H}_r \ . \tag{2}$$
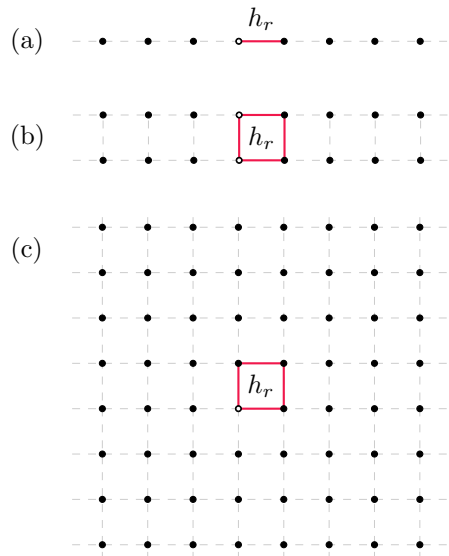
Figure 1. Sketch of the lattice geometry for (a) chains, (b) ladders, and (c) 2D square lattices. The interaction links associated with one exemplary local Hamiltonian h_r are indicated in color.

Its dimension is given by the product of all local Hilbert-space dimensions d,[1]

$$\dim \mathbb{H} = \prod_{r=1}^{L} \dim \mathbb{H}_r = d^L \tag{3}$$

and thus grows exponentially with the system size L.

1. Quantum Spin Model

Moving forward to actual physical models, the sites of a given lattice may for example be occupied by stationary spins with spin quantum number $s \in \{\frac{1}{2}, 1, \frac{3}{2}, \dots\}$. Each spin is represented by the corresponding spin vector operator $\mathbf{s}_r = (s_r^x, s_r^y, s_r^z)$. Its components obey the defining spin algebra,[2][3]

$$\left[s_r^j, s_{r'}^k \right] = i \, \delta_{rr'} \, \varepsilon_{jkl} \, s_r^l \ , \tag{4}$$

where $\delta_{rr'}$ is the Kronecker delta, ε_{jkl} is the antisymmetric Levi-Civita symbol, and $j, k, l \in \{x, y, z\}$. The pertinent local Hilbert space on each site is spanned by,

----

[1] We consider identical local dimensions in all models here. However, depending on the specific details of the quantum model defined on the lattice, these local dimensions can in general vary from site to site.
[2] $[A, B] \equiv AB - BA$ is the commutator.
[3] We set $\hbar = 1$ here and in the following.
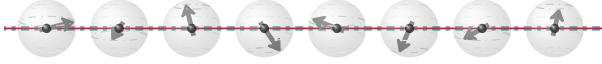
Figure 2. Exemplary sketch of a quantum spin chain with nearest-neighbor interactions described by the local Heisenberg Hamiltonians (5).

Figure 3. Sketch of the extended Fermi-Hubbard chain: spin-↑ and -↓ fermions with site-to-site hopping amplitudes $t_\downarrow$, $t_\uparrow$ and two-body interactions U and U'.

e.g., the $d = (2s+1)$ eigenstates $|s, m_s\rangle$ of the local s_r^z operators, labeled by the magnetization quantum number $m_s \in \{-s, -s+1, \ldots, s-1, s\}$.

The exchange interaction between the spins on sites r and r' is often described by the *Heisenberg model*, with local Hamiltonians

$$h_r = \sum_{\langle r,r'\rangle} J_{rr'} \left(s_r^x s_{r'}^x + s_r^y s_{r'}^y + \Delta s_r^z s_{r'}^z \right) , \qquad (5)$$

parametrized by the exchange coupling constant $J_{rr'}$ and anisotropy Δ along the quantization axis. Alternatively, Eq. (5) can be expressed in terms of the raising and lowering operators $s_r^\pm = s_r^x \pm i s_r^y$,[4]

$$h_r = \sum_{\langle r,r'\rangle} J_{rr'} \left[\tfrac{1}{2} \left(s_r^+ s_{r'}^- + \text{h.c.} \right) + \Delta s_r^z s_{r'}^z \right] . \qquad (6)$$

The corresponding commutation relations

$$\left[s_r^z, s_{r'}^\pm \right] = \pm \delta_{rr'} s_r^\pm \qquad (7)$$

$$\left[s_r^+, s_{r'}^- \right] = 2\, \delta_{rr'} s_r^z \qquad (8)$$

can simplify the numerical treatment of the Hamiltonian. In presence of an external (possibly site-dependent) magnetic field $\mathbf{B}_r$, the Hamiltonian is equipped with an additional Zeeman term,

$$h_r^{\text{Zeeman}} = g\mu_B \, \mathbf{s}_r \cdot \mathbf{B}_r \qquad (9)$$

with Bohr magneton μ_B and Landé factor g.

A related model, which may also be seen as a trimmed-down version of the Heisenberg model, is the *Ising model* with a transverse external magnetic field,

$$h_r = -J \left(\sum_{\langle r,r'\rangle} s_r^z s_{r'}^z + g s_r^x \right) . \qquad (10)$$

This model will not play a central role in this thesis, but it was primarily used as a test model in Pub. [P5] to benchmark a numerical technique.

2. Hubbard Model

Introducing another class of quantum lattice models, the *Hubbard model* in its various flavors basically describes interacting fermionic or bosonic particles moving from lattice site to lattice site. More specifically, this thesis focuses mainly on the *Fermi-Hubbard chain*, where spin-↑ and spin-↓ fermions move between the sites of a onedimensional chain whilst subject to an on-site interaction. The corresponding local Hamiltonian reads

$$h_r = - \sum_{\sigma=\uparrow,\downarrow} t_\sigma \left(c_{r,\sigma}^\dagger c_{r+1,\sigma} + \text{h.c.} \right) \qquad (11)$$
$$+ U \left(n_{r,\uparrow} - \tfrac{1}{2} \right) \left(n_{r,\downarrow} - \tfrac{1}{2} \right) ,$$

where t_σ is the spin-dependent hopping amplitude and U is the on-site interaction strength. The creation operator $c_{r,\sigma}^\dagger$ creates a spin-σ particle at site r, whereas the annihilation operator $c_{r,\sigma}$ annihilates a spin-σ particle at site r. They fulfill the fermionic anticommutation relations,[5]

$$\left\{ c_{r,\sigma}, c_{r',\sigma} \right\} = 0 \qquad (12)$$

$$\text{and} \quad \left\{ c_{r,\sigma}, c_{r',\sigma}^\dagger \right\} = \delta_{rr'} , \qquad (13)$$

and define the local particle number operator $n_{r,\sigma} = c_{r,\sigma}^\dagger c_{r,\sigma}$. The local Hilbert spaces on each site are spanned by, e.g., the $d = 4$ eigenstates $|n_{r,\uparrow}, n_{r,\downarrow}\rangle$ of the local particle number operators $n_{r,\sigma}$ with eigenvalues $n_{r,\sigma} \in \{0, 1\}$.

In addition to the on-site interaction, there may also be an interaction between neighboring sites, described by the additional terms

$$h_r' = U' \sum_{\sigma,\sigma'} (n_{r,\sigma} - \tfrac{1}{2})(n_{r+1,\sigma'} - \tfrac{1}{2}) . \qquad (14)$$

This is also referred to as the *extended Fermi-Hubbard chain* and is sketched in Fig. 3.

---

[4] h.c. denotes the Hermitian conjugate.

[5] $\{A, B\} \equiv AB + BA$ is the anticommutator.

6

Figure 4. Sketch of a spin-$\frac{1}{2}$ ladder with $XXYY$-interactions of strength J_1, J_2 along the legs and various ZZ-interactions of strength $J_\perp$ and 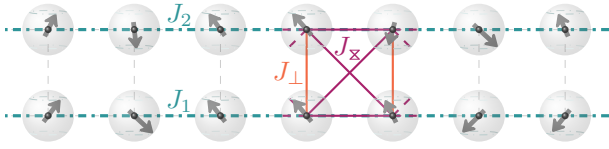$J_{\boxtimes}$ between the legs, as obtained by a Jordan-Wigner transformation of the extended Fermi-Hubbard model sketched in Fig. 3.

3. Jordan-Wigner Transformation

Though prima facie not necessarily obvious, the spin models and the Fermi-Hubbard model introduced above are not only structurally related, but in fact equivalent by Jordan-Wigner transformation [60]. Using this transformation, spin raising and lowering operators are transformed to fermionic creation and annihilation operators and vice versa. There are some technicalities involved to ensure the correct commutation relations of the transformed operators. For example, when equipped with an additional phase factor, fermionic creation and annihilation operators can be directly associated with the spin raising and lowering operators,

$$
\begin{aligned}
c_r^\dagger &= \tfrac{1}{2}\, \mathrm{e}^{-i\phi_r} s_r^+ \\
c_r &= \tfrac{1}{2}\, \mathrm{e}^{i\phi_r} s_r^- \ ,
\end{aligned}
\tag{15}
$$

with

$$
\phi_r = \pi \sum_{l<r} s_l^+ s_l^- \ .
\tag{16}
$$

Technical details aside, it is sufficient to keep the following correspondence in mind: local magnetizations in the spin language translate to occupation numbers in the Hubbard language,

$$
n_r = s_r^z + \frac{1}{2} \ .
\tag{17}
$$

With this, a onedimensional spin chain can be treated as a chain of spinless fermions. The Fermi-Hubbard model introduced in Eq. (11) is in turn equivalent to a spin ladder, where different legs of the latter are associated with the different particle species of the former. For completeness, the corresponding local Hamiltonian for the quantum spin ladder reads

$$
h_r = - \sum_{k=1,2} 2J_k \left(s_{r,k}^x s_{r+1,k}^x + s_{r,k}^y s_{r+1,k}^y \right)
\tag{18}
$$
$$
+ J_\perp\, s_{r,1}^z s_{r,2}^z
$$

and, corresponding to the extension (14),

$$
h_r' = - \sum_{k,k'} J_{\boxtimes}\, s_{r,k}^z s_{r+1,k'}^z \ ,
\tag{19}
$$

compare also the sketches in Fig. 4 and Fig. 3.

In the following, we will occasionally choose either one of the Hubbard or the spin language when coming across model-specific contexts, depending on the convenience and the given physical scenario. While doing so, we can always bear in mind that there are corresponding analogue formulations in the respective other language.

4. Symmetries

The models introduced above exhibit several symmetries, formally defined by groups[6] of operators $\mathcal{S}$ that commute with the Hamiltonian,

$$
[\mathcal{H}, \mathcal{S}] = 0 \ ,
\tag{20}
$$

entailing corresponding conservation laws. These symmetries stem from the underlying lattice geometry and from symmetry properties of the local exchange Hamiltonians.

Typical symmetries preserving the lattice structure are point-group symmetries like reflections or discrete rotations. Additionally, given an infinite lattice or periodic boundary conditions, Hamiltonians of the form (1) are invariant under lattice translations, which shift all sites simultaneously by one or multiple lattice vectors. In the specific case of a onedimensional lattice with L sites and periodic boundary conditions, the corresponding translation operator $\mathcal{T}$ generates the cyclic group C_L and

$$
[\mathcal{H}, \mathcal{T}^l] = 0
\tag{21}
$$

with powers $l = 0, \dots, L-1$.

Apart from lattice symmetries, notable examples for exchange interaction symmetries can be found in the local Heisenberg Hamiltonian (5). In the case of isotropic interactions, $\Delta = 1$, the total spin operator $\mathbf{S} = \sum_r \mathbf{s}_r$ commutes with the Hamiltonian,

$$
[\mathcal{H}, \mathbf{S}^2] = 0
\tag{22}
$$

and is the generator of the associated continuous symmetry group $SU(2)$ of rotations in spin space. For

---
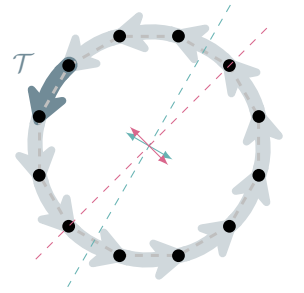
[6] Groups as in group theory.

7

any anisotropy, $\Delta \neq 1$, only the total magnetization $S^z = \sum_r s_r^z$ is conserved,

$$[\mathcal{H}, S^z] = 0 , \tag{23}$$

and generates the corresponding symmetry group $U(1)$ of rotations around the z-axis. Translated into the language of Hubbard models with the correspondence (17), this symmetry corresponds to the particle number conservation. In fact, for the Fermi-Hubbard model described by Eq. (11), particle numbers $N_\sigma = \sum_r n_{r,\sigma}$ for each spin σ are conserved separately.

The general strategy for the utilization of symmetries as well as specific examples will be discussed in Sec. II D 6.

B. Physical Properties and Observables

The quantum state of a given system, which in general may be a mixed state comprised of an ensemble of pure states $\{|\Psi_k\rangle\}$ with probabilities p_k, is described by the density operator

$$\rho = \sum_k p_k |\Psi_k\rangle \langle \Psi_k| , \tag{24}$$

with $\mathrm{Tr}[\rho] = 1$ and $\rho^\dagger = \rho$. For any operator $\mathcal{A}$, the corresponding expectation value with respect to that state is calculated as an ensemble average,

$$\langle \mathcal{A} \rangle = \mathrm{Tr}[\rho \mathcal{A}] . \tag{25}$$

This simple expression lays the foundation for the calculation of any thermodynamic or dynamic quantity, as discussed in the following.

1. Thermodynamics

According to textbook quantum statistical mechanics, the possible states of a system with fixed temperature T are gathered in the *canonical ensemble*, represented by

$$\rho_\beta = \frac{\mathrm{e}^{-\beta \mathcal{H}}}{\mathcal{Z}_\beta} \tag{26}$$

with the partition function $\mathcal{Z}_\beta = \mathrm{Tr}\left[\mathrm{e}^{-\beta \mathcal{H}}\right]$ and inverse temperature $\beta = 1/k_B T$, where k_B is the Boltzmann constant. Inserted in Eq. (25), the temperature-dependent expectation value of any thermodynamic observable $\mathcal{A}$ is calculated via

$$\langle \mathcal{A} \rangle_{\mathrm{eq}} = \frac{1}{\mathcal{Z}_\beta} \mathrm{Tr}\left[\mathrm{e}^{-\beta \mathcal{H}} \mathcal{A}\right] . \tag{27}$$

Common examples are the magnetization $M(T) = -g\mu_B \langle S^z \rangle_{\mathrm{eq}}$ in a spin system and the internal energy $U(T) = \langle \mathcal{H} \rangle_{\mathrm{eq}}$, as well as their variances, known as mag-

netic susceptibility,

$$\chi(T) = (g\mu_B)^2 \beta \left[\langle (S^z)^2 \rangle_{\mathrm{eq}} - \langle S^z \rangle_{\mathrm{eq}}^2\right] , \tag{28}$$

and the heat capacity,

$$C(T) = k_B \beta^2 \left[\langle \mathcal{H}^2 \rangle_{\mathrm{eq}} - \langle \mathcal{H} \rangle_{\mathrm{eq}}^2\right] . \tag{29}$$

The expectation values $\langle \bullet \rangle_{\mathrm{eq}}$ above are labeled as equilibrium expectation values, reflecting that the state ρ_β is time-independent by construction. The following part is concerned with the dynamics of expectation values, e.g., in situations where the state ρ may evolve in time.

2. Dynamics

Starting from any initial state $\rho(0)$, its subsequent time evolution under the governing Hamiltonian is given by the von-Neumann equation,

$$\tfrac{d}{dt}\rho(t) = -i[\mathcal{H}, \rho(t)] , \tag{30}$$

which is formally solved by

$$\rho(t) = \mathrm{e}^{-i\mathcal{H}t}\rho(0)\,\mathrm{e}^{i\mathcal{H}t} . \tag{31}$$

With that, the expectation value of an observable $\mathcal{A}$ acquires a nontrivial time dependence for any state ρ that does not commute with the Hamiltonian,

$$\langle \mathcal{A}(t) \rangle = \mathrm{Tr}[\rho(t)\mathcal{A}] . \tag{32}$$

A simple example for such a nonequilibrium state is an eigenstate (or thermal state ρ_β) of some different Hamiltonian $\mathcal{H}'$, which is not an eigenstate of the Hamiltonian $\mathcal{H}$ generating the dynamics. Dynamical quantities of particular interest in the context of transport in lattice models are densities ϱ_r of some local charges q_r,

$$\varrho_r(t) = \langle q_r(t) \rangle = \mathrm{Tr}[\rho(t)\,q_r] \tag{33}$$

where the q_r could, for example, involve local magnetizations s_r^z in a spin model or local particle numbers $n_{r,\sigma}$ in a Hubbard model.

The expressions above refer to the *Schrödinger picture*, where the time dependence is a feature of the quantum state while observables itself are time-independent. Another dynamical picture is considered in the context of time-dependent equilibrium correlation functions of two observables $\mathcal{A}$, $\mathcal{A}'$, reading

$$C_{\mathcal{A}\mathcal{A}'}(t) \equiv \langle \mathcal{A}(t)\mathcal{A}' \rangle_{\mathrm{eq}} = \mathrm{Tr}[\rho_\beta \mathcal{A}(t)\mathcal{A}'] . \tag{34}$$

Here, the state is given by the canonical equilibrium ensemble and thus stationary while observables evolve in time according to the *Heisenberg picture*. However, in the limit of high temperatures $\beta \to 0$, these correlation functions can still be constructed in the spirit of Eq. (32)

by deploying special initial states of the form

$$\rho(0) \propto \mathrm{e}^{-\beta(\mathcal{H}-\epsilon\mathcal{A})} , \qquad (35)$$

which, in good approximation for $\beta \to 0$ and $\beta\epsilon > 0$, can be expanded as

$$\rho(0) \propto \mathbb{1} + \beta\epsilon\mathcal{A} . \qquad (36)$$

These states are in general time-dependent and the high-temperature limit of the correlation function (34) can be obtained as the expectation value of $\mathcal{A}'$,

$$\begin{aligned}\langle \mathcal{A}'(t)\rangle &= \mathrm{Tr}\left[\rho(t)\,\mathcal{A}'\right] \qquad (37)\\ &\propto \mathrm{Tr}\left[\mathcal{A}(t)\mathcal{A}'\right] ,\end{aligned}$$

provided that $\mathrm{Tr}\left[\mathcal{A}'\right] = 0$.[7] Note that, apart from the context of thermodynamic quantities, we always consider the limit of infinite temperatures, $\beta \to 0$.

C. Transport and Relaxation

The main focus of this thesis is placed on transport and relaxation dynamics in onedimensional quantum lattice models. Key aspects in that regard will be introduced in this section. A starting point for further reading on the topic of transport in onedimensional quantum lattice models is given by the comprehensive review article [14] and references therein.

1. Quantum Lattice Transport Quantities

The notion of transport generally involves a conserved quantity $Q = \sum_r q_r$, composed of local terms on each lattice site r,

$$[\mathcal{H}, Q] = 0 . \qquad (38)$$

Heisenberg's equation of motion

$$\tfrac{d}{dt} q_r = i\left[\mathcal{H}, q_r\right] \qquad (39)$$

in combination with the lattice continuity equation

$$\tfrac{d}{dt} q_r = j_{r-1}^{(Q)} - j_r^{(Q)} \qquad (40)$$

induces the definition of the associated local current as

$$j_r^{(Q)} = i\left[q_r, h_r\right] . \qquad (41)$$

From these local currents, the total current is again defined as

$$\mathcal{J}^{(Q)} = \sum_r j_r^{(Q)} . \qquad (42)$$

Both the local charge terms and the associated current[8] are conveniently studied to assess the transport behavior in a given setting.

2. Phenomenology of Different Transport Types

There is a range of possible transport behaviors a system could show, from insulation, where no charge is transported at all, up to free conduction, where charge is transported ballistically. In between, transport may be best described by diffusion equations, where anomalous sub- or superdiffusion constitute the transitional regions to ballistic transport and insulating behavior.
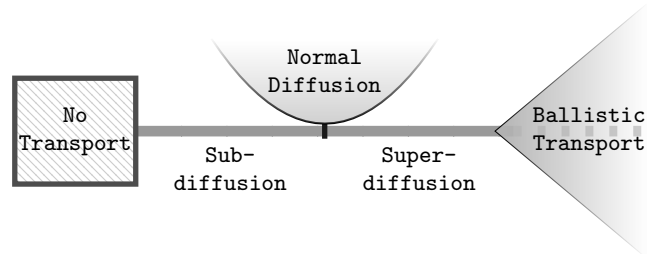
The transport properties of a system can be examined based on the dynamics of the associated local densities, i.e., the time-dependent expectation values of the local charge terms $\varrho_r(t) = \langle q_r(t)\rangle$. These densities show diffusive transport, if they fulfill the lattice diffusion equation,

$$\tfrac{d}{dt}\varrho_r(t) = D\left[\varrho_{r-1}(t) - 2\varrho_r(t) + \varrho_{r+1}(t)\right] \qquad (43)$$

with some diffusion constant D. First indications for diffusive transport may be observed in the temporal growth of the spatial width for some inhomogeneous density distribution,

$$\Sigma^2(t) = \sum_{r=1}^{L} r^2 \delta\varrho_r(t) - \left[\sum_{r=1}^{L} r\,\delta\varrho_r(t)\right]^2 , \qquad (44)$$

where we define $\delta\varrho_r(t) \propto \varrho_r(t) - \varrho_{\mathrm{eq}}$ with $\varrho_{\mathrm{eq}} = \langle q_r\rangle_{\mathrm{eq}}$ and normalization $\sum_r \delta\varrho_r(t) = 1$ for all times t. In case of diffusion, i.e., whenever Eq. (43) is fulfilled, the spatial width grows proportional to the diffusion constant,

$$\tfrac{d}{dt}\Sigma^2(t) = 2D . \qquad (45)$$

---

[7] Without loss of generality, any operator $\mathcal{A}'$ can be shifted such that $\mathrm{Tr}\left[\mathcal{A}'\right] = 0$.

[8] As there will only be one transport quantity of interest at a time, we drop the label for the current in the following for the sake of clean notation.

A similar but slightly more general relation can be borrowed from the framework of *linear response theory* (LRT), which describes the response of a transport quantity to weak perturbations of the system. Here, the growth of the spatial width is described as

$$\frac{d}{dt}\Sigma^2(t) = 2D(t) \tag{46}$$

with a now time-dependent diffusion coefficient that can be obtained from current-current correlation functions [61],

$$D(t) = \frac{\beta}{\chi}\int_0^t dt' \frac{\langle \mathcal{J}(t')\mathcal{J}\rangle}{L} . \tag{47}$$

For high temperatures $\beta \to 0$

$$\frac{\chi}{\beta} = \frac{\langle Q^2\rangle - \langle Q\rangle^2}{L} = \frac{1}{4} . \tag{48}$$

It is worth mentioning that the above relation (47) can actually be generalized to finite temperatures as well, where the autocorrelation function $\langle \mathcal{J}(t)\mathcal{J}\rangle$ is essentially replaced by a *Kubo scalar product* [61–63]. Further, note that the derivation of Eq. (47) in fact requires special initial states that are constructed close to the canonical equilibrium state ρ_β, where the inhomogeneous density distribution is incorporated via a weak perturbation to the Hamiltonian. However, with the introduction of quantum typicality in the upcoming Sec. II D 2, the details about the specific design of the initial states become less important. The central requirement for Eq. (47) to hold is that they feature some density distribution whose support is sufficiently confined to the center of the lattice.

Interestingly, the relation (47) entails insights on different scaling behaviors of $D(t)$ beyond standard diffusion: First, owing to a mean free time where interactions are still due to come into effect, there is always a short initial period of ballistic transport with $D(t) \propto t$, due to the current remaining approximately constant. Then, if after some time τ the autocorrelation function $\langle \mathcal{J}(t)\mathcal{J}\rangle$ is decayed completely, normal diffusion sets in with $D(\tau > t) \approx$ const. If $\langle \mathcal{J}(t)\mathcal{J}\rangle$ does not decay to zero, for example due to some overlap of $\mathcal{J}$ with conserved quantities [64, 65], the diffusion coefficient continues to grow in the long-time limit with ballistic scaling $D(t) \propto t$. Transferred to the spatial width (44), a scaling according to $\Sigma(t) \propto t^\alpha$ is called *ballistic* for $\alpha = 1$, *superdiffusive* for $1/2 < \alpha < 1$, *diffusive* for $\alpha = 1/2$, *subdiffusive* for $0 < \alpha < 1/2$, and *insulating* for $\alpha = 0$.

In search of diffusive transport, the scaling analysis of the spatial width can merely serve as an indication of its existence, while a genuine confirmation can be achieved by looking at the full density distribution. To this end, consider an initial state featuring a sharp density peak

in the middle[9] of the chain – on top of an equilibrium background,

$$\delta\varrho_r(0)\begin{cases} \neq 0 & , r = L/2 \\ = 0 & , \text{else} \end{cases} . \tag{49}$$

For this initial condition, the lattice solution[10] of Eq. (43) can be well approximated by Gaussian profiles,

$$\delta\varrho_r(t) = \frac{1}{\Sigma(t)\sqrt{2\pi}}\exp\left[-\frac{(r-L/2)^2}{2\Sigma^2(t)}\right] . \tag{50}$$

Thus, in case of standard diffusion, the initial density peak is expected to broaden over time while keeping an overall Gaussian shape. Its full spatial dependence is described by a single parameter $\Sigma(t)$ that can again be obtained by Eq. (44) or from current-current correlation functions via Eq. (47). The time domain where this holds is naturally delimited by the time where a significant share of the density distribution reaches the boundaries of the system.

When transitioning to anomalous diffusion, the density profiles are expected to deviate from the Gaussian shape. In the particular case of subdiffusion, the profiles assume a more exponential shape, which to some extent can be described as $\delta\varrho_r(t) \propto \exp\left[-\gamma|r-L/2|^\nu\right]$ with a decreasing exponent $\nu \to 1$.

Complementary to the real-space perspective, it is instructive to examine the density dynamics in momentum space as well. The corresponding density modes are obtained via a discrete Fourier transformation,

$$\varrho_q(t) = \frac{1}{\sqrt{L}}\sum_{r=1}^{L}e^{iqr}\varrho_r(t) \tag{51}$$

with the momentum $q = 2\pi k/L$ and wave numbers $k = 0, 1, \ldots, L-1$. Also by Fourier transformation, the diffusion equation (43) is decoupled into rate equations for the density modes $\varrho_q(t)$,

$$\frac{d}{dt}\varrho_q(t) = -\tilde{q}^2 D \varrho_q(t) , \tag{52}$$

with $\tilde{q}^2 = 2(1 - \cos q)$. Consequently, diffusion manifests itself in momentum space by exponentially decaying modes

$$\varrho_q(t) \propto e^{-\tilde{q}^2 Dt} . \tag{53}$$

Note that this exponential decay can best be observed for momenta q away from the vicinity of corresponding

---

[9] For the sake of a clean notation, consider even L here. Otherwise, to cover both even and odd system sizes, the middle of the chain should be defined more carefully as $\lfloor L/2\rfloor$.

[10] The time dependence of each local density is given by $\delta\varrho_r(t) = e^{-2Dt}I_{r-L/2}(2Dt)$, where $I_r(t)$ is the modified Bessel function of first kind.

characteristic real-space length scales $l = 2\pi/q$ such as, e.g., the mean free path.

3. Localization Effects in Transport Dynamics

A multitude of quantum systems has been reported to show some form of transport, where initial nonequilibrium distributions of associated local charges would either relax to equilibrium by normal or anomalous diffusion, or spread ballistically throughout the system (for an overview see, e.g., Ref. [14] and references therein). However, aside from these, there are systems that are instead *localized*, exhibiting neither diffusive nor ballistic transport. A particularly interesting mechanism producing localization was proposed by Anderson in 1958 [25] and came to be known as *Anderson localization*. The paradigmatic Anderson model comprises free particles on a lattice subject to disorder, caused by a potential with randomly varying strength from site to site. Specifically, consider the model

$$\mathcal{H}_A = \mathcal{H}_{\text{free}} + \mathcal{H}_{\text{disorder}} \ , \tag{54}$$

where noninteracting spinless fermions are described by the term

$$\mathcal{H}_{\text{free}} = t_{\text{h}} \sum_r \left(c_r^\dagger c_{r+1} + \text{h.c.} \right) \tag{55}$$

and disorder is introduced by the potential term

$$\mathcal{H}_{\text{disorder}} = \sum_r W_r \, n_r \tag{56}$$

with random field strengths $W_r \in [-W, W]$. For any disorder strength W, the random energy landscape causes the particles to localize near[11] their initial location on the lattice and thus transport of particle densities $\varrho_r(t) = \langle n_r \rangle$ is suppressed. As before, let us consider an initial state featuring a sharply peaked distribution of the densities $\varrho_r(0)$ like in Eq. (49). After some short initial period where the particles may locally adjust their positions, they are stuck and not able to spread further on the lattice. Accordingly, particle currents vanish, the spatial width of the distribution remains at a constant value[12] corresponding to the localization length, and the system fails to equilibrate, forever retaining memory of its initial state.

For strong enough disorder strength W, this effect is expected to prevail even in presence of interactions, i.e.,

———

[11] In the sense that the distance stays below the localization length.
[12] In fact, for finite system sizes, the spatial width is always expected to saturate at a constant L-dependent value, see Pub [P4].

after introducing an additional term

$$\mathcal{H}_{\text{int}} = U \sum_r \left(n_r - \tfrac{1}{2} \right) \left(n_{r+1} - \tfrac{1}{2} \right) \tag{57}$$

to the Hamiltonian (54). The corresponding topic of many-body localization (MBL) has evolved into a vast field of ongoing research from both the theoretical and the experimental side [27, 28, 30]. One particular question that grew in this context is whether MBL can be realized in translationally invariant systems, particularly in systems without disorder [27, 31–43]. Amongst other candidates like frustrated systems [66] or flat band systems [66, 67] the Fermi-Hubbard model (11) with a mass imbalance between spin-↑ and spin-↓ particles was studied in that respect [39, 43, 68]. This mass imbalance is realized through spin-dependent hopping amplitudes t_σ in the Hamiltonian (11) and parametrized by the imbalance ratio $\eta = t_\downarrow/t_\uparrow$ (with $t_\uparrow$ fixed), ranging from $\eta = 0$ for $t_\downarrow = 0$ to $\eta = 1$ in the case $t_\downarrow = t_\uparrow$. It is suggested that, given a strong on-site interaction between both particle species, the much heavier spin-↓ particles might localize the lighter spin-↑ particles by means of a dynamically induced effective disorder potential. This suggestion stands to reason when looking at the limit of infinite mass imbalance, $\eta = 0$, known as the Falicov-Kimball limit [69, 70]. In this limit, i.e., when $t_\downarrow = 0$, the Hamiltonian (11) simplifies to

$$\mathcal{H}_{\text{FK}} = \sum_r -t_\uparrow \left(c_{r,\uparrow}^\dagger c_{r+1,\uparrow} + \text{h.c.} \right)$$
$$+ U \left(n_{r,\uparrow} - \tfrac{1}{2} \right) \left(n_{r,\downarrow} - \tfrac{1}{2} \right) \ , \tag{58}$$

which leaves the occupation numbers $n_{r,\downarrow}$ as strictly conserved quantities,

$$[\mathcal{H}, n_{r,\downarrow}] = [n_{r,\downarrow}, n_{r',\downarrow}] = 0 \ . \tag{59}$$

Accordingly, the pertinent Hilbert space is decoupled into 2^L independent subspaces, each corresponding to one particular configuration of the occupation numbers $\{n_{r,\downarrow}\}$. Each of these configurations in turn serves as a different realization of a random binary on-site potential $\{\pm U/2 \, (n_{r,\uparrow} - 1/2)\}$ for the lighter particles. Hence, the Falicov-Kimball limit effectively reproduces the single-particle Anderson model for the spin-↑ particles. Allowing a small mobility of the heavy particles, i.e., a small but nonzero $t_\uparrow > 0$, one might expect a similar behavior – at least for small time scales on which the heavy particles appear to be static to the light particles. The possibility of the existence of localization for a finite imbalance ratio is studied in, e.g., Refs. [39, 43, 68]. In the opposing limit of equal masses, $\eta = 1$, initial nonequilibrium distributions are expected to decay by diffusion [71]. The density dynamics in the mass-imbalanced Fermi-Hubbard model are discussed in detail in Pub. [P4] for the full range of imbalance ratios $0 \leq \eta \leq 1$.

4. Dynamics Under the Influence of Perturbations

Consider the dynamics of an observable $\mathcal{A}$ under some Hamiltonian $\mathcal{H}_0$, which is perturbed by an operator $\mathcal{V}$ with strength ε and thus changes to

$$\mathcal{H} = \mathcal{H}_0 + \varepsilon \mathcal{V} \ . \tag{60}$$

Understanding the effect of this perturbation on the dynamics of $\mathcal{A}$ is paramount to many theoretical investigations such as in, e.g., Refs. [15, 44–48]. A desirable outcome would be a simple and universal relation between perturbed and unperturbed dynamics. Indeed, this relation is in many cases expected to be given by a simple exponential damping function, based on typicality and random-matrix arguments [46–48]. For example, consider the autocorrelation function $\langle \mathcal{A}(t)\mathcal{A} \rangle$. In case of exponential damping, the relation between the perturbed ($\varepsilon > 0$) and unperturbed ($\varepsilon = 0$) dynamics is of the simple form

$$\frac{\langle \mathcal{A}(t)\mathcal{A} \rangle_{\varepsilon>0}}{\langle \mathcal{A}(t)\mathcal{A} \rangle_{\varepsilon=0}} = \exp\left[-\varepsilon^2 \gamma t\right] \ . \tag{61}$$

To put this into the context of transport, the observable $\mathcal{A}$ could for instance be the current $\mathcal{J}$ of some transport quantity. Recalling the discussions in Sec. II C 2, transport properties of the perturbed quantum system can be directly inferred from the behavior of the corresponding current autocorrelation functions $\langle \mathcal{J}(t)\mathcal{J} \rangle_{\varepsilon>0}$ by calculating the diffusion coefficient with Eq. (47). For instance, let the current be conserved in the unperturbed system, i.e., $[\,\mathcal{J}, \mathcal{H}_0\,] = 0$ and thus $\langle \mathcal{J}(t)\mathcal{J} \rangle_{\varepsilon=0} = \mathrm{const.}$, which implies a ballistic scaling of the diffusion coefficient, $D(t) \propto t$. Assuming an exponential damping of the form (61), the current autocorrelation function $\langle \mathcal{J}(t)\mathcal{J} \rangle_{\varepsilon>0}$ decays to zero and the diffusion coefficient remains effectively constant after some time τ, i.e., diffusion sets in with $D(t > \tau) = D$. The decay time τ and the final value of the diffusion constant D depend on the damping rate γ and the perturbation strength ε.

Naturally, simple damping functions like the exponential damping described in Eq. (61) cannot be universally expected in every single instance, although their enhanced immanent stability against generic perturbations gives grounds to expect a certain prevalence of such types of relaxation dynamics [44]. Specifically, it remains unclear how frequent and under which conditions counterexamples to the exponential damping occur. Pub. [P6] studies the effect of perturbations on dynamics from the perspective of projection-operator techniques, which will be introduced in Sec. II D 5. In particular, the possibility of nontrivial damping is discussed and illustrated with numerical simulations in an exemplary physical model (see also Sec. III [P6]).

D. Numerical and (Semi-)Analytical Toolkit

This section will provide an overview over all methods that were used in the works presented in this thesis.

1. Exact Diagonalization

The most straightforward yet powerful numerical approach to quantum physics is to solve the stationary Schrödinger equation,

$$\mathcal{H} |\Psi\rangle = E |\Psi\rangle \ , \tag{62}$$

directly by numerical exact diagonalization (ED) of the matrix representation of the Hamiltonian $\mathcal{H}$. The obtained eigenstates $|n\rangle$ and corresponding energy eigenvalues E_n fulfill the eigenvalue equation

$$\mathcal{H} |n\rangle = E_n |n\rangle \ . \tag{63}$$

With knowledge of the full eigensystem of $\mathcal{H}$, the trace operation in the calculation of expectation values as described in Sec. II B can be conveniently carried out in the energy eigenbasis. This greatly reduces the computational complexity in the calculation of both thermodynamic and dynamic quantities. In particular, Eq. (27) reduces to a simple sum over the eigenstates,

$$\langle \mathcal{A} \rangle_{\mathrm{eq}} = \frac{1}{\mathcal{Z}_\beta} \mathrm{Tr}\left[\mathrm{e}^{-\beta\mathcal{H}} \mathcal{A}\right] \tag{64}$$

$$= \left(\sum_n \underbrace{\langle n| \mathcal{A} |n\rangle}_{\mathcal{A}_{nn}} \mathrm{e}^{-\beta E_n}\right) \Big/ \left(\sum_n \mathrm{e}^{-\beta E_n}\right)$$

where the $\mathcal{A}_{nn}$ are the diagonal matrix elements of $\mathcal{A}$ in the energy eigenbasis. Similarly, Eq. (32) takes on the form

$$\langle \mathcal{A}(t) \rangle = \mathrm{Tr}\left[\rho(t) \mathcal{A}\right] \tag{65}$$

$$= \sum_{n,m} \underbrace{\langle n| \rho(0) |m\rangle}_{\rho_{nm}} \underbrace{\langle m| \mathcal{A} |n\rangle}_{\mathcal{A}_{mn}} \mathrm{e}^{i(E_n - E_m)t} \ .$$

Certainly, while the above calculations on its own are very inexpensive, ED itself is in turn very demanding and (mainly for its memory requirements) only feasible for matrix sizes of about $10^5 \times 10^5$ or less on customary workstations. Still, not least due to its reliability and unbiasedness, ED remains an important tool for, e.g., benchmarks of other approximate techniques.

2. Quantum Typicality

One important tool harnessed in most of the work here is the concept of quantum typicality, which will be briefly introduced in the following. A more in-depth review of this technique is covered by Pub. [P2], which can be read

supplementary to this section. The central statement of typicality is that a single pure quantum state can imitate the full statistical ensemble or, in other words, that the expectation values of typical pure states are very close to the expectation values of the ensemble [18–21, 51, 72]. Simply put, typicality allows to replace the trace in the canonical ensemble average (27) by a scalar product involving a single pure state $|\phi_\beta\rangle$,

$$\mathrm{Tr}\left[\rho_\beta \mathcal{A}\right] = \langle\phi_\beta|\mathcal{A}|\phi_\beta\rangle + \epsilon \ , \tag{66}$$

with

$$|\phi_\beta\rangle = \frac{\sqrt{\rho_\beta}\,|\phi\rangle}{\sqrt{\langle\phi|\,\rho_\beta\,|\phi\rangle}} \ . \tag{67}$$

Compared to the trace operation over all eigenstates of the system, the computational cost of this trace estimation is greatly reduced. The so-called typical reference state $|\phi\rangle$ is constructed as a random superposition of states $|k\rangle$ in any arbitrary orthonormal basis,

$$|\phi\rangle = \sum_{k=1}^{d^L} c_k\,|k\rangle \ , \tag{68}$$

where the complex coefficients c_k are randomly drawn from a distribution which is invariant under all unitary transformations in the Hilbert space (Haar measure) [52, 73]. In practice, the real and imaginary parts of these coefficients can be drawn independently from a standard normal distribution, though other distributions work as well [54, 57, 74].

Importantly, the statistical error $\epsilon = \epsilon(|\phi\rangle)$ arising in Eq. (66) has zero mean and a standard deviation that is bounded from above,[13]

$$\sigma(\epsilon) < \mathcal{O}\left(\frac{1}{\sqrt{\mathcal{Z}_{\mathrm{eff}}}}\right) \ , \tag{69}$$

where the partition function $\mathcal{Z}_{\mathrm{eff}} = \mathrm{Tr}\left[\mathrm{e}^{-\beta(\mathcal{H}-E_0)}\right]$ with ground-state energy E_0 embodies the effective Hilbert-space dimension for finite temperatures. In the limit of high temperatures, $\lim_{\beta\to 0}\mathcal{Z}_{\mathrm{eff}} = d^L$. As a consequence, ϵ decreases exponentially with increasing system size L, which renders the approximation (66) close to exact already for moderate system sizes. This exponential decrease of ϵ is expected to slow down for finite temperatures $\beta > 0$. To further reduce the typicality error, the calculation can additionally be averaged over multiple random states. More details on typicality errors can be found in, e.g., Refs. [57, 75–77]. The finite-size scaling and temperature dependence of typicality errors is the

main focus of the work published in Ref. [P3], which will be introduced in Sec. III [P3].

The typicality concept can be extended to the calculation of dynamical quantities as well and is referred to as dynamical quantum typicality (DQT) in this context. It essentially states that if two pure states feature the same expectation value at some point in time, they will most likely continue to do so after some arbitrarily long time evolution [52, 53]. For example, time-dependent correlation functions like those introduced in Eq. (34) can by calculated as

$$\langle\mathcal{A}(t)\mathcal{A}'\rangle_{\mathrm{eq}} = \mathrm{Tr}\left[\rho_\beta\,\mathcal{A}(t)\mathcal{A}'\right] \tag{70}$$
$$= \langle\varphi_\beta(t)|\mathcal{A}|\phi_\beta(t)\rangle + \epsilon$$

using the two auxiliary pure states

$$|\varphi_\beta(t)\rangle = \mathrm{e}^{-i\mathcal{H}t}\mathcal{A}'|\phi_\beta\rangle \tag{71}$$
$$\text{and}\quad |\phi_\beta(t)\rangle = \mathrm{e}^{-i\mathcal{H}t}|\phi_\beta\rangle \ .$$

The time evolution of these pure states can be efficiently obtained by iterative forward propagation, which will be discussed in the next section.

Overall, typicality has proven to be a powerful and versatile tool for the numerical treatment of various problems and systems, with basically the only prerequisite being the large (effective) Hilbert-space dimension. Recent work even describe possible applications of typicality in the context of noisy intermediate-scale quantum (NISQ) devices [57, 78].

3. Pure-State Propagation

Due to DQT, the principal computational cost in the study of many-body quantum dynamics can be essentially reduced to the time evolution of pure states. The latter is described by the time-dependent Schrödinger equation,

$$\frac{\partial}{\partial t}|\psi(t)\rangle = -i\mathcal{H}|\psi(t)\rangle \ , \tag{72}$$

which is solved by employing the time-evolution operator $\mathcal{U}(t) = \mathrm{e}^{-i\mathcal{H}t}$,

$$|\psi(t)\rangle = \mathrm{e}^{-i\mathcal{H}t}|\psi(0)\rangle \ . \tag{73}$$

Numerically, this time evolution is discretized into small time steps δt and thus achieved by an iterative forward propagation with respect to $\mathcal{U}(\delta t)$. There is a variety of methods available to efficiently evaluate the action of $\mathcal{U}(\delta t)$ on $|\psi\rangle$ by approximation, including Chebyshev polynomials [79–82], Krylov-space techniques [83], and Trotter decompositions [84, 85]. Here, we mainly use a fourth-order Runge-Kutta scheme [86, 87], which essen-

---

[13] Assuming that $\mathcal{A}$ is a local operator (or a low-degree polynomial in system size as, e.g., a sum of L local operators).

tially is a Taylor expansion of $\mathcal{U}(\delta t)$ to fourth order,

$$|\psi(t + \delta t)\rangle = \mathrm{e}^{-i\mathcal{H}\delta t} |\psi(t)\rangle \tag{74}$$

$$\approx \sum_{k=0}^{4} \frac{(-i\mathcal{H}\delta t)^k}{k!} |\psi(t)\rangle \ .$$

All methods above operate on the basis of repetitive matrix-vector multiplications and thus benefit from the sparse matrix structure of generic Hamiltonians with few-body interactions. In particular, the greatly reduced memory requirement for the matrix storage pushes the limit of accessible system sizes substantially beyond the scope of ED. In memory-critical applications, the matrix elements could even be calculated on the fly without saving them in memory.

In analogy to the evolution in real time, the finite-temperature state

$$|\psi_\beta\rangle = \mathrm{e}^{-\beta\mathcal{H}/2} |\psi\rangle \tag{75}$$

is obtained by means of an iterative forward propagation in small steps of the inverse temperature β. Since this imaginary-time evolution does not conserve the norm of the state, corresponding countermeasures might be necessary to ensure sufficient accuracy in the numerics.

4. Numerical Linked-Cluster Expansion

In the framework of numerical linked-cluster expansions (NLCE) [88, 89], the per-site value of an extensive quantity on an infinite lattice can be expanded as a sum over its respective weights W_c calculated on all linked (sub-)clusters c,

$$\lim_{L \to \infty} \langle X(t)\rangle = \sum_c \mathcal{L}_c W_c(t) \ . \tag{76}$$

The multiplicity factor $\mathcal{L}_c$ above accounts for topologically, symmetrically, or otherwise computationally equivalent clusters and avoids redundant calculations in clusters yielding the same weight. For each cluster c, its weight is calculated via an inclusion-exclusion principle,

$$W_c(t) = \langle X(t)\rangle^{(c)} - \sum_{s \subset c} W_s(t) \ , \tag{77}$$

where the weights of all subclusters $s \subset c$ are subtracted from the finite-size value of the desired quantity $\langle X(t)\rangle^{(c)}$ calculated on cluster c. Limited by the available computational resources, the expansion in Eq. (76) has to be truncated to a maximum cluster size $c_{\max}$. Due to this truncation, the NLCE yields reliable results up to a certain maximum time, which increases with the maximum

cluster size $c_{\max}$ included in the expansion [58, 90, 91].[14] Here, DQT proves itself particularly useful to treat cluster sizes as large as possible. Since NLCE can be sensitive to small statistical errors in the DQT results, additional averaging over multiple random states might be necessary.

For onedimensional lattices, the only linked subclusters of the lattice are open-boundary chains of different lengths with multiplicity factor $\mathcal{L}_c = 1$. After application of Eq. (77), the truncated expansion reduces to the simple expression

$$\sum_{c=2}^{c_{\max}} W_c(t) = \langle X(t)\rangle^{(c_{\max})} - \langle X(t)\rangle^{(c_{\max}-1)} \ , \tag{78}$$

i.e., the thermodynamic limit of $\langle X(t)\rangle$ can be approximated by taking the difference of the corresponding finite-size values on the two largest clusters with $c_{\max}$ and $c_{\max} - 1$.

Beyond onedimensional systems, the NLCE approach quickly gets more demanding; not solely because of the rapidly increasing cluster sizes to treat, but rather due to the immense combinatorial task of identifying all linked clusters in higher dimensions. Therefore, it may be worth to make use of the freedom to choose different expansion types, i.e., to reorganize the sum in Eq. (76) to cut away certain types of subclusters with the truncation. For example, in two dimensions, the expansion may be restricted exclusively to rectangular clusters. This way, the variety in subclusters to take into account in the calculation of the weight $W_{(x,y)}$ of one particular rectangular cluster $c = (x, y)$ of $L = xy$ sites is greatly reduced and leaves the manageable expression [93]

$$W_{(x,y)}(t) = \langle X(t)\rangle_{(x,y)} \tag{79}$$

$$- \sum_{x'=1}^{x} \sum_{\substack{y'=1 \\ x'y' < xy}}^{y} (x - x' + 1)(y - y' + 1) W_{(x',y')} \ .$$

Taking into account the numbers of possible translations for a particular finite rectangular cluster on an infinite square lattice conveniently yields the corresponding multiplicity factor $\mathcal{L}_c = 1$ in the expansion (76) in rectangular clusters. This expansion type has been successfully used in the past for entanglement studies [94] and is central to Pub. [P5], where it is applied to study quantum quench dynamics in the transverse-field Ising model (10), see also Sec. III [P5].

----

[14] NLCEs are also commonly used to calculate thermodynamic quantities. Here, the convergence of the truncated expansion is improved to lower temperatures with increasing $c_{\max}$ [89, 92].

5. Time-Convolutionless Projection Operator Technique

The time-convolutionless (TCL) projection-operator technique is applied in a perturbation scenario where a system described by the Hamiltonian $\mathcal{H}_0$ is perturbed by some operator $\mathcal{V}$ with strength ε,

$$\mathcal{H} = \mathcal{H}_0 + \varepsilon \mathcal{V} . \tag{80}$$

The core concept is to obtain the reduced dynamics of the system by projecting its density matrix onto the relevant degrees of freedom. This is achieved with the projection operator $\mathcal{P}$ defined by

$$\mathcal{P} \rho(t) = \frac{1}{d^L} + \frac{\langle \mathcal{A}\rho(t) \rangle}{\langle \mathcal{A}^2 \rangle} \mathcal{A} , \tag{81}$$

where $\mathcal{A}$ represents some observable of interest.[15] The TCL formalism then yields a time-local differential equation for the time evolution of the projected density matrix in the interaction picture [96, 97],

$$\frac{\partial}{\partial t} \mathcal{P}\rho_{\mathrm{I}}(t) = \mathcal{G}(t)\,\mathcal{P}\rho_{\mathrm{I}}(t) + \mathcal{I}(t)\,(1 - \mathcal{P})\,\rho(0) \tag{82}$$

with $\rho_{\mathrm{I}}(t) = e^{i\mathcal{H}_0 t}e^{-i\mathcal{H}t}\rho(0)e^{i\mathcal{H}t}e^{-i\mathcal{H}_0 t}$. By choosing the initial state $\rho(0)$ to be in the span of 1 and $\mathcal{A}$, the inhomogeneity on the right hand side of Eq. (82) vanishes due to $\mathcal{P}\rho(0) = \rho(0)$. Additionally, the time-dependent part of the projected density matrix in Eq. (81) can be related to certain types of correlation functions. In the Schrödinger picture, this is just the familiar autocorrelation function of $\mathcal{A}$,

$$C(t) = \langle \mathcal{A}\rho(t) \rangle \propto \langle \mathcal{A}(t)\mathcal{A} \rangle . \tag{83}$$

In the interaction picture, the related correlation function has a more complicated time dependence,

$$C_{\mathrm{I}}(t) = \langle \mathcal{A}\rho_{\mathrm{I}}(t) \rangle \propto \langle \mathcal{A}(t)\mathcal{A}_{\mathrm{I}}(t) \rangle . \tag{84}$$

Continuing with Eq. (82), the generator $\mathcal{G}(t)$ is expanded in powers of the perturbation strength,

$$\mathcal{G}(t) = \sum_{k=1}^{\infty} \varepsilon^k \mathcal{G}_k(t) , \quad \mathcal{G}_{2k-1} = 0 , \tag{85}$$

where odd orders usually vanish, as in all cases considered here. Thus, to lowest order,

$$\frac{\partial}{\partial t} \mathcal{P}\rho_{\mathrm{I}}(t) = \varepsilon^2 \mathcal{G}_2(t)\,\mathcal{P}\rho_{\mathrm{I}}(t) , \tag{86}$$

where

$$\mathcal{G}_2(t) = \varepsilon^2 \int_0^t \mathrm{d}t'\, \mathcal{P}\mathcal{L}(t)\mathcal{L}(t')\mathcal{P} \tag{87}$$

with the Liouvillian superoperator $\mathcal{L}(t)\bullet = -i[\mathcal{V}_{\mathrm{I}}(t), \bullet]$ and $\mathcal{V}_{\mathrm{I}}(t) = e^{i\mathcal{H}_0 t}\,\mathcal{V}(0)\,e^{-i\mathcal{H}_0 t}$. This leads to a rate equation for the time evolution of Eq. (84) in the interaction picture,

$$\frac{\partial}{\partial t} \langle \mathcal{A}(t)\mathcal{A}_{\mathrm{I}}(t) \rangle = -\varepsilon^2\, \gamma_2(t)\, \langle \mathcal{A}(t)\mathcal{A}_{\mathrm{I}}(t) \rangle , \tag{88}$$

where the corresponding time-dependent damping rate $\gamma_2(t)$ is calculated from

$$\gamma_2(t) = \int_0^t \mathrm{d}\tau\, k_2(\tau) \tag{89}$$

with the second-order kernel $k_2(\tau)$,

$$k_2(\tau) = \frac{\langle i[\mathcal{A}, \mathcal{V}_{\mathrm{I}}(\tau)]i[\mathcal{A}, \mathcal{V}_{\mathrm{I}}] \rangle}{\langle \mathcal{A}^2 \rangle} . \tag{90}$$

If the kernel decays and stays zero after some time τ', $k_2(\tau > \tau') = 0$, the damping rate assumes a constant value, $\gamma_2(\tau > \tau') = \mathrm{const.}$, afterwards.

Finally, Eq. (88) is solved by an exponential decay of the correlation function $\langle \mathcal{A}(t)\mathcal{A}_{\mathrm{I}}(t) \rangle$,

$$\frac{\langle \mathcal{A}(t)\mathcal{A}_{\mathrm{I}}(t) \rangle}{\langle \mathcal{A}^2 \rangle} = \exp\left[-\varepsilon^2 \int_0^t \mathrm{d}t'\, \gamma_2(t') \right] . \tag{91}$$

Consequently, with knowledge of the kernel k_2 and the reference dynamics with respect to the unperturbed $\mathcal{H}_0$, the dynamics for different perturbation strengths ε can be produced without much effort. In contrast, calculating the correlation functions $\langle \mathcal{A}(t)\mathcal{A}_{\mathrm{I}}(t) \rangle$ directly for various values of ε would require substantially more work. If we were to employ DQT, the calculation could be done in analogy to Eq. (70),

$$\langle \mathcal{A}(t)\mathcal{A}_{\mathrm{I}}(t) \rangle = \frac{\langle \phi(t)|\,\mathcal{A}\,|\varphi(t)\rangle}{\langle \phi|\phi\rangle} + \epsilon \tag{92}$$

with the auxiliary pure states

$$|\phi(t)\rangle = e^{-i\mathcal{H}t}\,e^{i\mathcal{H}_0 t}\,|\phi\rangle \tag{93}$$
$$\text{and} \quad |\varphi(t)\rangle = e^{-i\mathcal{H}t}\,e^{i\mathcal{H}_0 t}\mathcal{A}\,|\phi\rangle$$

using the typical state (68). Numerically calculating the time dependence of these states is considerably more demanding compared to Eq. (70), since each time step involves an additional backwards propagation with respect to the reference Hamiltonian $\mathcal{H}_0$.

The TCL technique is typically used in situations where the observable of interest is conserved under the

---

[15] This projection can be extended to additional observables by adding $\sum_i \left(\langle \mathcal{A}_i\rho(t) \rangle / \langle \mathcal{A}_i^2 \rangle \right) \mathcal{A}_i$. All operators $\{1, \mathcal{A}, \mathcal{A}_i\}$ participating in the projection are without loss of generality assumed to be orthogonal under the trace operation, $\langle \mathcal{A} \rangle = \langle \mathcal{A}_i \rangle = \langle \mathcal{A}\mathcal{A}_i \rangle = \langle \mathcal{A}_i\mathcal{A}_{j\neq i} \rangle = 0$ [95].

reference Hamiltonian, i.e., when $[\mathcal{A}, \mathcal{H}_0] = 0$. In this case, since $\mathcal{A}_\mathrm{I}(t) = \mathcal{A}$, the exponential damping in Eq. (91) carries over to the standard autocorrelation function $\langle \mathcal{A}(t)\mathcal{A} \rangle$. For small enough time scales, this is still reasonable to assume in situations where $\mathcal{A}$ may not be conserved under $\mathcal{H}_0$, but shows sufficiently slow dynamics, i.e., $[\mathcal{A}, \mathcal{H}_0] \approx 0$. Additionally, the expression for the damping kernel $k_2(t)$ in Eq. (90) can be simplified and calculated with DQT in analogy to Eq. (70),

$$k_2(t) \propto \langle \mathcal{K}_\mathrm{I}(t)\mathcal{K} \rangle = \frac{\langle \phi(t)|\, \mathcal{K}\, |\varphi(t) \rangle}{\langle \phi | \phi \rangle} + \epsilon\ . \qquad (94)$$

We define $\mathcal{K} = [\mathcal{A}, \mathcal{V}]$ and $\mathcal{K}_\mathrm{I}(t) = e^{i\mathcal{H}_0 t}\mathcal{K}e^{-i\mathcal{H}_0 t}$ and use the two auxiliary states

$$|\phi(t)\rangle = e^{-i\mathcal{H}_0 t}\,|\phi\rangle \qquad (95)$$
$$\text{and}\quad |\varphi(t)\rangle = e^{-i\mathcal{H}_0 t}\mathcal{K}\,|\phi\rangle$$

where $|\phi\rangle$ again is the typical state (68). When $\mathcal{A}$ is not conserved under the reference Hamiltonian, i.e., when $[\mathcal{A}, \mathcal{H}_0] \neq 0$, the damping kernel can still by obtained with DQT in a similar fashion. With some rearrangements of the commutators in Eq. (90) and a different set of auxiliary states,

$$|\phi(t)\rangle = e^{-i\mathcal{H}_o t}\,|\phi\rangle \qquad (96)$$
$$\text{and}\quad |\varphi(t)\rangle = e^{-i\mathcal{H}_0 t}\,[\mathcal{A}, [\mathcal{V}, \mathcal{A}]]\,|\phi\rangle\ ,$$

we find

$$k_2(t) \propto \langle [\mathcal{A}, \mathcal{V}_\mathrm{I}(t)]\,[\mathcal{A}, \mathcal{V}] \rangle \qquad (97)$$
$$= \frac{\langle \phi(t)|\, \mathcal{V}\, |\varphi(t) \rangle}{\langle \phi | \phi \rangle} + \epsilon\ .$$

From a numerical point of view, this formulation is especially handy if the perturbation $\mathcal{V}$ is diagonal in the employed working basis.

Let us conclude this introduction of the TCL technique with a short remark on the roles of the correlation functions in Eqs. (83) and (84). Naturally, the interest is primarily on the standard autocorrelation function $\langle \mathcal{A}(t)\mathcal{A} \rangle$, which is why TCL is usually employed in situations where $[\mathcal{A}, \mathcal{H}_0] \approx 0$. Otherwise, in cases where $[\mathcal{A}, \mathcal{H}_0] \neq 0$, the corresponding correlation function $\langle \mathcal{A}(t)\mathcal{A}_\mathrm{I}(t) \rangle$ yields no immediate information on the more physical quantity $\langle \mathcal{A}(t)\mathcal{A} \rangle$. However, from a conceptional point of view, it still does provide interesting insights into the damping mechanism in that scenario, see Pub. [P6] and Sec. III [P6] for more information.

6. Symmetry-Adapting Procedure

Any numerical treatment of quantum many-body systems, regardless of its particular nature, is in one way or another ultimately limited by the exponential growth of the underlying Hilbert-space dimension. To alleviate this, one often resorts to the use of symmetries like those discussed in Sec. II A 4 in order to push the limit of computationally available system sizes. The basic underlying strategy here is to carry out calculations in smaller symmetry-invariant subspaces of the Hilbert space by transforming to a symmetry-adapted basis. With this transformation, the Hamiltonian matrix is brought to a block diagonal form (sketched below), where each block is assigned to a different value of a conserved quantum number Q and can be treated independently.
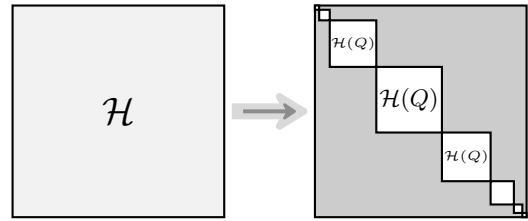
Some symmetries can be conveniently employed by simply choosing an appropriate orthonormal basis from the start, as is the case for the continuous spin-rotational $U(1)$ and $SU(2)$ symmetries in the Heisenberg spin model introduced in Sec. II A 4. For example, given a spin-s chain of length L, the product basis

$$\mathcal{B}_{U(1)} = \left\{ |m_1, \ldots, m_L\rangle \,\middle|\, m_r \in \{-s, \ldots, s\} \right\} \qquad (98)$$

is constructed from all eigenstates $|m_r\rangle$ of the local s_r^z operators.[16] This is also the eigenbasis of the total S^z operator and therefore already adapted to the corresponding $U(1)$ symmetry by design. The block diagonal form of $\mathcal{H}$ is thus conveniently achieved by sorting the states $|m_1, \ldots, m_L\rangle$ according to their total magnetic quantum number $M = \sum_r m_r$. Corresponding subspace dimensions $\dim \mathbb{H}(M)$ can be found in a combinatorial manner.

A symmetrized basis with respect to the $SU(2)$ symmetry can be formed from the eigenstates of the associated total spin operator $\mathbf{S}^2$,

$$\mathcal{B}_{SU(2)} = \left\{ |\alpha S M\rangle \right\}, \qquad (99)$$

which is an eigenbasis of S^z as well, since $U(1)$ is a subgroup of $SU(2)$. Sorting the states $|\alpha S M\rangle$ with respect to the total spin quantum number S and additionally by M then splits the block diagonal form of $\mathcal{H}$ into even smaller blocks, compared to using $\mathcal{B}_{U(1)}$. Furthermore,

---

[16] For the sake of a cleaner notation, the spin quantum number s is dropped here.

invoking the *Wigner-Eckart theorem*, the matrix blocks are actually independent of M and it suffices to consider only the subspaces with, e.g., $S = M$. The basis states in $\mathcal{B}_{SU(2)}$ are constructed by coupling all L spins according to some arbitrary but fixed coupling scheme. Here, α contains the (possibly different) local spin quantum numbers s_r, arranged with an additional set of intermediate spin quantum numbers $\bar{S}_i$, to encode the coupling scheme and to distinguish different states of the basis. For instance, the basis states corresponding to four successively coupled spins read $|\alpha S M\rangle = |(((s_1, s_2)\bar{S}_1, s_3)\bar{S}_2, s_4)SM\rangle$. The set of possible intermediate spin quantum numbers is determined by the well-known fundamental spin coupling rule, where two spins s and s' are coupled to $\bar{S} \in \{|s - s'|, |s - s'| + 1, \ldots, s + s'\}$. It should be mentioned that implementing the matrix representation of the Heisenberg spin Hamiltonian with respect to the basis $\mathcal{B}_{U(1)}$ using the form Eq. (6) is a straightforward task, while in the basis $\mathcal{B}_{SU(2)}$ some extra work is required. Specifically, the Hamiltonian has to be expressed in terms of irreducible tensor operators that are connected to compound tensors according to the same coupling scheme as the states $|\alpha S M\rangle$ (see Ref. [98] and references therein). In principle, a change of basis between $\mathcal{B}_{U(1)}$ and $\mathcal{B}_{SU(2)}$ can be achieved with the help of a transformation matrix comprised of a multitude of Clebsch-Gordan coefficients.

Other symmetries, like the discrete lattice symmetries mentioned in Sec. II A 4, may involve a more complicated symmetry adapting procedure, although it can be stated in a very general manner. A universal understanding of this procedure requires a little detour into the realm of group and representation theory, which is narrowed down to the theoretical minimum below. Let G be a discrete group of symmetry operations g commuting with the Hamiltonian $\mathcal{H}$,

$$[\mathcal{H}, \mathcal{D}(g)] = 0 \quad \forall g \in G . \tag{100}$$

$\mathcal{D}(g)$ denotes the operator associated with the symmetry operation g acting on the same Hilbert space as the Hamiltonian $\mathcal{H}$. As a central result from group theory, the representation of $\mathcal{D}(g)$ with respect to any orthonormal basis $\{|\Psi_i\rangle \,|\, i = 1, \ldots, d^L\}$ is in general reducible, meaning that it can be simultaneously block-diagonalized for all g. In other words, the Hilbert space $\mathbb{H}$ can be decomposed into smaller subspaces $\mathbb{H}(k)$ that are invariant under all symmetry transformations contained in G. Here, k labels different irreducible representations (irreps) of G. Amongst other properties, their dimensions d_k as well as their characters[17] $\Gamma^{(k)}(g)$ associated with each group element g are completely known for any finite group. The corresponding basis states $|\Psi_i^{(k)}\rangle$ can be

obtained by applying the symmetry projection operator

$$\mathcal{P}^{(k)} = \frac{d_k}{|G|} \sum_{g \in G} \overline{\Gamma^{(k)}}(g) \mathcal{D}(g) \tag{101}$$

to the initial basis states $|\Psi_i\rangle$, where $|G|$ is the order of the group and $\overline{\Gamma}$ denotes the complex conjugate of Γ. Importantly, with Eq. (100), the matrix representation of $\mathcal{H}$ transforms into the same block-diagonal shape as for the $\mathcal{D}(g)$ when using the symmetrized basis $|\Psi_i^{(k)}\rangle$.

The simplest example for the symmetry projection (101) is the (anti-)symmetrization of any two-particle wave function $\Psi(x_1, x_2)$ to obtain

$$\Psi^\pm(x_1, x_2) = \tfrac{1}{2} \left[\Psi(x_1, x_2) \pm \Psi(x_2, x_1) \right] , \tag{102}$$

which are eigenstates of the operator $\mathcal{S}$ exchanging the two particles,

$$\mathcal{S}\Psi^\pm(x_1, x_2) = \pm \Psi^\pm(x_2, x_1) . \tag{103}$$

The underlying symmetry group here is the cyclic group of order two, $\mathbb{Z}_2$, with $d_k = 1$ and characters $\Gamma^{(k)}(g) = \pm 1$.

Another commonly used symmetry is the translational symmetry of lattice systems with periodic boundary conditions, generated by the operator $\mathcal{T}$ that shifts each site $r \to r + 1$. The characters of the associated symmetry group C_L are given by the L-th roots of unity

$$\Gamma^{(k)}(\mathcal{T}^l) = \mathrm{e}^{\frac{2\pi i k l}{L}} \tag{104}$$

with $k, l = 0, \ldots, L - 1$. With this, the projection operator

$$\mathcal{P}_{C_L}^{(k)} = \frac{1}{L} \sum_{l=0}^{L-1} \overline{\Gamma^{(k)}}(\mathcal{T}^l) \, \mathcal{T}^l \tag{105}$$

yields the symmetrized basis states for L invariant subspaces of approximately equal dimension [99].

In principle, the exploitation of symmetries by means of the projection operator (101) is very straightforward from a mathematical point of view. However, the actual numerical implementation may get quite challenging with various hurdles and subtleties emerging along the way to potentially obstruct the benefits of the symmetry reduction. For instance, the action of the projection operator (101) on the states of a given basis set may be very complicated and difficult to handle numerically. Publication [P1] is exclusively dedicated to one particular example, where the spin-rotational symmetry and the translational symmetry of isotropic spin systems are combined, see also Sec. III [P1].

---

[17] The character of an irrep is a complex number and given by its trace.

III.   GUIDE TO PUBLICATIONS

This section gives an overview over the work that has been published in Refs. [P1–P6] and a brief discussion of the results presented therein. Refs. [P1–P3, P5] focus on rather methodological aspects such as details of the quantum typicality approach, symmetry adaptation and NLCE studies in two dimensions. With a stronger link to physical questions in the broader context of transport dynamics in quantum lattice models, Refs. [P4] and [P6] came about in the context of localization and perturbation effects on dynamics, as outlined in Secs. II C 3 and II C 4.

[P1].   Combined Use of Translational and Spin-Rotational Invariance for Spin Systems

The work published in Pub. [P1] originated in the pre-PhD phase and addresses the simultaneous utilization of two available symmetries. Specifically, the spin-rotational $SU(2)$ symmetry is used in combination with the translational symmetry C_L to enable the complete exact diagonalization of comparatively large isotropic Heisenberg spin rings. To this end, the $SU(2)$-invariant basis $\mathcal{B}_{SU(2)}$ described in Sec. II D 6 serves as a starting point and is adapted to the translational symmetry C_L by application of the corresponding symmetry projection operator (105). As indicated earlier, the application of the symmetry projection to the states of $\mathcal{B}_{SU(2)}$, though mathematically straightforward, entails some intricacies in the practical implementation. The main difficulty here is that the translated states $\mathcal{T}^l \, | \, \alpha SM \, \rangle$ arising in the projection generally belong to different basis sets $\mathcal{B}'_{SU(2)}$ since the defining coupling scheme is changed by each translation. For example, considering the state $| \, \alpha SM \, \rangle = | \, (((s_1, s_2)\bar{S}_1, s_3)\bar{S}_2, s_4)SM \, \rangle$, one translation yields $\mathcal{T} \, | \, \alpha SM \, \rangle = | \, (((s_2, s_3)\bar{S}'_1, s_4)\bar{S}'_2, s_1)SM \, \rangle$. In order to proceed with the translated states, they have to be expressed in terms of the basis states in the original coupling scheme,

$$\mathcal{T}^l \, | \alpha SM \rangle = \sum_{\alpha'} | \alpha' SM \rangle \, \langle \alpha' SM | \, \mathcal{T}^l \, | \alpha SM \rangle \ .$$

This is a crucial difference compared to the basis $\mathcal{B}_{U(1)}$, where each translated state yields just another state from the same basis set,

$$\mathcal{T} \, | \, m_1, \ldots, m_{L-1}, m_L \, \rangle = | \, m_2, \ldots, m_L, m_1 \, \rangle \ .$$

For that reason, translational symmetries are very commonly applied in the basis $\mathcal{B}_{U(1)}$, whereas $\mathcal{B}_{SU(2)}$ is rarely used in combination with any point-group symmetries (see, e.g., Ref. [98] and references therein), if at all. The computational cost of the symmetry adaption in the basis $\mathcal{B}_{SU(2)}$ strongly depends on the complexity of the so-called recoupling coefficients $\langle \alpha' SM | \mathcal{T}^l | \alpha SM \rangle$ and

could potentially exceed the cost of just using the original basis $\mathcal{B}_{SU(2)}$ without any additional symmetries. The key for a beneficial combination of C_L and $SU(2)$ is to find a coupling scheme that itself obeys the given real-space symmetry as closely as possible and therefore produces simple recoupling coefficients. For small point groups containing just a few reflections and or rotations, like D_2 and D_4, this can easily be achieved. However, the more symmetries are taken into account, the more difficult it gets to find a suitable coupling scheme. For C_L (as well as presumably other symmetry groups), a suited coupling scheme was found to be one comprising a hierarchical structure with equally sized groups of coupled (intermediate) spins on each level. The respective group sizes should be as small as possible and are thus given by the prime factors of the system size L. Combined with the right arrangement of the original spins in the coupling tree, the coupling scheme is only locally affected by a translation of all sites (see exemplary sketch below). This effect is the strongest for system sizes containing small prime factors, with the ideal case being $L = 2^n$ with $n \in \{2, 3, 4, \ldots\}$.
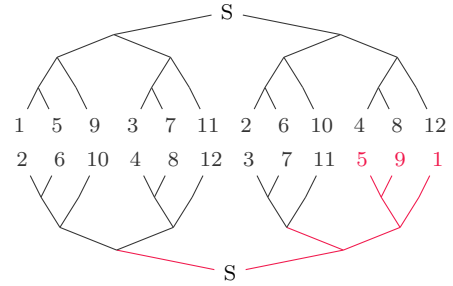
The publication also includes some illustrating numerical results, showing energy spectra as well as thermodynamic observables obtained from the exact diagonalization of comparably large spin systems.

It is worth pointing out some possible future directions where the results in Pub. [P1] could be employed, particularly in combination with other concepts discussed in this thesis. Recalling the introduction of quantum typicality in Sec. II D 2, the typical reference states (68) can be constructed in any orthonormal basis, including the symmetry adapted basis $\mathcal{B}_{SU(2)}$. Of course, to really benefit from the corresponding symmetry reduction, the observable of interest should possess the same symmetries as those incorporated in the symmetrized basis. Possible choices include energy currents or thermodynamic quantities such as heat capacity or magnetic susceptibility. Regarding the latter, other typicality-based techniques such as the finite-temperature Lanczos method (FTLM) could also be employed in the symmetrized basis $\mathcal{B}_{SU(2)}$. Either way, the sparseness of the matrix blocks of $\mathcal{H}$ is the key to go far beyond the treatable system sizes in ED. Then again, the sparseness heavily depends on the coupling scheme chosen for $\mathcal{B}_{SU(2)}$ (with and without additional point-group symmetries), see App. A 1 for a short demonstration. Lastly, any use case mentioned above

can potentially be combined with NLCE. Here, the use of lattice symmetries is very restricted, which in turn favors the higher spin-space symmetry $SU(2)$ against $U(1)$.

[P2]. Selected Applications of Typicality to Real-Time Dynamics of Quantum Many-Body Systems

Pub. [P2] essentially presents a reference guide to selected applications of the quantum typicality concept and can therefore be read in tandem with the brief introduction in Sec. II D 2. In particular, Pub. [P2] provides a detailed overview of implications of DQT for the calculation of the density of states (DOS) as well as dynamical quantities such as, e.g., time-dependent equilibrium correlation functions and far-from-equilibrium dynamics with possibly non-stationary Hamiltonians. Additionally, the versatility of DQT in combination with other (numerical or analytical) techniques is described by the example of NLCE (see also Sec. II D 4) and TCL (see also Sec. II D 5). Key aspects are demonstrated based on specific examples and accompanied by illustrative figures and plots showing data from previous publications.

[P3]. Finite-Size Scaling of Typicality-Based Estimates

Recalling the introduction of the typicality concept in Sec. II D 2, the canonical expectation value (27) of a given observable can be approximated by a single random state according to Eq. (66). The accuracy of this approximation is assessed on basis of Eq. (69), i.e., an upper bound for the standard deviation $\sigma(\epsilon)$ of the statistical error that arises during the random-state approximation of the trace. Similar estimates also exist for other closely related techniques that all rely on some kind of random-state based approach [57, 75, 76, 100]. In Pub. [P3], the accuracy of typicality-based estimates is probed numerically with a focus on (i) the full probability distribution of random-vector expectation values, as well as (ii) the full temperature dependence of corresponding standard deviations. As a testing ground, the magnetic susceptibility $\chi(T)$ [cf. Eq. (28)] and the heat capacity $C(T)$ [cf. Eq. (29)] are considered in various quantum spin systems.

In the first part of Pub. [P3], the probability distributions of random-vector expectation values are studied in the isotropic spin-1/2 Heisenberg chain (5) for different chain lengths $L \leq 20$ and inverse temperatures $\beta J = 0$ and $\beta J = 1$. To this end, a large sample of estimates

$$\frac{\langle r | \, \mathcal{A} \, \mathrm{e}^{-\beta \mathcal{H}} \, | r \rangle}{\frac{1}{R} \sum_{r=1}^{R} \langle r | \, \mathrm{e}^{-\beta \mathcal{H}} \, | r \rangle}$$

is obtained from $R \sim 10^4 - 10^6$ different random states $|r\rangle$ and subsequently collected in histograms. Starting in the high-temperature limit $\beta J = 0$, the resulting dis-
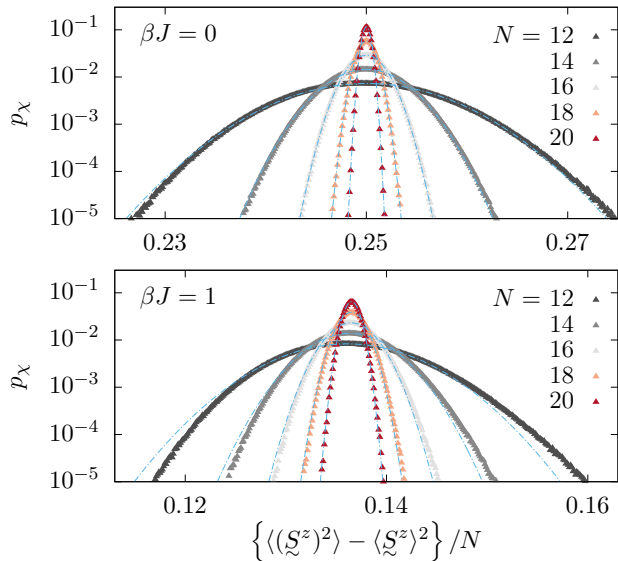

Figure 5. Exemplary plot of expectation-value distributions for the magnetic susceptibility at different temperatures adapted from Pub. [P3].

tributions are well described by Gaussian functions over several orders of magnitude, in line with Ref. [77]. Comparing the distributions for different system sizes L, the width of these Gaussians (i.e., the standard deviation) evidently decreases with the square root of the Hilbert-space dimension d^L, in accordance with Eq. (69). Switching to finite temperature $\beta J = 1$, a similar picture is observed, while the width of the distributions is generally larger and some asymmetry is visible for the broader distributions. Additionally, the standard deviation scales slower with system size L, due to the smaller effective Hilbert-space dimension $\mathcal{Z}_{\mathrm{eff}} < d^L$.

In the second part of Pub. [P3], the temperature dependence of the standard deviation $\sigma(\epsilon)$ is studied for various quantum spin models, including spin-$\frac{1}{2}$ and spin-1 Heisenberg chains, critical spin-$\frac{1}{2}$ delta chains, as well as cuboctahedra with spins $s = \frac{3}{2}$, 2, and $\frac{5}{2}$. A Krylov-space expansion is used to treat considerably larger system sizes, which in turn yield much narrower expectation value distributions. The results show the expected scaling of $\sigma(\epsilon) \propto 1/\sqrt{\mathcal{Z}_{\mathrm{eff}}}$ for sufficiently high temperatures. For very low temperatures, the scaling of the standard deviation becomes more complicated and depends on the specific model and observable under consideration. This fact notwithstanding, the trace estimation by random vectors is shown to provide very accurate approximations for thermodynamic observables and can, in any case, be improved by averaging over multiple independent random vectors.

[P4]. Density Dynamics in the Mass-Imbalanced Hubbard Chain

In the context of Sec. II C 3, the mass-imbalanced version of the Fermi-Hubbard model (11) with imbalance $\eta = t_\downarrow/t_\uparrow$ between the hopping amplitudes was introduced as a candidate for a translationally invariant quantum many-body system featuring localization. Pub. [P4] studies how this mass imbalance affects the equilibration dynamics of the lighter spin-$\uparrow$ particles by inspecting the dynamics of local densities

$$p_{r,\uparrow}(t) = \langle\psi(t)|\,n_{r,\uparrow}\,|\psi(t)\rangle \ ,$$

from the time evolution of pure states featuring a sharply peaked density profile at time $t = 0$. In particular, the initial states are prepared via the projection

$$|\psi(0)\rangle \propto n_{L/2,\uparrow}\,|\phi\rangle \ ,$$

where the state $|\phi\rangle$ is constructed as the typical random state (68). With this choice of $|\psi\rangle$, the initial profile of the local densities $p_{r,\uparrow}$ takes a peaked shape, similar to Eq. (49). Additionally, with typicality arguments, the obtained dynamics can be related to spatio-temporal equilibrium correlation functions,

$$p_{r,\uparrow}(t) - p_{\text{eq.}} = 2\,\langle(n_{L/2,\uparrow} - p_{\text{eq.}})[n_{r,\uparrow}(t) - p_{\text{eq.}}]\rangle + \epsilon \ .$$

Using an efficient pure-state propagation scheme for the time evolution (cf. Sec. II D 3) in combination with available symmetries, systems with sizes of up to $L = 15$ are simulated for various imbalance ratios $0 \leq \eta \leq 1$. The obtained data is assessed from multiple perspectives, such as the shape of the full density distributions for fixed times, the scaling of the corresponding spatial width, as well as the decay of density modes in momentum space (cf. Sec. II C 2).

Starting in the Falicov-Kimball limit, $\eta = 0$, the immobile spin-$\downarrow$ particles are expected to act as a static disorder potential[18] for the spin-$\uparrow$ particles, as outlined in Sec. II C 3. Indeed, in accordance with the anticipated Anderson localization, the initial density peak broadens just a little but stays concentrated around the center of the chain, while the spatial width remains constant at a value that corresponds to the Anderson localization length. In contrast, in the opposing limit of equal masses, $\eta = 1$, we see clean signatures of diffusion as also reported in Ref. [71]. In particular, the density pro-
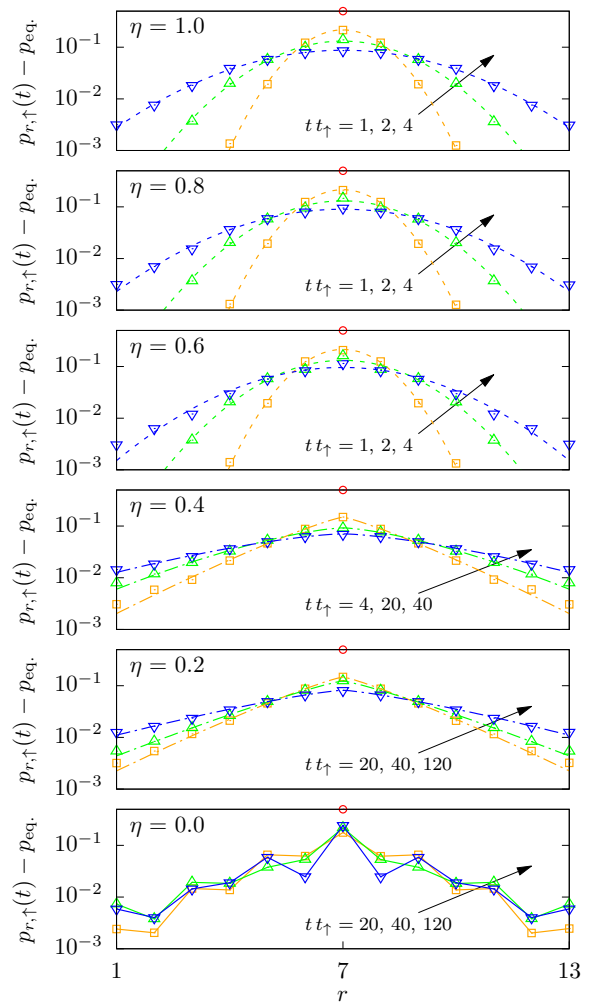
———

[18] On a side note, let us explore some interesting numerical implications of the Falicov-Kimball limit: In principle, we could make use of the occupation number conservation in this limit and decouple the computation into 2^L independent subspaces. However, in not doing so, we automatically average over all possible disorder realizations encoded in the superposition of all 2^L configurations of spin-$\downarrow$ particles, which may be seen as a digital quantum simulation of the random potential [101].

Figure 6. Exemplary plot of density profiles for different times and mass-imbalance ratios adapted from Pub. [P4].

files for fixed times t are very well described by Gaussian functions [cf. Eq. (50)], where the corresponding width $\Sigma(t)$ is obtained via Eq. (44). The spatial width in turn shows a diffusive scaling $\Sigma(t) \propto \sqrt{t}$. Additionally, a discrete Fourier transformation of the real-space density data according to Eq. (51) reveals exponentially decaying density modes in momentum space in line with Eq. (53). Away from the balanced limit, diffusive transport can still be observed for moderate imbalance ratios $\eta \gtrsim 0.6$, though first indications of a shift to anomalous diffusion become noticeable. A slight slowdown in the equilibration dynamics is apparent, hinting at a shift to anomalous diffusion with increasing imbalance. Indeed, moving to stronger imbalance ratios $\eta \lesssim 0.6$, the anomalous diffusion becomes more pronounced and manifests in an exponential shape of the density profiles and subdiffusive scaling of the spatial width, as well as significantly slower decaying density modes. However, for any finite imbalance ratio $\eta > 0$, the behavior is clearly distinct from the localizing case $\eta = 0$, as seen in a direct com-

parison of the dynamics of the central density $p_{L/2,\uparrow}(t)$, the spatial width $\Sigma(t)$, and the density mode $p_{q,\uparrow}(t)$ with $q = 2\pi/L$. For very small η, the corresponding curves may agree with the localizing limit $\eta = 0$ for some short time period, but they all separate and slowly start to equilibrate eventually. As discussed in more detail in Pub. [P4], this separation time can be interpreted as an η-dependent "lifetime" of the effective Anderson insulator, i.e., a time scale on which the heavy spin-↓ particles appear to be static to the spin-↑ particles. This lifetime is found to grow fast with decreasing η, but remain finite for any $\eta > 0$. Consequently, anomalous diffusion ultimately impedes localization for any finite mobility $t_\downarrow > 0$. This is in line with the results of Refs. [39, 43, 68] and in particular Ref. [102], where the mass-imbalanced Fermi-Hubbard model was recently probed experimentally.

[P5]. Quantum Quench Dynamics in the Transverse-Field Ising Model: A Numerical Expansion in Linked Rectangular Clusters

In Pub. [P5], the NLCE approach (cf. Sec. II D 4) is employed to study quantum quench dynamics in the transverse field Ising model (10) for different lattice geometries in one and two dimensions. Here, the physical scenario serves primarily as a test environment to evaluate the performance of the NLCE technique. In particular, an expansion comprising only rectangular clusters [cf. Eq. (79)] is tested in the twodimensional square lattice, where the time scales numerically attainable by other computational approaches are still comparatively short. The dynamics are obtained from the time evolution of initial states that are fully aligned in either the x- or the z-direction, $|\psi(0)\rangle = |\uparrow\rangle$ and $|\psi(0)\rangle = |\rightarrow\rangle$. These states are each eigenstates of the Ising Hamiltonian for either one of the limits $g = 0$ and $g \to \infty$, respectively. The dynamics of the transverse and longitudinal magnetization

$$\langle X(t)\rangle = \frac{1}{L}\sum_r \langle\psi(t)|\, s_r^x\, |\psi(t)\rangle$$

$$\text{and} \quad \langle Z(t)\rangle = \frac{1}{L}\sum_r \langle\psi(t)|\, s_r^z\, |\psi(t)\rangle$$

are studied for different finite values of g, where the states $|\uparrow\rangle$ and $|\rightarrow\rangle$ are no longer eigenstates of $\mathcal{H}$ and acquire a nontrivial time dependence. In order to simulate cluster sizes as large as possible while at the same time achieving sufficiently accurate results, the time evolution of the states $|\psi(t)\rangle$ is obtained by means of an efficient pure-state propagation via Chebyshev polynomials.

Starting in one dimension with the exactly solvable Ising chain, the NLCE is readily performed using Eq. (78). The obtained dynamics are compared to direct simulations of finite chains with open and periodic boundary conditions and additionally benchmarked against analytical results. As an intermediate step to-

wards two dimensions, quasi-onedimensional two- and three-leg ladders are studied, where the NLCE is still obtained by Eq. (78) using ladders of different lengths. Lastly, for the twodimensional square lattice, the NLCE is carried out in rectangular clusters following Eq. (79). In addition to the comparison to direct simulations of finite systems, the NLCE results are compared to other numerical results from relevant literature. In general, the data reveals good convergence times of the NLCE that gradually increase with the maximum chain length $c_{\max}$. In most cases, NLCE yields a better convergence to the thermodynamic limit than any direct simulations of finite systems, particularly when finite-size effects are comparatively strong. When applied to twodimensional lattices, NLCE is shown to be competitive to other state-of-the-art numerical methods. Additionally, the practical advantage of using the rectangular expansion is demonstrated in a direct comparison to a "full" NLCE comprising all (including nonrectangular) clusters.

[P6]. Nontrivial Damping of Quantum Many-Body Dynamics

As discussed in Sec. II C 4, the perturbation of a given Hamiltonian is often expected to give rise to an exponential damping of the dynamics governed by that Hamiltonian. Pub. [P6] studies the effect of perturbations on time-dependent correlation functions from the perspective of the TCL projection-operator technique (cf. Sec. II D 5). Within this framework, the first part of Pub. [P6] establishes the main result: perturbation-induced exponential damping may only emerge for the time-dependent part of the density matrix in the interaction picture, but not necessarily in the Schrödinger picture. As also evident from the descriptions in Sec. II D 5, the time-dependent part $C(t)$ of the projected density matrix is a central quantity within the TCL approach. The latter is innately formulated in the interaction picture and predicts an exponential damping of $C_{\mathrm{I}}(t)$ in the lowest-order contribution of an expansion in the perturbation strength ε. Relating $C(t)$ and $C_{\mathrm{I}}(t)$ to different kinds of correlation functions,

$$C(t) \propto \langle \mathcal{A}(t)\mathcal{A}\rangle$$

$$\text{and} \quad C_{\mathrm{I}}(t) \propto \langle \mathcal{A}(t)\mathcal{A}_{\mathrm{I}}(t)\rangle \ ,$$

the exponential damping can be equivalently expected for $\langle \mathcal{A}(t)\mathcal{A}_{\mathrm{I}}(t)\rangle$,

$$\frac{\langle \mathcal{A}(t)\mathcal{A}_{\mathrm{I}}(t)\rangle}{\langle \mathcal{A}^2\rangle} = \exp\left[-\varepsilon^2 \int\limits_0^t \mathrm{d}t'\, \gamma_2(t') \right] \ ,$$

but not necessarily for the "standard" correlation function $\langle \mathcal{A}(t)\mathcal{A}\rangle$. Only if the observable $\mathcal{A}$ commutes with $\mathcal{H}_0$, i.e., if $C(t) = C_{\mathrm{I}}(t)$, the TCL prediction carries over to $\langle \mathcal{A}(t)\mathcal{A}\rangle$. However, in general, the Schrödinger and
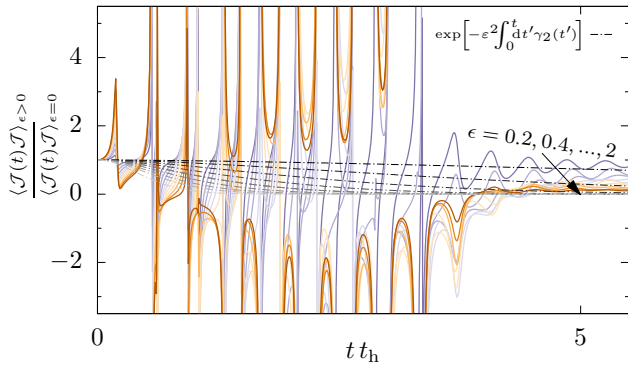
Figure 7. Exemplary plot of a nontrivial relation between perturbed and unperturbed dynamics adapted from Pub. [P6].

the interaction picture are not the same,[19]

$$\frac{\langle \mathcal{A}(t)\mathcal{A} \rangle_{\varepsilon>0}}{\langle \mathcal{A}(t)\mathcal{A} \rangle_{\varepsilon=0}} \neq \frac{\langle \mathcal{A}(t)\mathcal{A}_{\mathrm{I}}(t) \rangle}{\langle \mathcal{A}^2 \rangle} \ .$$

In particular, the relation between perturbed and unperturbed dynamics in the Schrödinger picture may be far from trivial when the dynamics in the unperturbed system possesses rich features.

The second part of Pub. [P6] provides illustrating results from numerical simulations of charge transport in the extended Fermi-Hubbard chain [cf. Eqs. (11)+(14)]. For two different perturbation scenarios, time-dependent correlation functions of the charge current $\mathcal{A} \equiv \mathcal{J}$ are calculated for different perturbation strengths ε using DQT [cf. Eqs. (70)+(92)]. In order to compare the DQT results to the lowest-order TCL prediction, the corresponding time-dependent kernel $k_2(t)$ is calculated according to Eq. (97) to obtain the damping rate $\gamma_2(t)$. While the DQT data is obtained for system sizes of up to $L = 16$, the behavior of the TCL damping rate $\gamma_2(t)$ in the limit $L \to \infty$ can be extrapolated from the finite-size scaling of the kernel $k_2(t)$.

First, a noninteracting reference Hamiltonian $\mathcal{H}_0$ is considered, where the charge current is conserved,

$$[\, \mathcal{J}, \mathcal{H}_0 \,] = 0 \quad \Rightarrow \quad C(t) = C_{\mathrm{I}}(t) \ .$$

Additional particle-particle interactions then act as a perturbation which leads to the decay of the current auto-correlation function $\langle \mathcal{J}(t)\mathcal{J} \rangle = \langle \mathcal{J}(t)\mathcal{J}_{\mathrm{I}}(t) \rangle$. This decay gets faster with increasing ε while changing from exponential to Gaussian relaxation for stronger ε, in line with the lowest-order TCL prediction. A direct comparison of the DQT and the TCL results shows a remarkably good agreement over a wide range of perturbation strengths, where small deviations might be either related to residual finite-size effects in the DQT data or missing higher-order corrections in the TCL results.

In the second perturbation scenario, a strongly interacting reference Hamiltonian is considered, where $\mathcal{J}$ is not conserved,

$$[\, \mathcal{J}, \mathcal{H}_0 \,] \neq 0 \quad \Rightarrow \quad C(t) \neq C_{\mathrm{I}}(t) \ ,$$

and the unperturbed dynamics of $\langle \mathcal{J}(t)\mathcal{J} \rangle$ instead exhibits strong oscillations. Perturbed by additional nearest-neighbor interactions, frequencies and zero crossings of these oscillations vary with the perturbation strength ε. The corresponding ratio between perturbed and unperturbed dynamics is thus highly nontrivial, as also shown in Fig. 7. Conversely, in the interaction picture, the behavior of the correlation function $\langle \mathcal{J}(t)\mathcal{J}_{\mathrm{I}}(t) \rangle$ for different perturbation strengths is comparable to the one observed in the first perturbation scenario and matches the lowest-order TCL prediction. The DQT results agree well with the TCL results, albeit with stronger finite-size effects inherited from the reference dynamics. Owing to the considerably higher computational cost in calculating the more complicated correlation function $\langle \mathcal{J}(t)\mathcal{J}_{\mathrm{I}}(t) \rangle$, the DQT and the TCL data is compared for a smaller system size $L = 12$.

The results in Pub. [P6] suggest various future directions of research, including further testing of similar perturbation scenarios in a wider selection of models. In particular, the possibility of nontrivial damping in other scenarios, e.g., induced by random perturbations, as well as the influence of integrability (of the unperturbed Hamiltonian) remain to be explored in detail.

---

[19] Note that, in the context of this publication, the distinction between Schrödinger picture and interaction picture always refers to the time dependence of the projected density matrix.

IV. SUMMARY AND CONCLUSION

The publications [P1–P6] have addressed various aspects in theoretical studies of isolated quantum many-body systems. Different topics have been studied in the broader context of transport and relaxation dynamics in quantum lattice systems. First, the alteration of relaxation dynamics induced by a mass imbalance between interacting particle species was investigated in Pub. [P4]. Numerical studies of density dynamics in the mass-imbalanced Fermi-Hubbard chain have shown that diffusive transport persists beyond the limit of small imbalances to moderate imbalances and becomes anomalous for stronger imbalances. On the other hand, while transport is suppressed in the limit of infinite mass imbalance (i.e., if one particle species is immobile), this effective localization has been shown to give way to anomalous diffusion as soon as the heavy particles gain a finite mobility.

Second, the way in which generic perturbations affect given reference dynamics was investigated from the perspective of projection-operator techniques in Pub. [P6]. As a main result, it was shown that simple exponential damping, which is expected in the overwhelming majority of cases, may only occur for the density matrix in the interaction picture. Within this approach, this simple damping only carries over to the time dependence of standard correlation functions in certain cases. In particular, it was demonstrated that nontrivial damping can occur in physically relevant perturbation scenarios.

A considerable portion of this work concerned methodological aspects in the implementation of powerful numerical and (semi-)analytical tools to overcome the enhanced computational complexity in numerical studies of quantum many-body systems. The concept of typicality was harnessed in most of the numerical studies and in the focus of Pubs. [P2] and [P3]. It also proved versatile in combination with other approaches such as numerical linked-cluster expansions and projection operator techniques. Numerical linked-cluster expansions in two dimensions were in the focus of Pub. [P5]. The utilization of available symmetries played an important role throughout the work and was improved in Pub. [P1] for specific use cases.

ACKNOWLEDGMENTS

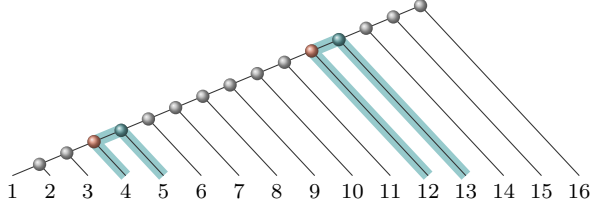### 1. Sparse-Matrix Techniques in the $SU(2)$-Symmetric Spin-Coupling Basis

Figure 8. Successive coupling scheme of 16 spins in ascending order. The connecting paths between interacting spins for two exemplary local Hamiltonians $h_4 = \mathbf{s}_4 \cdot \mathbf{s}_5$ and $h_{12} = \mathbf{s}_{12} \cdot \mathbf{s}_{13}$ are highlighted in color. Red color indicates the relevant intermediate spin quantum numbers on each path.

The sparse matrix structure of generic few-body Hamiltonians is crucial for the efficiency of numerical methods that rely on repetitive matrix-vector multiplications. When using the $SU(2)$ symmetry of isotropic spin Hamiltonians [cf. Eq. (5)], the corresponding matrix structure of $\mathcal{H}$ depends heavily on the chosen coupling scheme in the spin-coupling basis $\mathcal{B}_{SU(2)}$ (cf. Sec. II D 6). A detailed description of the selection rules for non-vanishing matrix elements of $\mathcal{H}$ in $\mathcal{B}_{SU(2)}$ would require an in-depth analysis of the underlying formalism (see Ref. [98] and references therein) and goes beyond the scope of this short outline. Let us rather formulate a rule of thumb for nonvanishing matrix elements $\langle \alpha SM | \mathcal{H} | \alpha' SM \rangle$ on the basis of the coupling scheme

Figure 10. Successive coupling scheme of 16 spins in adapted order. In analogy to Fig. 8, connecting paths for local Hamiltonians h_6, h_3, and in particular h_{16} are highlighted in color.

and illustrate it with two examples. To begin with, recall that each state $|\alpha SM\rangle$ in the basis $\mathcal{B}_{SU(2)}$ is uniquely defined through the set of intermediate spin quantum numbers $\bar{S}_i$ encoded in α. For any local Hamiltonian $h_r = \mathbf{s}_r \cdot \mathbf{s}_{r+1}$, the only quantum numbers $\bar{S}_i$ that are allowed to differ between two states $|\alpha SM\rangle$ and $|\alpha' SM\rangle$ such that $\langle \alpha SM | h_r | \alpha' SM \rangle \neq 0$ are those crossed by the connecting path between the interacting spins in the coupling tree. The shorter these connecting paths are (i.e., the less intermediate spins are crossed by each path), the less nonvanishing matrix elements arise. To illustrate this, two exemplary coupling schemes are shown in Figs. 8 and 10. The corresponding matrix plots are shown in Figs. 9 and 11 for each individual local Hamiltonian h_r. In the first coupling scheme, most paths involve only one relevant intermediate spin $\bar{S}_i$, which reflects itself in very few nonvanishing off-diagonal elements in the corresponding matrix plots. However, the path connecting the spins s_1 and s_{16} crosses every single $\bar{S}_i$, which in turn results in a rather dense matrix structure. In comparison, the second coupling scheme yields similar sparse matrix structures for every h_r, including h_{16}, since every connecting path in the coupling scheme involves at most two intermediate spin quantum numbers.
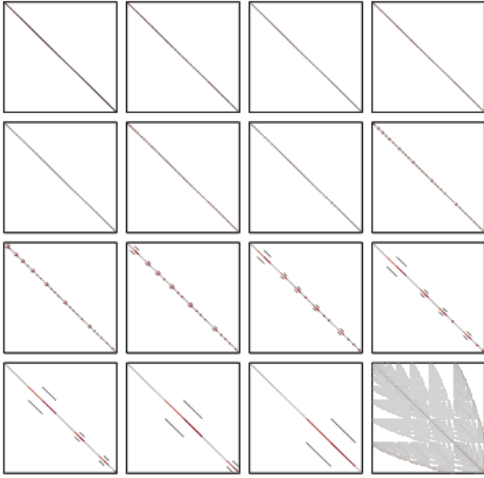

Figure 9. Each panel shows the matrix structure corresponding to one of the local terms $h_r = \mathbf{s}_r \cdot \mathbf{s}_{r+1}$ of the isotropic Heisenberg Hamiltonian (5) with $L = 16$ in the ($S = 4$)-subspace, represented in the basis $\mathcal{B}_{SU(2)}$ using the coupling scheme depicted in Fig. 8. The bottom right panel corresponds to the term $h_{16} = \mathbf{s}_{16} \cdot \mathbf{s}_1$.
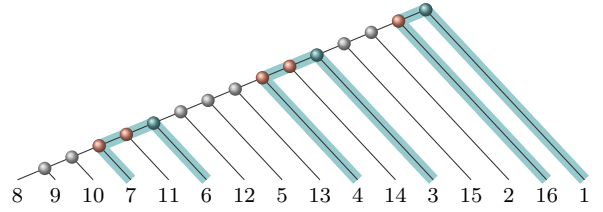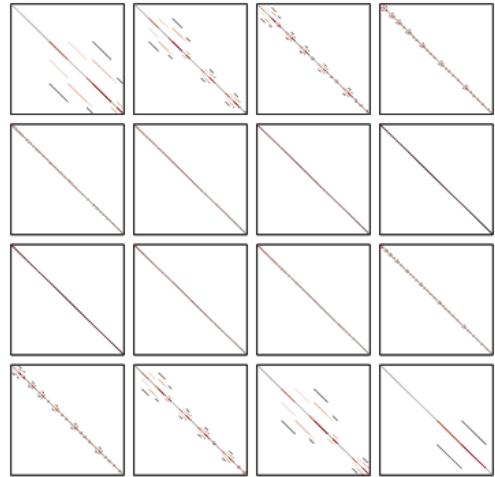

Figure 11. Same data as in Fig. 9, but for the coupling scheme depicted in Fig. 10.

All graphics were created using PGF/TikZ.

[P1] T. Heitmann and J. Schnack, *Combined use of translational and spin-rotational invariance for spin systems,* Phys. Rev. B **99**, 134405 (2019).

[P2] T. Heitmann, J. Richter, D. Schubert, and R. Steinigeweg, *Selected applications of typicality to real-time dynamics of quantum many-body systems,* Z. Naturforsch. A **75**, 421 (2020).

[P3] J. Schnack, J. Richter, T. Heitmann, J. Richter, and R. Steinigeweg, *Finite-Size Scaling of Typicality-Based Estimates,* Z. Naturforsch. A **75**, 465 (2020).

[P4] T. Heitmann, J. Richter, T. Dahm, and R. Steinigeweg, *Density dynamics in the mass-imbalanced Hubbard chain,* Phys. Rev. B **102**, 045137 (2020).

[P5] J. Richter, T. Heitmann, and R. Steinigeweg, *Quantum quench dynamics in the transverse-field Ising model: A numerical expansion in linked rectangular clusters,* SciPost Phys. **9**, 031 (2020).

[P6] T. Heitmann, J. Richter, J. Gemmer, and R. Steinigeweg, *Nontrivial damping of quantum many-body dynamics,* Phys. Rev. E **104**, 054145 (2021).

[7] A. Polkovnikov, K. Sengupta, A. Silva, and M. Vengalattore, *Colloquium : Nonequilibrium dynamics of closed interacting quantum systems,* Rev. Mod. Phys. **83**, 863 (2011).

[8] I. Bloch, J. Dalibard, and S. Nascimbène, *Quantum simulations with ultracold quantum gases,* Nat. Phys. **8**, 267 (2012).

[9] R. Blatt and C. F. Roos, *Quantum simulations with trapped ions,* Nat. Phys. **8**, 277 (2012).

[10] J. Eisert, M. Friesdorf, and C. Gogolin, *Quantum many-body systems out of equilibrium,* Nat. Phys. **11**, 124 (2015).

[11] L. D'Alessio, Y. Kafri, A. Polkovnikov, and M. Rigol, *From quantum chaos and eigenstate thermalization to statistical mechanics and thermodynamics,* Adv. Phys. **65**, 239 (2016).

[12] C. Gogolin and J. Eisert, *Equilibration, thermalisation, and the emergence of statistical mechanics in closed quantum systems,* Rep. Prog. Phys. **79**, 056001 (2016).

[13] F. Borgonovi, F. Izrailev, L. F. Santos, and V. Zelevinsky, *Quantum chaos and thermalization in isolated systems of interacting particles,* Phys. Rep. **626**, 1 (2016).

[14] B. Bertini, F. Heidrich-Meisner, C. Karrasch, T. Prosen, R. Steinigeweg, and M. Žnidarič, *Finite-temperature transport in one-dimensional quantum lattice models,* Rev. Mod. Phys. **93**, 025003 (2021).

[15] J. M. Deutsch, *Quantum statistical mechanics in a closed system,* Phys. Rev. A **43**, 2046 (1991).

[16] M. Srednicki, *Chaos and quantum thermalization,* Phys. Rev. E **50**, 888 (1994).

[17] M. Rigol, V. Dunjko, and M. Olshanii, *Thermalization and its mechanism for generic isolated quantum systems,* Nature **452**, 854 (2008).

[18] S. Lloyd, *Pure state quantum statistical mechanics and black holes*, Phd thesis, The Rockefeller University (1988), arXiv:1307.0378.

[19] J. Gemmer, M. Michel, and G. Mahler, *Quantum Thermodynamics*, Lecture Notes in Physics, Vol. 657 (Springer, Berlin, Heidelberg, 2004).

[20] S. Popescu, A. J. Short, and A. Winter, *Entanglement and the foundations of statistical mechanics,* Nat. Phys. **2**, 754 (2006).

[21] S. Goldstein, J. L. Lebowitz, R. Tumulka, and N. Zanghì, *Canonical Typicality,* Phys. Rev. Lett. **96**, 050403 (2006).

[22] S. Erne, R. Bücker, T. Gasenzer, J. Berges, and J. Schmiedmayer, *Universal dynamics in an isolated one-dimensional Bose gas far from equilibrium,* Nature **563**, 225 (2018).

[23] M. Prüfer, P. Kunkel, H. Strobel, S. Lannig, D. Linnemann, C.-M. Schmied, J. Berges, T. Gasenzer, and M. K. Oberthaler, *Observation of universal dynamics in a spinor Bose gas far from equilibrium,* Nature **563**, 217 (2018).

[24] M. Buchanan, *Heated debate in different dimensions,* Nat. Phys. **1**, 71 (2005).

[25] P. W. Anderson, *Absence of Diffusion in Certain Random Lattices,* Phys. Rev. **109**, 1492 (1958).

[26] E. Abrahams, P. W. Anderson, D. C. Licciardello, and T. V. Ramakrishnan, *Scaling theory of localization: Absence of quantum diffusion in two dimensions,* Phys. Rev. Lett. **42**, 673 (1979).

[27] E. Altman and R. Vosk, *Universal Dynamics and Renormalization in Many-Body-Localized Systems,* Annu. Rev. Condens. Matter Phys. **6**, 383 (2015).

[28] R. M. Nandkishore and D. A. Huse, *Many-Body Localization and Thermalization in Quantum Statistical Mechanics,* Annu. Rev. Condens. Matter Phys. **6**, 15 (2015).

[29] M. Schreiber, S. S. Hodgman, P. Bordia, H. P. Luschen, M. H. Fischer, R. Vosk, E. Altman, U. Schneider, and I. Bloch, *Observation of many-body localization of interacting fermions in a quasirandom optical lattice,* Science **349**, 842 (2015).

[30] D. A. Abanin, E. Altman, I. Bloch, and M. Serbyn, *Colloquium : Many-body localization, thermalization, and entanglement,* Rev. Mod. Phys. **91**, 021001 (2019).

[31] G. Carleo, F. Becca, M. Schiró, and M. Fabrizio, *Localization and Glassy Dynamics Of Many-Body Quantum Systems,* Sci. Rep. **2**, 243 (2012).

[32] W. De Roeck and F. Huveneers, *Scenario for delocalization in translation-invariant systems,* Phys. Rev. B **90**, 165137 (2014).

[33] W. De Roeck and F. Huveneers, in *From Part. Syst. to Partial Differ. Equations II*, edited by P. Gonçalves and A. J. Soares (Springer International Publishing, Cham, 2015) pp. 173–192.

[34] T. Grover and M. P. A. Fisher, *Quantum disentangled liquids,* J. Stat. Mech. **2014**, P10010 (2014).

[35] M. Schiulaz and M. Müller, in *AIP Conf. Proc.*, Vol. 1610 (2014) pp. 11–23.

[36] Z. Papić, E. M. Stoudenmire, and D. A. Abanin, *Many-body localization in disorder-free systems: The importance of finite-size constraints,* Ann. Phys. (NY) **362**, 714 (2015).

[37] M. Schiulaz, A. Silva, and M. Müller, *Dynamics in many-body localized quantum systems without disorder,* Phys. Rev. B **91**, 184202 (2015).

[38] J. M. Hickey, S. Genway, and J. P. Garrahan, *Signatures of many-body localisation in a system without disorder and the relation to a glass transition,* J. Stat. Mech. **2016**, 054047 (2016).

[39] N. Y. Yao, C. R. Laumann, J. I. Cirac, M. D. Lukin, and J. E. Moore, *Quasi-Many-Body Localization in Translation-Invariant Systems*, Phys. Rev. Lett. **117**, 240601 (2016).

[40] A. Smith, J. Knolle, D. L. Kovrizhin, and R. Moessner, *Disorder-Free Localization*, Phys. Rev. Lett. **118**, 266601 (2017).

[41] A. A. Michailidis, M. Žnidarič, M. Medvedyeva, D. A. Abanin, T. Prosen, and Z. Papić, *Slow dynamics in translation-invariant quantum lattice models*, Phys. Rev. B **97**, 104307 (2018).

[42] M. Brenes, M. Dalmonte, M. Heyl, and A. Scardicchio, *Many-Body Localization Dynamics from Gauge Invariance*, Phys. Rev. Lett. **120**, 030601 (2018).

[43] J. Sirker, *Exploration of the existence of a distinct quasi many-body localized phase: Numerical study of a translationally invariant system in the thermodynamic limit*, Phys. Rev. B **99**, 075162 (2019).

[44] L. Knipschild and J. Gemmer, *Stability of quantum dynamics under constant Hamiltonian perturbations*, Phys. Rev. E **98**, 062103 (2018).

[45] C. Nation and D. Porras, *Quantum chaotic fluctuation-dissipation theorem: Effective Brownian motion in closed quantum systems*, Phys. Rev. E **99**, 052139 (2019).

[46] L. Dabelow and P. Reimann, *Relaxation Theory for Perturbed Many-Body Quantum Systems versus Numerics and Experiment*, Phys. Rev. Lett. **124**, 120602 (2020).

[47] L. Dabelow and P. Reimann, *Typical relaxation of perturbed quantum many-body systems*, J. Stat. Mech. **2021**, 013106 (2021).

[48] J. Richter, F. Jin, L. Knipschild, H. De Raedt, K. Michielsen, J. Gemmer, and R. Steinigeweg, *Exponential damping induced by random and realistic perturbations*, Phys. Rev. E **101**, 062133 (2020).

[49] U. Schollwöck, *The density-matrix renormalization group in the age of matrix product states*, Ann. Phys. (NY) **326**, 96 (2011).

[50] S. Paeckel, T. Köhler, A. Swoboda, S. R. Manmana, U. Schollwöck, and C. Hubig, *Time-evolution methods for matrix-product states*, Ann. Phys. (NY) **411**, 167998 (2019).

[51] P. Reimann, *Typicality for Generalized Microcanonical Ensembles*, Phys. Rev. Lett. **99**, 160404 (2007).

[52] C. Bartsch and J. Gemmer, *Dynamical Typicality of Quantum Expectation Values*, Phys. Rev. Lett. **102**, 110403 (2009).

[53] P. Reimann, *Dynamical typicality of isolated many-body quantum systems*, Phys. Rev. E **97**, 062129 (2018).

[54] R. Alben, M. Blume, H. Krakauer, and L. Schwartz, *Exact results for a three-dimensional alloy with site diagonal disorder: comparison with the coherent potential approximation*, Phys. Rev. B **12**, 4090 (1975).

[55] H. De Raedt and P. de Vries, *Simulation of two and three-dimensional disordered systems: Lifshitz tails and localization properties*, Z. Phys. B **77**, 243 (1989).

[56] J. Jaklič and P. Prelovšek, *Lanczos method for the calculation of finite-temperature quantities in correlated systems*, Phys. Rev. B **49**, 5065 (1994).

[57] F. Jin, D. Willsch, M. Willsch, H. Lagemann, K. Michielsen, and H. De Raedt, *Random State Technology*, J. Phys. Soc. Jpn. **90**, 012001 (2021).

[58] J. Richter and R. Steinigeweg, *Combining dynamical quantum typicality and numerical linked cluster expansions*, Phys. Rev. B **99**, 094419 (2019).

[59] A. W. Sandvik, *Computational Studies of Quantum Spin Systems*, AIP Conf. Proc. **1297**, 135 (2010).

[60] P. Jordan and E. Wigner, *Über das Paulische Äquivalenzverbot*, Z Physik **47**, 631 (1928).

[61] R. Steinigeweg, H. Wichterich, and J. Gemmer, *Density dynamics from current auto-correlations at finite time- and length-scales*, EPL (Europhys. Lett.) **88**, 10004 (2009).

[62] R. Kubo, *Statistical-Mechanical Theory of Irreversible Processes. I. General Theory and Simple Applications to Magnetic and Conduction Problems*, J. Phys. Soc. Jpn. **12**, 570 (1957).

[63] R. Kubo, M. Toda, and N. Hashitsume, *Statistical Physics II*, 2nd ed., Springer Series in Solid-State Sciences, Vol. 31 (Springer Berlin Heidelberg, 1991).

[64] P. Mazur, *Non-ergodicity of phase functions in certain systems*, Physica **43**, 533 (1969).

[65] X. Zotos, F. Naef, and P. Prelovšek, *Transport and conservation laws*, Phys. Rev. B **55**, 11029 (1997).

[66] P. A. McClarty, M. Haque, A. Sen, and J. Richter, *Disorder-free localization and many-body quantum scars from magnetic frustration*, Phys. Rev. B **102**, 224303 (2020).

[67] M. Daumann, R. Steinigeweg, and T. Dahm, *Many-Body Localization in Translational Invariant Diamond Ladders with Flat Bands*, arXiv:2009.09705.

[68] F. Jin, R. Steinigeweg, F. Heidrich-Meisner, K. Michielsen, and H. De Raedt, *Finite-temperature charge transport in the one-dimensional Hubbard model*, Phys. Rev. B **92**, 205103 (2015).

[69] L. M. Falicov and J. C. Kimball, *Simple Model for Semiconductor-Metal Transitions: SmB_6 and Transition-Metal Oxides*, Phys. Rev. Lett. **22**, 997 (1969).

[70] R. Lyżwa and Z. Domański, *Falicov-Kimball model and its relation to the Hubbard model: Studies on clusters*, Phys. Rev. B **50**, 11381 (1994).

[71] R. Steinigeweg, F. Jin, H. De Raedt, K. Michielsen, and J. Gemmer, *Charge diffusion in the one-dimensional Hubbard model*, Phys. Rev. E **96**, 020105(R) (2017).

[72] J. Gemmer and G. Mahler, *Distribution of local entropy in the Hilbert space of bi-partite quantum systems: origin of Jaynes' principle*, Eur. Phys. J. B **31**, 249 (2003).

[73] C. Bartsch and J. Gemmer, *Transient fluctuation theorem in closed quantum systems*, EPL (Europhys. Lett.) **96**, 60008 (2011).

[74] T. Iitaka and T. Ebisuzaki, *Random phase vector for calculating the trace of a large matrix*, Phys. Rev. E **69**, 057701 (2004).

[75] A. Hams and H. De Raedt, *Fast algorithm for finding the eigenvalue distribution of very large matrices*, Phys. Rev. E **62**, 4365 (2000).

[76] S. Sugiura and A. Shimizu, *Canonical Thermal Pure Quantum State*, Phys. Rev. Lett. **111**, 010401 (2013).

[77] P. Reimann and J. Gemmer, *Full expectation-value statistics for randomly sampled pure states in high-dimensional quantum systems*, Phys. Rev. E **99**, 012126 (2019).

[78] J. Richter and A. Pal, *Simulating Hydrodynamics on Noisy Intermediate-Scale Quantum Devices with Random Circuits*, Phys. Rev. Lett. **126**, 230501 (2021).

[79] H. Tal-Ezer and R. Kosloff, *An accurate and efficient scheme for propagating the time dependent Schrödinger*

equation, J. Chem. Phys. **81**, 3967 (1984).

[80] R. Kosloff, *Propagation Methods for Quantum Molecular Dynamics,* Annu. Rev. Phys. Chem. **45**, 145 (1994).

[81] V. V. Dobrovitski and H. A. De Raedt, *Efficient scheme for numerical simulations of the spin-bath decoherence,* Phys. Rev. E **67**, 056702 (2003).

[82] A. Weiße, G. Wellein, A. Alvermann, and H. Fehske, *The kernel polynomial method,* Rev. Mod. Phys. **78**, 275 (2006).

[83] A. Nauts and R. E. Wyatt, *New approach to many-state quantum dynamics: The recursive-residue- generation method,* Phys. Rev. Lett. **51**, 2238 (1983).

[84] P. de Vries and H. De Raedt, *Solution of the time-dependent Schrödinger equation for two-dimensional spin-1/2 Heisenberg systems,* Phys. Rev. B **47**, 7929 (1993).

[85] H. De Raedt, K. Michielsen, H. D. Raedt, and K. Michielsen, *Computational Methods for Simulating Quantum Computers,* Host Publ. , 248 (2006).

[86] T. A. Elsayed and B. V. Fine, *Regression Relation for Pure Quantum States and Its Implications for Efficient Computing,* Phys. Rev. Lett. **110**, 070404 (2013).

[87] R. Steinigeweg, J. Gemmer, and W. Brenig, *Spin-Current Autocorrelations from Single Pure-State Propagation,* Phys. Rev. Lett. **112**, 120601 (2014).

[88] M. Rigol, T. Bryant, and R. R. P. Singh, *Numerical Linked-Cluster Approach to Quantum Lattice Models,* Phys. Rev. Lett. **97**, 187202 (2006).

[89] B. Tang, E. Khatami, and M. Rigol, *A short introduction to numerical linked-cluster expansions,* Comput. Phys. Commun. **184**, 557 (2013).

[90] I. G. White, B. Sundar, and K. R. A. Hazzard, *Quantum dynamics from a numerical linked cluster expansion,* arXiv:1710.07696.

[91] K. Mallayya and M. Rigol, *Quantum Quenches and Relaxation Dynamics in the Thermodynamic Limit,* Phys. Rev. Lett. **120**, 070603 (2018).

[92] K. Bhattaram and E. Khatami, *Lanczos-boosted numerical linked-cluster expansion for quantum lattice models,* Phys. Rev. E **100**, 013305 (2019).

[93] S. Dusuel, M. Kamfor, K. P. Schmidt, R. Thomale, and J. Vidal, *Bound states in two-dimensional spin systems near the Ising limit: A quantum finite-lattice study,* Phys. Rev. B **81**, 064412 (2010).

[94] A. B. Kallin, K. Hyatt, R. R. P. Singh, and R. G. Melko, *Entanglement at a Two-Dimensional Quantum Critical Point: A Numerical Linked-Cluster Expansion Study,* Phys. Rev. Lett. **110**, 135702 (2013).

[95] R. Steinigeweg, *Decay of currents for strong interactions,* Phys. Rev. E **84**, 011136 (2011).

[96] H.-P. Breuer and F. Petruccione, *The Theory of Open Quantum Systems* (Oxford University Press, 2007).

[97] S. Chaturvedi and F. Shibata, *Time-convolutionless projection operator formalism for elimination of fast variables. Applications to Brownian motion,* Z. Phys. B **35**, 297 (1979).

[98] R. Schnalle and J. Schnack, *Calculating the energy spectra of magnetic molecules: application of real- and spin-space symmetries,* Int. Rev. Phys. Chem. **29**, 403 (2010).

[99] K. Bärwinkel, H.-J. Schmidt, and J. Schnack, *Structure and relevant dimension of the Heisenberg model and applications to spin rings,* J. Magn. Magn. Mater. **212**, 240 (2000).

[100] J. Schnack, J. Richter, and R. Steinigeweg, *Accuracy of the finite-temperature Lanczos method compared to simple typicality-based estimates,* Phys. Rev. Research **2**, 013186 (2020).

[101] B. Paredes, F. Verstraete, and J. I. Cirac, *Exploiting Quantum Parallelism to Simulate Quantum Random Many-Body Systems,* Phys. Rev. Lett. **95**, 140501 (2005).

[102] N. D. Oppong, G. Pasqualetti, O. Bettermann, P. Zechmann, M. Knap, I. Bloch, and S. Fölling, *Probing transport and slow relaxation in the mass-imbalanced Fermi-Hubbard model,* arXiv:2011.12411.

Preprint of Publication [P1]

[P1] <u>Tjark Heitmann</u> and Jürgen Schnack,
  Combined Use of Translational and Spin-Rotational Invariance for Spin Systems,
  Journal reference: Phys. Rev. B **99**, 134405 (2019)
  DOI: 10.1103/PhysRevB.99.134405
  Preprint: `arXiv:1902.02093`

Combined Use of Translational and Spin-Rotational Invariance for Spin Systems

Tjark Heitmann [iD][1, *] and Jürgen Schnack [iD][2, †]

[1]*Fachbereich Physik, Universität Osnabrück, Barbarastr. 7, D-49076 Osnabrück, Germany*
[2]*Fakultät für Physik, Universität Bielefeld, Postfach 100131, D-33501 Bielefeld, Germany*

Exact diagonalization and other numerical studies of quantum spin systems are notoriously limited by the exponential growth of the Hilbert space dimension with system size. A common and well-known practice to reduce this increasing computational effort is to take advantage of the translational symmetry C_N in periodic systems. This represents a rather simple yet elegant application of the group theoretical symmetry projection operator technique. For isotropic exchange interactions, the spin-rotational symmetry $SU(2)$ can be used, where the Hamiltonian matrix is block-structured according to the total spin- and magnetization quantum numbers. Rewriting the Heisenberg Hamiltonian in terms of irreducible tensor operators allows for an efficient and highly parallelizable implementation to calculate its matrix elements recursively in the spin-coupling basis. When combining both C_N and $SU(2)$, mathematically, the symmetry projection technique leads to ready-to-use formulas. However, the evaluation of these formulas is very demanding in both computation time and memory consumption, problems which are said to outweigh the benefits of the symmetry reduced matrix shape. We show a way to minimize the computational effort for selected systems and present the largest numerically accessible cases.

I. INTRODUCTION

A typical system that possesses both spin-rotational as well as translational symmetry is a Heisenberg spin ring [1–19] which models, e.g., certain magnetic molecules or chains with the following Hamiltonian, where periodic boundary conditions are applied,

$$\underset{\sim}{H} = -2J \sum_{i=1}^{N} \underset{\sim}{\vec{s}}_i \cdot \underset{\sim}{\vec{s}}_{i+1} , \quad \underset{\sim}{\vec{s}}_{N+1} \equiv \underset{\sim}{\vec{s}}_1 . \tag{1}$$

The dot-product between the spin vector operators ensures spin rotational symmetry, since dot-products do not change upon simultaneous rotations of both vectors. The same value J of interactions between adjacent neighbors gives rise to translational invariance, since the spin ring can be collectively moved by one spacing without changing the Hamiltonian.

Both symmetries can be employed for various purposes. One is of course the perception of fundamental properties without even evaluating the energy spectrum: the energy eigenvalues form multiplets, i.e. total spin S and its magnetic quantum number M are good quantum numbers. The same holds for the momentum quantum number $k = 0, \ldots N-1$, that also explains certain degeneracies, namely between k and $N-k$ [7, 20–24]. Together with the notion of bipartiteness these quantum numbers can be assigned to, for instance, the ground state, again without diagonalizing the Hamiltonian [25–27].

The other application is the reduction of dimensionality when diagonalizing the Hamiltonian. This is achieved by block-structuring the Hamiltonian matrix according to the available quantum numbers, or in the language of group theory, the available irreducible representations. This powerful tool, that is heavily used in exact diagonalization studies, is the topic of this investigation. In order to guide the reader to the achievements and problems of combining full spin-rotational symmetry with translational symmetry, we present important precursors first.

For spin problems, where at least the total magnetization M is a good quantum number, i.e. $[\underset{\sim}{H}, \underset{\sim}{S}^z] = 0$, one can subdivide the full Hilbert space $\mathcal{H}$ into the direct sum of all eigenspaces $\mathcal{H}(M)$ of $\underset{\sim}{S}^z$

$$\mathcal{H} = \bigoplus_{M=-S_{\max}}^{+S_{\max}} \mathcal{H}(M) . \tag{2}$$

This is easily achieved by sorting the product basis states $|m_1, m_2, \ldots, m_N\rangle$ according to their total magnetic quantum number $M = \sum_{i=1}^{N} m_i$, which yields basis states $|m_1, m_2, \ldots, m_N; M\rangle$ in each orthogonal subspace $\mathcal{H}(M)$ [28]. This scheme is employed in many popular codes for exact and approximate diagonalization, as for instance, by means of Density Matrix Renormalization Group (DMRG), compare, e.g., the ALPS package [29, 30].

To marry the $\underset{\sim}{S}^z$-symmetry with translational symmetry is again rather easy since the irreducible representations of the translations can be constructed analytically starting from states $|m_1, m_2, \ldots, m_N; M\rangle$. If $\underset{\sim}{T}$ denotes a translation of the chain by one site, i.e. the generating group operation of the translation group C_N, then

$$|m_1, m_2, \ldots, m_N; M, k\rangle \propto \tag{3}$$

$$\sum_{\nu=0}^{N-1} \left(e^{i2\pi k/N} \underset{\sim}{T} \right)^{\nu} |m_1, m_2, \ldots, m_N; M\rangle$$

is both an eigenstate of $\underset{\sim}{S}^z$ and $\underset{\sim}{T}$ with eigenvalues M and $\exp(-i2\pi k/N)$, respectively, $k = 0, \ldots N-1$ being

———————
* tjark.heitmann@uos.de
† jschnack@uni-bielefeld.de

the shift quantum number (lattice momentum). After considering that cyclic permutations of $m_1, m_2, \ldots, m_N$ yield the same $|m_1, m_2, \ldots, m_N; M, k\rangle$ and that some patterns $m_1, m_2, \ldots, m_N$ with additional symmetry do contribute only to certain k, one can set up a very straight forward generation of the basis states in the subspaces $\mathcal{H}(M, k)$, whose dimensions are about $1/N$th of the respective dimensions of $\mathcal{H}(M)$ [7, 31–34]. This scheme is also used in many programs, among which `spinpack` is a freely available one [35]. Application in DMRG seems to be restricted since matrix-product states are constructed according to positions of spins, therefore each state breaks translational invariance. Nevertheless, very recently ideas have been developed how to incorporate translational symmetry into DMRG [36].

Then, what is the problem with the combination of full spin-rotational symmetry and translational symmetry?

The paper is organized as follows. In Section II we recapitulate how spin rotational and translational symmetry can be applied simultaneously and discuss the numerical implications. Thereafter in Section III we present some of the largest numerically exact calculations for spin rings followed by a discussion in Section IV.

II.   SPIN-ROTATIONAL AND TRANSLATIONAL SYMMETRY

The major obstacle when combining spin-rotational and translational symmetry is given by the fact, that a translated eigenstate of $\underset{\sim}{\vec{S}}^2$ in general does not belong to the same basis set as the original state, in contrast to the basis $\{|m_1, m_2, \ldots, m_N; M\rangle\}$, where translations yield just another member of the same basis set. In order to understand this better, we quickly repeat how spin-rotational symmetry – $SU(2)$ – can be realized. This is done by means of spin coupling according to some arbitrary coupling scheme. The basis states

$$|s_1, s_2, S_{12}, s_3, S_{123}, \ldots, s_N, S, M\rangle \qquad (4)$$

are e.g. generated by sequential coupling of spins along the chain. They are by construction eigenstates of $\underset{\sim}{\vec{S}}^2$ and $\underset{\sim}{S}^z$. If the Hamiltonian is then written in terms of irreducible tensor operators that are connected to compound tensors according to the same coupling scheme, matrix elements of the Hamiltonian can be easily evaluated by recursive decoupling. A detailed description of this powerful method can be found in references [37–44]. The computer program `MAGPACK`, that completely diagonalizes the Heisenberg Hamiltonian using $SU(2)$ symmetry, is freely available [45]. Also for DMRG $SU(2)$ codes have been developed [46–51]. In other fields such as nuclear physics this method was also adapted to model finite Fermi systems such as nuclei [52] as was the case for Hubbard models, where one can actually exploit two $SU(2)$ symmetries [53–56]. Solutions for models with $SU(N)$ symmetry work along similar lines [46, 57–60].
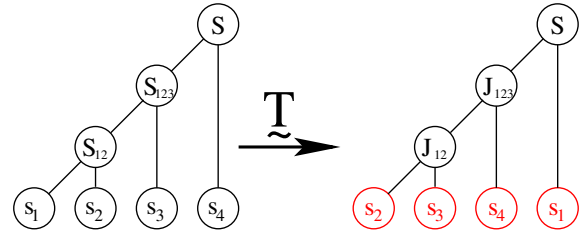

Figure 1. (Color online) Coupling schemes can be represented as coupling trees. The original sequential coupling (l.h.s.) is transformed into a sequential coupling that starts with the spin at position 2 (r.h.s.). The intermediate spins are labeled with a different letter to denote the different coupling scheme, although they acquire the original value, i.e. $J_{12} = S_{12}$.

The construction of a new basis that is in addition an eigenbasis of the translation operator $\underset{\sim}{T}$ involves the projection operator already introduced in (3),

$$|\alpha, S, M, k\rangle \propto \sum_{\nu=0}^{N-1} \left(e^{i2\pi k/N} \underset{\sim}{T}\right)^\nu |\alpha, S, M\rangle . \qquad (5)$$

Here α is now a short-hand notation for the full coupling scheme $s_1, s_2, S_{12}, s_3, S_{123}, \ldots, s_N$. To be used as a basis, the states $|\alpha, S, M, k\rangle$ still need to be orthonormalized. The application of $\underset{\sim}{T}$ in (5) generates a plethora of new states that belong to *different* coupling schemes, i.e. to *different* basis sets. Figure 1 demonstrates the action of $\underset{\sim}{T}$ on a coupling scheme of a ring of four spins. The translation of all spins by one unit modifies the whole coupling scheme, which is in stark contrast to the action on product states $|m_1, m_2, \ldots, m_N\rangle$, where only a new member of the same basis set is produced.

In order to evaluate matrix elements of the Hamiltonian each state $\underset{\sim}{T}^\nu |\alpha, S, M\rangle$ has to be represented in the original basis, i.e.

$$\underset{\sim}{T}^\nu |\alpha, S, M\rangle =$$
$$\sum_{\alpha'} |\alpha', S, M\rangle\langle\alpha', S, M| \underset{\sim}{T}^\nu |\alpha, S, M\rangle . \qquad (6)$$

Thanks to symmetry this needs to be done only for e.g. $M = S$, but it nevertheless involves a huge number of so-called recoupling coefficients $\langle\alpha', S, M = S| \underset{\sim}{T}^\nu |\alpha, S, M = S\rangle$. Graph-theoretical methods can be used to evaluate these coefficients [43, 44, 61, 62], which contain Wigner-6J symbols, phase factors, square roots as well as possibly summations over additional indices. The composition of these coefficients is crucial for the computational costs of not only their calculation but also the time and memory efficiency of the whole basis symmetrization. Defining an equivalence relation

$$|\alpha', S, M\rangle \cong |\alpha, S, M\rangle$$
$$\Leftrightarrow \quad \exists \nu : \langle\alpha', S, M| \underset{\sim}{T}^\nu |\alpha, S, M\rangle \neq 0 \qquad (7)$$

enables to distinguish orthogonal sets of projected states which can be orthonormalized separately. The number and size of these sets is closely related to the complexity of the recoupling coefficients, where simple coefficients lead to many small sets. In the worst case, where all states are equivalent, orthonormalization becomes cumbersome and one needs to store an order of $[\dim(\mathcal{H}(S, M = S))]^2 / N$ basis coefficients. This prevents a general use even for relatively small systems.

The complexity of the recoupling coefficients depends on several circumstances, in particular the used point group and the employed coupling scheme [43, 44]. The relevant question is therefore, whether coupling schemes exist that are substantially less demanding than others. In an earlier publication it could be shown that if one chooses compatible point groups and coupling schemes, only phase factors appear in the recoupling coefficients [21]. Since especially low-symmetry groups such as D_2 or D_4 often allow for the construction of an appropriate coupling scheme [63–65], we wonder whether also the group of translations C_N can be combined with a clever coupling scheme.

The mentioned graph-theoretical methods [43, 44, 61, 62] help to understand what one is looking for: recoupling coefficients without summations over additional indices and with as few as possible Wigner symbols and square roots. The ultimate goal – no sums, no symbols, no square roots – can be achieved for chain lengths of $N = 2^n, n = 2, 3, 4, \ldots$. Then the recoupling coefficients can be evaluated in the graph-theoretical framework by spin exchange processes as depicted in Fig. 2. Such processes generate only a phase, as for example in $\langle s_1 s_2 S \,|\, s_2 s_1 S \rangle = (-1)^{S-s_1-s_2}$. For the example shown on the r.h.s. of Fig. 2 this yields ($M = S$ omitted)

$$\langle s_1, s_3, S_{13}, s_2, s_4, S_{24}, S \,|\, s_2, s_4, J_{13}, s_3, s_1, J_{24}, S \rangle$$
$$= (-1)^{J_{24}-s_3-s_1}(-1)^{S-J_{13}-J_{24}}\delta_{S_{13}J_{24}}\delta_{S_{24}J_{13}}$$
$$= (-1)^{S-J_{13}-s_3-s_1}\delta_{S_{13}J_{24}}\delta_{S_{24}J_{13}} \,. \tag{8}$$

For chain lengths that are not powers of two, it turns out that a universal coupling strategy is to „prime factorize" the coupling scheme, i.e. the chain length. $N = 6$ for instance would be coded as $2 \cdot 3$, and so on. The recoupling coefficients contain more and more Wigner symbols
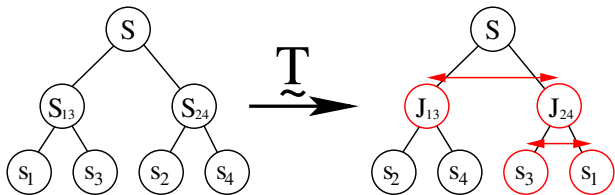

Figure 2. (Color online) Optimal coupling scheme for chain lengths of $N = 2^n$ (l.h.s.). The translated scheme (r.h.s.) can be transformed back into the old coupling scheme by spin exchange operations on the coupling graph, leading to a very simple recoupling coefficient.

as well as square roots the larger the prime factors p_i are. The maximum number of symbols per coefficient is given
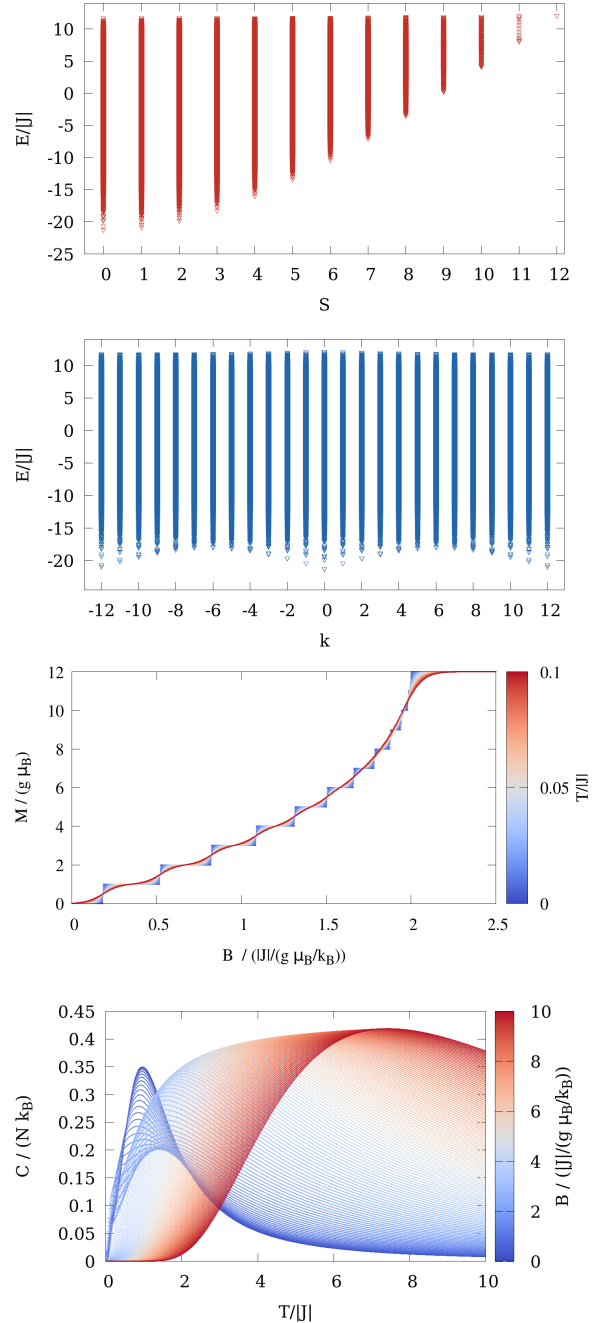

Figure 3. (Color online) Spectra and observables for an antiferromagnetic Heisenberg ring with $N = 24$, $s = 1/2$: energy spectrum vs total spin S, the same spectrum but now vs k, the magnetization vs the applied field B for various temperatures as well as the specific heat vs temperature T for various external fields (top to bottom).
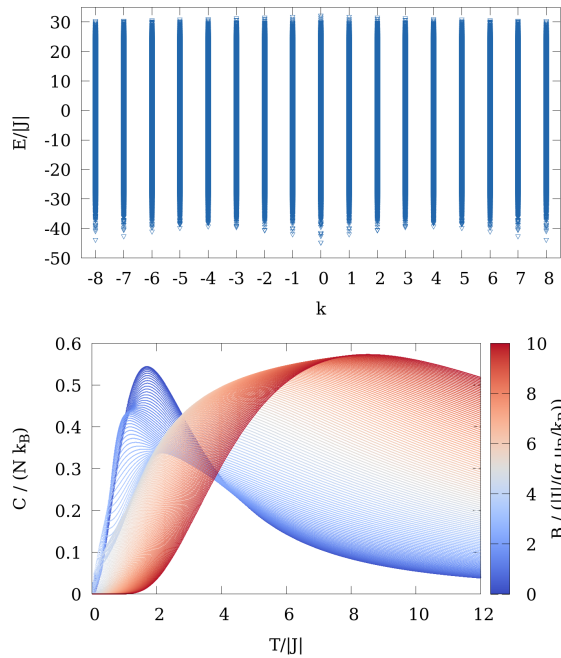
Figure 4. (Color online) Spectra and observables for an antiferromagnetic Heisenberg ring with $N = 16$, $s = 1$: energy spectrum vs k as well as the specific heat vs temperature T for various external fields (top to bottom).

by

$$N_{\text{Wigner-6J}} = \sum_{i=1}^{N_{\text{primes}}} (p_i - 2) \cdot \sum_{j=i+1}^{N_{\text{primes}}} p_j \ . \tag{9}$$

$N = 2^n$ fits into this scheme as the optimal case, since only the smallest possible prime factors appear. This finding explains why a combination of spin-rotational and translational symmetry is not easily possible for the majority of system sizes – it turns into a prohibitive numerical effort to evaluate a massive number of recoupling coefficients.

III. NUMERICAL RESULTS

Finally we would like to present some of the largest cases one can actually solve nowadays. We choose Heisenberg spin rings with antiferromagnetic nearest-neighbor interaction as examples.

The first example shows spectra and magnetic observables for a spin ring with $N = 24$ sites of spins $s = 1/2$. The dimension of the total Hilbert space is $\dim(\mathcal{H}) = 16,777,216$, which can be subdivided into subspaces $\mathcal{H}(S, M = S, k)$ as outlined above. In particular, $24 = 2 * 2 * 2 * 3$. The dimension of the largest subspace $\mathcal{H}(S, M = S, k)$ is $27,275$; it occurs for $S = 2$ and even $k \neq 0, 12$. Figure 3 shows from top to bottom the energy spectrum vs total spin S, the same spectrum but now vs
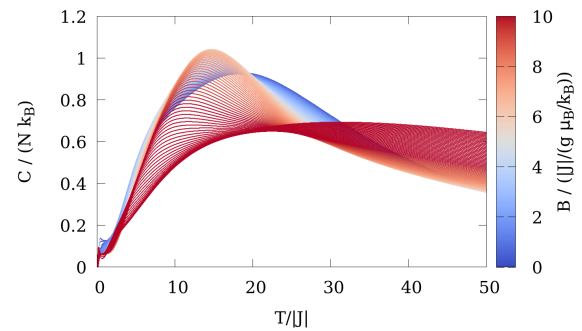
Figure 5. (Color online) Specific heat vs temperature T for various external fields for an antiferromagnetic Heisenberg ring with $N = 8$, $s = 5$.

k, the magnetization vs the applied field B for various temperatures as well as the specific heat vs temperature T for various external fields. The figures merely serve as visual proofs of the feasibility of the program than as sources for specific curves. Readers interested in the spectra or specific functions are welcome to contact the authors.

The second example presents the results for a spin ring of $N = 16$ sites of spins $s = 1$. In this case the total dimension assumes a value of $\dim(\mathcal{H}) = 43,046,721$, which reduces to $59,143$ for the largest subspace $\mathcal{H}(S, M = S, k)$ occurring for $S = 3$ and odd k. Figure 4 depicts the energy spectrum vs k as well as the specific heat vs temperature T for various external fields.

The final example of our selection deals with a fictitious spin ring of $N = 8$ spins with single-spin quantum number $s = 5$. Its main purpose is to demonstrate that the combined use of spin-rotational as well as translational symmetry allows to reduce the staggering dimension of the full Hilbert space of $\dim(\mathcal{H}) = 214,358,881$ to a rather moderate size of the largest subspace $\mathcal{H}(S, M = S, k)$ of $77,970$ which occurs for $S = 9$ and odd k. Figure 5 shows the specific heat vs temperature T for various external fields calculated from all 214,358,881 levels.

IV. DISCUSSION AND CONCLUSIONS

The outlined method provides a valuable tool in cases where a complete and numerically exact diagonalization of a large spin system provides additional benefits compared to approximate methods. The knowledge of exact quantum numbers such as S, M, and k provides such benefits for instance in spectroscopic experiments as, for instance, inelastic neutron scattering (INS), where selection rules can be inferred [66–68].

The method also complements other existing exact methods, in particular Bethe ansatz methods. These work for isotropic nearest-neighbor interactions of arbitrary spin s [69–73], but only for certain linear combinations of powers of $\vec{\underline{s}}_i \cdot \vec{\underline{s}}_{i+1}$. The most general isotropic

nearest-neighbor interaction for spin s is of the form $p_s(\vec{\underline{s}}_i \cdot \vec{\underline{s}}_{i+1})$, where p_s denotes a polynomial of degree $2s$. For $s = 1/2$ the polynomial is simply the proportional function, which means that the Heisenberg spin-1/2 chain is integrable by Bethe ansatz. For spin-1 chains the polynomial turns out as $p_1(x) = x \pm x^2$ or $p_1(x) = x^2$, which means that certain bilinear/biquadratic chains can be solved by Bethe ansatz [74]. Generally, the Bethe ansatz is not applicable to Heisenberg chains with only bilinear terms for $s > \frac{1}{2}$. Here (and in many other cases) our diagonalization scheme provides the exact spectra and eigenfunctions, albeit for periodic chains of restricted lengths.

Although the theoretical calculations appear straight forward, we showed that in many cases a vast number of recoupling coefficients is generated which in the worst cases yields $\dim(\mathcal{H}(S, M = S))$ coefficients for each of the $\dim(\mathcal{H}(S, M = S))/N$ states belonging to an irreducible representation (S, M, k). This renders a practical use impossible. Nevertheless, we could also outline, for which system sizes a combined use of spin-rotational and trans-lational symmetry is feasible. It then delivers numerically exact results for both spectra as well as observables.

Very recent numerical studies show that the range of applicability of the method can be extended, at least somewhat, by using D_N combined with parity instead of C_N symmetry [75]. Complex valued basis coefficients and matrix elements can thereby be avoided at the cost of additional symmetry operations. This way, a complete diagonalization of a spin ring with $N = 27$ and $s = 1/2$ becomes possible, for instance.

ACKNOWLEDGMENT

[1] H. Bethe, Z Physik **71**, 205 (1931).
[2] K. L. Taft, C. D. Delfs, G. C. Papaefthymiou, S. Foner, D. Gatteschi, and S. J. Lippard, J. Am. Chem. Soc. **116**, 823 (1994).
[3] U. Schollwöck, O. Golinelli, and T. Jolicœur, Phys. Rev. B **54**, 4038 (1996).
[4] S. P. Watton, P. Fuhrmann, L. E. Pence, S. J. Lippard, A. Caneschi, A. Cornia, and G. L. Abbati, Angew. Chem. Int. Ed. **36**, 2774 (1997).
[5] T. Xiang, Phys. Rev. B **58**, 9142 (1998).
[6] K. Maisinger and U. Schollwöck, Phys. Rev. Lett. **81**, 445 (1998).
[7] K. Bärwinkel, H.-J. Schmidt, and J. Schnack, J. Magn. Magn. Mater. **212**, 240 (2000).
[8] O. Waldmann, Phys. Rev. B **65**, 024424 (2001).
[9] O. Waldmann, Europhys. Lett. **60**, 302 (2002).
[10] O. Waldmann, T. Guidi, S. Carretta, C. Mondelli, and A. L. Dearden, Phys. Rev. Lett. **91**, 237202 (2003).
[11] A. V. Postnikov, J. Kortus, and S. Bluegel, Mol. Phys. Reports **38**, 56 (2003).
[12] M. Affronte, T. Guidi, R. Caciuffo, S. Carretta, G. Amoretti, J. Hinderer, I. Sheikin, A. G. M. Jansen, A. A. Smith, R. E. P. Winpenny, J. van Slageren, and D. Gatteschi, Phys. Rev. B **68**, 104403 (2003).
[13] L. Engelhardt and M. Luban, Phys. Rev. B **73**, 054430 (2006).
[14] O. Waldmann, T. C. Stamatatos, G. Christou, H. U. Güdel, I. Sheikin, and H. Mutka, Phys. Rev. Lett. **102**, 157202 (2009).
[15] A. Bianchi, S. Carretta, P. Santini, G. Amoretti, T. Guidi, Y. Qiu, J. R. D. Copley, G. Timco, C. Muryn, and R. E. P. Winpenny, Phys. Rev. B **79**, 144422 (2009).
[16] J. Dreiser, O. Waldmann, C. Dobe, G. Carver, S. T. Ochsenbein, A. Sieber, H. U. Güdel, J. van Duijn, J. Tay-

lor, and A. Podlesnyak, Phys. Rev. B **81**, 024408 (2010).
[17] M. L. Baker, G. A. Timco, S. Piligkos, J. S. Mathieson, H. Mutka, F. Tuna, P. Kozlowski, M. Antkowiak, T. Guidi, T. Gupta, H. Rath, R. J. Woolfson, G. Kamieniarz, R. G. Pritchard, H. Weihe, L. Cronin, G. Rajaraman, D. Collison, E. J. L. McInnes, and R. E. P. Winpenny, Proc. Natl. Acad. Sci. USA **109**, 19113 (2012).
[18] J. Ummethum, J. Nehrkorn, S. Mukherjee, N. B. Ivanov, S. Stuiber, T. Strässle, P. L. W. Tregenna-Piggott, H. Mutka, G. Christou, O. Waldmann, and J. Schnack, Phys. Rev. B **86**, 104403 (2012).
[19] E. Garlatti, S. Bordignon, S. Carretta, G. Allodi, G. Amoretti, R. De Renzi, A. Lascialfari, Y. Furukawa, G. A. Timco, R. Woolfson, R. E. P. Winpenny, and P. Santini, Phys. Rev. B **93**, 024424 (2016).
[20] M. Karbach, *Finite-Size-Effekte im eindimensionalen Spin-1/2-XXZ-Modell*, Phd thesis, Bergische Universität Wuppertal (1994).
[21] O. Waldmann, Phys. Rev. B **61**, 6138 (2000).
[22] K. Bärwinkel, H.-J. Schmidt, and J. Schnack, J. Magn. Magn. Mater. **220**, 227 (2000).
[23] J. Schnack, Phys. Rev. B **62**, 14855 (2000).
[24] K. Bärwinkel, H.-J. Schmidt, and J. Schnack, Eur. Phys. J. B **33**, 285 (2003).
[25] W. Marshall, Proc. Royal. Soc. A (London) **232**, 48 (1955).
[26] E. Lieb, T. Schultz, and D. Mattis, Ann. Phys. (NY) **16**, 407 (1961).
[27] E. Lieb and D. Mattis, J. Math. Phys. **3**, 749 (1962).
[28] J. Schnack, P. Hage, and H.-J. Schmidt, J. Comput. Phys. **227**, 4512 (2008).
[29] A. Albuquerque, F. Alet, P. Corboz, P. Dayal, A. Feiguin, S. Fuchs, L. Gamper, E. Gull, S. Gürtler, A. Honecker,

R. Igarashi, M. Körner, A. Kozhevnikov, A. Läuchli, S. Manmana, M. Matsumoto, I. McCulloch, F. Michel, R. Noack, G. Pawłowski, L. Pollet, T. Pruschke, U. Schollwöck, S. Todo, S. Trebst, M. Troyer, P. Werner, and S. Wessel, J. Magn. Magn. Mater. **310**, 1187 (2007).

[30] B. Bauer, L. D. Carr, H. G. Evertz, A. Feiguin, J. Freire, S. Fuchs, L. Gamper, J. Gukelberger, E. Gull, S. Guertler, A. Hehn, R. Igarashi, S. V. Isakov, D. Koop, P. N. Ma, P. Mates, H. Matsuo, O. Parcollet, G. Pawłowski, J. D. Picon, L. Pollet, E. Santos, V. W. Scarola, U. Schollwöck, C. Silva, B. Surer, S. Todo, S. Trebst, M. Troyer, M. L. Wall, P. Werner, and S. Wessel, J. Stat. Mech. **2011**, P05001 (2011).

[31] H. J. Schulz, T. A. Ziman, and D. Poilblanc, J. Phys. I **6**, 675 (1996).

[32] J. Richter, J. Schulenburg, A. Honecker, and D. Schmalfuß, Phys. Rev. B **70**, 174454 (2004).

[33] I. Rousochatzakis, A. M. Läuchli, and F. Mila, Phys. Rev. B **77**, 094420 (2008).

[34] J. Richter and J. Schulenburg, Eur. Phys. J. B **73**, 117 (2010).

[35] J. Schulenburg, *spinpack 2.56* (Magdeburg University, 2017).

[36] V. Zauner-Stauber, L. Vanderstraeten, J. Haegeman, I. P. McCulloch, and F. Verstraete, Phys. Rev. B **97**, 235155 (2018).

[37] D. Gatteschi and L. Pardi, Gazz. Chim. Ital. **123**, 231 (1993).

[38] J. J. Borrás-Almenar, J. M. Clemente-Juan, E. Coronado, and B. S. Tsukerblat, Inorg. Chem. **38**, 6081 (1999).

[39] A. Bencini and D. Gatteschi, *Electron Paramagnetic Resonance of Exchange Coupled Systems* (Springer Berlin Heidelberg, Berlin, Heidelberg, 1990).

[40] B. S. Tsukerblat, *Group Theory in Chemistry and Spectroscopy: A Simple Guide to Advanced Usage*, 2nd ed. (Dover Publications, Mineola, New York, 2006).

[41] B. Tsukerblat, Inorg. Chim. Acta **361**, 3746 (2008).

[42] A. S. Boyarchenkov, I. G. Bostrem, and A. S. Ovchinnikov, Phys. Rev. B **76**, 224410 (2007).

[43] R. Schnalle and J. Schnack, Phys. Rev. B **79**, 104419 (2009).

[44] R. Schnalle and J. Schnack, Int. Rev. Phys. Chem. **29**, 403 (2010).

[45] J. J. Borrás-Almenar, J. M. Clemente-Juan, E. Coronado, and B. S. Tsukerblat, J. Comput. Chem. **22**, 985 (2001).

[46] I. P. McCulloch and M. Gulácsi, Europhys. Lett. **57**, 852 (2002).

[47] I. P. McCulloch, J. Stat. Mech. **2007**, P10014 (2007).

[48] A. Fledderjohann, A. Klümper, and K.-H. Mütter, J. Phys. A **44**, 475302 (2011).

[49] G. Alvarez, Comput. Phys. Commun. **183**, 2226 (2012).

[50] A. Weichselbaum, Ann. Phys. (NY) **327**, 2972 (2012).

[51] R. Zadourian, A. Fledderjohann, and A. Klümper, J. Stat. Mech. **2016**, 083101 (2016).

[52] J. Dukelsky and S. Pittel, Rep. Prog. Phys. **67**, 513 (2004).

[53] I. Affleck, Z. Zou, T. Hsu, and P. W. Anderson, Phys. Rev. B **38**, 745 (1988).

[54] S. Zhang, Int. J. Mod. Phys. B **05**, 153 (1991).

[55] P. A. Lee, N. Nagaosa, T.-K. Ng, and X.-G. Wen, Phys. Rev. B **57**, 6003 (1998).

[56] R. Schumann, Ann. Phys. **11**, 49 (2002).

[57] R. Thomale, S. Rachel, P. Schmitteckert, and M. Greiter, Phys. Rev. B **85**, 195149 (2012).

[58] P. Nataf and F. Mila, Phys. Rev. Lett. **113**, 127204 (2014).

[59] P. Nataf and F. Mila, Phys. Rev. B **93**, 155134 (2016).

[60] K. Wan, P. Nataf, and F. Mila, Phys. Rev. B **96**, 115159 (2017).

[61] V. Fack, S. Pitre, and J. Van der Jeugt, Comput. Phys. Commun. **86**, 105 (1995).

[62] V. Fack, S. Pitre, and J. Van der Jeugt, Comput. Phys. Commun. **101**, 155 (1997).

[63] C. Delfs, D. Gatteschi, L. Pardi, R. Sessoli, K. Wieghardt, and D. Hanke, Inorg. Chem. **32**, 3099 (1993).

[64] I. G. Bostrem, A. S. Ovchinnikov, and V. E. Sinitsyn, Theor. Math. Phys. **149**, 1527 (2006).

[65] V. E. Sinitsyn, I. G. Bostrem, and A. S. Ovchinnikov, J. Phys. A **40**, 645 (2007).

[66] A. Furrer, Int. J. Mod. Phys. B **24**, 3653 (2010).

[67] M. L. Baker, T. Guidi, S. Carretta, J. Ollivier, H. Mutka, H. U. Güdel, G. A. Timco, E. J. L. McInnes, G. Amoretti, R. E. P. Winpenny, and P. Santini, Nat. Phys. **8**, 906 (2012).

[68] A. Furrer and O. Waldmann, Rev. Mod. Phys. **85**, 367 (2013).

[69] P. P. Kulish, N. Y. Reshetikhin, and E. K. Sklyanin, Lett. Math. Phys. **5**, 393 (1981).

[70] L. Takhtajan, Phys. Lett. A **87**, 479 (1982).

[71] H. Babujian, Nucl. Phys. B **215**, 317 (1983).

[72] A. Tsvelick, Nucl. Phys. B **305**, 675 (1988).

[73] H. Frahm, N.-C. Yu, and M. Fowler, Nucl. Phys. B **336**, 396 (1990).

[74] S. R. Manmana, A. M. Läuchli, F. H. L. Essler, and F. Mila, Phys. Rev. B **83**, 184433 (2011).

[75] A. W. Sandvik, AIP Conf. Proc. **1297**, 135 (2010).

Preprint of Publication [P2]

[P2] <u>Tjark Heitmann</u>, Jonas Richter, Dennis Schubert, and Robin Steinigeweg,
Selected Applications of Typicality to Real-Time Dynamics of Quantum Many-Body Systems,
Journal reference: Z. Naturforsch. A **75**, 421 (2020) [Open Access]
DOI: 10.1515/zna-2020-0010
Preprint: `arXiv:2001.05289`

Selected Applications of Typicality to Real-Time Dynamics of Quantum Many-Body Systems

Tjark Heitmann 🔸,* Jonas Richter 🔸, Dennis Schubert, and Robin Steinigeweg 🔸†

Department of Physics, University of Osnabrück, D-49069 Osnabrück, Germany

Loosely speaking, the concept of quantum typicality refers to the fact that a single pure state can imitate the full statistical ensemble. This fact has given rise to a rather simple but remarkably useful numerical approach to simulate the dynamics of quantum many-body systems, called *dynamical quantum typicality* (DQT). In this paper, we give a brief overview of selected applications of DQT, where particular emphasis is given to questions on transport and thermalization in low-dimensional lattice systems like chains or ladders of interacting spins or fermions. For these systems, we discuss that DQT provides an efficient means to obtain time-dependent equilibrium correlation functions for comparatively large Hilbert-space dimensions and long time scales, allowing the quantitative extraction of transport coefficients within the framework of, e.g., linear response theory. Furthermore, it is discussed that DQT can also be used to study the far-from-equilibrium dynamics resulting from sudden quench scenarios, where the initial state is a thermal Gibbs state of the pre-quench Hamiltonian. Eventually, we summarize a few combinations of DQT with other approaches such as numerical linked cluster expansions or projection operator techniques. In this way, we demonstrate the versatility of DQT.

I. INTRODUCTION

Unraveling the dynamics of isolated quantum many-body systems is a central objective of modern experimental and theoretical physics. On the one hand, new experimental platforms composed of cold atoms or trapped ions have opened the door to perform quantum simulations with a high amount of control over Hamiltonian parameters and initial conditions [1, 2]. On the other hand, there has been substantial progress from the theoretical side to understand (i) experimental observations and (ii) long-standing questions about the fundamentals of statistical mechanics [3–7]. One such question is how to reconcile the emergence of thermodynamic behavior with the unitary time evolution of isolated quantum systems, i.e., to explain whether and in which way an isolated system relaxes towards a stationary long-time state which agrees with the predictions from standard statistical mechanics. Another similarly intriguing question in this context is to explain the onset of conventional hydrodynamic transport, i.e., diffusion, from truly microscopic principles [8–10]. The numerical analysis of thermalization and transport in isolated quantum many-body systems is at the heart of this paper.

Generally, the theoretical analysis of quantum many-body dynamics is notoriously difficult. Given a quantum system $\mathcal{H}$ and an arbitrary nonequilibrium state $\rho(0)$, universal concepts to describe the resulting dynamics are rare [11–13], and one is usually required to solve the microscopic equation of motion for the density matrix $\rho(t)$, i.e., the von-Neumann equation

$$\frac{\mathrm{d}}{\mathrm{d}t}\rho(t) = -i[\mathcal{H}, \rho(t)] \tag{1}$$

($\hbar = 1$) which, in the case of a pure state $\rho(t) = |\psi(t)\rangle\langle\psi(t)|$, reduces to the Schrödinger equation

$$\frac{\mathrm{d}}{\mathrm{d}t}|\psi(t)\rangle = -i\mathcal{H}|\psi(t)\rangle \ . \tag{2}$$

While the presence of strong interactions often prohibits any analytical solution, numerical studies of Eq. (2) are plagued by the exponential growth of the Hilbert space upon increasing the number of degrees of freedom. Moreover, since thermalization and transport can potentially be very slow processes, the necessity to study long time scales adds another layer of complexity.

Of course, for situations close to equilibrium, e.g., a system being weakly perturbed by an external force, linear response theory provides a successful framework to describe the system's response in terms of dynamical correlation functions evaluated exactly at equilibrium [14]. However, analogous to Eqs. (1) and (2), the calculation of such time-dependent correlation functions for large system sizes and long time scales is a severe challenge in practice.

Despite these difficulties, significant progress has been made over the years thanks to the augmented availability of computational resources and the development of sophisticated numerical techniques. Especially for one-dimensional systems the time-dependent density matrix renormalization group (tDMRG), including related methods based on matrix product states, provides a powerful approach to dynamical properties in the thermodynamic limit (for reviews, see [15, 16]). However, due to the inevitable build-up of entanglement, this approach is limited in the time scales which can be reached in simulations.

In the present paper, the focus is on another useful numerical approach to the dynamics of quantum many-body systems, which is based on the concept of dynamical quantum typicality (DQT) [17, 18]. In a nutshell,

────────
* tjark.heitmann@uos.de
† rsteinig@uos.de

DQT means that "the vast majority of all pure states featuring a common expectation value of some generic observable at a given time will yield very similar expectation values of the same observable at any later time" [17]. In fact, the idea of using random vectors has a long and fruitful history [19–26]. By virtue of an iterative forward propagation of these vectors in real or imaginary time, dependencies on time and temperature can be obtained. Since DQT can be implemented rather memory efficiently, it is possible to study dynamical properties of quantum many-body systems with Hilbert-space dimensions significantly larger compared to standard exact diagonalization (ED). Moreover, there are no conceptual limitations on the reachable time scales.

It is worth pointing out that DQT can not only be used to obtain time-dependent properties [27–29] or spectral functions [22, 30–32] but also static properties such as the density of states [33] or thermodynamic quantities [34–37]. However, it is the aim of this paper to discuss the usefulness and versatility of DQT especially in the context of thermalization and transport.

This paper is structured as follows. In Sec. II, we give a brief introduction to the concept of typicality and also elaborate on the differences between typicality and the eigenstate thermalization hypothesis. In Sec. III, we discuss various applications of typicality to the dynamics of quantum many-body systems. Finally, we summarize and conclude in Sec. IV, where we also provide an outlook on further applications of DQT.

II.   WHAT IS TYPICALITY?

Loosely speaking, the notion of typicality means that even a single pure quantum state can imitate the full statistical ensemble, or, more precisely, expectation values of typical pure states are close to the expectation value of the statistical ensemble [20, 23–26]. While typicality has been put forward as an important insight to explain the emergence of thermodynamic behavior (see e.g. Ref. [23] for an overview), let us here focus on the practical consequences of typicality. In particular, let us consider the, e.g., canonical equilibrium expectation value $\langle A \rangle_{\text{eq}}$ of some (quasi-local) operator A defined as

$$\langle A \rangle_{\text{eq}} = \frac{\text{Tr}[A e^{-\beta \mathcal{H}}]}{\mathcal{Z}} = \frac{\text{Tr}[e^{-\beta \mathcal{H}/2} A e^{-\beta \mathcal{H}/2}]}{\mathcal{Z}} , \quad (3)$$

where $\mathcal{Z} = \text{Tr}\left[\exp(-\beta \mathcal{H})\right]$ is the canonical partition function, $\beta = 1/T$ ($k_{\text{B}} = 1$) is the inverse temperature, and we have used the cyclic invariance of the trace. Exploiting typicality, it is possible to rewrite $\langle A \rangle_{\text{eq}}$ according to

$$\langle A \rangle_{\text{eq}} = \frac{\langle \psi_\beta | A | \psi_\beta \rangle}{\langle \psi_\beta | \psi_\beta \rangle} + \epsilon , \quad (4)$$

where we have introduced the abbreviation $|\psi_\beta\rangle = e^{-\beta \mathcal{H}/2} |\psi\rangle$, which is sometimes referred to as thermal

pure quantum state [36]. The reference pure state $|\psi\rangle$ is drawn at random from the full Hilbert space with finite dimension d according to the unitary invariant Haar measure [17], i.e.,

$$|\psi\rangle = \sum_{k=1}^{d} (a_k + i b_k) |k\rangle , \quad (5)$$

where the coefficients a_k and b_k are drawn from a Gaussian distribution with zero mean (other types of randomness have been suggested as well [19, 38]), and the pure states $|k\rangle$ denote orthogonal basis states of the Hilbert space. (Note that $|\psi\rangle$ is almost maximally entangled [39, 40].) Importantly, the variance of the statistical error $\epsilon = \epsilon(|\psi\rangle)$ of the approximation (4) scales as $\sigma \propto 1/\sqrt{d_{\text{eff}}}$, where $d_{\text{eff}} = \text{Tr}[\exp(-\beta(\mathcal{H} - E_0))]$ is the effective dimension of the Hilbert space with E_0 being the ground-state energy of $\mathcal{H}$. Here we assume that A is a local operator (or a low-degree polynomial in system size), which applies to all examples discussed in this paper. For more details on error bounds see, e.g., Refs. [18, 36]. For empirical estimates, see, e.g., Ref. [41]. Thus, d_{eff} is essentially the number of thermally occupied states and, for $\beta = 0$, we have $d_{\text{eff}} = d$. As a consequence, increasing the number of degrees of freedom of a quantum many-body system, e.g., the number of lattice sites L, leads to an exponential improvement of the accuracy (the higher the temperature, the faster), and Eq. (4) becomes exact in the thermodynamic limit $L \to \infty$.

The typicality approximation (4) has proven to be very useful to calculate equilibrium quantities of quantum many-body systems such as the specific heat, entropy, or magnetic susceptibility [34–37, 41]. For the purpose of this review, however, it is most important to note that typicality is not just restricted to equilibrium properties, but also extends to the real-time dynamics of quantum expectation values [17, 27–29, 42–44]. This dynamical version of typicality forms the basis of the numerical approach to time-dependent correlation functions and out-of-equilibrium dynamics more generally, which is discussed in Sec. III.

Let us briefly discuss the relationship between typicality and the eigenstate thermalization hypothesis (ETH) [45–47]. The ETH states that the expectation values of local observables evaluated within individual eigenstates $|n\rangle$ of generic (nonintegrable) Hamiltonians coincide with the microcanonical ensemble average at the corresponding energy density,

$$A_{nn} = \langle n | A | n \rangle = A_{\text{mc}}(E) . \quad (6)$$

While this fact (i.e. pure states can approximate ensemble expectation values) appears similar to our discussion of typicality in the context of Eq. (4), let us stress that typicality and ETH are two distinct concepts. On the one hand, while the ETH is assumed to hold for a variety of few-body operators and nonintegrable models [5, 48–55], a rigorous proof for its validity is still absent. On the

other hand, typicality is no assumption and essentially requires the largeness of the effective Hilbert-space dimension. This difference becomes particularly clear from the following point of view: since the distribution of the a_k and b_k in Eq. (5) is invariant under any unitary transformation, the state $|\psi\rangle$ is a random superposition also in the eigenbasis of $\mathcal{H}$ (whereas the ETH just refers to single eigenstates). Due to this randomness, Eq. (4) holds even in cases where the ETH breaks down, i.e., where the expectation values of observables exhibit strong eigenstate-to-eigenstate fluctuations.

Since typicality is independent of the validity of the ETH, it can be used in integrable or many-body localized models, where the ETH is expected to be violated [56–59]. As a side remark, typicality can also be used to test the ETH [60].

Eventually, let us emphasize that the choice of the specific basis $|k\rangle$ in Eq. (5) is arbitrary. Therefore, the random state $|\psi\rangle$ can be conveniently constructed in the working basis which is used to set up the Hamiltonian and all other observables. For instance, when working with spin-1/2 systems, a common choice is the so-called Ising basis, i.e., the states $|k\rangle$ then denote the 2^L different combinations of $\uparrow$ and $\downarrow$. Naturally, it is possible to combine DQT with the use of symmetries [61], where a random state is then drawn independently within each subsector.

III.   DQT AS A NUMERICAL TOOL

We now discuss the use of dynamical quantum typicality as a numerical method. To begin with, we discuss in Sec. III A the iterative forward propagation of pure states in large Hilbert spaces. Afterwards, as a first application, we demonstrate in Sec. III B how typicality can be used to study the (local) density of states. In Sec. III C, we then show how DQT can be used to evaluate equilibrium correlation functions within the framework of linear response theory. Sec. III D is concerned with the out-of-equilibrium dynamics in certain quantum-quench scenarios. Eventually, in Sec. III E, we discuss how DQT can be combined with other approaches such as numerical linked cluster expansions or projection operator techniques.

A.   Pure-state propagation

From a numerical point of view, a central advantage of the typicality approach comes from the fact that one can work with pure states instead of having to deal with full density matrices. This fact leads to a substantial reduction of the memory requirements, since it is possible to efficiently generate time and temperature dependencies of pure states. (Note that, while it is always possible to purify a density matrix, the DQT approach in contrast does not require to square the Hilbert-space dimension [62].)

Specifically, let us consider the pure state $|\psi_\beta\rangle = e^{-\beta\mathcal{H}/2}|\psi\rangle$ introduced in Eq. (4). The time evolution of $|\psi_\beta\rangle$ is given by $|\psi_\beta(t)\rangle = e^{-i\mathcal{H}t}|\psi_\beta\rangle$. The full evolution up to time t can be subdivided into a product of consecutive steps,

$$|\psi_\beta(t)\rangle = \left(e^{-i\mathcal{H}\delta t}\right)^N |\psi_\beta\rangle \ , \qquad (7)$$

where $\delta t = t/N$ is a discrete time step. If δt is chosen sufficiently small, there is a variety of methods to accurately evaluate the action of the matrix exponential $e^{-i\mathcal{H}\delta t}$ without diagonalization of $\mathcal{H}$. A particularly simple approach in this context is a fourth-order Runge-Kutta (RK4) scheme, where the time evolution is approximated as [28, 29],

$$|\psi_\beta(t+\delta t)\rangle \approx |\psi_\beta(t)\rangle + \sum_{k=1}^{4}|f_k\rangle \ . \qquad (8)$$

The four auxiliary states $|f_1\rangle$ - $|f_4\rangle$ are constructed according to [28, 29],

$$|f_k\rangle = \frac{-i\mathcal{H}\delta t}{k}|f_{k-1}\rangle \ , \qquad |f_0\rangle = |\psi_\beta(t)\rangle \ , \qquad (9)$$

and the error of the approximation (8) scales as $\mathcal{O}(\delta t^5)$. Note that the RK4 scheme in Eqs. (8) and (9) is equivalent to a Taylor expansion of the exponential $e^{-i\mathcal{H}\delta t}$ up to fourth order. Note further that, in complete analogy to the propagation in real time, the temperature dependence of $|\psi_\beta\rangle$ can be generated by an evolution in small imaginary time steps $i\delta\beta$.

Apart from RK4, other common and more sophisticated methods to propagate pure states without diagonalization are, e.g., Trotter decompositions [34, 63], Krylov subspace techniques [64], as well as Chebyshev polynomial expansions [65–69]. A unifying property of all these methods and RK4 is the necessity to calculate matrix-vector products, i.e., to evaluate the action of the Hamiltonian $\mathcal{H}$ onto pure states. Importantly, such matrix-vector multiplications can be carried out relatively memory efficiently thanks to the sparse matrix structure of $\mathcal{H}$ in models with short-range interactions such as nearest-neighbor couplings. As a consequence, it is possible to numerically treat comparatively large system sizes, i.e., with huge Hilbert-space dimensions far beyond the range of exact diagonalization.

B.   Calculating the (local) density of states

As a first useful application, let us describe how pure states, in combination with a forward propagation in real time, can be used to evaluate the (local) density of states [33]. To begin with, we note that the density of states of some Hamiltonian $\mathcal{H}$ with eigenvalues E_n can be written

as

$$\Omega(E) = \sum_n \delta(E - E_n) \tag{10}$$

$$= \frac{1}{2\pi} \int_{-\infty}^{\infty} e^{itE} \, \mathrm{Tr}[e^{-i\mathcal{H}t}] \, \mathrm{d}t \ , \tag{11}$$

where we have used the definition of the δ function. In the spirit of Eq. (4), we can approximate the trace in Eq. (11) by a scalar product with a randomly drawn pure state $|\psi\rangle$,

$$\mathrm{Tr}[e^{-i\mathcal{H}t}] \propto \langle\psi| e^{-i\mathcal{H}t} |\psi\rangle = \langle\psi|\psi(t)\rangle \ , \tag{12}$$

such that Eq. (11) can be approximated as

$$\Omega(E) \propto \int_{-t_{\max}}^{+t_{\max}} e^{itE} \langle\psi|\psi(t)\rangle \, \mathrm{d}t \ , \tag{13}$$

where $\langle\psi(0)|\psi(-t)\rangle = \langle\psi(0)|\psi(t)\rangle^*$, and $t_{\max}$ is the maximum time to which $|\psi(t)\rangle$ is evolved. Due to this cutoff time, the resulting energy resolution of $\Omega(E)$ is given by $\Delta E = \pi/t_{\max}$. Thus, the density of states of some Hamiltonian $\mathcal{H}$ can be obtained from the Fourier transform of the survival probability $\langle\psi|\psi(t)\rangle$ of a random pure state [33].

In fact, the relation (13) turns out to be useful for any arbitrary pure state $|\tilde\psi\rangle$ (which is not necessarily drawn at random). The local density of states $P(E)$ of $|\tilde\psi\rangle$, i.e., the spectral distribution of $|\tilde\psi\rangle$, is then defined as

$$P(E) = \sum_n |\langle n|\tilde\psi\rangle|^2 \, \delta(E - E_n) \ , \tag{14}$$

where $|n\rangle$ are the eigenvectors of $\mathcal{H}$ with corresponding eigenvalues E_n. Analogous to Eq. (13), $P(E)$ can be written as the Fourier transform of the survival probability of $|\tilde\psi\rangle$ [33, 70],

$$P(E) \propto \int_{-t_{\max}}^{+t_{\max}} e^{itE} \langle\tilde\psi|\tilde\psi(t)\rangle \, \mathrm{d}t \ . \tag{15}$$

Relying on the forward propagation of pure states discussed in Sec. III A, it is thus possible to access $\Omega(E)$ and $P(E)$. Note that Eqs. (13) and (15) only provide the overall shape (within the resolution ΔE) of $\Omega(E)$ and $P(E)$, while single eigenstates are difficult to resolve [71, 72].

As an example, let us consider the spin-1/2 XXZ chain,

$$\mathcal{H} = J \sum_{\ell=1}^{L} \left(S_\ell^x S_{\ell+1}^x + S_\ell^y S_{\ell+1}^y + \Delta S_\ell^z S_{\ell+1}^z \right) \ , \tag{16}$$

where S_ℓ^α, $\alpha \in \{x, y, z\}$ are the components of the corresponding spin-1/2 operators at the site ℓ, L is the number of lattice sites, $J = 1$ describes the antiferromagnetic coupling constant, and $\Delta > 0$ is the anisotropy in the z-
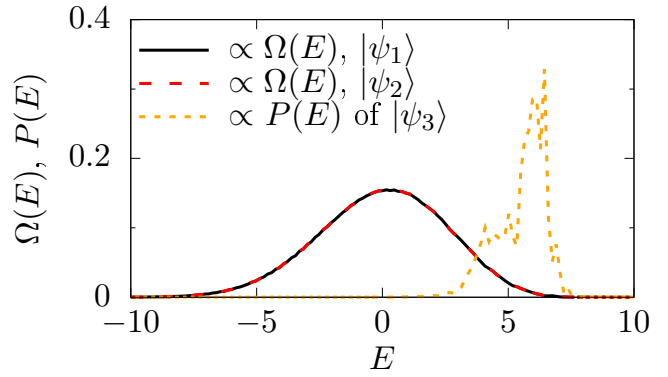

Figure 1. (Color online) Density of states $\Omega(E)$ of a spin-1/2 XXZ chain with $\Delta = 1.5$ and $L = 24$ sites, obtained from two independently drawn random states $|\psi_1\rangle$ and $|\psi_2\rangle$. The local density of states $P(E)$ is shown for a nonrandom state $|\psi_3\rangle$. Data is adapted from [71].

direction. In Fig. 1, the density of states $\Omega(E)$ is shown for the XXZ chain (16) with $L = 24$ and $\Delta = 1.5$, obtained via Eq. (13) with two independently drawn random states $|\psi_1\rangle$ and $|\psi_2\rangle$. As can be seen in Fig. 1, $\Omega(E)$ has a broad and Gaussian shape. Moreover, $\Omega(E)$ is essentially the same for the two random states, which confirms the accuracy of the typicality approach. In addition, we show $P(E)$ for a nonrandom state $|\psi_3\rangle$, which is sharply peaked at the borders of the spectrum [71].

C.   Time-dependent equilibrium correlation functions

Let us now turn to quantum many-body dynamics within the framework of linear response theory (LRT). Within LRT, central quantities of interest are time-dependent correlation functions $C_{AB}(t)$ of two operators A and B evaluated in equilibrium,

$$C_{AB}(t) = \langle A(t)B\rangle_{\mathrm{eq}} = \frac{\mathrm{Tr}\left[A(t)Be^{-\beta\mathcal{H}}\right]}{\mathcal{Z}} \ , \tag{17}$$

where $\mathcal{Z}$ is again the canonical partition function as defined in Eq. (3), and $A(t)$ is the time-evolved operator in the Heisenberg picture. Analogous to Eq. (4), $C_{AB}(t)$ can be rewritten according to [27–29],

$$\langle A(t)B\rangle_{\mathrm{eq}} \approx \frac{\langle\psi_\beta(t)|A|\varphi_\beta(t)\rangle}{\langle\psi_\beta(0)|\psi_\beta(0)\rangle} \ , \tag{18}$$

where we have introduced two auxiliary pure states,

$$|\varphi_\beta(t)\rangle = e^{-i\mathcal{H}t}Be^{-\beta\mathcal{H}/2} |\psi\rangle \ , \tag{19}$$

$$|\psi_\beta(t)\rangle = e^{-i\mathcal{H}t}e^{-\beta\mathcal{H}/2} |\psi\rangle \ , \tag{20}$$

and $|\psi\rangle$ is a random state drawn from the full Hilbert space, cf. Eq. (5). Importantly, in contrast to Eq. (17), the time (and temperature) argument in Eq. (18) is now
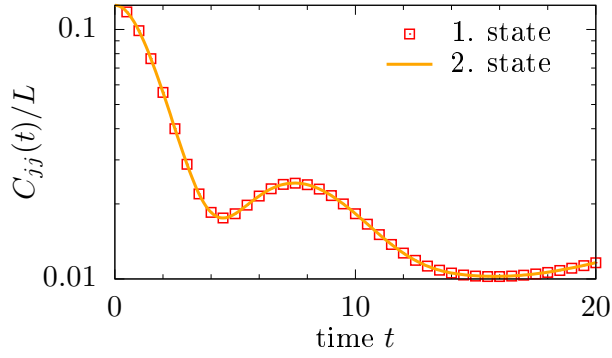
Figure 2. (Color online) Current autocorrelation function $C_{jj}(t)$ at $\beta = 0$ for the spin-1/2 XXZ chain with $\Delta = 1$, obtained by DQT for $L = 33$ sites. The calculation is done for two independently drawn states (from the symmetry subsector with momentum $k = 0$). Data is adapted from Ref. [74].

a property of the pure states and not of the operators anymore. According to, e.g., Eq. (8), $|\varphi_\beta(t)\rangle$ and $|\psi_\beta(t)\rangle$ can be evolved in real (and imaginary) time.

In the context of transport, an interesting quantity is the current autocorrelation function $C_{jj}(t)$, which is defined according to Eq. (17) with $A = B = j$, where j is the current operator. Note that the Fourier transform of $C_{jj}(t)$ is related to the conductivity via the Kubo formula [14, 73].

For concreteness, let us (again) consider the XXZ chain (16). In this case, the spin current operator j takes on the form [73],

$$j = J \sum_{\ell=1}^{L} \left(S_\ell^x S_{\ell+1}^y - S_\ell^y S_{\ell+1}^x \right) \ . \tag{21}$$

In Refs. [29, 74], $C_{jj}(t)$ was studied by means of DQT for the XXZ chain with particular focus on infinite temperature $\beta = 0$. This infinite-temperature current autocorrelation function is exemplarily shown in Fig. 2 for $\Delta = 1$ and $L = 33$. To demonstrate the smallness of the statistical error of DQT, we show results obtained from two independently drawn random states. As can be seen in Fig. 2, both curves coincide very well with each other for this choice of β and L, even in the semi-logarithmic plot used. (For further numerical data of $C_{jj}(t)$ see also Fig. 8 below.)

In addition to the XXZ chain, DQT has been used to study $C_{jj}(t)$ for a variety of other low-dimensional systems, such as spin chains with next-nearest neighbor interactions [71] and with spin quantum number $S > 1/2$ [59], spin ladders [75–77] (also for energy currents), as well as Fermi-Hubbard chains [78]. The possibility to calculate $C_{jj}(t)$ by means of DQT for large systems and long time scales has proven to be very useful to extract transport coefficients, including (the finite-size scaling of) dc conductivities, diffusion constants, and Drude weights,
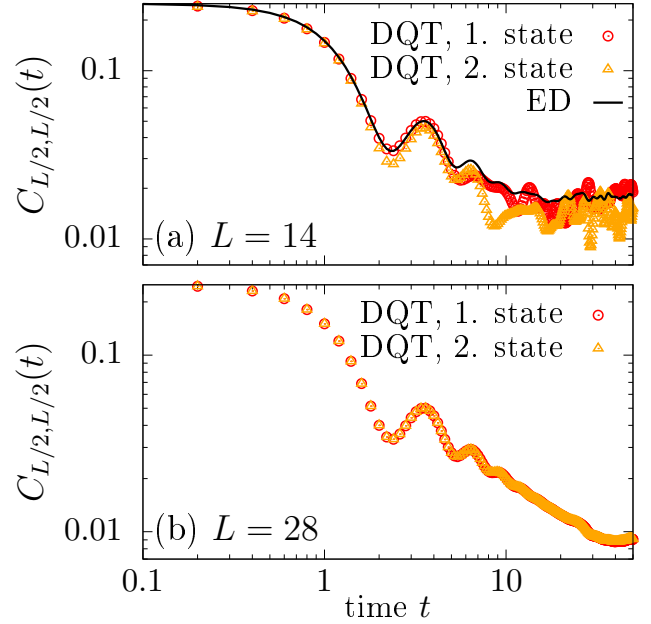

Figure 3. (Color online) Equal-site spin-spin correlation function $C_{L/2,L/2}(t)$ for spin-1/2 XXZ chains ($\Delta = 1$) with (a) $L = 14$ sites and (b) $L = 28$ sites. For $L = 14$, exact diagonalization is compared to DQT for two different random pure states. While ED is unfeasible for $L = 28$, the statistical fluctuations of the typicality approximation become negligible for this system size. Data is adapted from Ref. [79].

for integrable and nonintegrable models [29, 56, 59, 71, 74–78].

Another interesting quantity in the context of transport are the spatio-temporal correlation functions $C_{\ell,\ell'}(t)$ of, e.g., spin, which are defined according to Eq. (17) with $A = S_\ell^z$ and $B = S_{\ell'}^z$,

$$C_{\ell,\ell'}(t) = \langle S_\ell^z(t) S_{\ell'}^z \rangle_{\rm eq} \ . \tag{22}$$

While a calculation of $C_{\ell,\ell'}(t)$ can be done according to Eq. (18), a simplification is possible at infinite temperature $\beta = 0$. Namely, at $\beta = 0$, one can introduce the pure state [77]

$$|\psi'(0)\rangle = \frac{\sqrt{S_{\ell'}^z + c}\,|\psi\rangle}{\sqrt{\langle\psi|\psi\rangle}} \ , \tag{23}$$

where $|\psi\rangle$ is again drawn randomly according to Eq. (5), and the constant c is chosen such that $S_\ell^z + c$ has nonnegative eigenvalues. Using Eq. (23), one finds

$$C_{\ell,\ell'}(t) \approx \langle\psi'(t)|S_\ell^z|\psi'(t)\rangle \ . \tag{24}$$

Thus, it is possible to calculate $C_{\ell,\ell'}(t)$ just from one auxiliary state [59], in contrast to the current autocorrelations $C_{jj}(t)$, where two states have to be evolved in time, cf. Eqs. (19) and (20).

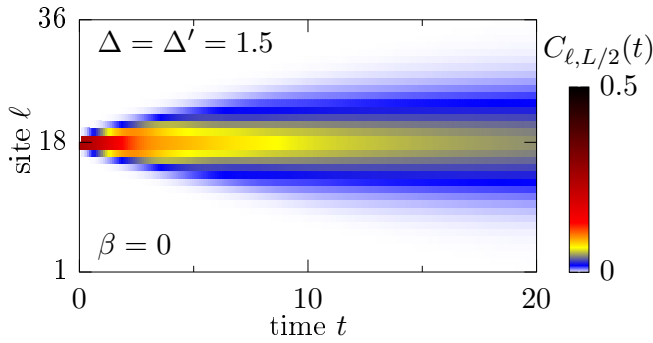As an example, the equal-site spin-spin correlation

Figure 4.   (Color online) Time-space plot of the infinite-temperature spin-spin correlation function $C_{\ell,L/2}(t) = \langle S^z_\ell(t) S^z_{L/2} \rangle_{\mathrm{eq}}$ for a spin-1/2 XXZ chain of length $L = 36$, nearest neighbor ($\Delta = 1.5$) and next-nearest neighbor ($\Delta' = 1.5$) coupling. Data is adapted from Ref. [71].

function $C_{L/2,L/2}(t)$ at lattice site $\ell = L/2$ is shown in Fig. 3 for spin-1/2 XXZ chains with two different lengths $L = 14$ and $L = 28$ [79]. (Note that due to periodic boundary conditions, the specific lattice site ℓ is arbitrary.) As a demonstration of the accuracy of the DQT approach, the calculation is done for two independently drawn pure states $|\psi\rangle$. While the DQT data closely follows the exact result at $L = 14$, the residual statistical fluctuations disappear almost completely for $L = 28$. Note that while we have chosen the XXZ chain to demonstrate the accuracy of DQT for $C_{jj}(t)$ [Fig. 2] and for $C_{L/2,L/2}(t)$ [Fig. 3], similar curves can be obtained for other models and observables as well. For additional comparisons between DQT data and exact ensemble averages, see, e.g., Refs. [29, 60].

As another example, the full time-space profile $C_{\ell,L/2}(t)$ is shown in Fig. 4 for a spin-1/2 XXZ chain with next-nearest neighbor interactions and $L = 36$ sites [71]. While at $\beta = 0$ different lattice sites are uncorrelated at $t = 0$, correlations start to build up for $t > 0$.

A very similar example is shown in Fig. 5, where the spatio-temporal correlations for spin and energy densities are depicted at fixed times. Yet, the model is a spin-1/2 Heisenberg ladder,

$$\mathcal{H} = J_\parallel \sum_{l=1}^{L} \sum_{k=1}^{2} \mathbf{S}_{l,k} \cdot \mathbf{S}_{l+1,k} + J_\perp \sum_{l=1}^{L} \mathbf{S}_{l,1} \cdot \mathbf{S}_{l,2} , \quad (25)$$

where $J_\parallel$ ($J_\perp$) denotes the coupling on the legs (rungs). The data in Fig. 5 are obtained for $J_\parallel = J_\perp = 1$ and $L = 20$, i.e., 40 lattice sites in total [77]. For all times shown in Fig. 5, one finds that the profiles $C_{\ell,L/2}(t)$ are convincingly described by Gaussians, which illustrates once again the high accuracy of the DQT approach in the semi-logarithmic plot used. Such a Gaussian spreading has been interpreted as a clear signature of high-temperature spin and energy diffusion in this and other models [57, 59, 71, 80, 81].
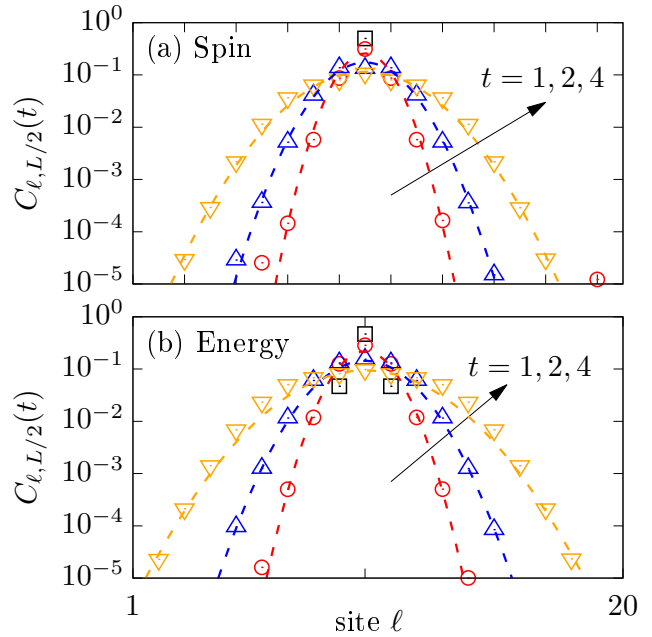

Figure 5.   (Color online) Spin-spin correlation function $C_{\ell,L/2}(t)$ at fixed times, $t = 0$ (δ peak) and $t = 1, 2, 4$ (arrow), for a spin-1/2 Heisenberg ladder of length $L = 20$ (i.e. 40 lattice sites), at high temperatures $\beta = 0$. Dashed lines are Gaussian fits to the data. Panel (a) shows spin densities, while panel (b) shows local energies. Data is adapted from Ref. [77].

In addition, DQT has been used to obtain spatio-temporal correlation functions $C_{\ell,\ell'}(t)$ in a number of other models. Remarkably, clean Gaussian profiles have been found in various parameter regimes, even for integrable models such as the spin-1/2 XXZ chain [57] or the one-dimensional Fermi-Hubbard model [80]. Other classes of models which have been studied in this way include the spin-1 XXZ chain [59] as well as spin models with quenched disorder [59, 82].

D.   Applications to far-from-equilibrium dynamics

Nonequilibrium scenarios in isolated quantum systems can be induced via explicitly time-dependent Hamiltonians or, e.g., by means of quantum quenches [83]. For instance, the system can be initially in an eigenstate of some Hamiltonian $\mathcal{H}_1$ while the subsequent dynamics are governed by a different Hamiltonian $\mathcal{H}_2$.

Here, we discuss an alternative type of quench, where the system starts in a Gibbs state with respect to (w.r.t.) some initial Hamiltonian $\mathcal{H}_1$ (see Fig. 6),

$$\rho(0) = \frac{\mathrm{e}^{-\beta \mathcal{H}_1}}{\mathcal{Z}} . \quad (26)$$

We then consider a quantum quench, where $\mathcal{H}_1$ is changed to some other Hamiltonian $\mathcal{H}_2$. The system

$$\rho(0) = \frac{e^{-\beta \mathcal{H}_1}}{\text{Tr}\left[e^{-\beta \mathcal{H}_1}\right]}$$
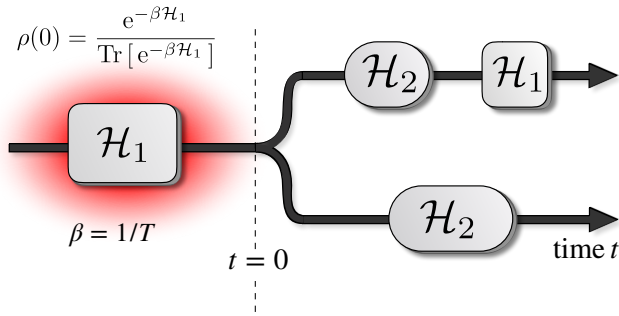

Figure 6. (Color online) Sketch of the quench protocol. The system starts in a Gibbs state with respect to some initial Hamiltonian $\mathcal{H}_1$. For times $t > 0$, the system evolves unitarily according to some other Hamiltonian $\mathcal{H}_2$ as per $\rho(t) = e^{-i\mathcal{H}_2 t}\,\rho(0)\,e^{i\mathcal{H}_2 t}$. This protocol can also be modified by switching back to the original Hamiltonian $\mathcal{H}_1$ (shown in the upper branch on the right hand side) or by further changes of the Hamiltonian in time.

then is in a nonequilibrium state and evolves unitarily according to the new Hamiltonian,

$$\rho(t) = e^{-i\mathcal{H}_2 t}\,\rho(0)\,e^{i\mathcal{H}_2 t} \ . \tag{27}$$

The post-quench Hamiltonian can, for instance, be created by adding or removing a static (weak or strong) force of strength ϵ to the initial Hamiltonian, i.e., $\mathcal{H}_2 = \mathcal{H}_1 \pm \epsilon A$, where the operator A is conjugated to the force [13, 58, 84, 85]. The resulting expectation value dynamics of, e.g., the operator A is given by

$$\langle A(t) \rangle = \text{Tr}\left[\rho(t) A\right] \ , \tag{28}$$

and its evaluation in principle requires complete diagonalization of both $\mathcal{H}_1$ and $\mathcal{H}_2$. As before, this diagonalization can be circumvented by preparing a typical pure state [13, 43, 58, 84, 85],

$$|\Psi(0)\rangle = \frac{e^{-\beta \mathcal{H}_1/2}\,|\psi\rangle}{\sqrt{\langle \psi|\,e^{-\beta \mathcal{H}_1}\,|\psi\rangle}} \ , \tag{29}$$

which mimics the density matrix (26), and the reference state $|\psi\rangle$ is again randomly drawn from the full Hilbert space, cf. Eq. (5). Both the imaginary-time evolution w.r.t. $\mathcal{H}_1$ and the real-time evolution w.r.t. $\mathcal{H}_2$ can be done following Sec. III A. In this way, one gets

$$\langle A(t) \rangle \approx \langle \Psi(t)|\,A\,|\Psi(t)\rangle \ . \tag{30}$$

It is worth pointing out that the (simple) quench protocol above can be modified by additional changes of the Hamiltonian in time. A static force switched on at time $t = 0$ can, for instance, be removed again at some later time $t > 0$, see also Fig. 6. Even for such protocols, the additional efforts of the DQT approach are minor compared to ED, where the diagonalization of multiple Hamiltonians has to be carried out.
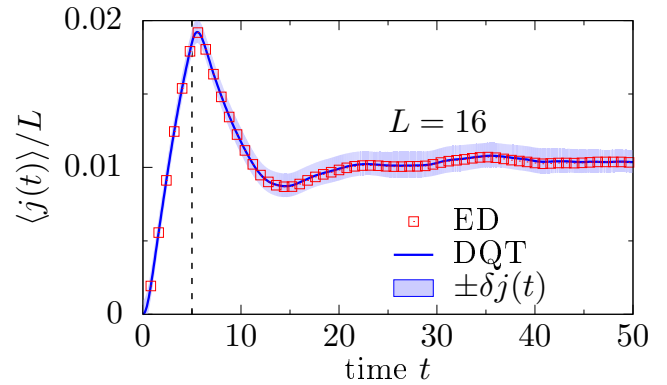

Figure 7. (Color online) Out-of-equilibrium dynamics of the spin current j in the spin-1/2 XXZ chain with $\Delta = 0.5$ and $L = 16$, starting from a thermal state with $\beta = 1$. For times $0 < t < 5$, an external force acts on the system, which gives rise to an additional term $\propto j$ within the Hamiltonian. Results from the typicality approach are compared to exact diagonalization. DQT data are averaged over $N = 100$ random initial states and the shaded area indicates the standard deviation. Data is adapted from Ref. [44].

In Fig. 7, the nonequilibrium dynamics $\langle j(t) \rangle$ of the spin current is exemplarily depicted for a XXZ chain which is initially prepared in a thermal state at the finite temperature $\beta = 1$ (see caption of Fig. 7 and Ref. [44] for a more detailed description of the protocol). Here, the accuracy of the DQT approach is demonstrated by comparing to data obtained by exact diagonalization.

E. DQT and its extensions

In addition to the direct applications discussed above, DQT also is a useful tool to "boost" other (numerical or analytical) techniques, which can profit from accurate data for large system sizes. Two examples of such techniques, which have recently been combined with DQT, are numerical linked-cluster expansions (NLCE) and projection operator techniques.

1. NLCE

The key feature used in NLCE is the fact that the per-site value of an extensive quantity on an infinite lattice can be expanded in terms of its respective weights on all linked (sub-)clusters that can be embedded in the lattice. While NLCE is described in detail and generality in [86, 87], this section focuses on practical aspects of NLCE, particularly on its combination with DQT to calculate, e.g., current-current correlation functions of one-dimensional systems. The starting point of a correspond-

ing NLCE is the expression

$$\frac{\langle j(t)j\rangle_{\text{eq}}}{L} = \sum_c \mathcal{L}_c W_c(t) ,\qquad(31)$$

where W_c is the weight of a cluster c with multiplicity $\mathcal{L}_c$. To avoid redundant computations, the multiplicity factor (divided by the total number of lattice sites) accounts for all clusters, which are symmetrically or topologically related to one representative cluster and therefore yield the same weight. The weight of each cluster is evaluated by the inclusion-exclusion principle

$$W_c(t) = \langle j(t)j\rangle_{\text{eq}}^{(c)} - \sum_{s \subset c} W_s(t) ,\qquad(32)$$

where the weights of all embedded clusters s are subtracted from $\langle j(t)j\rangle_{\text{eq}}^{(c)}$ evaluated on the cluster c.

Since the maximum treatable cluster size is naturally limited by the available computational resources, the sum in Eq. (31) has to be truncated to a maximum size c_{max}. In one dimension, this truncated sum reduces to the difference of the autocorrelation functions of the two largest open-boundary chains with length c_{max} and $c_{\text{max}}-1$, i.e.,

$$\sum_{c=2}^{c_{\text{max}}} W_c(t) = \langle j(t)j\rangle_{\text{eq}}^{(c_{\text{max}})} - \langle j(t)j\rangle_{\text{eq}}^{(c_{\text{max}}-1)} .\qquad(33)$$

As demonstrated in Ref. [88], this rather simple formula can have a better convergence towards the thermodynamic limit than a standard finite-size scaling at effectively equal computational cost.

As shown in Fig. 8, the current autocorrelation function for the spin-1/2 Heisenberg chain directly obtained by DQT for a large system with $L = 36$ still exhibits notable finite-size effects for times $t > 20$, whereas corresponding DQT+NLCE data is already converged for these times. Due to the truncation to a maximum cluster size c_{max}, however, the expansion eventually breaks down and only yields reliable results up to a maximum time, which increases with c_{max} [88–90]. For the specific example in Fig. 8, this maximum time is $t_{\text{max}} \sim 40$ for the maximum cluster size $c_{\text{max}} = 39$ calculated.

When studying thermodynamic quantities, for which the NLCE was originally introduced, using larger cluster sizes similarly improves the convergence of the expansion down to lower temperatures [87, 91]. Either way, it is thus desirable to access cluster sizes as large as possible and DQT can be used to evaluate the contributions of clusters beyond the range of ED. Since the difference in Eq. (33) could be sensitive to small statistical errors, it might be recommended to average the DQT results over multiple random pure states, in particular in higher dimensions, where the NLCE expression is not just a single difference.
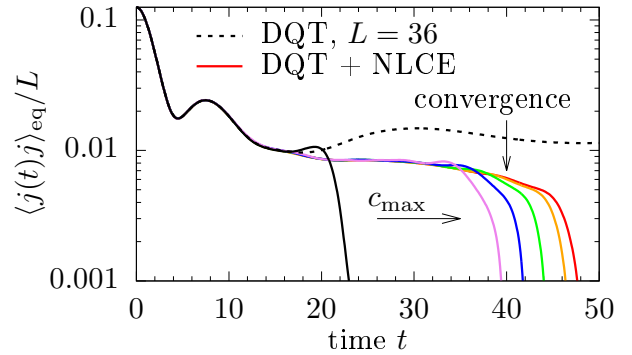

Figure 8. (Color online) Current-current correlation function $\langle j(t)j\rangle_{\text{eq}}/L$ in the XXZ chain ($\Delta = 1$) at $\beta = 0$. Dashed line indicates data obtained by DQT for $L = 36$ and periodic boundary conditions. Solid lines are obtained by the combination of DQT and NLCE for expansion orders $c_{\text{max}} = 18, 32, 34, 36, 38, 39$ (arrow). Data is adapted from Refs. [88, 92].

2. Projection operator techniques

The DQT approach can also be used in the context of projection operator techniques, e.g., the so-called time-convolutionless (TCL) projection operator method. These techniques can be applied to situations where a closed quantum system with Hamiltonian $\mathcal{H}_0$ is perturbed by an operator $\mathcal{V}$ with strength λ, such that the total Hamiltonian takes on the form

$$\mathcal{H} = \mathcal{H}_0 + \lambda \mathcal{V} .\qquad(34)$$

In this setting, one then chooses a suitable projection on the relevant degrees of freedom to obtain a systematic perturbation expansion for the reduced dynamics. Again, we refer to [92–95] for a detailed description of the TCL method and do not discuss it here in full generality.

Choosing a simple projection onto A only and considering the specific initial conditions $\rho(0) \sim A$ yields in second order of the perturbation [92, 95]

$$\langle A(t)\rangle_{\mathcal{H}} = \langle A(t)\rangle_{\mathcal{H}_0} \exp\left[-\lambda^2 \int_0^t dt' \gamma_2(t')\right] ,\qquad(35)$$

where the second-order damping rate $\gamma_2(t)$ is given by

$$\gamma_2(t) = -\int_0^t \frac{\text{Tr}\{[A, \mathcal{V}_{\text{I}}(t')][A, \mathcal{V}]\}}{\langle A^2\rangle} dt' \qquad(36)$$

and the index I indicates operators in the interaction picture.

The calculation of Eq. (36) can be conveniently done using typical states and becomes especially simple in the case where the observable of interest is conserved under the unperturbed Hamiltonian, i.e., $[A, \mathcal{H}_0] = 0$. By defining $\mathcal{K} = [A, \mathcal{V}]$ and $\mathcal{K}_{\text{I}}(t) = e^{i\mathcal{H}_0 t} \mathcal{K} e^{-i\mathcal{H}_0 t}$, the nu-
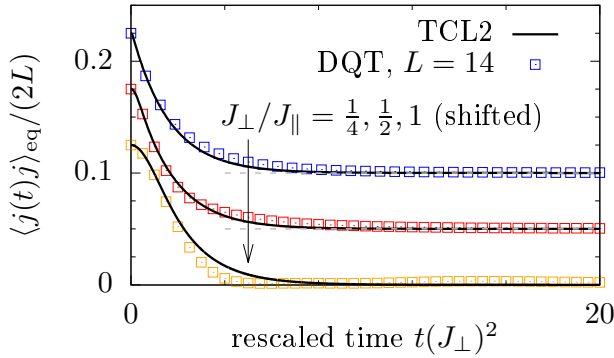
Figure 9. (Color online) Current-current correlation function for spin-1/2 XX ladders ($J_\parallel = 1$) with different interchain couplings $J_\perp$ (shifted for better visibility). Symbols denote exact data obtained by DQT for length $L = 14$, i.e., 28 spins in total. The solid lines indicate the prediction from the (second order) TCL projection operator method, cf. Eq. (35). Data is adapted from Ref. [92].

merator of Eq. (36) can be calculated as,

$$\mathrm{Tr}[\mathcal{K}_{\mathrm{I}}(t)\mathcal{K}] \propto \langle \psi(t)| \mathcal{K} |\varphi(t)\rangle \ , \tag{37}$$

with the auxiliary states

$$|\psi(t)\rangle = \mathrm{e}^{-i\mathcal{H}_0 t} |\psi\rangle \tag{38}$$

$$|\varphi(t)\rangle = \mathrm{e}^{-i\mathcal{H}_0 t} \mathcal{K} |\psi\rangle \ . \tag{39}$$

In [92], the quality of the second-order prediction (35) was numerically studied for the example of the current autocorrelation functions $\langle j(t)j\rangle_{\mathrm{eq}}$ in spin-1/2 ladder systems, where the interactions on the rungs of the ladder are treated as a perturbation to the otherwise uncoupled legs. As depicted in Fig. 9, the second-order prediction agrees convincingly with exact data obtained by DQT for different strengths of the perturbation.

IV.   CONCLUSION

To summarize, we have discussed several applications of dynamical quantum typicality and its usefulness as a numerical approach to the real-time dynamics of quantum many-body systems. The main idea of this typicality approach is to approximate ensemble expectation values via single pure states which are randomly drawn from a high-dimensional Hilbert space. In particular, time (temperature) dependencies of expectation values can be obtained by iteratively solving the Schrödinger equation in real (imaginary) time, e.g., by means of Runge-Kutta

schemes or more sophisticated methods.

First, we have described that DQT can be used to study the (local) density of states as well as equilibrium correlation functions for long time scales and comparatively large system sizes beyond the range of standard exact diagonalization. Especially in the context of transport, the calculation of current autocorrelations and density-density correlations by means of DQT is possible. Furthermore, we have outlined that DQT is suitable to investigate also the far-from-equilibrium dynamics resulting from certain quench protocols. For instance, an initial Gibbs state is properly imitated by a typical pure state and nonequilibrium conditions are induced by removing or adding an external force. Eventually, we have discussed that DQT can additionally be combined with other approaches. As one example, we have shown that the convergence of numerical linked-cluster expansions can be improved by evaluating the contributions of larger clusters by means of DQT. As another example, we have discussed that DQT allows to compute memory kernels which arise in projection operator methods such as the TCL technique.

While this paper has illustrated the usefulness of DQT for selected applications in the context of transport and thermalization, we should stress that there certainly are other applications of DQT which have not been mentioned by us. One such application, as done in, e.g., [96], is the spreading of quantum information measured by so-called out-of-time-ordered correlators (OTOCs) of the form [97],

$$C(t) = \frac{\mathrm{Tr}[A(t)BA(t)B]}{d} \ , \tag{40}$$

where the operators A and B are, for instance, local magnetization densities S_ℓ^z at two different lattice sites. Similar to the correlation functions discussed in Eq. (17), the OTOC in Eq. (40) can be approximated as the overlap $C(t) \approx \langle \psi_2(t)|\psi_1(t)\rangle$ of the two auxiliary states $|\psi_1(t)\rangle = A(t)B |\psi\rangle$ and $|\psi_2(t)\rangle = BA(t) |\psi\rangle$, where $|\psi\rangle$ is again a Haar-random state [96].

In conclusion, the concept of dynamical quantum typicality offers a rather simple yet remarkably useful approach to study the real-time dynamics of quantum many-body systems. It is our hope that the examples discussed in this paper motivate its application in other areas as well.

[1] I. Bloch, J. Dalibard, and S. Nascimbène, Nat. Phys. **8**, 267 (2012).

[2] R. Blatt and C. F. Roos, Nat. Phys. **8**, 277 (2012).

[3] A. Polkovnikov, K. Sengupta, A. Silva, and M. Vengalattore, Rev. Mod. Phys. **83**, 863 (2011).

[4] J. Eisert, M. Friesdorf, and C. Gogolin, Nat. Phys. **11**, 124 (2015).

[5] L. D'Alessio, Y. Kafri, A. Polkovnikov, and M. Rigol, Adv. Phys. **65**, 239 (2016).

[6] C. Gogolin and J. Eisert, Rep. Prog. Phys. **79**, 056001 (2016).

[7] F. Borgonovi, F. Izrailev, L. F. Santos, and V. Zelevinsky, Phys. Rep. **626**, 1 (2016).

[8] M. Buchanan, Nat. Phys. **1**, 71 (2005).

[9] V. Khemani, A. Vishwanath, and D. A. Huse, Phys. Rev. X **8**, 031057 (2018).

[10] B. Bertini, F. Heidrich-Meisner, C. Karrasch, T. Prosen, R. Steinigeweg, and M. Žnidarič, Rev. Mod. Phys. **93**, 025003 (2021).

[11] M. Prüfer, P. Kunkel, H. Strobel, S. Lannig, D. Linnemann, C.-M. Schmied, J. Berges, T. Gasenzer, and M. K. Oberthaler, Nature **563**, 217 (2018).

[12] S. Erne, R. Bücker, T. Gasenzer, J. Berges, and J. Schmiedmayer, Nature **563**, 225 (2018).

[13] J. Richter and R. Steinigeweg, Phys. Rev. E **99**, 012114 (2019).

[14] R. Kubo, M. Toda, and N. Hashitsume, *Statistical Physics II*, 2nd ed., Springer Series in Solid-State Sciences, Vol. 31 (Springer Berlin Heidelberg, 1991).

[15] U. Schollwöck, Ann. Phys. (NY) **326**, 96 (2011).

[16] S. Paeckel, T. Köhler, A. Swoboda, S. R. Manmana, U. Schollwöck, and C. Hubig, Ann. Phys. (NY) **411**, 167998 (2019).

[17] C. Bartsch and J. Gemmer, Phys. Rev. Lett. **102**, 110403 (2009).

[18] P. Reimann, Phys. Rev. E **97**, 062129 (2018).

[19] R. Alben, M. Blume, H. Krakauer, and L. Schwartz, Phys. Rev. B **12**, 4090 (1975).

[20] S. Lloyd, *Pure state quantum statistical mechanics and black holes*, Phd thesis, The Rockefeller University (1988), arXiv:1307.0378.

[21] H. De Raedt and P. de Vries, Z. Phys. B **77**, 243 (1989).

[22] J. Jaklič and P. Prelovšek, Phys. Rev. B **49**, 5065 (1994).

[23] J. Gemmer, M. Michel, and G. Mahler, *Quantum Thermodynamics*, Lecture Notes in Physics, Vol. 657 (Springer, Berlin, Heidelberg, 2004).

[24] S. Popescu, A. J. Short, and A. Winter, Nat. Phys. **2**, 754 (2006).

[25] S. Goldstein, J. L. Lebowitz, R. Tumulka, and N. Zanghì, Phys. Rev. Lett. **96**, 050403 (2006).

[26] P. Reimann, Phys. Rev. Lett. **99**, 160404 (2007).

[27] T. Iitaka and T. Ebisuzaki, Phys. Rev. Lett. **90**, 047203 (2003).

[28] T. A. Elsayed and B. V. Fine, Phys. Rev. Lett. **110**, 070404 (2013).

[29] R. Steinigeweg, J. Gemmer, and W. Brenig, Phys. Rev. Lett. **112**, 120601 (2014).

[30] S. Okamoto, G. Alvarez, E. Dagotto, and T. Tohyama, Phys. Rev. E **97**, 043308 (2018).

[31] Y. Yamaji, T. Suzuki, and M. Kawamura, arXiv:1802.02854.

[32] I. Rousochatzakis, S. Kourtis, J. Knolle, R. Moessner, and N. B. Perkins, Phys. Rev. B **100**, 045117 (2019).

[33] A. Hams and H. De Raedt, Phys. Rev. E **62**, 4365 (2000).

[34] P. de Vries and H. De Raedt, Phys. Rev. B **47**, 7929 (1993).

[35] S. Sugiura and A. Shimizu, Phys. Rev. Lett. **108**, 240401 (2012).

[36] S. Sugiura and A. Shimizu, Phys. Rev. Lett. **111**, 010401 (2013).

[37] A. Wietek, P. Corboz, S. Wessel, B. Normand, F. Mila, and A. Honecker, Phys. Rev. Research **1**, 033038 (2019).

[38] T. Iitaka and T. Ebisuzaki, Phys. Rev. E **69**, 057701 (2004).

[39] D. N. Page, Phys. Rev. Lett. **71**, 1291 (1993).

[40] L. Vidmar and M. Rigol, Phys. Rev. Lett. **119**, 220603 (2017).

[41] J. Schnack, J. Richter, and R. Steinigeweg, Phys. Rev. Research **2**, 013186 (2020).

[42] T. Monnai and A. Sugita, J. Phys. Soc. Jpn. **83**, 094001 (2014).

[43] H. Endo, C. Hotta, and A. Shimizu, Phys. Rev. Lett. **121**, 220601 (2018).

[44] J. Richter, M. H. Lamann, C. Bartsch, R. Steinigeweg, and J. Gemmer, Phys. Rev. E **100**, 032124 (2019).

[45] J. M. Deutsch, Phys. Rev. A **43**, 2046 (1991).

[46] M. Srednicki, Phys. Rev. E **50**, 888 (1994).

[47] M. Rigol, V. Dunjko, and M. Olshanii, Nature **452**, 854 (2008).

[48] L. F. Santos and M. Rigol, Phys. Rev. E **82**, 031130 (2010).

[49] R. Steinigeweg, J. Herbrych, and P. Prelovšek, Phys. Rev. E **87**, 012118 (2013).

[50] W. Beugeling, R. Moessner, and M. Haque, Phys. Rev. E **89**, 042112 (2014).

[51] H. Kim, T. N. Ikeda, and D. A. Huse, Phys. Rev. E **90**, 052105 (2014).

[52] R. M. Nandkishore and D. A. Huse, Annu. Rev. Condens. Matter Phys. **6**, 15 (2015).

[53] R. Mondaini and M. Rigol, Phys. Rev. E **96**, 012157 (2017).

[54] D. Jansen, J. Stolpp, L. Vidmar, and F. Heidrich-Meisner, Phys. Rev. B **99**, 155130 (2019).

[55] I. M. Khaymovich, M. Haque, and P. A. McClarty, Phys. Rev. Lett. **122**, 070601 (2019).

[56] R. Steinigeweg, J. Herbrych, F. Pollmann, and W. Brenig, Phys. Rev. B **94**, 180401 (2016).

[57] R. Steinigeweg, F. Jin, D. Schmidtke, H. De Raedt, K. Michielsen, and J. Gemmer, Phys. Rev. B **95**, 035155 (2017).

[58] J. Richter, J. Herbrych, and R. Steinigeweg, Phys. Rev. B **98**, 134302 (2018).

[59] J. Richter, N. Casper, W. Brenig, and R. Steinigeweg, Phys. Rev. B **100**, 144423 (2019).

[60] R. Steinigeweg, A. Khodja, H. Niemeyer, C. Gogolin, and J. Gemmer, Phys. Rev. Lett. **112**, 130403 (2014).

[61] T. Heitmann and J. Schnack, Phys. Rev. B **99**, 134405 (2019).

[62] L. P. Hughston, R. Jozsa, and W. K. Wootters, Phys. Lett. A **183**, 14 (1993).

[63] H. De Raedt, K. Michielsen, H. D. Raedt, and K. Michielsen, Host Publ. , 248 (2006).

[64] A. Nauts and R. E. Wyatt, Phys. Rev. Lett. **51**, 2238 (1983).

[65] H. Tal-Ezer and R. Kosloff, J. Chem. Phys. **81**, 3967 (1984).

[66] R. Kosloff, Annu. Rev. Phys. Chem. **45**, 145 (1994).

[67] V. V. Dobrovitski and H. A. De Raedt, Phys. Rev. E **67**, 056702 (2003).

[68] A. Weiße, G. Wellein, A. Alvermann, and H. Fehske, Rev. Mod. Phys. **78**, 275 (2006).

[69] R. Kosloff, J. Chem. Phys. **150**, 204105 (2019).

[70] M. Schiulaz, E. J. Torres-Herrera, and L. F. Santos, Phys. Rev. B **99**, 174313 (2019).

[71] J. Richter, F. Jin, H. De Raedt, K. Michielsen, J. Gemmer, and R. Steinigeweg, Phys. Rev. B **97**, 174430 (2018).

[72] D. M. Kennes, C. Karrasch, and A. J. Millis, Phys. Rev. B **101**, 081106(R) (2020).

[73] F. Heidrich-Meisner, A. Honecker, and W. Brenig, Eur. Phys. J. Spec. Top. **151**, 135 (2007).

[74] R. Steinigeweg, J. Gemmer, and W. Brenig, Phys. Rev. B **91**, 104404 (2015).

[75] R. Steinigeweg, F. Heidrich-Meisner, J. Gemmer, K. Michielsen, and H. De Raedt, Phys. Rev. B **90**, 094417 (2014).

[76] R. Steinigeweg, J. Herbrych, X. Zotos, and W. Brenig, Phys. Rev. Lett. **116**, 017202 (2016).

[77] J. Richter, F. Jin, L. Knipschild, J. Herbrych, H. De Raedt, K. Michielsen, J. Gemmer, and R. Steinigeweg, Phys. Rev. B **99**, 144422 (2019).

[78] F. Jin, R. Steinigeweg, F. Heidrich-Meisner, K. Michielsen, and H. De Raedt, Phys. Rev. B **92**, 205103 (2015).

[79] B. N. Balz, J. Richter, J. Gemmer, R. Steinigeweg, and P. Reimann, in Thermodynamics in the Quantum Regime (Springer, Cham, 2018) pp. 413–433.

[80] R. Steinigeweg, F. Jin, H. De Raedt, K. Michielsen, and J. Gemmer, Phys. Rev. E **96**, 020105(R) (2017).

[81] M. Ljubotina, M. Žnidarič, and T. Prosen, Nat. Commun. **8**, 16117 (2017).

[82] J. Richter, D. Schubert, and R. Steinigeweg, Phys. Rev. Research **2**, 013130 (2020).

[83] A. Mitra, Annu. Rev. Condens. Matter Phys. **9**, 245 (2018).

[84] C. Bartsch and J. Gemmer, EPL (Europhys. Lett.) **118**, 10006 (2017).

[85] J. Richter, J. Gemmer, and R. Steinigeweg, Phys. Rev. E **99**, 050104 (2019).

[86] M. Rigol, T. Bryant, and R. R. P. Singh, Phys. Rev. Lett. **97**, 187202 (2006).

[87] B. Tang, E. Khatami, and M. Rigol, Comput. Phys. Commun. **184**, 557 (2013).

[88] J. Richter and R. Steinigeweg, Phys. Rev. B **99**, 094419 (2019).

[89] I. G. White, B. Sundar, and K. R. A. Hazzard, arXiv:1710.07696.

[90] K. Mallayya and M. Rigol, Phys. Rev. Lett. **120**, 070603 (2018).

[91] K. Bhattaram and E. Khatami, Phys. Rev. E **100**, 013305 (2019).

[92] J. Richter, F. Jin, L. Knipschild, H. De Raedt, K. Michielsen, J. Gemmer, and R. Steinigeweg, Phys. Rev. E **101**, 062133 (2020).

[93] S. Chaturvedi and F. Shibata, Z. Phys. B **35**, 297 (1979).

[94] H.-P. Breuer and F. Petruccione, The Theory of Open Quantum Systems (Oxford University Press, 2007).

[95] R. Steinigeweg, Phys. Rev. E **84**, 011136 (2011).

[96] D. J. Luitz and Y. Bar Lev, Phys. Rev. B **96**, 020406 (2017).

[97] J. Maldacena, S. H. Shenker, and D. Stanford, J. High Energ. Phys. **2016**, 106 (2016).

Preprint of Publication [P3]

[P3] Jürgen Schnack, Johannes Richter, Tjark Heitmann, Jonas Richter, and Robin Steinigeweg,
Finite-Size Scaling of Typicality-Based Estimates,
Journal reference: Z. Naturforsch. A **75**, 465 (2020) [Open Access]
DOI: 10.1515/zna-2020-0031
Preprint: `arXiv:2002.00411`

Finite-Size Scaling of Typicality-Based Estimates

Jürgen Schnack [iD],[1, *] Johannes Richter [iD],[2, 3, †] Tjark Heitmann [iD],[4] Jonas Richter [iD],[4] and Robin Steinigeweg [iD][4, ‡]

[1]*Fakultät für Physik, Universität Bielefeld, Postfach 100131, D-33501 Bielefeld, Germany*
[2]*Institut für Theoretische Physik, Universität Magdeburg, P.O. Box 4120, D-39016 Magdeburg, Germany*
[3]*Max-Planck-Institut für Physik Komplexer Systeme, Nöthnitzer Straße 38, 01187 Dresden, Germany*
[4]*Fachbereich Physik, Universität Osnabrück, Barbarastr. 7, D-49076 Osnabrück, Germany*

According to the concept of typicality, an ensemble average can be accurately approximated by an expectation value with respect to a single pure state drawn at random from a high-dimensional Hilbert space. This random-vector approximation, or trace estimator, provides a powerful approach to, e.g., thermodynamic quantities for systems with large Hilbert-space sizes, which usually cannot be treated exactly, analytically or numerically. Here, we discuss the finite-size scaling of the accuracy of such trace estimators from two perspectives. First, we study the full probability distribution of random-vector expectation values and, second, the full temperature dependence of the standard deviation. With the help of numerical examples, we find pronounced Gaussian probability distributions and the expected decrease of the standard deviation with system size, at least above certain system-specific temperatures. Below and in particular for temperatures smaller than the excitation gap, simple rules are not available.

I.   INTRODUCTION

Methods such as the finite-temperature Lanczos method (FTLM) [1–7], that rest on trace estimators [1, 8–16] and thus – in more modern phrases – on the idea of typicality [17–20], approximate equilibrium thermodynamic observables with very high accuracy [2, 21]. In the canonical ensemble, the observable can be evaluated either with respect to a single random vector $|r\rangle$,

$$O^{\mathrm{r}}(T) \approx \frac{\langle r| \underset{\sim}{O} e^{-\beta \underset{\sim}{H}} |r\rangle}{\langle r| e^{-\beta \underset{\sim}{H}} |r\rangle} \ , \qquad (1)$$

or with respect to an average over R random vectors,

$$O^{\mathrm{FTLM}}(T) \approx \frac{\sum_{r=1}^{R} \langle r| \underset{\sim}{O} e^{-\beta \underset{\sim}{H}} |r\rangle}{\sum_{r=1}^{R} \langle r| e^{-\beta \underset{\sim}{H}} |r\rangle} \ , \qquad (2)$$

where numerator and denominator are averaged with respect to the same set of random vectors. The components of $|r\rangle$ with respect to an orthonormal basis are taken from a Gaussian distribution with zero mean (Haar measure [22–24]), but in practice other distributions work as well. T, β, and $\underset{\sim}{H}$ denote the temperature, inverse temperature and the Hamiltonian, respectively.

In this work, we discuss the accuracy of Eqs. (1) and (2), where we particularly focus on the dependence of this accuracy on the system size or, to be more precise, the dimension of the effective Hilbert space spanned by thermally occupied energy eigenstates. While it is well established that the accuracy of both equations increases with the square root of this dimension, we shed light on the size dependence from two less studied perspectives. First, we study the full probability distribution of random-vector expectation values, for the specific example of magnetic susceptibility and heat capacity in quantum spin systems on a one-dimensional lattice. At high temperatures, our numerical simulations unveil that these distributions are remarkably well described by simple Gaussian functions over several orders of magnitudes. Moreover, they clearly narrow with the inverse square root of the Hilbert-space dimension towards a δ function. Decreasing temperature at fixed system size, we find the development of broader and asymmetric distributions. Increasing the system size at fixed temperature, however, distributions become narrow and symmetric again. Thus, the mere knowledge of the standard deviation turns out to be sufficient to describe the full statistics of random-vector expectation values – at least at not too low temperatures.

The second central perspective of our work is taken by performing a systematic analysis of the scaling of the standard deviation with the system size, over the entire range of temperature and in various quantum spin models including spin-1/2 and spin-1 Heisenberg chains, critical spin-1/2 sawtooth chains, as well as cuboctahedra with spins 3/2, 2, and 5/2. We show a monotonous decrease of the standard deviation with increasing effective Hilbert-space dimension, as long as temperature is high compared to some system-specific low-energy scale. Below this scale, the scaling can become unsystematic if only a very few low-lying energy eigenstates contribute. However, when averaging according to Eq. (2) over a decent number (~ 100) of random vectors, one can still determine the thermodynamic average very accurately in all examples considered by us. A quite interesting example constitutes the critical spin-1/2 sawtooth chain, where a single state drawn at random is enough to obtain this average down to very low temperatures.

This paper is organized as follows. In Sec. II we briefly recapitulate models, methods, as well as typicality-based estimators. In Sec. III we present our numerical examples

----

[*] jschnack@uni-bielefeld.de
[†] Johannes.Richter@physik.uni-magdeburg.de
[‡] rsteinig@uos.de

both for frustrated and unfrustrated spin systems. The paper finally closes with a summary and discussion in Sec. IV.

II.   METHOD

In this article we study several spin systems at zero magnetic field. They are of finite size and described by the Heisenberg model,

$$\underset{\sim}{H} = \sum_{i<j} J_{ij}\, \vec{\underset{\sim}{s}}_i \cdot \vec{\underset{\sim}{s}}_j \; , \tag{3}$$

where the sum runs over ordered pairs of spins. Here and in the following operators are marked by a tilde, i.e. $\vec{\underset{\sim}{s}}_i$ denotes the spin-vector operator at site i. J_{ij} denotes the exchange interaction between a spin at site i and a spin at site j. With the sign convention in (3), $J_{ij} > 0$ corresponds to antiferromagnetic interaction.

Numerator and denominator of (2), the latter is the partition function, are evaluated using a Krylov-space expansion, i.e. a spectral representation of the exponential in a Krylov space with $|r\rangle$ as starting vector of the Krylov-space generation, compare [1, 4]. One could equally well employ Chebyshev polynomials [13, 25, 26] or integrate the imaginary-time Schrödinger equation with a Runge-Kutta method [27–29], the latter is used later in this paper as well.

If the Hamiltonian $\underset{\sim}{H}$ possesses symmetries, they can be used to block-structure the Hamiltonian matrix according to the irreducible representations of the employed symmetry groups [4, 5], which yields for the partition function

$$Z^{\mathrm{FTLM}}(T) \approx \sum_{\gamma=1}^{\Gamma} \frac{\dim[\mathcal{H}(\gamma)]}{R}$$
$$\times \sum_{r=1}^{R} \sum_{n=1}^{N_L} e^{-\beta \epsilon_n^{(r)}} |\langle n(r)\,|\,r\rangle|^2 \; . \tag{4}$$

$\mathcal{H}(\gamma)$ labels the subspace that belongs to the irreducible representation γ, N_L denotes the dimension of the Krylov space, and $|n(r)\rangle$ is the n-th eigenvector of $\underset{\sim}{H}$ in this Krylov space grown from $|r\rangle$. The energy eigenvalue is $\epsilon_n^{(r)}$. To perform the Lanczos diagonalization for larger system sizes, we use the public code *spinpack* [30, 31].

In our numerical studies we evaluate the uncertainty of a physical quantity by repeating its numerical evaluation N_S times. For this statistical sample we define the standard deviation of the observable in the following way:

$$\delta(O) = \sqrt{\frac{1}{N_S}\sum_{r=1}^{N_S} [O^{\mathrm{m}}(T)]^2 - \left[\frac{1}{N_S}\sum_{r=1}^{N_S} O^{\mathrm{m}}(T)\right]^2}$$
$$= \sqrt{\overline{[O^{\mathrm{m}}(T)]^2} - \left[\overline{O^{\mathrm{m}}(T)}\right]^2} \; . \tag{5}$$

$O^{\mathrm{m}}(T)$ is either evaluated according to (1) (m=r) or to (2) (m=FTLM), depending on whether the fluctuations of approximations with respect to one random vector or with respect to an average over R vectors shall be investigated.

We consider two physical quantities, the zero-field susceptibility as well as the heat capacity. Both are evaluated as variances of magnetization and energy, respectively, i.e.

$$\chi(T) = \frac{(g\mu_B)^2}{k_B T}\left[\left\langle (\underset{\sim}{S}^z)^2 \right\rangle - \left\langle \underset{\sim}{S}^z \right\rangle^2\right], \tag{6}$$

$$C(T) = \frac{k_B}{(k_B T)^2}\left[\left\langle \underset{\sim}{H}^2 \right\rangle - \left\langle \underset{\sim}{H} \right\rangle^2\right]. \tag{7}$$

We compare our results with the well-established high-temperature estimate

$$\delta\langle \underset{\sim}{Q}\rangle \simeq \langle \underset{\sim}{Q}\rangle \frac{\alpha}{\sqrt{Z_{\mathrm{eff}}}} \; , \qquad Z_{\mathrm{eff}} = \mathrm{tr}\left[e^{-\beta(\underset{\sim}{H}-E_0)}\right] \; . \tag{8}$$

Here E_0 denotes the ground-state energy. In general the prefactor α depends on the specific system, its structure and size, as well as on temperature [18, 19], but empirically often turns out to be a constant of order $\alpha \approx 1$ for high enough temperatures, compare [2, 6, 21]. Rigorous error bounds, see Refs. [19, 32], share the dependence on $1/\sqrt{Z_{\mathrm{eff}}}$, but lead to a prefactor that can be substantially larger than the empirical finding.

III.   NUMERICAL RESULTS

We now present our numerical results. First, in the following Sec. III A, the full probability distribution of random-vector expectation values is discussed for shorter spin chains, where this distribution can be easily obtained by generating a large set of different random vectors. In the remainder of Sec. III the size dependence of the standard deviation is investigated for longer spin chains of spin $s = 1/2$ and $s = 1$, respectively, which are treated by Lanczos methods. The interesting behavior of a quantum critical delta chain is studied as well. Finally, we discuss the dependence of the standard deviation on the spin quantum number for a body of fixed size, the cuboctahedron.

A. Distribution of random-vector expectation values for smaller antiferromagnetic spin-1/2 chains

As a first step, in order to judge the accuracy of the single-state estimate in (1), it is instructive to study its full probability distribution p, obtained by drawing many [here $\mathcal{O}(10^4 - 10^6)$] random vectors. To be more precise, we evaluate the numerator of (1) for different random states $|r\rangle$, while its denominator is calculated as the average over all $|r\rangle$,

$$\frac{\langle r|\, \underset{\sim}{Q} e^{-\beta \underset{\sim}{H}}\, |r\rangle}{\sum_{r=1}^{R}\, \langle r|\, e^{-\beta \underset{\sim}{H}}\, |r\rangle} \; . \tag{9}$$

The advantage of using this equation, instead of (1), is that the mean coincides with (2), the latter should be used to correctly obtain the low-temperature average in system of finite size [21]. However, at sufficiently high temperatures or in sufficiently large systems, one might equally well use (1), as we have checked.

The single results for (9) are then collected into bins of appropriate width in order to form a "smooth" distribution p. While one might expect that p will be approximately symmetric around the respective thermodynamic average, the width of the distribution indicates how reliable a single random vector can approximate the ensemble average.

In this Section, we study the probability distribution p (in the following denoted as p_χ and p_C) for the quantities $\chi(T)T/N$ and $C(T)T^2/N$, and exemplarily consider the one-dimensional spin-1/2 Heisenberg model with antiferromagnetic nearest-neighbor coupling $J > 0$ and chain length N. Note that, as discussed in the upcoming Secs. III B - III E, details of the model can indeed have an impact on the behavior of p in certain temperature regimes. Note further, that we focus in this Section on small to intermediate system sizes $N \leq 20$, where p can be easily obtained by generating a large set of different random vectors and evolving these vectors in imaginary time by, e.g., a simple Runge-Kutta scheme. We have checked that the Runge-Kutta scheme employed in this Section has practically no impact on p.

To begin with, in Fig. 1 (a), p_χ is shown for different chain lengths $N = 12, \ldots, 20$ at infinite temperature $\beta J = 0$. For all values of N shown here, we find that p_χ is well described by a Gaussian distribution [33] over several orders of magnitude. While the mean of these Gaussians is found to accurately coincide with the thermodynamic average $\lim_{T\to\infty} \chi(T)T/N = 1/4$ [34], we moreover observe that the width of the Gaussians becomes significantly narrower upon increasing N. This fact already visualizes that the accuracy of the estimate in (1) improves for increasing Hilbert-space dimension. In particular, as shown in the inset of Fig. 1, the standard deviation $\delta(\chi)$ scales as $\delta(\chi) \propto 1/\sqrt{d}$, where $d = 2^N$ is the dimension of the Hilbert space. This is in agreement with (8) for $\alpha \approx 1.2$ and $Z_{\text{eff}} = d$ at $\beta = 0$. Note
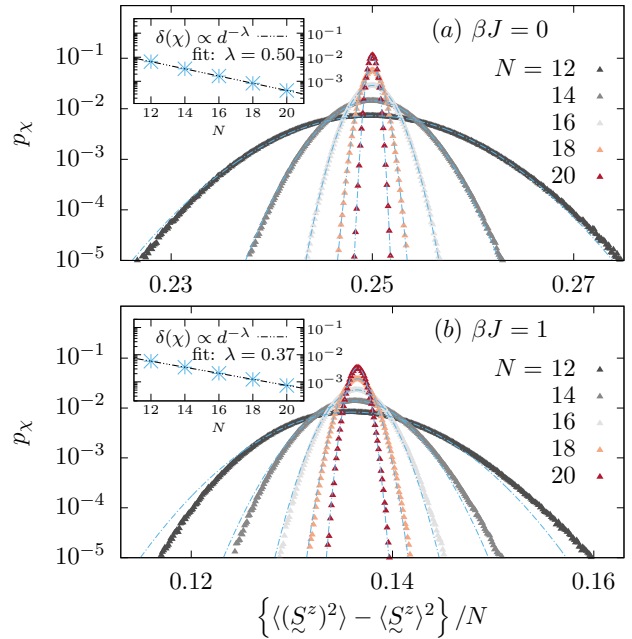

Figure 1. (a) Probability distribution of the susceptibility $\chi(T)T/N$ evaluated from independently drawn single states according to (9). Data is shown for different system sizes $N = 12, \ldots, 20$ at infinite temperature $\beta J = 0$. The dashed lines indicate Gaussian fits to the data. The inset shows the standard deviation $\delta(\chi)$ versus N, which scales as $\delta(\chi) \propto 1/\sqrt{d}$ with Hilbert-space dimension $d = 2^N$. (b) Same data as in (a) but now for the finite temperature $\beta J = 1$.

that since p_χ is found to be a Gaussian, the width $\delta(\chi)$ is sufficient to describe the whole distribution (apart from the average).

To proceed, Fig. 1 (b) again shows the probability distribution p_χ, but now for the finite temperature $\beta J = 1$. There are two important observations compared to the previous case of $\beta J = 0$. First, for small $N = 12$, one clearly finds that p_χ now takes on an asymmetric shape and the tails are not described by a Gaussian anymore. Importantly, however, upon increasing the system size N, p_χ becomes narrower and eventually turns into a Gaussian again. One may speculate about possible reasons for the observed asymmetry: It might reflect an asymmetry of the distribution, which is already present at $\beta = 0$ and small N, and then increases with increasing β; or it might also stem from the boundedness (positivity) of the observables, although the bounds are still far away for the presented case of $\beta J = 1$ in Fig. 1 (b). While this asymmetry remains to be explored in more detail in future work, it is expected that the Gaussian shape breaks down in small dimensions of the effective Hilbert space dimensions [33]. It is worth pointing out that, even for very large dimensions, the very outer tails of the distribution are expected to be of non-Gaussian nature [33]. Yet, these tails are hard to resolve in our numerical simulations, since a huge number of samples would be needed.
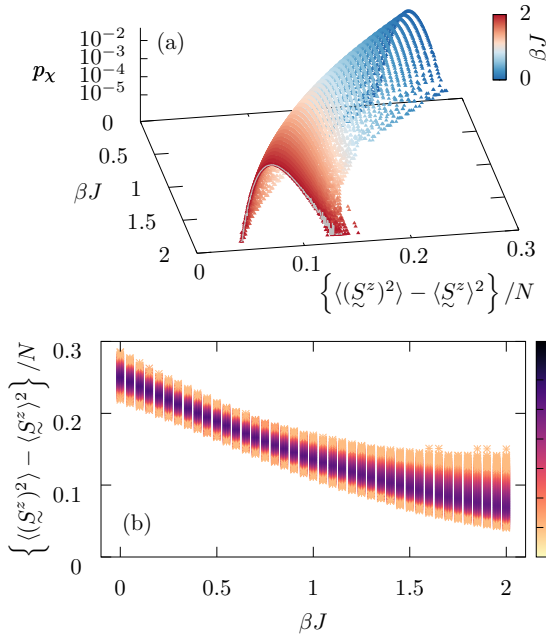
Figure 2. (a) Probability distribution of the susceptibility $\chi(T)T/N$ for various temperatures $0 \leq \beta J \leq 2$ at the fixed system size $N = 12$ obtained by ED (symbols). For comparison, data obtained by Runge-Kutta at $\beta J = 2$ is shown as well (curve). (b) Same data as in (a), but now as a contour plot.

Figure 3. Analogous data as in Fig. 1, but now for the heat capacity $C(T)T^2/N$.

As a second difference compared to $\beta J = 0$, we find that although p_χ becomes narrower for larger N also at $\beta J = 1$, this scaling is now considerably slower as a function of dimension d (see inset of Fig. 1 (b)). This is caused by the smaller effective Hilbert-space dimension $Z_{\mathrm{eff}} < d$ at $\beta J > 0$. As a consequence, for a fixed value of N, the single-state estimate in (1) becomes less reliable at $\beta J = 1$ compared to $\beta J = 0$. However, let us stress that accurate calculations are still possible at $T > 0$ as long as N is sufficiently large. (Recall, that $N \leq 20$ was chosen to be able to generate a large set of random vectors.)

In order to analyze the development of the probability distribution with respect to temperature in more detail, Fig. 2 (a) shows p_χ for various values of βJ in the range $0 \leq \beta J \leq 2$, for a fixed small system size $N = 12$. Note that the qualitative behavior in principle is independent of N, but better to visualize for small N with a broader p_χ. Starting from the high-temperature limit $\lim_{T \to \infty} \chi(T)T/N = 1/4$, we find that the maximum of p_χ gradually shifts towards smaller values upon decreasing T.

This shift of the maximum is clearly visualized also in Fig. 2 (b), which shows the same data, but in a different style. Moreover, Fig. 2 (b) additionally highlights the fact that the probability distribution p_χ for a fixed (and small) value of N becomes broader (and asymmetric) for intermediate values of T. Note, that p_χ might become narrower again for smaller values of T, see also discussion
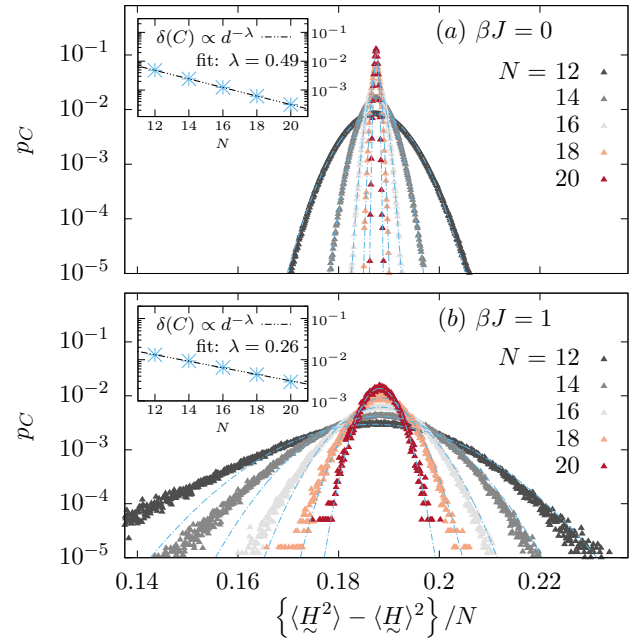
in Secs. III B - III C.

Eventually, in Fig. 3 and Fig. 4, we present analogous results for the full probability distribution p, but now for the heat capacity $C(T)T^2/N$. Overall, our findings for p_C are very similar compared to the previous discussion
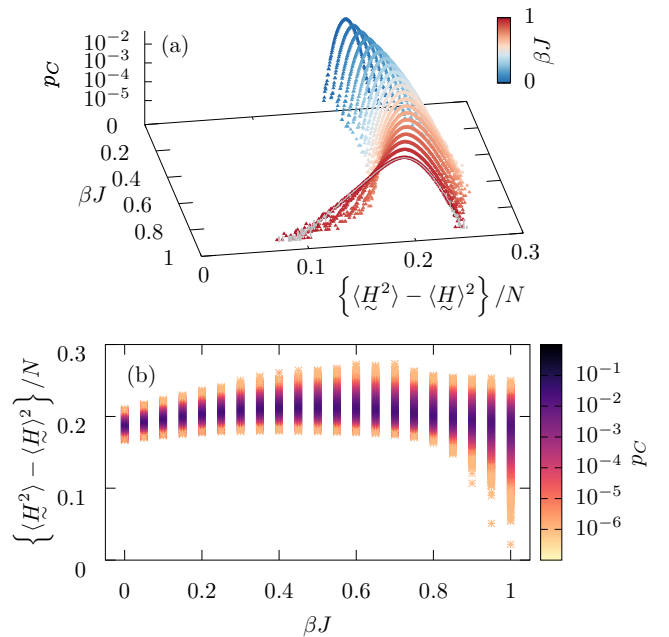

Figure 4. Analogous data as in Fig. 2, but now for the heat capacity $C(T)T^2/N$.

of p_χ. Namely, we find that at $\beta J = 0$, p_C is very well described by Gaussians over several orders of magnitude. Moreover, the standard deviation $\delta(C)$ again scales as $\propto 1/\sqrt{d}$ at $\beta = 0$. As shown in Fig. 3 (b) and also in Fig. 4, the emerging asymmetry of the probability distribution at small N and finite T is found to be even more pronounced for the heat capacity compared to the previous results for $\chi(T)$. Interestingly, we find that the maximum of p_C, on the contrary, displays only a minor dependence on temperature (at least for the values of βJ shown in Fig. 4 - naturally, it is expected to change at lower temperatures and will to go to zero at temperature $T = 0$).

B.   Larger antiferromagnetic spin-$1/2$ chains

Using a Krylov-space expansion one can nowadays reach large system sizes of $N \in [40, 50]$ for spins $s = 1/2$, see e.g. [35]. But since we also perform a statistical analysis we restrict calculations to $N \leq 36$ spins.

Following the scaling behavior of $\{\langle (\underset{\sim}{S}^z)^2 \rangle - \langle \underset{\sim}{S}^z \rangle^2\}$ as well as $\{\langle \underset{\sim}{H}^2 \rangle - \langle \underset{\sim}{H} \rangle^2\}$, which is shown in Figs. 1 and 3, one expects a very narrow distribution of both quantities for $N = 36$ compared to e.g. $N = 20$ since the dimension is $2^{16} = 65536$ times bigger for $N = 36$ which yields a 256 times narrower distribution. Such a distribution is smaller than the linewidth in a plot.

That the distributions are narrow can be clearly seen by eye inspection in Fig. 5 where the light blue curves depict thermal expectation values according to (1). For
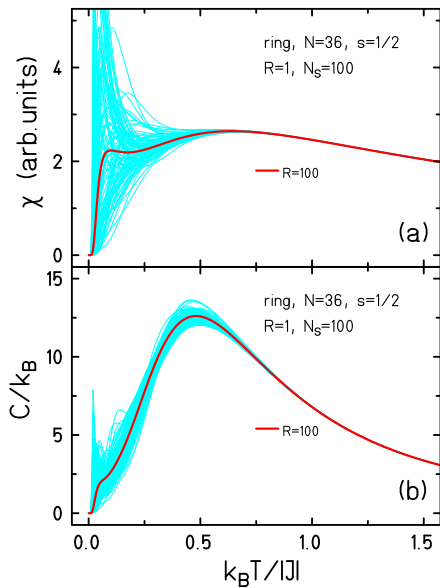

Figure 5. Spin ring $N = 36$, $s = 1/2$: The light-blue curves depict 100 different estimates of the susceptibility (a) as well as of the heat capacity (b). The FTLM estimate for $R = 100$ is also presented.
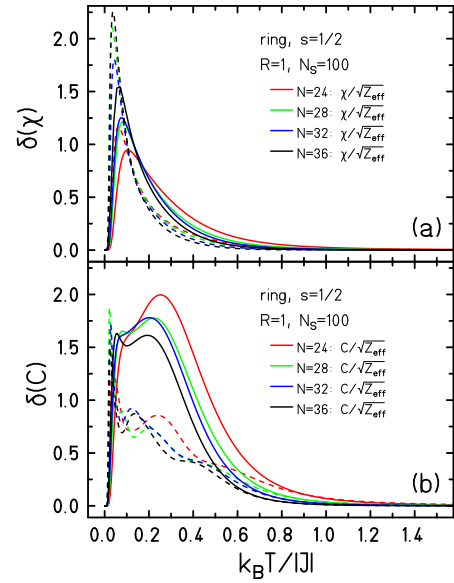

Figure 6. Spin rings, $s = 1/2$: Computed standard deviations (dashed curves) of the susceptibility (a) and the heat capacity (b) compared to the error estimate (solid curves) for various sizes N. The same color denotes the same system.

$k_B T > |J|$ they fall on top of each other and coincide with the average over $R = 100$ realizations. Below this temperature the distributions widen, which is magnified by the fact that the real physical quantities susceptibility and heat capacity contain factors of $1/T$ and $1/T^2$, respectively.

Their standard deviation is provided in Fig. 6. Coming from high temperatures, the universal behavior (8) switches to a behavior that in general depends on system (here chain) and size below a characteristic temperature, here $k_B T \approx |J|$. Nevertheless, the qualitative expectation that the standard deviation shrinks with increasing system size is met down to $k_B T \approx 0.2|J|$, below which no definite statement about the dependence on system size can be made. We conjecture that with growing N the increasing density of low-lying states as well as the vanishing excitation gap between singlet ground state and triplet first excited state influence the behavior at very low temperatures strongly.

C.   Antiferromagnetic spin-1 chains

In order to monitor an example where a vanishing excitation gap cannot be expected, not even in the thermodynamic limit, we study spin-1 chains that show a Haldane gap [36, 37], see Fig. 7. The scaling formula (8) indeed suggests that for $k_B T \lesssim (0.4 \ldots 0.5)|J|$ the standard deviations of the larger system with $N = 24$ should exceed those of the smaller system with $N = 20$, compare crossing curves of the estimator in Fig. 8. However, the actual simulations show that this is not the case.
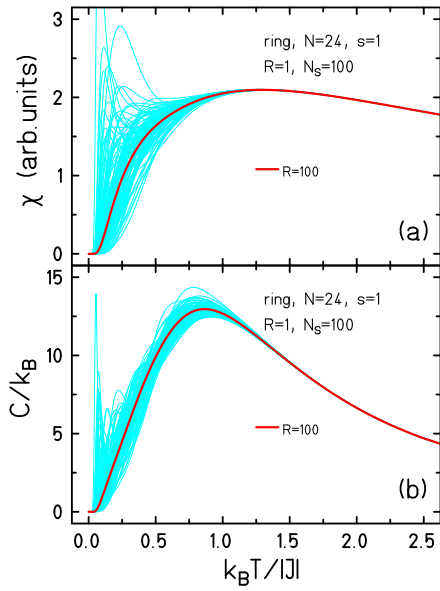
Figure 7. Spin ring $N = 24$, $s = 1$: The light-blue curves depict 100 different estimates of the susceptibility (a) as well as the heat capacity (b). The FTLM estimate for $R = 100$ is also presented.

The low-temperature fluctuations in the gap region are smaller for the larger system, at least for the two investigated system sizes.
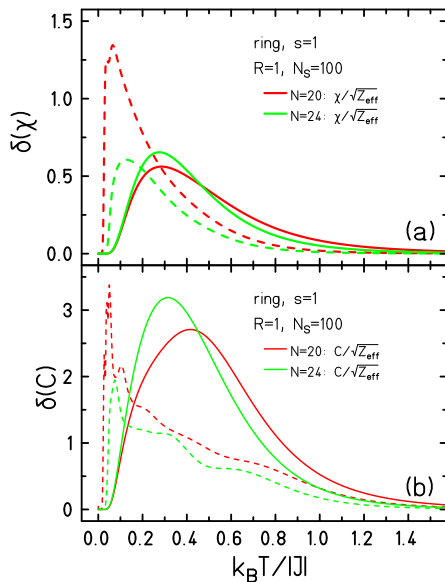

Figure 8. Spin rings, $s = 1$: Computed standard deviations (dashed curves) of the susceptibility (a) and the heat capacity (b) compared to the error estimate (solid curves) for various sizes N. The same color denotes the same system.
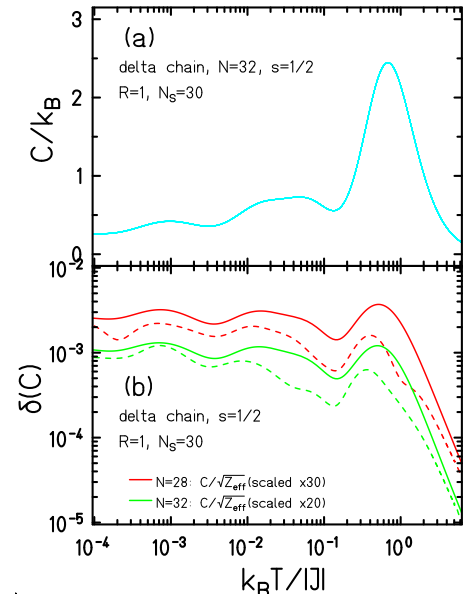

Figure 9. Delta chain $s = 1/2$, $|J_2/J_1| = 0.5$: heat capacity for $N = 32$ (a) and standard deviation for $N = 28$ and $N = 32$ (b). The light-blue curves depict $N_S = 30$ different estimates of the heat capacity (there are indeed 30 curves in this plot, which are indistinguishable by eye). Computed standard deviations (dashed curves) are compared to the error estimate (solid curves). The same color denotes the same system.

D.   Critical Spin-$1/2$ delta chains

As the final one-dimensional example we investigate a delta chain (also called sawtooth chain) in the quantum critical region, i.e., thermally excited above the quantum critical point (QCP) [38–40]. The QCP is met when the ferromagnetic nearest-neighbor interaction J_1 and the antiferromagnetic next-nearest neighbor interaction J_2 between spins on adjacent odd sites assume a ratio of $|J_2/J_1| = 1/2$. At the QCP the system features a massive ground-state degeneracy due to multi-magnon flat bands as well as a double-peak density of states [21, 38, 39]. Moreover, the typical finite-size gap is virtually not present at the QCP [38].

Since the QCP does not depend on the size of the system and the structure of the analytically known multi-magnon flat band energy eigenstates does not either, we do not expect to find large finite-size effects when investigating the standard deviation of observables, e.g. of the heat capacity. It turns even out that by eye inspection no fluctuations are visible in Fig. 9 (a). The figure shows $N_S = 30$ thermal expectation values (3) that virtually fall on top of each other. This means that a single random vector provides the equilibrium thermodynamic functions for virtually all temperatures. When evaluating the standard deviation, dashed curves in Fig. 9 (b), it turns out that it is unusually small, even for very low temperatures. The estimator (8) to which we compare had to be scaled in this case which might have two rea-
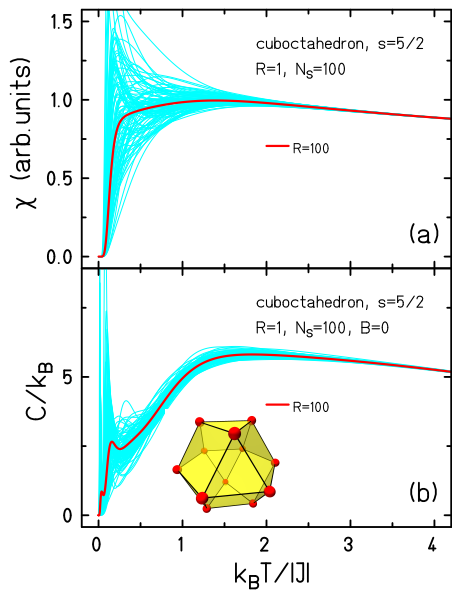
Figure 10. Cuboctahedron $N = 12$, $s = 5/2$: The light-blue curves depict 100 different estimates of the susceptibility (a) as well as the heat capacity (b). The FTLM estimate for $R = 100$ is also presented. The structure of the cuboctahedron is displayed in (b).
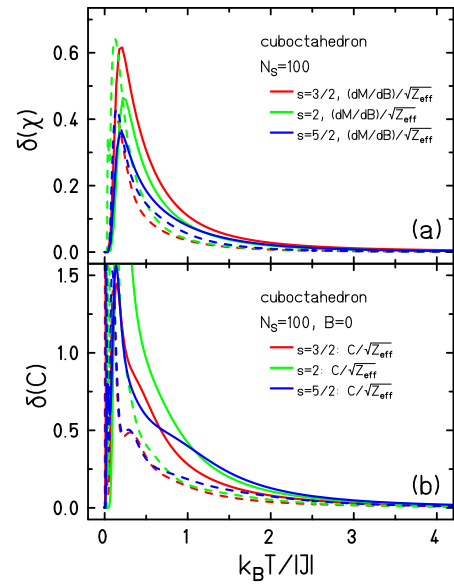

Figure 11. Cuboctahedron $N = 12$: Computed standard deviations (dashed curves) of the susceptibility (a) and the heat capacity (b) compared to the error estimate (solid curves) for various spin quantum numbers s. The same color denotes the same system.

sons. One reason could be that the large ground state degeneracy cannot be fully captured by the Krylov space expansion and thus the evaluation of the estimator (8) by means of (4) is inaccurate. The other reason could be that the empirical finding of $\alpha \approx 1$ is not appropriate in this special case of a quantum critical system. However, the general rule that trace estimators are more accurate in larger Hilbert spaces is also observed here. The standard deviation of the smaller delta chain with $N = 28$ is a few times larger than for $N = 32$.

The result is an impressive example for what it means that a quantum critical system does not possess any intrinsic scale in the quantum critical region [41, 42]. The only available scale is temperature. This means in particular that the low-energy spectrum is dense and therefore does not lead to any visible fluctuations of the estimated observables.

E. Antiferromagnetic cuboctahedra with spins 3/2, 2, and 5/2

Our last scaling analysis differs from the previous examples. The cuboctahedron is a finite-size body, that is equivalent to a kagome lattice with $N = 12$ [43–45]. The structure is shown in Fig. 10(b). Here, we vary the spin quantum number, not the size of the system. The dimension of the respective Hilbert spaces grows considerably which leads to the expected scaling (8) above temperatures of $k_B T \approx 1.5|J|$. But the low-temperature behavior, in particular of the heat capacity for temperatures

below the crossing of the estimators, eludes the expected order of more accurate results, i.e. smaller fluctuations for larger Hilbert-space dimension.

While the low-temperature behavior and the standard deviation of the susceptibility are largely governed by the energy gap between singlet ground state and triplet excited state, and this does not vary massively with the spin quantum number, the heat capacity is subject to stronger changes. When going from smaller to larger spin quantum numbers the strongly frustrated spin system looses some of its characteristic quantum properties while becoming more classical with increasing spin s. In particular, the low-lying singlet states below the first triplet state which dominate the low-temperature heat capacity move out of the gap for larger spin s [46, 47].

It may thus well be that the type of Hilbert space enlargement, due to growing system size which leads to the thermodynamic limit or growing spin quantum number which leads to the classical limit, is important for the behavior of the estimators (1) and (2) at low temperatures.

IV. DISCUSSION AND CONCLUSIONS

To summarize, we have studied the finite-size scaling of typicality-based trace estimators. In these approaches, the trace over the high-dimensional Hilbert space is approximated by either (i) a single random state $|r\rangle$ or (ii) the average over a set ($R \ll d$) of random vectors. In particular, we have focused on the evaluation of thermodynamic observables such as the heat capacity and the

magnetic susceptibility for various spin models of Heisenberg type. Here, the temperature dependence of these quantities has been generated by means of a Krylov-space expansion where the random states $|r\rangle$ are used as a starting vector for the expansion.

As a first step, we have studied the full probability distribution of expectation values evaluated with respect to single random states. As an important result, we have demonstrated that for sufficiently high temperatures and large enough system sizes (i.e. sufficiently large effective Hilbert-space dimension Z_{eff}), the probability distributions are very well described by Gaussians [33]. In particular, for comparatively high temperatures, our numerical analysis has confirmed that the standard deviation of the probability distribution scales as $\delta(O) \propto 1/\sqrt{Z_{\text{eff}}}$, and that this width already describes the full distribution.

In contrast, for lower temperatures, we have shown that (i) the probability distributions can become non-Gaussian and (ii) the scaling of $\delta(O)$ can become more complicated and generally depends on the specific model and observable under consideration. While a larger Hilbert-space dimension often leads to an improved accuracy of the random-state approach at low temperatures as well, compare the investigation on kagome lattice antiferromagnets of sizes $N = 30$ and $N = 42$ in [35], we have also provided examples where this expectation can break down for too small Z_{eff}, compare also [48].

A remarkable example is provided by the spin-1/2 sawtooth chain with coupling-ratio $|J_2/J_1| = 1/2$. Due to the (virtually) gapless dense low-energy spectrum at the quantum critical point, we have found that statistical fluctuations remain negligible throughout the entire temperature range with only minor dependence on system size (see also Ref. [49] for a similar finding in a spin-liquid model).

In conclusion, we have demonstrated that typicality-based estimators provide a convenient numerical tool in order to accurately approximate thermodynamic observables for a wide range of temperatures and models. While in some cases, even a single pure state is sufficient, the accuracy of the results can always be improved by averaging over a set of independently drawn states.

[1] J. Jaklič and P. Prelovšek, Phys. Rev. B **49**, 5065 (1994).
[2] J. Jaklič and P. Prelovšek, Adv. Phys. **49**, 1 (2000).
[3] I. Zerec, B. Schmidt, and P. Thalmeier, Phys. Rev. B **73**, 245108 (2006).
[4] J. Schnack and O. Wendland, Eur. Phys. J. B **78**, 535 (2010).
[5] O. Hanebaum and J. Schnack, Eur. Phys. J. B **87**, 194 (2014).
[6] P. Prelovšek, "The Finite Temperature Lanczos Method and its Applications," in *The Physics of Correlated Insulators, Metals, and Superconductors*, Modeling and Simulation, Vol. 7, edited by E. Pavarini, E. Koch, R. Scalettar, and R. Martin (Forschungszentrum Jülich, 2017) Chap. 7.
[7] B. Schmidt and P. Thalmeier, Phys. Rep. **703**, 1 (2017).
[8] J. Skilling, in *Maximum Entropy and Bayesian Methods* (Springer Netherlands, Dordrecht, 1989) pp. 455–466.
[9] M. Hutchinson, Commun. Stat. Simul. Comput. **18**, 1059 (1989).
[10] D. A. Drabold and O. F. Sankey, Phys. Rev. Lett. **70**, 3631 (1993).
[11] R. Silver and H. Röder, Int. J. Mod. Phys. C **05**, 735 (1994).
[12] G. H. Golub and U. von Matt, *Tikhonov regularization for large scale problems*, Technical Report SCCM-97-03 (Stanford University, 1997).
[13] A. Weiße, G. Wellein, A. Alvermann, and H. Fehske, Rev. Mod. Phys. **78**, 275 (2006).
[14] H. Avron and S. Toledo, J. ACM **58**, 1 (2011).

[15] F. Roosta-Khorasani and U. Ascher, Found. Comput. Math. **15**, 1187 (2015).
[16] A. K. Saibaba, A. Alexanderian, and I. C. F. Ipsen, Numer. Math. **137**, 353 (2017).
[17] K. Inoue, Y. Maeda, H. Nakano, and Y. Fukumoto, IEEE Trans. Magn. **55**, 1 (2019).
[18] S. Sugiura and A. Shimizu, Phys. Rev. Lett. **108**, 240401 (2012).
[19] S. Sugiura and A. Shimizu, Phys. Rev. Lett. **111**, 010401 (2013).
[20] S. Okamoto, G. Alvarez, E. Dagotto, and T. Tohyama, Phys. Rev. E **97**, 043308 (2018).
[21] J. Schnack, J. Richter, and R. Steinigeweg, Phys. Rev. Research **2**, 013186 (2020).
[22] B. Collins and P. Śniady, Commun. Math. Phys. **264**, 773 (2006).
[23] C. Bartsch and J. Gemmer, Phys. Rev. Lett. **102**, 110403 (2009).
[24] P. Reimann, Nat. Commun. **7**, 10821 (2016).
[25] H. Tal-Ezer and R. Kosloff, J. Chem. Phys. **81**, 3967 (1984).
[26] V. V. Dobrovitski and H. A. De Raedt, Phys. Rev. E **67**, 056702 (2003).
[27] R. Steinigeweg, J. Gemmer, and W. Brenig, Phys. Rev. Lett. **112**, 120601 (2014).
[28] R. Steinigeweg, J. Gemmer, and W. Brenig, Phys. Rev. B **91**, 104404 (2015).
[29] T. A. Elsayed and B. V. Fine, Phys. Rev. Lett. **110**, 070404 (2013).

[30] J. Schulenburg, *spinpack 2.56* (Magdeburg University, 2017).

[31] J. Richter and J. Schulenburg, Eur. Phys. J. B **73**, 117 (2010).

[32] A. Hams and H. De Raedt, Phys. Rev. E **62**, 4365 (2000).

[33] P. Reimann and J. Gemmer, Phys. Rev. E **99**, 012126 (2019).

[34] H.-J. Schmidt, J. Schnack, and M. Luban, Phys. Rev. B **64**, 224415 (2001).

[35] J. Schnack, J. Schulenburg, and J. Richter, Phys. Rev. B **98**, 094423 (2018).

[36] F. D. M. Haldane, Phys. Lett. A **93**, 464 (1983).

[37] F. D. M. Haldane, Phys. Rev. Lett. **50**, 1153 (1983).

[38] V. Y. Krivnov, D. V. Dmitriev, S. Nishimoto, S.-L. Drechsler, and J. Richter, Phys. Rev. B **90**, 014441 (2014).

[39] D. V. Dmitriev and V. Y. Krivnov, Phys. Rev. B **92**, 184422 (2015).

[40] A. Baniodeh, N. Magnani, Y. Lan, G. Buth, C. E. Anson, J. Richter, M. Affronte, J. Schnack, and A. K. Powell, npj Quantum Mater. **3**, 10 (2018).

[41] T. Vojta, Ann. Phys. **9**, 403 (2000).

[42] M. Vojta, Rep. Prog. Phys. **66**, 2069 (2003).

[43] I. Rousochatzakis, A. M. Läuchli, and F. Mila, Phys. Rev. B **77**, 094420 (2008).

[44] A. Honecker and M. E. Zhitomirsky, J. Phys. Conf. Ser. **145**, 012082 (2009).

[45] H.-J. Schmidt, A. Hauser, A. Lohmann, and J. Richter, Phys. Rev. E **95**, 042110 (2017).

[46] R. Schmidt, J. Richter, and J. Schnack, J. Magn. Magn. Mater. **295**, 164 (2005).

[47] J. Schnack and R. Schnalle, Polyhedron **28**, 1620 (2009).

[48] K. Morita and T. Tohyama, Phys. Rev. Research **2**, 013205 (2020).

[49] I. Rousochatzakis, S. Kourtis, J. Knolle, R. Moessner, and N. B. Perkins, Phys. Rev. B **100**, 045117 (2019).

Preprint of Publication [P4]

[P4] <u>Tjark Heitmann</u>, Jonas Richter, Thomas Dahm, and Robin Steinigeweg,
Density Dynamics in the Mass-Imbalanced Hubbard Chain,
Journal reference: Phys. Rev. B **102**, 045137 (2020) [Open Access]
DOI: 10.1103/PhysRevB.102.045137
Preprint: `arXiv:2004.13604`

Density Dynamics in the Mass-Imbalanced Hubbard Chain

Tjark Heitmann (iD),[1, *] Jonas Richter (iD),[1] Thomas Dahm,[2] and Robin Steinigeweg (iD)[1, †]

[1]*Fachbereich Physik, Universität Osnabrück, Barbarastr. 7, D-49076 Osnabrück, Germany*
[2]*Fakultät für Physik, Universität Bielefeld, Postfach 100131, D-33501 Bielefeld, Germany*

We consider two mutually interacting fermionic particle species on a one-dimensional lattice and study how the mass ratio η between the two species affects the (equilibration) dynamics of the particles. Focussing on the regime of strong interactions and high temperatures, two well-studied points of reference are given by (i) the case of equal masses $\eta = 1$, i.e., the standard Fermi-Hubbard chain, where initial non-equilibrium density distributions are known to decay, and (ii) the case of one particle species being infinitely heavy, $\eta = 0$, leading to a localization of the lighter particles in an effective disorder potential. Given these two opposing cases, the dynamics in the case of intermediate mass ratios $0 < \eta < 1$ is of particular interest. To this end, we study the real-time dynamics of pure states featuring a sharp initial non-equilibrium density profile. Relying on the concept of dynamical quantum typicality, the resulting non-equilibrium dynamics can be related to equilibrium correlation functions. Summarizing our main results, we observe that diffusive transport occurs for moderate values of the mass imbalance, and manifests itself in a Gaussian spreading of real-space density profiles and an exponential decay of density modes in momentum space. For stronger imbalances, we provide evidence that transport becomes anomalous on intermediate time scales and, in particular, our results are consistent with the absence of strict localization in the long-time limit for any $\eta > 0$. Based on our numerical analysis, we provide an estimate for the "lifetime" of the effective localization as a function of η.

I. INTRODUCTION

Understanding the dynamics of quantum many-body systems is a central objective of modern physics which has been reignited by experimental advancements featuring, e.g., cold atoms or trapped ions [1, 2], and has experienced an upsurge of interest also from the theoretical side [3–7]. In this context, an intriguing and fundamental direction of research is to explain if and how thermodynamic behavior can emerge from the unitary time evolution of isolated quantum systems. One notable explanation for this occurrence of thermalization is the eigenstate thermalization hypothesis (ETH) [8–10], which has been numerically verified in numerous instances [5].

However, despite thermalization certainly being a rather common observation, there are also classes of systems which generically evade to reach thermal equilibrium even at indefinitely long times. In particular, it has been realized early on by Anderson that non-interacting particles in one or two spatial dimensions localize for an arbitrarily weak disorder potential [11, 12] (for experimental confirmations see, e.g., [13, 14]). Moreover, it is now widely believed that for sufficiently strong disorder, localization is also possible in the presence of interactions [15, 16], which is supported by experimental results as well [17].

While the majority of studies on many-body localization (MBL) typically focus on one-dimensional and short-ranged models composed of, e.g., spin-1/2 degrees of freedom, there has been much effort recently to generalize the notion of MBL to a wider class of models [18]. This includes, e.g., systems which are weakly coupled to a thermal bath [19], models with long-range interactions [20] or degrees of freedom with higher spin $S > 1/2$ [21, 22], as well as Hubbard models where the disorder only couples to either one of the charge or spin degrees of freedom [23, 24].

A particularly interesting question is whether MBL can also occur in systems which are translational invariant, i.e., without any explicit disorder [25–39]. A convenient model to investigate this question is given by the mass-imbalanced Hubbard chain [29–31, 39–41]. In this model, two mutually interacting particle species are defined on a one-dimensional lattice and exhibit different hopping amplitudes. Here, the imbalance is parametrized by the ratio η between the two hopping strengths, ranging from $\eta = 0$, where the heavy particles are entirely static, to $\eta = 1$, where the hopping amplitudes are the same. On the one hand, in the balanced limit $\eta = 1$, numerical evidence for diffusive [42–44] (or superdiffusive [42, 45]) charge transport has been found in the regime of high temperatures and strong interactions. On the other hand, for $\eta = 0$, the static particle species creates an effective disorder potential which induces localization of the lighter particles [41, 46–49]. In view of these two opposing cases, it is intriguing to study the dynamics in the regime of intermediate imbalances $0 < \eta < 1$. While genuine localization (i.e. on indefinite time scales) is most likely absent for any $\eta > 0$ [35, 39], e.g., due to slow anomalous diffusion which ultimately leads to thermalization [35], this does not exclude the possibility of interesting dynamical properties such as a "quasi-MBL phase" at short to intermediate times [35].

In this paper, we scrutinize the impact of a finite mass imbalance $0 < \eta < 1$ from a different perspective

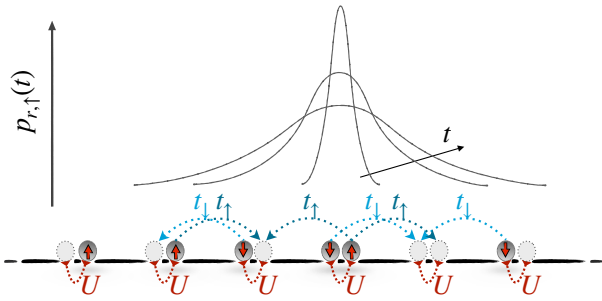* tjark.heitmann@uos.de
† rsteinig@uos.de

Figure 1. (Color online) Illustration of the imbalanced Fermi-Hubbard chain. Spin-↑ and -↓ particles with on-site interaction of strength U and different hopping amplitudes $t_\uparrow$ and $t_\downarrow$. Diffusive broadening of the initially peaked spin-↑ density profile is sketched as a possible scenario depending on the imbalance ratio $\eta = t_\downarrow/t_\uparrow$.

by studying the real-time dynamics of pure states featuring a sharp initial non-equilibrium density profile. Relying on the concept of dynamical quantum typicality, the resulting non-equilibrium dynamics can be related to equilibrium correlation functions. Summarizing our main results, we observe that diffusive transport occurs for moderate values of the mass imbalance, and that it manifests itself in a Gaussian spreading of real-space density profiles and an exponential decay of density modes in momentum space. Moreover, for stronger imbalances, we find evidence that on the time and length scales numerically accessible, transport properties become anomalous, albeit we cannot rule out that normal diffusion eventually prevails at even longer times. Furthermore, our results are consistent with the absence of genuine localization for any $\eta > 0$. In particular, we find that for smaller and smaller values of $\eta > 0$, the resulting dynamics resembles the localized $\eta = 0$ case for longer and longer time scales. However, we conjecture that this "lifetime" of effective localization always remains finite for a finite η.

This paper is structured as follows. After introducing the model in Sec. II, we give an introduction to the employed typicality approach, and the initial states and observables in Sec. III. We then present our results in Sec. IV and conclude with a discussion in Sec. V.

II.   MODEL

We study the Hubbard chain describing interacting spin-↑ and -↓ fermions on a one-dimensional lattice. The Hamiltonian for L lattice sites with periodic boundary conditions ($L + 1 \equiv 1$) reads

$$H = \sum_{r=1}^{L} h_r \tag{1}$$

with local terms

$$h_r = -\sum_{\sigma=\uparrow,\downarrow} t_\sigma \left(c_{r,\sigma}^\dagger c_{r+1,\sigma} + \text{h.c.} \right) \tag{2}$$

$$+ U \left(n_{r,\uparrow} - \frac{1}{2} \right) \left(n_{r,\downarrow} - \frac{1}{2} \right) ,$$

where the creation (annihilation) operator $c_{r,\sigma}^\dagger$ ($c_{r,\sigma}$) creates (annihilates) a fermion with spin σ at site r, and $n_{r,\sigma} = c_{r,\sigma}^\dagger c_{r,\sigma}$ is the particle-number operator. (We omit any additional operator symbols for the sake of clean notation.) The first term on the right hand side of Eq. (2) describes the site-to-site hopping of each particle species with amplitude t_σ. The second term is the on-site interaction between the particle species with strength U, see Fig. 1. The imbalance between $t_\uparrow$ and $t_\downarrow \leq t_\uparrow$ is parametrized by the ratio

$$\eta = \frac{t_\downarrow}{t_\uparrow} , \tag{3}$$

ranging from $\eta = 0$ for $t_\downarrow = 0$ to $\eta = 1$ in the case of $t_\downarrow = t_\uparrow$.

While the Hamiltonian H in Eqs. (1) and (2) is integrable in terms of the Bethe Ansatz for $\eta = 1$ (i.e. in the case of the standard Fermi-Hubbard chain, see, e.g., Ref. [50]), this integrability is broken for any finite imbalance $0 < \eta < 1$. Moreover, despite its integrability, there has been numerical evidence that, in the regime of high temperatures and strong interactions, charge transport in the one-dimensional Fermi-Hubbard model is diffusive [42–44] (or superdiffusive [42, 45]). In order to have this well-controlled point of reference for our analysis of finite imbalances $\eta \leq 1$, we here fix the interaction strength to the large value $U/t_\uparrow = 16$.

In addition to $\eta = 1$, another important point in parameter space is the so-called Falicov-Kimball limit $\eta = 0$ [51, 52]. In this limit, the spin-↓ particles become completely immobile ($t_\downarrow = 0$), implying that the local occupation numbers $n_{r,\downarrow}$ become strictly conserved quantities, i.e.,

$$[H, n_{r,\downarrow}] = [n_{r,\downarrow}, n_{r,\uparrow}] = 0 . \tag{4}$$

Using this symmetry, the Hamiltonian (1) can be decoupled into 2^L independent subspaces, effectively describing non-interacting spin-↑ particles on a one-dimensional lattice with random (binary) on-site potentials $\pm (U/2) (n_{r,\uparrow} - 1/2)$, which implies the onset of Anderson localization [11].

It is worth mentioning that by means of a Jordan-Wigner transformation, the fermionic model in Eqs. (1) and (2) can be mapped to a spin-1/2 model with ladder geometry [35]. This spin model is described by the local

terms

$$h_r = - \sum_{k=1,2} 2J_k \left(s^x_{r,k} s^x_{r+1,k} + s^y_{r,k} s^y_{r+1,k} \right) \qquad (5)$$
$$+ J_\perp \, s^z_{r,1} s^z_{r,2}$$

with $J_1 = t_\uparrow$, $J_2 = t_\downarrow$ and $J_\perp = U$. Here, the different particle species $\uparrow$ and $\downarrow$ are represented as local magnetizations on the two separate legs $k = 1, 2$ of the ladder. The hopping term and the interaction term in the Hubbard formulation correspond to the XY interaction along the legs and the Ising interaction on the rungs of the ladder, respectively. The particle number conservation $N_\sigma = \sum_r n_{r,\sigma} =$ const. for both particle types translates into magnetization conservation $M_k = \sum_r s^z_{r,k} =$ const. on each leg.

III.   SETUP AND NUMERICAL METHOD

A.   Initial states and observables

We investigate the real-time dynamics of local particle densities given by the expectation values

$$p_{r,\sigma}(t) = \text{Tr}\left[n_{r,\sigma} \rho(t) \right] \qquad (6)$$

with the density matrix

$$\rho(t) = \mathrm{e}^{-iHt} |\psi(0)\rangle \langle\psi(0)| \, \mathrm{e}^{iHt} \qquad (7)$$

for pure initial states $|\psi(0)\rangle$, such that

$$\text{Tr}\left[n_{r,\sigma} \rho(t) \right] = \langle\psi(t)| \, n_{r,\sigma} \, |\psi(t)\rangle \ . \qquad (8)$$

In order to realize inhomogeneous particle densities, we prepare the initial states via the projection

$$|\psi(0)\rangle \propto n_{L/2,\uparrow} |\phi\rangle \ . \qquad (9)$$

The reference pure state $|\phi\rangle$ is constructed as a random superposition,

$$|\phi\rangle = \sum_{k=1}^{d} c_k |\varphi_k\rangle \ , \qquad (10)$$

where the $|\varphi_k\rangle$ denote the common eigenbasis of the local occupation number operators $n_{r,\sigma}$, and the sum runs over the full Hilbert space with finite dimension $d = 4^L$. (In spin language, this simply is the Ising basis.) Moreover, the complex coefficients c_k are randomly drawn from a distribution which is invariant under all unitary transformations in the Hilbert space (Haar measure) [53, 54], i.e., real and imaginary parts of these coefficients are normally distributed with zero mean. As a consequence, the initial density profile exhibits a sharp delta peak for the spin-$\uparrow$ particles in the middle of the chain on top of a

homogeneous many-particle background [44, 55],

$$p_{r,\sigma}(0) \begin{cases} = 1 & r = L/2 \text{ and } \sigma = \uparrow \\ \approx 1/2 = p_{\text{eq.}} & \text{else} \end{cases} . \qquad (11)$$

Rather than taking the full Hilbert space into account, one could also consider the half-filling sector (respectively the zero-magnetization sector).

B.   Dynamical quantum typicality

Given the specific construction of the pure state $|\phi\rangle$ in Eq. (10), the concept of dynamical quantum typicality (DQT) provides a direct connection between the non-equilibrium expectation value $p_{r,\uparrow}(t)$ and an equilibrium correlation function (see Ref. [44] and also Appendix A),

$$p_{r,\uparrow}(t) - p_{\text{eq.}} = 2 \left\langle (n_{L/2,\uparrow} - p_{\text{eq.}})(n_{r,\uparrow}(t) - p_{\text{eq.}}) \right\rangle + \epsilon \ , \qquad (12)$$

where the thermodynamic average $\langle \bullet \rangle = \text{Tr}\left[\bullet \right]/d$ is carried out at formally infinite temperature. As a consequence, the dynamics of the non-equilibrium expectation value $p_{r,\uparrow}(t)$ can be used to study transport properties within the framework of linear response theory.

Importantly, the variance of the statistical error $\epsilon = \epsilon(|\phi\rangle)$ of Eq. (12) is bounded from above by

$$\text{Var}(\epsilon) < \mathcal{O}\left(\frac{1}{d} \right) = \mathcal{O}\left(4^{-L} \right) \ , \qquad (13)$$

i.e., the accuracy of the typicality approximation improves exponentially upon increasing the size of the system. In principle, this error can be further reduced by averaging over multiple realizations of the random state $|\phi\rangle$ [56, 57]. However, for the system sizes studied here, the DQT approach is already very accurate, and this additional sampling becomes unnecessary [58]. More details on the concept of dynamical quantum typicality (and on error bounds) can be found in Refs. [58–73].

C.   Time evolution via pure-state propagation

For the time evolution of the pure state

$$|\psi(t)\rangle = \mathrm{e}^{-iHt} |\psi(0)\rangle \qquad (14)$$

we can bypass the exact diagonalization of the Hamiltonian and rather solve the time-dependent Schrödinger equation directly via iterative forward propagation in small time steps δt. Aside from the many numerical methods such as Trotter decompositions [74, 75], Chebyshev polynomials [76–78] or Krylov-space methods [79], the action of the time-evolution operator in each step can be calculated by a fourth-order Runge-Kutta scheme

[68, 69],

$$|\psi(t + \delta t)\rangle = e^{-iH\delta t} |\psi(t)\rangle \qquad (15)$$

$$\approx \sum_{k=0}^{4} \frac{(-iH\delta t)^k}{k!} |\psi(t)\rangle \ .$$

Crucially, the matrix-vector multiplications in Eq. (15) can be implemented very memory efficiently due to the sparse matrix representation of the given Hamiltonian. While the action of H on $|\psi\rangle$ can also be calculated on-the-fly, we save the sparse Hamiltonian matrix for the sake of run time. Moreover, symmetries of the system can be exploited in order to split the problem into smaller sub-problems and to further reduce the computational effort [80]. In this paper, we exploit the particle number (magnetization) conservation for both particle species (legs) separately. As a consequence, the maximum memory consumption for the largest symmetry sector in a system of length $L = 15$, with full Hilbert-space dimension $d \sim 10^9$, amounts to about 20 GB (using double-precision complex numbers). While $L = 14$ or $L = 15$ are already comparatively large (especially in view of the extensive parameter screening and the long simulation times considered here), let us note that even larger system sizes can be treated by the usage of large-scale supercomputing (see, e.g., Refs. [41, 44]). The time step used in all calculations, if not stated otherwise, is $\delta t\, t_\uparrow = 0.005$.

D. Diffusion on a lattice

1. Real space

The dynamics of the densities $p_{r,\uparrow}(t)$ is diffusive, if it fulfills the lattice diffusion equation [81]

$$\frac{d}{dt}p_{r,\uparrow}(t) = D[p_{r-1,\uparrow}(t) - 2p_{r,\uparrow}(t) + p_{r+1,\uparrow}(t)] \qquad (16)$$

with the diffusion constant D. For the δ-peak initial conditions (11), the solution of Eq. (16) can be well approximated by the Gaussian function

$$p_{r,\uparrow}(t) - p_{\text{eq.}} = \frac{1}{2\sqrt{2\pi}\Sigma(t)} \exp\left[-\frac{(r - L/2)^2}{2\Sigma^2(t)}\right] \ , \qquad (17)$$

where the spatial variance scales as $\Sigma^2(t) = 2Dt$ and is given by

$$\Sigma^2(t) = \sum_{r=1}^{L} r^2 \delta p_{r,\uparrow}(t) - \left[\sum_{r=1}^{L} r \delta p_{r,\uparrow}(t)\right]^2 , \qquad (18)$$

with $\delta p_{r,\uparrow}(t) \propto p_{r,\uparrow}(t) - p_{\text{eq.}}$ fulfilling $\sum_r \delta p_{r,\uparrow}(t) = 1$ for all times t. More generally, a scaling of the variance according to $\Sigma(t) \propto t^\alpha$ is called ballistic for $\alpha = 1$, superdiffusive for $1/2 < \alpha < 1$, diffusive for $\alpha = 1/2$, subdiffusive for $0 < \alpha < 1/2$, and localized for $\alpha = 0$. Moreover, away

from the case $\alpha = 1/2$, the density profiles $p_{r,\uparrow}(t)$ are not expected to take on a Gaussian shape.

2. Connection to current-current correlation functions

Due to the typicality relation (12), the spatial variance in Eq. (18) can be related to the dynamics of current-current correlation functions via [82]

$$\frac{d}{dt}\Sigma^2(t) = 2D(t) \ , \qquad (19)$$

where the time-dependent diffusion coefficient $D(t)$ is given by

$$D(t) = \frac{4}{L} \int_0^t \langle j_\uparrow(t')j_\uparrow\rangle \, dt' \ , \qquad (20)$$

and $j_\uparrow$ denotes the total current operator of the spin-$\uparrow$ particles,

$$j_\uparrow = -t_\uparrow \sum_r \left(ic_{r,\uparrow}^\dagger c_{r+1,\uparrow} + \text{h.c.} \right) \ . \qquad (21)$$

(Note that the relation (19) requires $\delta p_{r,\uparrow}(t)$ to vanish at the boundaries of the chain [82].) We therefore can compare the spatial variance of density profiles calculated according to Eq. (18) to the one already obtained from current-current correlation functions [43, 82, 83],

$$\Sigma^2(t) = 2 \int_0^t D(t')dt' \ . \qquad (22)$$

A detailed analysis of transport in the mass-imbalanced Hubbard chain extracted from current-current correlation functions can be found in [41].

3. Momentum space

In addition to the real-space perspective, it is also instructive to look at momentum-space observables as given by the lattice Fourier transform of the density profiles,

$$p_{q,\uparrow}(t) = \frac{1}{\sqrt{L}} \sum_{r=1}^{L} e^{iqr} p_{r,\uparrow}(t) \qquad (23)$$

with the momentum $q = 2\pi k/L$ and wave numbers $k = 0, 1, \dots, L - 1$. In particular, the Fourier transformation of the diffusion equation (16) yields the corresponding diffusion equation for the $p_{q,\uparrow}(t)$,

$$\frac{d}{dt}p_{q,\uparrow}(t) = -\tilde{q}^2 D\, p_{q,\uparrow}(t) \ , \qquad (24)$$
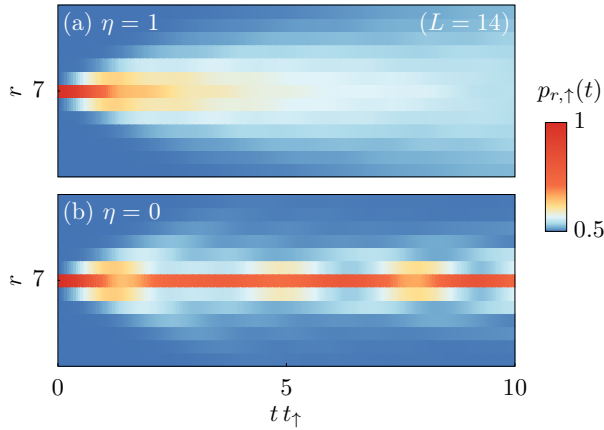
Figure 2. (Color online) Real-time broadening of the non-equilibrium density profile for limiting imbalance ratios (a) $\eta = 1$ and (b) $\eta = 0$. System size $L = 14$ and interaction strength $U/t_\uparrow = 16$. The initial density peak in the center of the chain spreads rather quickly over the system for $\eta = 1$, whereas it appears to be frozen for $\eta = 0$.
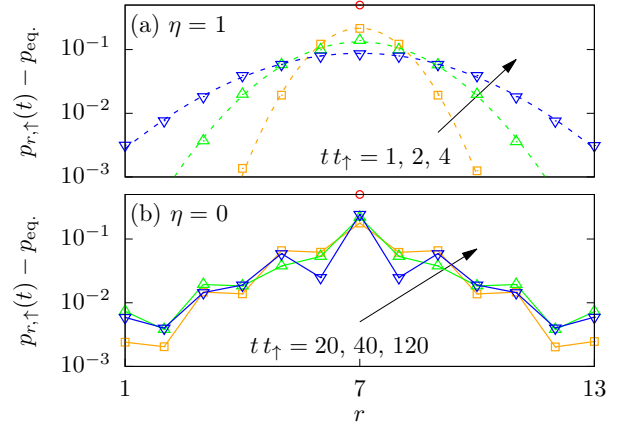

Figure 3. (Color online) Density profiles $p_{r,\uparrow}(t)$ at fixed times for (a) $\eta = 1$ and (b) $\eta = 0$. In the case $\eta = 1$, the profiles can be very well described via Gaussians (parabola in the semi-logarithmic plot) indicating clean diffusion for the time scales depicted. Note that the Gaussians (dashed lines) are no fit, but calculated from Eqs. (17) and (18). In the case $\eta = 0$, an overall triangular shape survives even for long times, with some local fluctuations.

with $\widetilde{q}^2 = 2(1 - \cos q)$. From Eq. (24), it becomes clear that diffusion manifests itself in momentum space by exponentially decaying modes

$$p_{q,\uparrow}(t) \propto \mathrm{e}^{-\widetilde{q}^2 D t} \; . \tag{25}$$

IV.   RESULTS

We now turn to our numerical results. To begin with, the two limiting cases $\eta = 1$ and $\eta = 0$ are presented in Sec. IV A. Intermediate imbalances $0 < \eta < 1$ are discussed in Secs. IV B and IV C.

A.   Limiting cases

In order to mark out the two completely different behaviors of the density dynamics in the limiting cases of the model, we first discuss the limit of equal particle masses ($\eta = 1$) and contrast it with the limit of infinite mass-imbalance ($\eta = 0$). Recall that the interaction strength is set to $U/t_\uparrow = 16$ in the following.

First, Fig. 2 shows the real-time broadening of the initially peaked density profiles $p_{r,\uparrow}(t)$ for both limits in a time-space density plot. While the particle density for $\eta = 1$ [Fig. 2 (a)] is found to spread over all sites of the chain, $p_{r,\uparrow}(t)$ for $\eta = 0$ [Fig. 2 (b)] appears to be essentially frozen at the central lattice sites, as it is expected in the Anderson insulating limit.

For a more detailed analysis, the spatial dependence of the profiles $p_{r,\uparrow}(t) - p_{\text{eq.}}$ is shown in Fig. 3 for fixed times t in a semi-logarithmic plot. Remarkably, the profiles for $\eta = 1$ in Fig. 3 (a) can be very well described by Gaussians [see Eq. (17)] over three orders of magnitude.

These Gaussian profiles indicate that charge transport in the integrable Fermi-Hubbard chain is diffusive [42–44], at least in this parameter regime (strong interactions and high temperatures) and for the time scales depicted, see also Refs. [42, 45] for the possibility of superdiffusive transport. Note that the Gaussians in Fig. 3 (a) are no fit, since the width $\Sigma(t)$ has been calculated exactly according to Eq. (18), i.e., there is no free parameter involved. In contrast, the profiles for $\eta = 0$ in Fig. 3 (b) are clearly non-Gaussian and remain, even for the long times shown, in an overall triangular shape with variations on short length scales.

B.   Small imbalances

1.   Real space

Next, let us study a finite imbalance between the particle masses. In analogy to Fig. 2, time-space density plots are shown in Fig. 4 for $\eta = 0.8$ and $\eta = 0.6$. For these ratios the broadening of the initial density peak apparently happens on a time scale comparable to the one observed for $\eta = 1$ in Fig. 2, with a barely noticeable slowdown with the increasing imbalance. Similar observations can be made for the density profiles at fixed times, as shown in Fig. 5. At weak imbalance $\eta = 0.8$ [Fig. 5 (a)], the profiles are still in very good agreement with Gaussians [see Eq. (17)] which suggests that diffusion occurs also for $\eta \neq 1$. Even for stronger imbalance $\eta = 0.6$ [Fig. 5 (b)], the profiles appear to be of Gaussian shape, although small deviations start to appear at $t\,t_\uparrow = 4$, which might be seen as the onset of a drift from normal to anomalous diffusion, see also the discussion below.
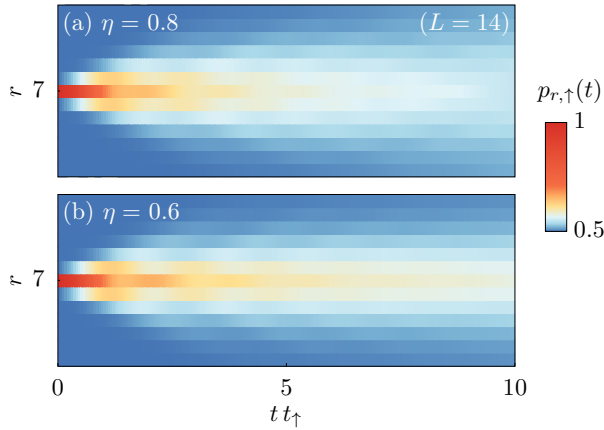
Figure 4. (Color online) Real-time broadening of the initially peaked density profile for weak imbalances (a) $\eta = 0.8$ and (b) $\eta = 0.6$.

2. Spatial width

In order to analyze the broadening of the density profiles further, Fig. 6 shows the time-dependence of the spatial width $\Sigma(t)$ obtained by Eq. (18) for moderate imbalance $\eta = 0.8$ and different system sizes $L = 10, \ldots, 14$. Necessarily, there is an initial linear increase $\Sigma(t) \propto t$ for $t\,t_{\uparrow} \lesssim 1$, indicating ballistic transport, as it is expected for short times below the mean-free time. Subsequently, $\Sigma(t)$ shows a scaling $\propto \sqrt{t}$, consistent with diffusion. However, for later times, we find that $\Sigma(t)$ approaches a saturation value which increases with increasing L. This behavior of $\Sigma(t)$ can be easily understood since the width

Figure 5. (Color online) Density profiles $p_{r,\uparrow}(t)$ at fixed times for the same system parameters and imbalance ratios as shown in Fig. 4. The dashed lines are Gaussian functions calculated from Eqs. (17) and (18). At moderate imbalance (a) $\eta = 0.8$, the profiles can be very well described by Gaussians. At slightly smaller (b) $\eta = 0.6$, the density profiles are still in good agreement with Gaussians, although small deviations become apparent at $t\,t_{\uparrow} = 4$.
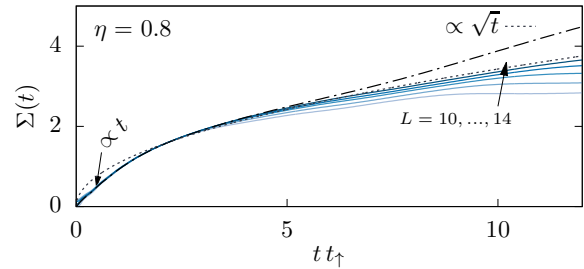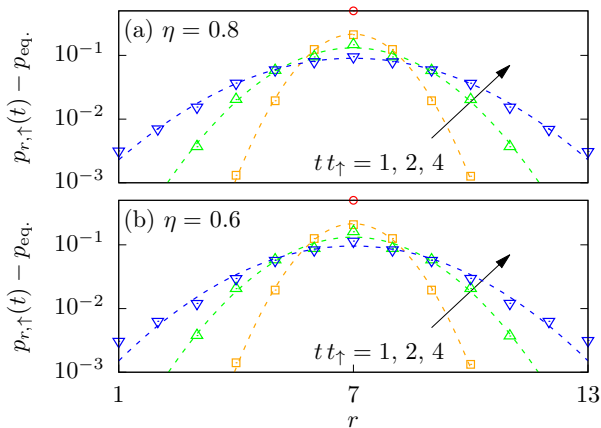

Figure 6. (Color online) Spatial width $\Sigma(t)$ as obtained by Eq. (18) for imbalance ratio $\eta = 0.8$ and different system sizes $L = 10, \ldots, 14$ (arrow). The dotted line with the scaling $\Sigma(t) \propto \sqrt{t}$ is a fit to the $L = 14$ curve. The width $\Sigma(t)$ (dashed-dotted line) as calculated by Eq. (22) is shown for comparison ($L = 14$).

of a density profile on a finite lattice with L sites is obviously bounded from above. Namely, assuming equilibration, i.e., a perfectly homogeneous distribution of the $p_{r,\uparrow}$ for $t \to \infty$ with $\delta p_{r,\uparrow} = 1/L$ at each site, we obtain the saturation value

$$\Sigma^2(t \to \infty) = \sum_{r=1}^{L} \frac{r^2}{L} - \left[\sum_{r=1}^{L} \frac{r}{L}\right]^2 \qquad (26)$$
$$= \frac{1}{12}\left(L^2 - 1\right) \ .$$

This L-dependent saturation value is reached quickly for the weakly imbalanced case $\eta = 0.8$ in Fig. 6, e.g., $\Sigma \approx 4$ for $L = 14$.

Moreover, for the biggest size $L = 14$, Fig. 6 also shows $\Sigma(t)$ calculated from current-current correlation functions via Eq. (22). Overall, the behavior of this $\Sigma(t)$ is in good agreement with the one described above. Note that the small deviations between the two widths setting in at $t\,t_{\uparrow} \sim 6$ presumably arise when the tails of the density distribution reach the boundaries of the system (cf. Fig. 5). Additionally, we note that the finite-size saturation value (26) does not apply to Eq. (22), which, by definition, is not bounded. Rather, for times $t\,t_{\uparrow} \gtrsim 6$, we find an accelerated increase of $\Sigma(t)$. This is caused by the fact that the current-current correlation function $\langle j_{\uparrow}(t)j_{\uparrow}\rangle$ does not completely decay to zero in a system of finite size, see also Refs. [41, 81].

3. Momentum space

Complementary to the real-space data for $\eta = 0.8, 0.6$ shown in Fig. 5, the corresponding Fourier modes $p_{q,\uparrow}(t)$ with momentum $q = 2\pi k/L$ are shown in Fig. 7 for the four longest wavelengths available, i.e., $k = 1, \ldots, 4$. While $p_{q,\uparrow}(t)$ decays rather quickly for $k \geq 2$ (with the decay rate increasing with k), we find that at least for $k = 1$, $p_{q,\uparrow}(t)$ is to good quality described by an exponential decay [see Eq. (25)], consistent with the onset of
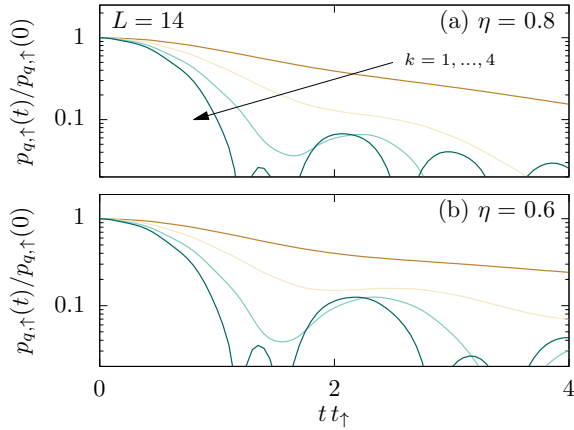
Figure 7. (Color online) Discrete Fourier transform $p_{q,\uparrow}(t)$ of the density profile with momentum $q = 2\pi k/L$ and wave numbers $k = 1, 2, 3, 4$ (arrow) for weak imbalances (a) $\eta = 0.8$ and (b) $\eta = 0.6$.

Figure 9. (Color online) Time-space density plot as in Fig. 4 but for (a) $\eta = 0.4$ and (b) $\eta = 0.2$.

diffusion on the corresponding length scales.

C. Strong mass imbalance

Now, let us study how the equilibration dynamics alter for stronger imbalances and also discuss the possibility of localization for $\eta > 0$.

1. Real-space dynamics

Before discussing the full density profile in detail, let us for simplicity focus on the decay of the central peak $p_{L/2,\uparrow}(t)$, as shown in Fig. 8 for imbalance ratios $\eta = 0, \ldots, 1$ and two system sizes $L = 12$ and $L = 14$. While $p_{L/2,\uparrow}(t) \propto t^{-1/2}$ to good quality for

$\eta = 1$, consistent with diffusive transport, this decay is slowed down with decreasing η. At small but finite $\eta = 0.1$, we find that $p_{L/2,\uparrow}(t)$ approximately coincides with the $\eta = 0$ curve up to times $t\,t_\uparrow \approx 40$, until it eventually starts to decay towards the equilibrium value $p_{L/2,\uparrow}(t \to \infty) - p_{\text{eq.}} = (1 - p_{\text{eq.}})/L$. Note that the two curves for $L = 12, 14$ agree very well with each other before the equilibration value is reached. On these time scales, the behavior of the density dynamics thus appears to be independent of the system size. This also illustrates the accuracy of the DQT approach, since there is no sign of sample-dependence in the time-dependent fluctuations of the strongly imbalanced curves. For additional data with smaller η and longer time scales, see Appendix B. Moreover, a more detailed finite-size analysis can be found in Appendix C.

Next, let us come back to a discussion of the full den-
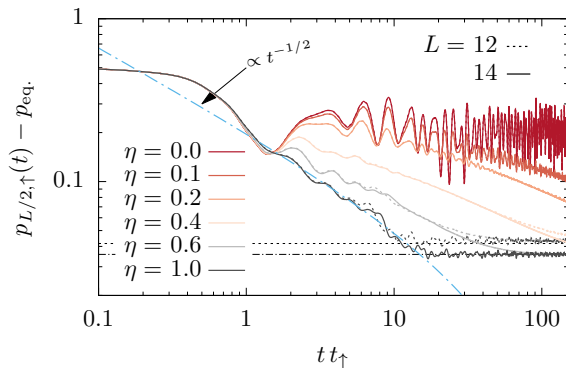

Figure 8. (Color online) Decay of the central peak $p_{L/2,\uparrow}(t)$ at different imbalances ranging from $\eta = 0$ to $\eta = 1$ (from top to bottom) for system sizes $L = 12$ (dotted) and $L = 14$ (solid). Dashed lines indicate the expected L-dependent long-time value $(1 - p_{\text{eq.}})/L$.
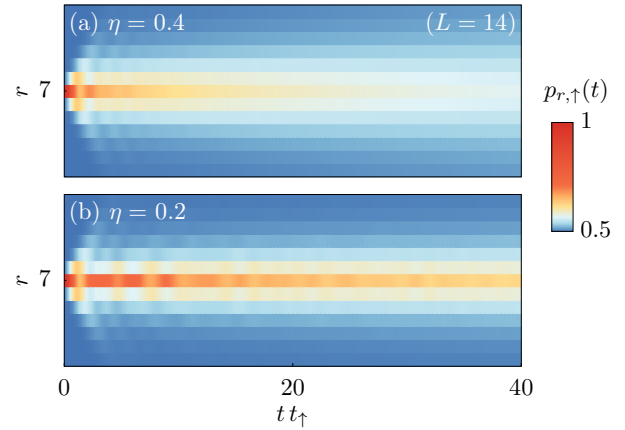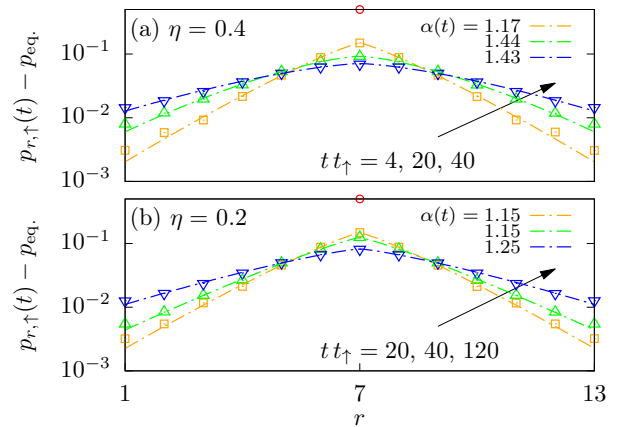

Figure 10. (Color online) Density profiles $p_{r,\uparrow}(t)$ as in Fig. 5 but for smaller (a) $\eta = 0.4$ and (b) $\eta = 0.2$. The profiles broaden much slower and take on a triangular shape in the semi-logarithmic plot used. The fit parameter $\alpha(t)$ is the exponent used in Eq. (27).
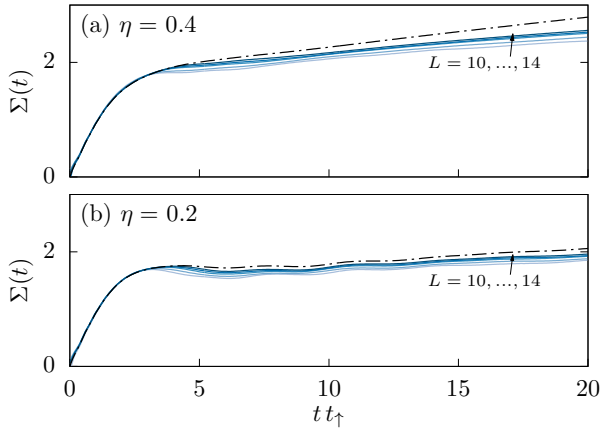
Figure 11. (Color online) Spatial width $\Sigma(t)$ for different system sizes $L = 10, \ldots, 14$ (arrows) as obtained by Eq. (18) at (a) $\eta = 0.4$ and (b) $\eta = 0.2$. The width $\Sigma(t)$ (dashed-dotted lines) as calculated according to Eq. (22) is shown for comparison ($L = 14$).

Figure 12. (Color online) Spatial width $\Sigma(t)$ for fixed system size $L = 14$ and varying imbalances ranging from $\eta = 0$ to $\eta = 1$ (arrow) in steps of 0.05. In the balanced case $\eta = 1$, the width reaches its natural saturation value (dashed line) of $\Sigma \approx 4$ [cf. Eq. (26)] rather quickly, while the other curves grow slower as η goes to zero. The curve for $\eta = 0$ remains at around $\Sigma \approx 2$.

sity profile. To this end, Fig. 9 shows time-space density plots for the two $\eta = 0.4$ and $\eta = 0.2$. We find that the broadening of the density profiles visibly slows down with decreasing η, until no substantial spreading of the density can be observed for $\eta = 0.2$ up to the maximum time $t\,t_\uparrow = 40$ shown here, consistent with Fig. 8 discussed before.

The corresponding cuts of the density profiles at fixed times are shown in Figs. 10 (a) and (b). Note that, owing to the slow broadening of the profiles, we show cuts at later times compared to Fig. 5. One clearly sees that the profiles are not Gaussian anymore, but rather exhibit a pronounced triangular shape in the semi-logarithmic plot used. In particular, they can be well described by the function

$$p_{r,\uparrow}(t) - p_{\text{eq.}} = \beta(t) \exp\left[-\frac{|r - L/2|^{\alpha(t)}}{2\Sigma_{\text{f}}^2(t)}\right] \qquad (27)$$

with the time-dependent fit parameters $\alpha(t)$, $\Sigma_{\text{f}}(t)$, and $\beta(t)$. In particular, the exponent $\alpha(t) \in [1, 2]$ is introduced to capture the triangular shape. This shape indicates a crossover to anomalous diffusion for small ratios $\eta \lesssim 0.4$ [84]. This is another central result of this paper.

2.   *Spatial width*

Additionally, Fig. 11 shows the width $\Sigma(t)$ of the density profiles for $\eta = 0.4$ and $\eta = 0.2$, as calculated by Eqs. (18) and (22). Compared to the weakly imbalanced case shown in Fig. 6, $\Sigma(t)$ now grows much slower, and Eqs. (18) and (22) are in better agreement, since the distribution is still well concentrated in the center of the chain. For $\eta = 0.2$, $\Sigma(t)$ appears to remain at a constant plateau up to the maximum time $t\,t_\uparrow = 20$ shown.

To analyze the η-dependence of the width in more detail, Fig. 12 shows $\Sigma(t)$ in Eq. (18) on a longer time scale $t\,t_\uparrow \leq 150$ for various values of η and a fixed system size $L = 14$. While the growth of $\Sigma(t)$ towards the saturation value becomes slower and slower with decreasing η, we find that even for the smallest value of $\eta = 0.05$ shown here, $\Sigma(t)$ clearly increases at long times. In contrast, the width in the $\eta = 0$ case fluctuates around a constant and lower value, which might be interpreted as the Anderson localization length.

Figure 13. (Color online) Discrete Fourier transform $p_{q,\uparrow}(t)$ of the density profile with momentum $q = 2\pi k/L$ and wave numbers $k = 1, 2, 3$ (arrow) for two imbalance ratios (a) $\eta = 0.2$ and (b) $\eta = 0.1$ ($L = 15$). Another density mode $p_{q,\uparrow}(t)$ (dashed line) for a smaller system size $L = 10$ with wave number $k = 2$ is shown for comparison, which has the same momentum $q = 2\pi/5$ as the mode $k = 3$ for $L = 15$.

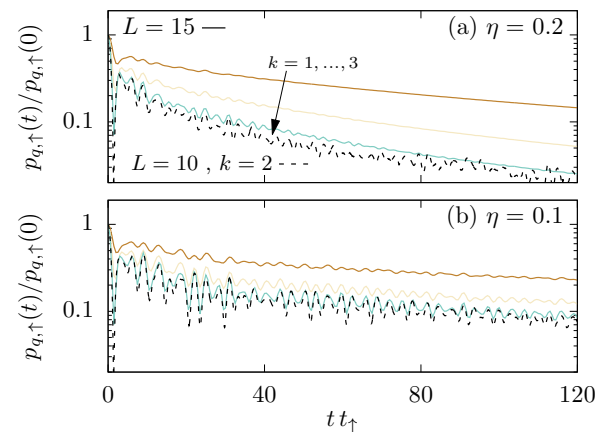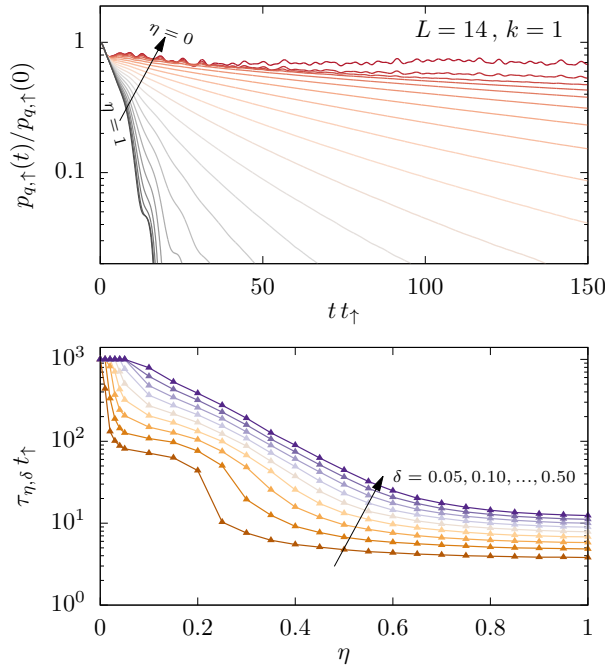Figure 14. (Color online) (a) Discrete Fourier transform $p_{q,\uparrow}(t)$ of the density profile for fixed momentum $q = 2\pi/14$ and (b) "lifetime" according to the definition (28) for various distances $\delta = 0.05, \ldots, 0.5$ in steps of 0.05.

3.   Momentum-space dynamics

Let us now turn to momentum-space dynamics again. To this end, Figs. 13 (a) and (b) show the discrete Fourier modes $p_{q,\uparrow}(t)$ for imbalance ratios $\eta = 0.2$ and $\eta = 0.1$. Note that the data is obtained for an even larger system with $L = 15$ lattice sites and for momenta $q = 2\pi k/L$ with $k = 1, 2, 3$. Compared to Fig. 7, we find that the $p_{q,\uparrow}(t)$ now decay visibly slower for all wave numbers k. Moreover, in contrast to the scaling of decay rates in the case of normal diffusion [cf. Eq. (25)], the density modes now seem to decay at a similar rate for all k. Furthermore, even for small $\eta = 0.1$ and $k = 1$, we find that $p_{q,\uparrow}(t)$ is clearly non-constant, which suggests that genuine localization is absent for $\eta > 0$.

To analyze the dependence on system size, Fig. 13 also shows the Fourier mode $p_{q,\uparrow}(t)$ for $L = 10$ and wave number $k = 2$. This mode has the same momentum $q = 2\pi/5$ as the mode $k = 3$ for $L = 15$. We find that for both $\eta = 0.2$ and $\eta = 0.1$ the decay of $p_{q,\uparrow}(t)$ is almost independent of L. Especially for $\eta = 0.1$, the curves show no significant differences up to the maximum time $t\, t_\uparrow = 120$ shown.

Finally, Fig. 14 (a) shows the relaxation of the Fourier mode $p_{q,\uparrow}(t)$ with the smallest wave number $k = 1$ for various $0 \leq \eta \leq 1$. The decay appears to be exponential for $\eta \gtrsim 0.2$, albeit very slow for strong imbalances. While for sufficiently small times, all $\eta > 0$ curves agree with the

$\eta = 0$ curve, they start to deviate at a certain point in time. In order to analyze this separation time from the $\eta = 0$ curve in more detail, we define

$$\tau_{\eta,\delta} = \max\left\{ t \mid \frac{|\bar{p}^{\eta}_{q,\uparrow}(t) - \bar{p}^{0}_{q,\uparrow}(t)|}{\bar{p}^{0}_{q,\uparrow}(t)} < \delta \right\} \qquad (28)$$

using the running averages of the density modes

$$\bar{p}^{\eta}_{q,\uparrow}(t) = \frac{1}{t} \int_0^t p^{\eta}_{q,\uparrow}(t')dt' \,. \qquad (29)$$

It measures the maximum time up to which $\eta = 0$ and $\eta > 0$ curves do not deviate up to a distance δ. (Note that this maximum time can not exceed the maximum simulation time, here $t_{\max}\, t_\uparrow = 1000$. Moreover, the running averages are used to mitigate the fluctuations of the $p_{q,\uparrow}(t)$, which complicate the extraction of precise separation times.)

The physical picture for this analysis can be understood as follows. For very small but nonzero η, the heavy particles still appear as a quasi-static disorder potential for the lighter particles, which induces localization analogous to $\eta = 0$. At some point in time, however, the residual hopping of the heavy particles becomes relevant, which can be seen as an η-dependent "lifetime" of the Anderson insulator. The corresponding data for different distances δ is shown in Fig. 14 (b). For every δ, the lifetime grows fast with decreasing η, but apparently is always finite for all η considered. A complementary analysis of $\tau_{\eta,\delta}$, based on the spatial width $\Sigma(t)$ (cf. Fig. 12), can be found in Appendix D and provides a similar picture.

V.   CONCLUSION

In this paper, we have studied the real-time dynamics of local charge densities in the Fermi-Hubbard chain with a mass-imbalance between the spin-$\uparrow$ and -$\downarrow$ particles. To this end, we have prepared a certain class of pure states featuring a sharp initial peak of the density profile for the (lighter) spin-$\uparrow$ particles in the middle of the chain and investigated the resulting non-equilibrium dynamics. Relying on dynamical quantum typicality, this dynamics can be related to time-dependent correlation functions at equilibrium.

In the regime of weak and moderate imbalance, $\eta \gtrsim 0.6$, we have provided evidence for the emergence of diffusive dynamics, manifesting in (i) Gaussian shape of density profiles, (ii) square-root scaling of the spatial variance in time, and (iii) exponentially decaying modes for small momenta.

In contrast, in the regime of strong imbalance, $\eta \lesssim 0.6$, we have observed signatures of anomalous transport, emerging as an exponential rather than a Gaussian shape of density profiles and subdiffusive scaling of spatial vari-

ance and density modes in time, consistent with other works [35, 41]. However, we cannot rule out that this anomalous transport is just a transient effect which crosses over to normal diffusion at even longer times, e.g., at time scales much longer than the "lifetime" of the Anderson insulator.

For very small but nonzero η, our results are consistent with the absence of genuine localization and support long but finite equilibration times.

Promising future research directions include extensions of the model such as nearest-neighbor interactions and the study of lower temperatures, including potential relations between static and dynamical properties at such temperatures [85].

Appendix A: Typicality relation

To make this paper self-contained, we here derive the typicality relation (12), see also [44]. To this end, we start with the correlation function

$$C_{r,\uparrow}(t) = 2 \langle (n_{L/2,\uparrow} - p_{\text{eq.}})(n_{r,\uparrow}(t) - p_{\text{eq.}}) \rangle + p_{\text{eq.}} \quad \text{(A1)}$$

and use $\langle n_{r,\uparrow}(t) \rangle = p_{\text{eq.}} = 1/2$, while carrying out the multiplication of the brackets, to obtain

$$C_{r,\uparrow}(t) = 2 \langle n_{L/2,\uparrow} n_{r,\uparrow}(t) \rangle = \frac{\text{Tr}\left[n_{L/2,\uparrow} n_{r,\uparrow}(t) \right]}{d/2} \quad . \quad \text{(A2)}$$

This expression, using cyclic invariance of the trace and the projection property $n_{L/2,\uparrow}^2 = n_{L/2,\uparrow}$, can be written as

$$C_{r,\uparrow}(t) = \frac{\text{Tr}\left[n_{L/2,\uparrow} n_{r,\uparrow}(t) n_{L/2,\uparrow} \right]}{d/2} \quad . \quad \text{(A3)}$$

Exploiting typicality, the trace can be approximated by a single typical pure state $|\phi\rangle$ as

$$C_{r,\uparrow}(t) = \frac{\langle \phi | n_{L/2,\uparrow} n_{r,\uparrow}(t) n_{L/2,\uparrow} | \phi \rangle}{\langle \phi | \phi \rangle / 2} + \epsilon(|\phi\rangle) \quad \text{(A4)}$$

$$\approx \frac{\left(\langle \phi | n_{L/2,\uparrow}^\dagger e^{iHt} \right) n_{r,\uparrow} \left(e^{-iHt} n_{L/2,\uparrow} | \phi \rangle \right)}{\langle \phi | \phi \rangle / 2} \quad ,$$

where the the variance of the statistical error $\epsilon(|\phi\rangle)$ is bounded from above by $\text{Var}(\epsilon)(|\phi\rangle) < \mathcal{O}(1/d)$ (at formally infinite temperature) and becomes negligibly small already for intermediate system sizes. With
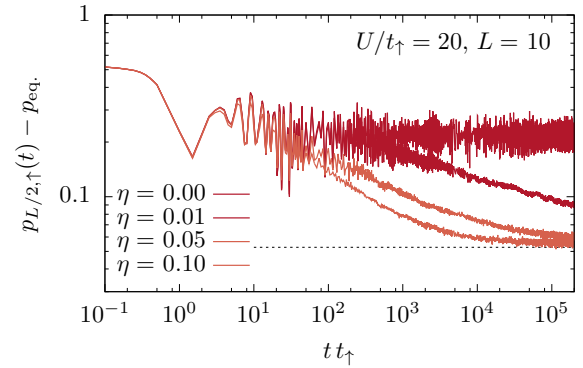

Figure 15. (Color online) Decay of the central peak $p_{L/2,\uparrow}(t)$ for $L = 10$ and long times at $\eta \leq 0.1$.

$|\psi(0)\rangle = n_{L/2,\uparrow} |\phi\rangle / \sqrt{\langle \phi | \phi \rangle / 2}$ we arrive at

$$C_{r,\uparrow}(t) \approx \langle \psi(t) | n_{r,\uparrow} | \psi(t) \rangle = p_{r,\uparrow}(t) \quad \text{(A5)}$$

and finally, comparing to (A1),

$$p_{r,\uparrow}(t) - p_{\text{eq.}} \approx 2 \langle (n_{L/2,\uparrow} - p_{\text{eq.}})(n_{r,\uparrow}(t) - p_{\text{eq.}}) \rangle \quad . \quad \text{(A6)}$$

Appendix B: Equilibration for small η

Complementary to Fig. 8, Fig. 15 shows data for the central peak $p_{L/2,\uparrow}(t)$, but now for a smaller system size $L = 10$ (in the half-filling sector $N_\uparrow + N_\downarrow = L$) and significantly longer time scales. We find that $p_{L/2,\uparrow}(t)$ ultimately decays towards its equilibrium value, even for very small values of η. Note that the interaction strength in Fig. 15 is chosen as $U/t_\uparrow = 20$, analogous to earlier investigations in Ref. [35], where similar findings were presented for momentum-space observables.

Appendix C: L-independence of density profiles

To demonstrate the L-independence for the scaling of the density profiles, Fig. 16 shows $p_{r,\uparrow}(t)$ for two system sizes with $L = 13$ and 14 and exemplary values for times t and imbalances η. Apart from small deviations at the tails, we find that the profiles for different L are in very good agreement. This fact also demonstrates the accuracy of the typicality approach.

Appendix D: Anderson lifetime

In addition to Fig. 14 (b), Fig. 17 shows another analysis of the lifetime $\tau_{\eta,\delta}$. Here, $\tau_{\eta,\delta}$ is calculated in analogy
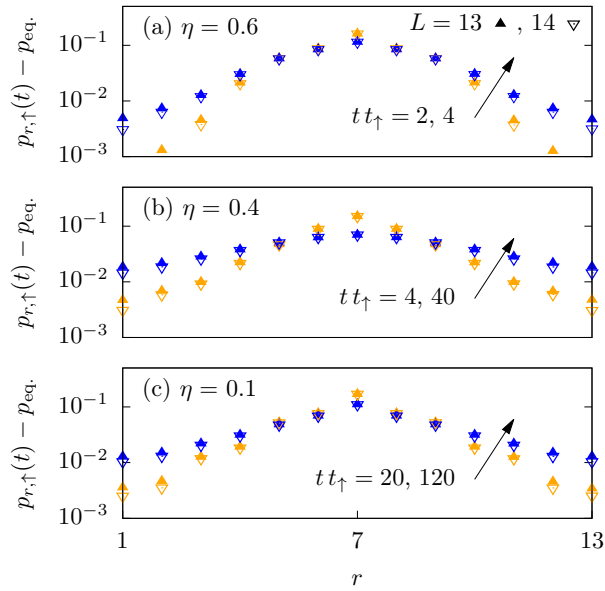
Figure 16. (Color online) Comparison of density profiles for two system sizes $L = 13, 14$ and a few exemplary imbalance ratios η. The overall behavior coincides nicely for both L, apart from slight deviations at the boundaries.
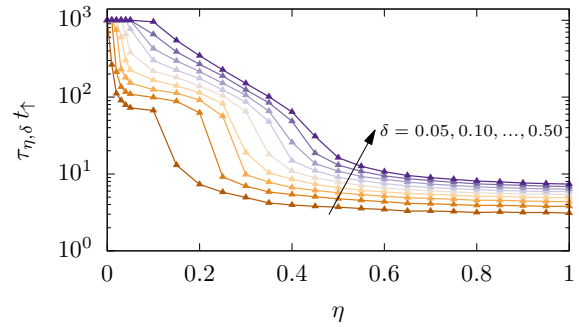

Figure 17. (Color online) "Lifetime" in analogy to the definition (28) for various distances $\delta = 0.05, \ldots, 0.5$ in steps of 0.05, now based on the spatial width $\Sigma(t)$ shown in Fig. 12.

to (28), but based on the spatial width $\Sigma(t)$ (cf. Fig. 12),

$$\tau_{\eta,\delta} = \max\left\{ t \;\middle|\; \frac{|\overline{\Sigma}^{\eta}(t) - \overline{\Sigma}^{0}(t)|}{\overline{\Sigma}^{0}(t)} < \delta \right\} \qquad (D1)$$

with

$$\overline{\Sigma}^{\eta}(t) = \frac{1}{t}\int_{0}^{t} \Sigma^{\eta}(t')dt' \;. \qquad (D2)$$

In comparison to Fig. 14 (b), Fig. 17 provides a very similar picture for the η-dependent lifetime.

[1] I. Bloch, J. Dalibard, and S. Nascimbène, Nat. Phys. **8**, 267 (2012).

[2] R. Blatt and C. F. Roos, Nat. Phys. **8**, 277 (2012).

[3] A. Polkovnikov, K. Sengupta, A. Silva, and M. Vengalattore, Rev. Mod. Phys. **83**, 863 (2011).

[4] J. Eisert, M. Friesdorf, and C. Gogolin, Nat. Phys. **11**, 124 (2015).

[5] L. D'Alessio, Y. Kafri, A. Polkovnikov, and M. Rigol, Adv. Phys. **65**, 239 (2016).

[6] C. Gogolin and J. Eisert, Rep. Prog. Phys. **79**, 056001 (2016).

[7] F. Borgonovi, F. Izrailev, L. F. Santos, and V. Zelevinsky, Phys. Rep. **626**, 1 (2016).

[8] J. M. Deutsch, Phys. Rev. A **43**, 2046 (1991).

[9] M. Srednicki, Phys. Rev. E **50**, 888 (1994).

[10] M. Rigol, V. Dunjko, and M. Olshanii, Nature **452**, 854 (2008).

[11] P. W. Anderson, Phys. Rev. **109**, 1492 (1958).

[12] E. Abrahams, P. W. Anderson, D. C. Licciardello, and T. V. Ramakrishnan, Phys. Rev. Lett. **42**, 673 (1979).

[13] G. Roati, C. D'Errico, L. Fallani, M. Fattori, C. Fort, M. Zaccanti, G. Modugno, M. Modugno, and M. Inguscio, Nature **453**, 895 (2008).

[14] J. Billy, V. Josse, Z. Zuo, A. Bernard, B. Hambrecht, P. Lugan, D. Clément, L. Sanchez-Palencia, P. Bouyer, and A. Aspect, Nature **453**, 891 (2008).

[15] R. M. Nandkishore and D. A. Huse, Annu. Rev. Condens. Matter Phys. **6**, 15 (2015).

[16] D. A. Abanin, E. Altman, I. Bloch, and M. Serbyn, Rev. Mod. Phys. **91**, 021001 (2019).

[17] M. Schreiber, S. S. Hodgman, P. Bordia, H. P. Luschen, M. H. Fischer, R. Vosk, E. Altman, U. Schneider, and I. Bloch, Science **349**, 842 (2015).

[18] S. Gopalakrishnan and S. A. Parameswaran, Phys. Rep. **862**, 1 (2020).

[19] H. P. Lüschen, P. Bordia, S. S. Hodgman, M. Schreiber, S. Sarkar, A. J. Daley, M. H. Fischer, E. Altman, I. Bloch, and U. Schneider, Phys. Rev. X **7**, 011034 (2017).

[20] J. Smith, A. Lee, P. Richerme, B. Neyenhuis, P. W. Hess, P. Hauke, M. Heyl, D. A. Huse, and C. Monroe, Nat. Phys. **12**, 907 (2016).

[21] J. Richter, N. Casper, W. Brenig, and R. Steinigeweg, Phys. Rev. B **100**, 144423 (2019).

[22] J. Richter, D. Schubert, and R. Steinigeweg, Phys. Rev. Research **2**, 013130 (2020).

[23] P. Prelovšek, O. S. Barišić, and M. Žnidarič, Phys. Rev. B **94**, 241104(R) (2016).

[24] M. Kozarzewski, P. Prelovšek, and M. Mierzejewski, Phys. Rev. Lett. **120**, 246602 (2018).

[25] G. Carleo, F. Becca, M. Schiró, and M. Fabrizio, Sci. Rep. **2**, 243 (2012).

[26] W. De Roeck and F. Huveneers, Phys. Rev. B **90**, 165137 (2014).

[27] W. De Roeck and F. Huveneers, Commun. Math. Phys. **332**, 1017 (2014).

[28] W. De Roeck and F. Huveneers, in *From Part. Syst. to Partial Differ. Equations II*, edited by P. Gonçalves and A. J. Soares (Springer International Publishing, Cham, 2015) pp. 173–192.

[29] T. Grover and M. P. A. Fisher, J. Stat. Mech. **2014**, P10010 (2014).

[30] M. Schiulaz and M. Müller, in *AIP Conf. Proc.*, Vol. 1610 (2014) pp. 11–23.

[31] E. Altman and R. Vosk, Annu. Rev. Condens. Matter Phys. **6**, 383 (2015).

[32] Z. Papić, E. M. Stoudenmire, and D. A. Abanin, Ann. Phys. (NY) **362**, 714 (2015).

[33] M. Schiulaz, A. Silva, and M. Müller, Phys. Rev. B **91**, 184202 (2015).

[34] J. M. Hickey, S. Genway, and J. P. Garrahan, J. Stat. Mech. **2016**, 054047 (2016).

[35] N. Y. Yao, C. R. Laumann, J. I. Cirac, M. D. Lukin, and J. E. Moore, Phys. Rev. Lett. **117**, 240601 (2016).

[36] A. Smith, J. Knolle, D. L. Kovrizhin, and R. Moessner, Phys. Rev. Lett. **118**, 266601 (2017).

[37] A. A. Michailidis, M. Žnidarič, M. Medvedyeva, D. A. Abanin, T. Prosen, and Z. Papić, Phys. Rev. B **97**, 104307 (2018).

[38] M. Brenes, M. Dalmonte, M. Heyl, and A. Scardicchio, Phys. Rev. Lett. **120**, 030601 (2018).

[39] J. Sirker, Phys. Rev. B **99**, 075162 (2019).

[40] O. Gamayun, O. Lychkovskiy, and V. Cheianov, Phys. Rev. E **90**, 032132 (2014).

[41] F. Jin, R. Steinigeweg, F. Heidrich-Meisner, K. Michielsen, and H. De Raedt, Phys. Rev. B **92**, 205103 (2015).

[42] T. Prosen and M. Žnidarič, Phys. Rev. B **86**, 125118 (2012).

[43] C. Karrasch, T. Prosen, and F. Heidrich-Meisner, Phys. Rev. B **95**, 060406(R) (2017).

[44] R. Steinigeweg, F. Jin, H. De Raedt, K. Michielsen, and J. Gemmer, Phys. Rev. E **96**, 020105(R) (2017).

[45] E. Ilievski, J. De Nardis, M. Medenjak, and T. Prosen, Phys. Rev. Lett. **121**, 230602 (2018).

[46] B. Paredes, F. Verstraete, and J. I. Cirac, Phys. Rev. Lett. **95**, 140501 (2005).

[47] F. Andraschko, T. Enss, and J. Sirker, Phys. Rev. Lett. **113**, 217201 (2014).

[48] Y. Zhao, F. Andraschko, and J. Sirker, Phys. Rev. B **93**, 205146 (2016).

[49] T. Enss, F. Andraschko, and J. Sirker, Phys. Rev. B **95**, 045121 (2017).

[50] F. H. L. Essler, H. Frahm, F. Göhmann, A. Klümper, and V. E. Korepin, *The One-Dimensional Hubbard Model* (Cambridge University Press, 2005).

[51] L. M. Falicov and J. C. Kimball, Phys. Rev. Lett. **22**, 997 (1969).

[52] R. Lyżwa and Z. Domański, Phys. Rev. B **50**, 11381 (1994).

[53] C. Bartsch and J. Gemmer, Phys. Rev. Lett. **102**, 110403 (2009).

[54] C. Bartsch and J. Gemmer, EPL (Europhys. Lett.) **96**, 60008 (2011).

[55] R. Steinigeweg, F. Jin, D. Schmidtke, H. De Raedt, K. Michielsen, and J. Gemmer, Phys. Rev. B **95**, 035155 (2017).

[56] J. Schnack, J. Richter, and R. Steinigeweg, Phys. Rev. Research **2**, 013186 (2020).

[57] J. Schnack, J. Richter, T. Heitmann, J. Richter, and R. Steinigeweg, Z. Naturforsch. A **75**, 465 (2020).

[58] T. Heitmann, J. Richter, D. Schubert, and R. Steinigeweg, Z. Naturforsch. A **75**, 421 (2020).

[59] J. Gemmer and G. Mahler, Eur. Phys. J. B **31**, 249 (2003).

[60] T. Iitaka and T. Ebisuzaki, Phys. Rev. Lett. **90**, 047203 (2003).

[61] T. Iitaka and T. Ebisuzaki, Phys. Rev. E **69**, 057701 (2004).

[62] S. Goldstein, J. L. Lebowitz, R. Tumulka, and N. Zanghì, Phys. Rev. Lett. **96**, 050403 (2006).

[63] S. Popescu, A. J. Short, and A. Winter, Nat. Phys. **2**, 754 (2006).

[64] P. Reimann, Phys. Rev. Lett. **99**, 160404 (2007).

[65] S. R. White, Phys. Rev. Lett. **102**, 190601 (2009).

[66] S. Sugiura and A. Shimizu, Phys. Rev. Lett. **108**, 240401 (2012).

[67] S. Sugiura and A. Shimizu, Phys. Rev. Lett. **111**, 010401 (2013).

[68] T. A. Elsayed and B. V. Fine, Phys. Rev. Lett. **110**, 070404 (2013).

[69] R. Steinigeweg, J. Gemmer, and W. Brenig, Phys. Rev. Lett. **112**, 120601 (2014).

[70] R. Steinigeweg, A. Khodja, H. Niemeyer, C. Gogolin, and J. Gemmer, Phys. Rev. Lett. **112**, 130403 (2014).

[71] T. Monnai and A. Sugita, J. Phys. Soc. Jpn. **83**, 094001 (2014).

[72] P. Reimann, Nat. Commun. **7**, 10821 (2016).

[73] P. Reimann, Phys. Rev. E **97**, 062129 (2018).

[74] P. de Vries and H. De Raedt, Phys. Rev. B **47**, 7929 (1993).

[75] H. De Raedt, K. Michielsen, H. D. Raedt, and K. Michielsen, Host Publ. , 248 (2006).

[76] H. Tal-Ezer and R. Kosloff, J. Chem. Phys. **81**, 3967 (1984).

[77] V. V. Dobrovitski and H. A. De Raedt, Phys. Rev. E **67**, 056702 (2003).

[78] A. Weiße, G. Wellein, A. Alvermann, and H. Fehske, Rev. Mod. Phys. **78**, 275 (2006).

[79] A. Nauts and R. E. Wyatt, Phys. Rev. Lett. **51**, 2238 (1983).

[80] T. Heitmann and J. Schnack, Phys. Rev. B **99**, 134405 (2019).

[81] B. Bertini, F. Heidrich-Meisner, C. Karrasch, T. Prosen, R. Steinigeweg, and M. Žnidarič, Rev. Mod. Phys. **93**, 025003 (2021).

[82] R. Steinigeweg, H. Wichterich, and J. Gemmer, EPL (Europhys. Lett.) **88**, 10004 (2009).

[83] Y. Yan, F. Jiang, and H. Zhao, Eur. Phys. J. B **88**, 11 (2015).

[84] M. Žnidarič, A. Scardicchio, and V. K. Varma, Phys. Rev. Lett. **117**, 040601 (2016).

[85] M. Tezuka and A. M. García-García, Phys. Rev. A **85**, 031602(R) (2012).

Preprint of Publication [P5]

[P5] Jonas Richter, <u>Tjark Heitmann</u>, and Robin Steinigeweg,
Quantum Quench Dynamics in the Transverse-Field Ising Model:
A Numerical Expansion in Linked Rectangular Clusters,
Journal reference: SciPost Phys. **9**, 031 (2020) [Open Access]
DOI: 10.21468/SciPostPhys.9.3.031
Preprint: `arXiv:2005.03104`

Quantum Quench Dynamics in the Transverse-Field Ising Model: A Numerical Expansion in Linked Rectangular Clusters

Jonas Richter [iD],* Tjark Heitmann [iD], and Robin Steinigeweg [iD]

Department of Physics, University of Osnabrück, D-49069 Osnabrück, Germany

We study quantum quenches in the transverse-field Ising model defined on different lattice geometries such as chains, two- and three-leg ladders, and two-dimensional square lattices. Starting from fully polarized initial states, we consider the dynamics of the transverse and the longitudinal magnetization for quenches to weak, strong, and critical values of the transverse field. To this end, we rely on an efficient combination of numerical linked cluster expansions (NLCEs) and a forward propagation of pure states in real time. As a main result, we demonstrate that NLCEs comprising solely rectangular clusters provide a promising approach to study the real-time dynamics of two-dimensional quantum many-body systems directly in the thermodynamic limit. By comparing to existing data from the literature, we unveil that NLCEs yield converged results on time scales which are competitive to other state-of-the-art numerical methods.

I.   INTRODUCTION

Understanding the dynamics of isolated quantum many-body systems out of equilibrium is an active area of research of modern theoretical and experimental physics [1–3]. A popular nonequilibrium protocol in this context is a so-called quantum quench [4]. In such quench protocols, the system's Hamiltonian $\mathcal{H}$ depends on some parameter λ, and the system is prepared in an eigenstate $|\psi(0)\rangle$ of $\mathcal{H}$, e.g., the groundstate, for an initial value λ_i. Next, the value of λ is suddenly changed, $\lambda_i \to \lambda_f$, such that $|\psi(0)\rangle$ is no eigenstate of $\mathcal{H}(\lambda_f)$, and the system exhibits nontrivial dynamics. For an isolated quantum system undergoing unitary time evolution, it is then intriguing to study if and in which way the system relaxes back to equilibrium. Central questions are, for instance, how the (short- or long-time) dynamics can be described in terms of "universal" principles [1, 5–11], what are the relevant time scales of relaxation [12–14], and whether or not the long-time values of physical observables agree with the prediction of, e.g., a microcanonical or canonical ensemble (i.e. thermalization) [15–17].

One possible mechanism to explain the emergence of thermalization in isolated quantum systems is given by the eigenstate thermalization hypothesis (ETH) [18–20]. While the validity of the ETH has been numerically tested for a variety of models and observables (see, e.g., [21–27]), there are also classes of systems which violate the ETH and fail to thermalize. One such class is given by integrable models, where the extensive number of conservation laws prevents the applicability of standard statistical ensembles [28]. Instead, it has been proposed that integrable models equilibrate towards a generalized Gibbs ensemble (GGE), which maximizes the entropy with respect to the conserved charges [29–31]. In addition, it is now widely believed that some strongly disordered systems can undergo a transition to a many-body localized (MBL) phase, where the ETH is violated as well [32, 33].

Moreover, there has been plenty of interest recently in models which are, in a sense, intermediate cases between "fully ETH" and "fully MBL". This includes, e.g., models featuring "quantum scars" where rare ETH-violating states are embedded in an otherwise thermal spectrum [34–38], as well as models which exhibit a strong fragmentation of the Hilbert space due to additional constraints [39, 40].

From a numerical point of view, studying the nonequilibrium dynamics of isolated quantum many-body systems is a challenging task. This is not least caused by the fact that for an interacting quantum system, the Hilbert space grows exponentially in the number of constituents. Nevertheless, thanks to the continuous increase of computational resources and the development of sophisticated numerical methods including, e.g., dynamical mean field theory [41], Krylov subspace techniques [42, 43], dynamical quantum typicality [44], or classical representations in phase space [45], significant progress has been made. Especially for one-dimensional systems, the time-dependent density-matrix renormalization group, as well as related methods based on matrix-product states (MPS), provide a powerful tool to study dynamical properties for system sizes practically in the thermodynamic limit [46, 47]. However, since these methods rely on an efficient compression of moderately entangled wave functions, the reachable time scales in simulations are eventually limited due to the inevitable buildup of entanglement during the unitary time evolution.

The growth of entanglement becomes even more severe in spatial dimensions larger than one. Despite recent advances involving MPS-based or tensor-network algorithms [48–53], as well as the advent of innovative machine-learning approaches [54–56], the time scales numerically attainable for two-dimensional quantum many-body systems are still comparatively short. While the dynamics of such two-dimensional systems can nowadays be accessed in experiments with quantum simulators [57–59], the development of efficient numerical techniques is paramount. On the one hand, unbiased numerical simulations are important to confirm the accuracy of the

* jonasrichter@uos.de

experimental results. On the other hand, numerical simulations can also serve as an orientation for experiments to explore certain models or parameter regimes in more detail.

In this paper, we scrutinize the nonequilibrium dynamics for quantum quenches in the Ising model with transverse magnetic field. While this model is exactly solvable in the case of a chain and has been studied in numerous instances, our main focus is on nonintegrable geometries such as two- and three-leg ladders and, in particular, two-dimensional square lattices. To this end, we rely on an efficient combination of numerical linked cluster expansions (NLCEs) and the iterative forward propagation of pure states in real time via Chebyshev polynomials. Depending on the model geometry, the initial state, and the strength of the quench, the nonequilibrium dynamics is found to display a variety of different behaviors ranging from rapid equilibration, over slower monotonous relaxation, to persistent (weakly damped) oscillations. Most importantly, from a methodological point of view, we demonstrate that NLCEs comprising solely rectangular clusters provide a promising approach to study the real-time dynamics of two-dimensional quantum many-body systems directly in the thermodynamic limit. By comparing to existing data from the literature, we unveil that NLCEs yield converged results on time scales which are competitive to other state-of-the-art numerical methods.

This paper is structured as follows. In Sec. II, we introduce the models, observables, and quench protocols which are studied. In Sec. III, we then discuss the employed numerical methods, while our results are presented in Sec. IV. We summarize and conclude in Sec. V.

II.   MODELS, OBSERVABLES, AND QUENCH PROTOCOLS

We study the Ising model with ferromagnetic nearest-neighbor interactions and transverse magnetic field, described by the Hamiltonian

$$\mathcal{H} = -J \left(\sum_{\langle \ell, m \rangle} \sigma_\ell^z \sigma_m^z + g \sum_{\ell=1}^{L} \sigma_\ell^x \right) , \qquad (1)$$

where the first sum on the right hand side runs over all pairs of nearest neighbors ℓ and m, L is the total number of sites, $J > 0$ sets the energy scale, $g > 0$ denotes the strength of the transverse field, and $\sigma_\ell^{x,z}$ are Pauli matrices at site ℓ. Note that the Hamiltonian (1) is symmetric under the global spin-flip operation $\sigma_\ell^z \to -\sigma_\ell^z$.

In this paper, the transverse-field Ising model (1) is considered for different lattice geometries such as chains ($L = L_x$), two- and three-leg ladders ($L = L_x \times 2$, $L = L_x \times 3$), and two-dimensional square lattices ($L = L_x \times L_y$). While we generally intend to obtain results in the thermodynamic limit $L \to \infty$ (see Sec. III A for our nu-

merical approach), we consider finite system sizes as well. In the case $L < \infty$, one has to distinguish between open boundary conditions (OBC) and periodic boundary conditions (PBC), where for chains and ladders the latter only applies in the x direction.

On the one hand, in the case of a chain, $\mathcal{H}$ is a paradigmatic example of an integrable model and can be solved exactly by subsequent Jordan-Wigner, Fourier, and Bogoliubov transforms [60], see also Appendix A. For $g < 1$, $\mathcal{H}$ is in a ferromagnetic phase with a two-fold degenerate groundstate. At the critical point $g = 1$, $\mathcal{H}$ undergoes a quantum phase transition towards a paramagnetic phase with unique groundstate for $g > 1$. On the other hand, for a two-dimensional square lattice, $\mathcal{H}$ is nonintegrable [24, 25, 61], and the quantum phase transition between an ordered phase and an unordered phase occurs at the larger transverse field $g = g_c \approx 3.044$ [62]. For intermediate cases, such as multi-leg ladders on a cylinder geometry, the value of g_c can vary since these cases are quasi-one-dimensional [50].

In this paper, we consider quench protocols starting from fully polarized initial states $|\psi(0)\rangle$. Namely, we either study quenches starting from $|\psi(0)\rangle = |\uparrow\rangle$,

$$|\uparrow\rangle = |\uparrow\uparrow \cdots \uparrow\rangle , \qquad (2)$$

where all spins are initially aligned along the z axis, or quenches starting from the state $|\psi(0)\rangle = |\rightarrow\rangle$,

$$|\rightarrow\rangle = |\rightarrow\rightarrow \cdots \rightarrow\rangle , \qquad (3)$$

where all spins point in the x direction. Note that written in the common eigenbasis of the local σ_ℓ^z, $|\rightarrow\rangle$ is a uniform superposition of all 2^L basis states. Moreover, while the state $|\uparrow\rangle$ is an eigenstate of $\mathcal{H}$ for vanishing field $g = 0$, the state $|\rightarrow\rangle$ is the groundstate of $\mathcal{H}$ for $g \to \infty$. Given the states $|\uparrow\rangle$ and $|\rightarrow\rangle$, we study the nonequilibrium dynamics resulting from quantum quenches to weak ($g < g_c$), strong ($g > g_c$), or critical values ($g = g_c$) of the transverse field, i.e., depending on the initial state these are quenches either within the same equilibrium phase, or to or across the critical point.

Due to the quench, the fully polarized states $|\uparrow\rangle$ and $|\rightarrow\rangle$ are no eigenstates of $\mathcal{H}$ anymore and evolve unitarily in time ($\hbar = 1$),

$$|\psi(t)\rangle = e^{-i\mathcal{H}t} |\psi(0)\rangle . \qquad (4)$$

Consequently, the expectation values of observables acquire a dependence on time as well. In particular, we here consider the dynamics of the transverse and the longitudinal magnetization,

$$\langle X(t) \rangle = \frac{1}{L} \sum_{\ell=1}^{L} \langle \psi(t) | \sigma_\ell^x | \psi(t) \rangle , \qquad (5)$$

$$\langle Z(t) \rangle = \frac{1}{L} \sum_{\ell=1}^{L} \langle \psi(t) | \sigma_\ell^z | \psi(t) \rangle . \qquad (6)$$

III. NUMERICAL APPROACH

We now discuss the numerical methods which are employed in this paper. Throughout this section, we exemplarily focus on the transverse magnetization $\langle X(t) \rangle$. The calculations for $\langle Z(t) \rangle$ are carried out analogously.

A. Numerical linked cluster expansion

Numerical linked cluster expansions provide a means to access the properties of quantum many-body systems directly in the thermodynamic limit. Originally introduced to study thermodynamic quantities [63, 64] (see also [65–67]), NLCEs have more recently been employed to obtain entanglement entropies [68], to calculate steady-state properties in driven-dissipative systems [69], to study quantum quenches with mixed or pure initial states [58, 70–74], as well as to simulate time-dependent equilibrium correlation functions [75, 76].

The main idea of NLCEs is that the per-site value of an extensive quantity in the thermodynamic limit can be obtained as a sum over contributions from all linked clusters which can be embedded on the lattice [77],

$$\lim_{L \to \infty} \langle X(t) \rangle = \sum_c \mathcal{L}_c W_c(t) \ , \tag{7}$$

where the sum runs over all connected clusters c with multiplicities $\mathcal{L}_c$ and weights $W_c(t)$. Specifically, $\mathcal{L}_c$ is the number of ways (normalized by the size of the lattice) a cluster c can be embedded on the lattice [see also the discussion around Eq. (10) below]. Moreover, the notion of a *connected* cluster refers to a finite number of lattice sites, where every site of the cluster has to be directly connected to at least one other cluster site by terms of the underlying Hamiltonian. Given a two-dimensional square lattice and the nearest-neighbor Hamiltonian in Eq. (1), for instance, the lattice sites (i, j) and $(i, j+1)$ form a connected cluster of size two. In contrast, the sites (i, j) and $(i+1, j+1)$ do not form a connected cluster as $\mathcal{H}$ does not contain terms along the diagonal. However, in combination, the sites (i, j), $(i, j+1)$, and $(i+1, j+1)$ would be a connected cluster of size three.

Given a cluster c, its weight $W_c(t)$ is obtained by an inclusion-exclusion principle. That is, the quantity of interest (here the dynamics of the magnetization X) is evaluated on the cluster c (with OBC) and, subsequently, the weights $W_s(t)$ of all subclusters s of c have to be subtracted [77],

$$W_c(t) = \langle X(t) \rangle_{(c)} - \sum_{s \subset c} W_s(t) \ . \tag{8}$$

While NLCEs yield results in the thermodynamic limit (such that a finite-size scaling becomes unnecessary), it is instead crucial to check the convergence of the series. To this end, the sum in Eq. (7) is usually organized in terms of expansion orders [77]. For instance, one could group together all clusters which comprise a certain number of lattice sites. Then, an expansion up to order C refers to the fact that all clusters with up to C lattice sites are considered in Eq. (7). Moreover, the NLCE is said to be converged if the outcome of Eq. (7) does not depend on the value of C.

At this point, it is important to note that in actual simulations, the maximum order C that can be reached is limited by two factors: (i) the exponential growth of the Hilbert-space dimension with increasing cluster size, and (ii) the necessity to identify the (possibly very large number of) distinct clusters and to calculate their weights. Since a larger expansion order typically leads to a convergence of Eq. (7) up to longer times [75] (or down to lower temperatures for thermodynamic quantities [66]), it is desirable to include clusters as large as possible. In this paper, we therefore aim to mitigate the limitations (i) and (ii) by two complementary approaches. First, instead of using full exact diagonalization to evaluate $\langle X(t) \rangle_{(c)}$, we here employ an efficient forward propagation of pure states (see Sec. III B), which is feasible for significantly larger Hilbert-space dimensions. Secondly, in order to reduce the enormous combinatorial costs to generate (and evaluate) all clusters with a given number of sites, we rely on the fact that the sum in Eq. (7) can also converge for different types of expansions, as long as clusters and subclusters can be defined in a self-consistent manner [77]. In this paper, we specifically restrict ourselves to only those clusters which have a rectangular shape. This restriction is particularly appealing as the number of distinct clusters is significantly reduced and the calculation of the weights $W_c(t)$ becomes rather simple since all subclusters are rectangles as well, see Fig. 1. Furthermore, the rectangle expansion has been successfully used before to obtain entanglement entropies [68], and it also appears to be a promising candidate to study dynamical properties as it involves clusters with many different length scales. In this context, let us note that other restricted expansions for the two-dimensional square lattice, e.g., clusters consisting of corner-sharing 2×2 squares, have proven to be a good choice to extract thermodynamic quantities [66]. In this paper, however, we focus on rectangular clusters as a first case study.

Given a rectangular cluster $c = (x, y)$ of width x and height y, the inclusion-exclusion principle from Eq. (8) to obtain the weight $W_{(x,y)}(t)$ takes on the form [78]

$$W_{(x,y)}(t) = \langle X(t) \rangle_{(x,y)} \tag{9}$$
$$- \sum_{\substack{x'=1 \\ x'y' < xy}}^{x} \sum_{y'=1}^{y} (x - x' + 1)(y - y' + 1) W_{(x',y')} \ .$$

where the sum runs over all rectangular subclusters. Next, in order to carry out the expansion (7), the multiplicity $\mathcal{L}_c$ is required. Given a two-dimensional square lattice of size $L_x \times L_y$ with OBC, the number of ways per
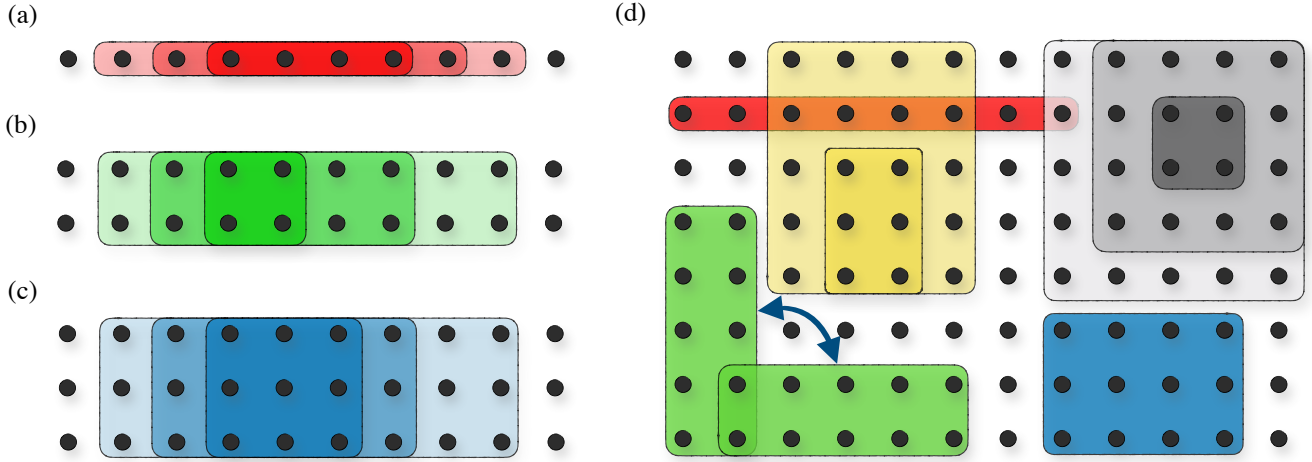
Figure 1. Examples of clusters which are used in the NLCE. (a) For a chain geometry, all clusters and subclusters are chains. (b) and (c) In case of a ladder geometry, we only consider clusters and subclusters which are ladders as well. (c) For the two-dimensional square lattice, we restrict ourselves to clusters with a rectangular shape. Given the Hamiltonian $\mathcal{H}$ in Eq. (1), we note that a cluster $c = (x, y)$ with $x > y$ is equivalent to its $90°$-rotated counterpart $c' = (y, x)$. To speed up the simulations, we therefore only need to consider clusters c with $x \geq y$, where square-shaped clusters with $x = y$ enter Eq. (7) once, while rectangular clusters with $x > y$ enter the expansion twice.

lattice site a rectangular cluster $c = (x, y)$ (with finite x and y) can be embedded on the lattice follows as,

$$\mathcal{L}_c = \frac{(L_x - x + 1)(L_y - y + 1)}{L_x L_y} \; , \tag{10}$$

as there are $(L_x - x + 1)$ possible translations in the x direction and $(L_y - y + 1)$ in the y direction. Thus, if one is interested in the properties of the lattice in the thermodynamic limit, $L_x, L_y \to \infty$, one finds,

$$\mathcal{L}_c = 1 \; . \tag{11}$$

Furthermore, in order to speed up the simulations, it is useful to take into account that the Hamiltonian $\mathcal{H}$ in Eq. (1) is invariant under rotations in the sense that a rectangular cluster $c = (x, y)$ with $x \geq y$ yields the exact same weight $W_c(t)$ as the cluster $c' = (y, x)$, i.e., c rotated by 90 degrees. Thus, in practice, we only need to consider clusters with $x \geq y$, where square-shaped cluster with $x = y$ enter Eq. (7) once, while rectangular clusters with $x > y$ then enter the expansion twice.

Let us add some comments on the NLCE for chains and ladders. First, we note that in the case of chains, all clusters are just chains as well, see Fig. 1 (a). In this case, the expansion in Eq. (7) reduces to a single difference between $\langle X(t) \rangle_{(c)}$ evaluated on the largest and the second-largest cluster [75]. Secondly, while for two-leg (or three-leg) ladders, rectangular clusters can in principle have a height $y = 1, 2$ (or $y = 1, 2, 3$) with different lengths x, we here restrict ourselves even further to those clusters which are two-leg or three-leg ladders as well, see

Figs. 1 (b) and (c). In this case, the expansion (7) again reduces to a single difference between $\langle X(t) \rangle_{(c)}$ evaluated on the largest and the second-largest cluster. Despite this simplicity, however, we find that this type of expansion for ladders in practice yields convincing convergence times.

B.   Pure-state propagation

Evaluating the unitary time evolution of the initial states $|\psi(0)\rangle$ according to Eq. (4) in principle requires the full exact diagonalization (ED) of the Hamiltonian $\mathcal{H}$. In order to access system (and cluster) sizes beyond the range of full ED, we here subdivide the evolution up to time t into a product of discrete time steps,

$$|\psi(t)\rangle = e^{-i\mathcal{H}t} |\psi(0)\rangle = \left(e^{-i\mathcal{H}\delta t} \right)^Q |\psi(0)\rangle \; , \tag{12}$$

where $\delta t = t/Q$. If the time step δt is chosen sufficiently small, then there exist various approaches to accurately approximate the action of the exponential $\exp(-i\mathcal{H}\delta t)$ such as, e.g., Trotter decompositions [79], Krylov subspace techniques [42], or Runge-Kutta schemes [80, 81]. In this paper, we rely on an expansion of the time-evolution operator in terms of Chebyshev polynomials, for a comprehensive overview see [82–85]. Let us emphasize that the evaluation of Eq. (12) to a high precision is crucial for the convergence of the NLCE. Even relatively small numerical errors for the contribution of each individual cluster could eventually spoil the convergence of the series when combined according to Eq. (7). In this

context, the Chebyshev polynomial expansion is known to yield very accurate results for a given step size δt. In contrast, we have checked that reaching the same level of accuracy by means of a fourth-order Runge-Kutta scheme requires a significantly smaller δt which, in turn, increases the overall runtime of the simulation.

Since the Chebyshev polynomials are defined on the interval $[-1, 1]$, the spectrum of the original Hamiltonian $\mathcal{H}$ has to be rescaled [85],

$$\widetilde{\mathcal{H}} = \frac{\mathcal{H} - b}{a} \ , \tag{13}$$

where a and b are suitably chosen parameters. In practice, we use the fact that the (absolute of the) extremal eigenvalue of $\mathcal{H}$ can be bounded from above according to [83]

$$\max(|E_{\min}|, |E_{\max}|) \leq J \left(N_{\langle \ell, m \rangle} + gL \right) = \mathcal{E} \ , \tag{14}$$

where $E_{\max}$ ($E_{\min}$) is the largest (smallest) eigenvalue of $\mathcal{H}$, and $N_{\langle \ell, m \rangle}$ denotes the number of nearest-neighbor pairs $\langle \ell, m \rangle$, i.e., the number of bonds of the lattice. By choosing $a \geq \mathcal{E}$, it is guaranteed that the spectrum of $\widetilde{\mathcal{H}}$ lies within $[-1, 1]$. As a consequence, we can set $b = 0$. Note that while this choice of a and b is not necessarily optimal, it proves to be sufficient [83] (see also Appendix B).

Within the Chebyshev-polynomial formalism, the time evolution of a state $|\psi(t)\rangle$ can then be approximated as an expansion up to order M [85],

$$|\psi(t + \delta t)\rangle \approx c_0 |v_0\rangle + \sum_{k=1}^{M} 2c_k |v_k\rangle \ , \tag{15}$$

where the expansion coefficients $c_0, c_1, \ldots, c_M$, are given by

$$c_k = (-i)^k \mathcal{J}_k(a\delta t) \ , \tag{16}$$

with $\mathcal{J}_k(a\delta t)$ being the k-th order Bessel function of the first kind evaluated at $a\delta t$. [Note that the notation in Eqs. (15) and (16) assumes $b = 0$.] Moreover, the vectors $|v_k\rangle$ are recursively generated according to

$$|v_{k+1}\rangle = 2\widetilde{\mathcal{H}} |v_k\rangle - |v_{k-1}\rangle \ , \qquad k \geq 1 \ , \tag{17}$$

with $|v_1\rangle = \widetilde{\mathcal{H}} |v_0\rangle$ and $|v_0\rangle = |\psi(t)\rangle$. Given a time step δt (and the parameter a), the expansion order M has to be chosen large enough to ensure negligible numerical errors. In this paper, we typically have $\delta t J = 0.02$ and $M = 15$, which turns out to yield very accurate results (see Appendix B).

As becomes apparent from Eqs. (15) and (17), the time evolution of the pure state $|\psi(t)\rangle$ requires the evaluation of matrix-vector products. Since $\widetilde{\mathcal{H}}$ is a sparse matrix, these matrix-vector multiplications can be implemented comparatively time and memory efficient. In particular,

we here calculate the matrix elements of $\widetilde{\mathcal{H}}$ *on the fly* and use parallelization to reduce the runtime. Thus, the memory requirements are essentially given by the size of the state $|\psi(t)\rangle$ and the auxiliary states $|v_{k-1}\rangle$, $|v_k\rangle$, and $|v_{k+1}\rangle$. As a consequence, it is possible to treat system (or cluster) sizes significantly larger compared to full ED (here up to 28 lattice sites with a Hilbert-space dimension of $d \approx 10^8$). Since the transverse-field Ising model (1) does not conserve the total magnetizations X or Z, the corresponding quantum numbers cannot be used to block-diagonalize $\mathcal{H}$. Moreover, the clusters entering the NLCE are defined with open boundary conditions such that translational invariance cannot be exploited. Let us note that the clusters do have a reflection (parity) symmetry, which in principle can be used to reduce the memory requirements (though the reduction is less strong compared to the other symmetries mentioned before). In this paper, however, we do not exploit the reflection symmetry and always work in the full Hilbert space with dimension $d = 2^L$.

IV.   RESULTS

We now present our numerical results for the quench dynamics of $\langle X(t) \rangle$ and $\langle Z(t) \rangle$ in chains, ladders, and two-dimensional lattices. Our main focus is to analyze the convergence properties of the NLCE by comparing to direct simulations of finite systems with periodic boundary conditions (for open boundary conditions, see Appendix C) and to existing data from the literature.

A.   Chains

The transverse-field Ising chain is a paradigmatic example of an exactly solvable model and analytical solutions have been known for a long time [60, 86–88] (see also Appendix A). Since quantum quenches in the Ising chain have been studied extensively before (see, e.g., Refs. [89–96]), the present section should be mainly understood as a consistency check for our numerical methods and a preparation for the study of ladders and two-dimensional lattices in Secs. IV B and IV C. (It might be fair to say, however, that explicit visualizations of the analytical solutions, e.g., for the full time-dependent relaxation process of $\langle X(t) \rangle$ for specific initial states and transverse fields g, are less often available in the literature.)

In Figs. 2 (a)-(c), the dynamics of the transverse magnetization $\langle X(t) \rangle$ is shown for quenches starting from the initial state $|\psi(0)\rangle = |\!\uparrow\rangle$ and different values of the transverse field $g = 0.5, 1, 2$. (Recall that the quantum critical point is $g = 1$ for the chain geometry.) Numerical data obtained by NLCE for expansion orders $C = 24, 25$ are compared to (i) a simulation for a finite chain with $L_x = 25$ and PBC, and (ii) the exact, analytically known result [see Eq. (A3) in Appendix A]. Note that we here choose to compare to systems with PBC, since finite-size
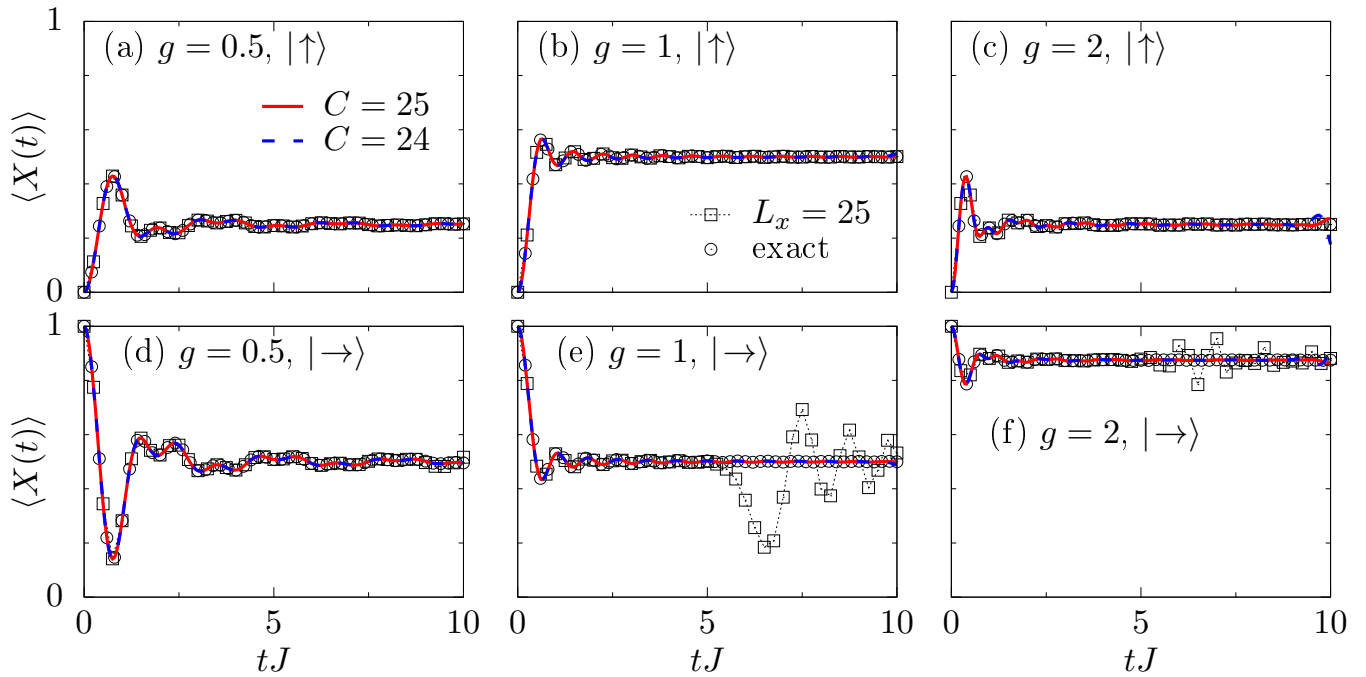
Figure 2. Dynamics of the transverse magnetization $\langle X(t) \rangle$ resulting from the initial state $|\psi(0)\rangle = |\uparrow\rangle$ [(a) - (c)], or $|\psi(0)\rangle = |\rightarrow\rangle$ [(d) - (f)], for chains with transverse fields $g = 0.5, 1, 2$. Numerical data obtained by NLCE for expansion orders $C = 24, 25$ (blue and red curves) are compared to direct simulations for chains with $L_x = 25$ and PBC (open boxes), as well as to the exact, analytically known result [86–88] given in Eq. (A3) (open circles). In panel (b), we exemplarily show additional NLCE data for lower expansion orders $C = 10, 12, \ldots, 20$.

effects are typically weaker in this case. For an additional comparison of NLCE results (also with lower expansion orders) to direct simulations of systems with OBC, see Appendix C.

Starting from its initial value $\langle X(0) \rangle = 0$, we find that the transverse magnetization $\langle X(t) \rangle$ in Figs. 2 (a)-(c) quickly increases and exhibits a peak at short times, before equilibrating towards a constant long-time value. This stationary value is reached already for times $tJ \approx 2$. While this overall behavior of $\langle X(t) \rangle$ is very similar for all values of g considered, the long-time value $\langle X(t \to \infty) \rangle$ is found to vary with g. In particular, it is known that this long-time value can be described in terms of a suitable GGE [28].

Generally, we find that the NLCE results in Figs. 2 (a)-(c) are well converged on the time scales depicted, i.e., the curves for expansion orders $C = 24$ and $C = 25$ agree convincingly with each other. To visualize the convergence properties of the NLCE further, Fig. 2 (b) shows additional NLCE data for lower expansion orders $C = 10, 12, \ldots, 20$. Apparently, the convergence time of the expansion gradually increases with increasing C. Furthermore, we find that the curves for the finite chain with $L_x = 25$ also nicely coincide with the NLCE data for $L \to \infty$, i.e., finite-site effects appear to be less relevant in these cases. Importantly, our numerical results for $\langle X(t) \rangle$ agree perfectly with the analytical solution.

Next, in Figs. 2 (d)-(f), we consider quenches starting

from the state $|\psi(0)\rangle = |\rightarrow\rangle$. Despite the obvious difference that $\langle X(t) \rangle$ now starts at a maximum, $\langle X(0) \rangle = 1$, the general picture is very similar compared to the previous case of $|\psi(0)\rangle = |\uparrow\rangle$. Namely, $\langle X(t) \rangle$ exhibits a rapid decay and equilibrates rather quickly towards its long-time value. Especially for $g = 1$ [Fig. 2 (e)], however, we now observe pronounced finite-size effects, i.e., the curve for $L_x = 25$ deviates from the analytical solution for times $tJ \gtrsim 5$ and exhibits oscillations. In contrast, the NLCE results for $C = 24, 25$ remain converged up to at least $tJ = 10$. This is a remarkable result since the largest cluster in the NLCE also only has 25 lattice sites, i.e., the computational complexities of the NLCE and the simulation of the finite system are essentially the same.

Depending on the details of the quench, we thus find that performing a NLCE can yield a numerical advantage over the direct simulation of finite systems, see also Appendix C. On the one hand, if finite-size effects are weak, the results for finite chains can be very similar to the actual $L \to \infty$ dynamics (and also remain meaningful on longer time scales where the NLCE breaks down). On the other hand, the presence of strong finite-size effects [e.g. at the quantum critical point, cf. Fig. 2 (e)] appears to favor the usage of NLCEs which yield the dynamics directly in the thermodynamic limit. This is a first result of the present paper. As will be discussed in more detail in the upcoming sections, a similar parameter-dependent advantage (or disadvantage) of performing a NLCE oc-

curs for ladder geometries and two-dimensional lattices as well.

B.   Ladders

Let us now turn to the results for two- and three-leg ladders, which can be seen as intermediate cases between the chain geometry (cf. Sec. IV A) and the two-dimensional square lattice (cf. Sec. IV C). Since exact solutions for the dynamics of ladders are absent, we cannot compare our numerical data to analytical results. (For additional remarks on the transition from integrability to nonintegrability, see also Appendix D.)

In Fig. 3, we consider quenches starting from the state $|\psi(0)\rangle = |\uparrow\rangle$ in two-leg ladders with different transverse fields g. Here, the data is obtained by NLCE for expansion orders $C = 24$ and $C = 26$, i.e., the largest clusters involved are of size 12×2 or 13×2. As shown in Fig. 3 (a), the dynamics of the longitudinal magnetization $\langle Z(t) \rangle$ displays a strong dependence on the value of g. On the one hand, for $g = 2$, $\langle Z(t) \rangle$ rapidly decays, exhibits a minimum at $tJ \approx 1$, and equilibrates to zero for $tJ \gtrsim 3$. On the other hand, for $g = 1$, the decay of $\langle Z(t) \rangle$ towards zero is distinctly slower and much more monotonous. Moreover, for $g = 0.5$ (i.e. a quench within the same equilibrium phase), the decay of $\langle Z(t) \rangle$ is almost indiscernible on the time scale shown, and we additionally observe that $\langle Z(t) \rangle$ exhibits small oscillations for this value of g. The corresponding dynamics of the transverse magnetization $\langle X(t) \rangle$ is shown in Fig. 3 (b). While $\langle X(t) \rangle$ quickly equilibrates towards a stationary value for $g = 2$, $\langle X(t) \rangle$ displays oscillations for $g = 0.5, 1$ which, especially in the case of $g = 0.5$, do not equilibrate on the time scale shown here.

Let us comment on the convergence properties of the NLCE data in Fig. 3. Both for $\langle Z(t) \rangle$ and $\langle X(t) \rangle$, we observe that the NLCE remains converged for longer times if the value of g is smaller. Specifically, we find that the series breaks down at $tJ \approx 4$ for $g = 2$, at $tJ \approx 8$ for $g = 1$, while no breakdown can be seen for $g = 0.5$. Comparing these NLCE data to direct simulations of ladders with periodic boundary conditions and $L_x = 12$, a good agreement is found on short to intermediate time scales (or even longer for $g = 0.5$). In particular, the simulation for the finite ladder turns out to be advantageous for a strong transverse field $g = 2$, since it captures the stationary value of $\langle Z(t) \rangle$ and $\langle X(t) \rangle$ for a longer time than the NLCE. Similar to our previous results for chains, however, it becomes clear from Fig. 3 (a) that the usage of NLCEs is in turn beneficial for $g = 1$, where finite-size effect appear to be stronger and the NLCE captures the monotonous decay of $\langle Z(t) \rangle$ up to longer times compared to the finite-system data.

To proceed, Fig. 4 shows results for quantum quenches starting from the initial state $|\psi(0)\rangle = |\rightarrow\rangle$, with data for two-leg ladders in Fig. 4 (a) and data for three-leg ladders in Fig. 4 (b). Since $\langle Z(t) \rangle = 0$ due to the spin-flip sym-

metry of $\mathcal{H}$, we only have to consider $\langle X(t) \rangle$ in this case. We find that $\langle X(t) \rangle$ generally behaves very similar for the two different ladder geometries. Specifically, $\langle X(t) \rangle$ rapidly decays towards an (approximately constant) stationary value which is naturally higher for a higher value of g. Note however, that for $L_y = 2$ and $g = 0.5$, as well as for $L_y = 3$ and $g = 2$, $\langle X(t) \rangle$ still exhibits some residual fluctuations, i.e., perfect equilibration is absent. Concerning the convergence properties of the NLCE, we find that analogous to the previous case of $|\psi(0)\rangle = |\uparrow\rangle$ (cf. Fig. 3), the NLCE remains converged significantly longer for $g = 0.5$ compared to $g = 2$. Especially the early breakdown of convergence for $L_y = 3$ and $g = 2$ in Fig. 4 (b) emphasizes the fact that NLCEs are not necessarily the method of choice if one aims to study thermalization which typically requires the analysis of long time scales. (There exist, however, also examples where NLCEs yield converged results even in the infinite-time limit, i.e., converged results for the so-called diagonal ensemble [70].) Eventually, let us note that the NLCE results and the data for systems with PBC in Fig. 4 yield a considerably longer convergence compared to analogous simulations for systems with OBC, see Appendix C for details.

As a side remark to conclude the study of ladder geometries, let us note that Ref. [97] has recently discussed the possibility of quantum scars in transverse-field Ising ladders. Specifically, Ref. [97] has considered small values of g and "density-wave" initial states of the form $|\psi(0)\rangle \sim |\uparrow\downarrow\uparrow\downarrow \cdots\rangle$. These initial states were found to exhibit a large overlap with rare, weakly entangled eigenstates, leading to quasi-periodic revivals in the dynamics. As detailed in Appendix D, the fully polarized states $|\uparrow\rangle$ and $|\rightarrow\rangle$ studied in the present paper, in contrast, do not exhibit such a significant overlap with the weakly entangled eigenstates. These special eigenstates therefore do not play a distinguished role for the quench dynamics presented in Figs. 3 and 4.

C.   Two-dimensional square lattice

We now come to the last part of this paper, i.e., the quantum quench dynamics in the two-dimensional transverse-field Ising model. Note that dynamical properties of this model [50, 52, 56, 58, 98, 99], as well as the emergence of thermalization [24, 25, 61], have been studied before by a variety of approaches. By comparing our results to existing data from the literature, let us demonstrate in this section that numerical linked cluster expansions based on rectangular clusters only, combined with an efficient forward propagation of pure states, provide a competitive alternative to other state-of-the-art numerical approaches.

As a first step, it is instructive to compare our results to earlier NLCE data from Ref. [72]. This comparison is shown in Figs. 5 (a) and (b), where the dynamics of the transverse magnetization $\langle X(t) \rangle$ is studied for quenches from $|\rightarrow\rangle$ and $|\uparrow\rangle$ with $g = 1$. (Recall that $g_c \approx 3.044$
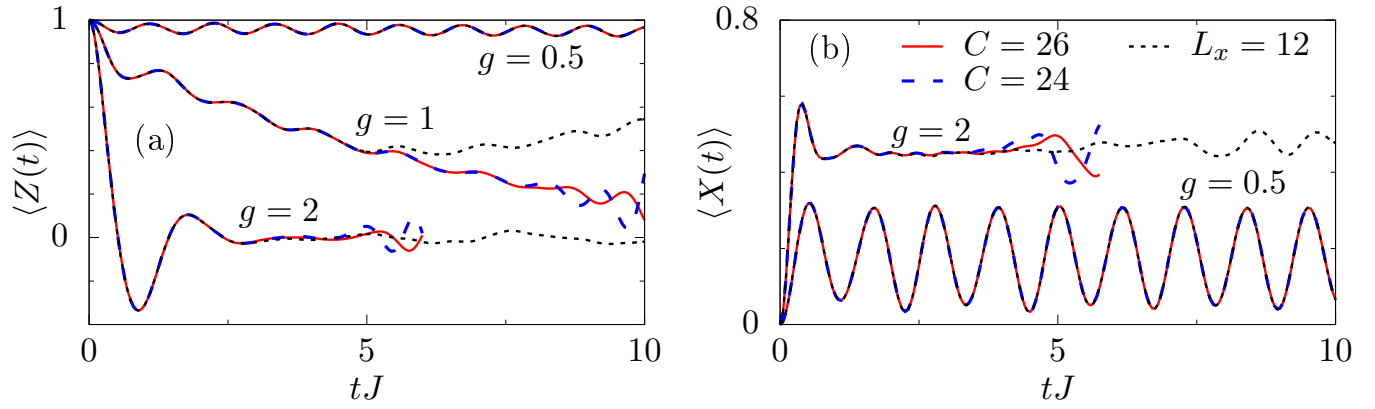
Figure 3. Dynamics of the (a) longitudinal magnetization $\langle Z(t) \rangle$ and (b) transverse magnetization $\langle X(t) \rangle$, in two-leg ladders with initial state $|\psi(0)\rangle = |\uparrow\rangle$ and different transverse fields g. Numerical data obtained by NLCE for expansion orders $C = 24, 26$ are compared to direct simulations for ladders with $L_x = 12$ and PBC.
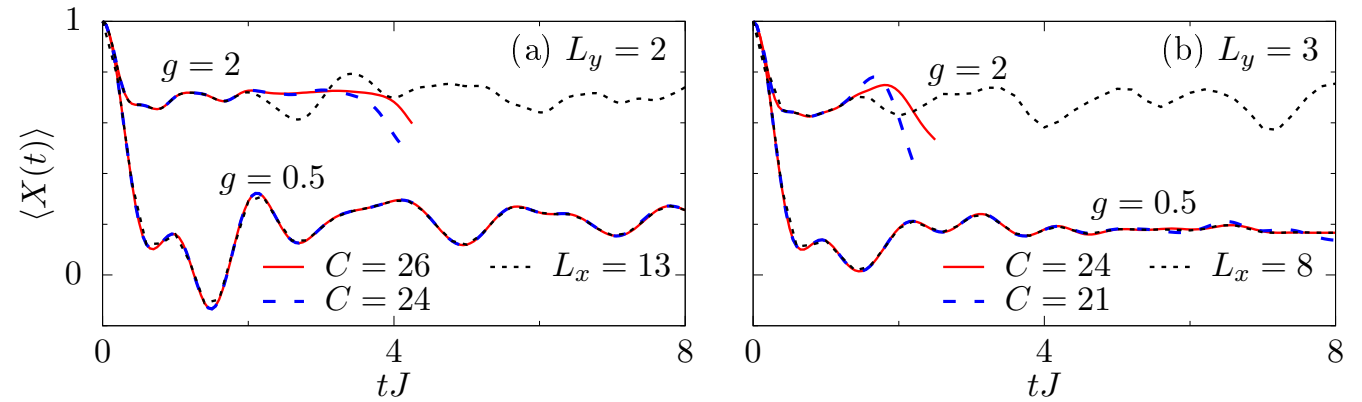

Figure 4. Dynamics of the transverse magnetization $\langle X(t) \rangle$ resulting from the initial state $|\psi(0)\rangle = |\rightarrow\rangle$ for (a) two-leg ladders and (b) three-leg ladders with $g = 0.5$ and $g = 2$. Numerical data obtained by NLCE for different expansion orders C are compared to direct simulations of finite ladders with PBC. For additional NLCE data with lower expansion orders and a comparison to direct simulations of systems with OBC, see Appendix C.
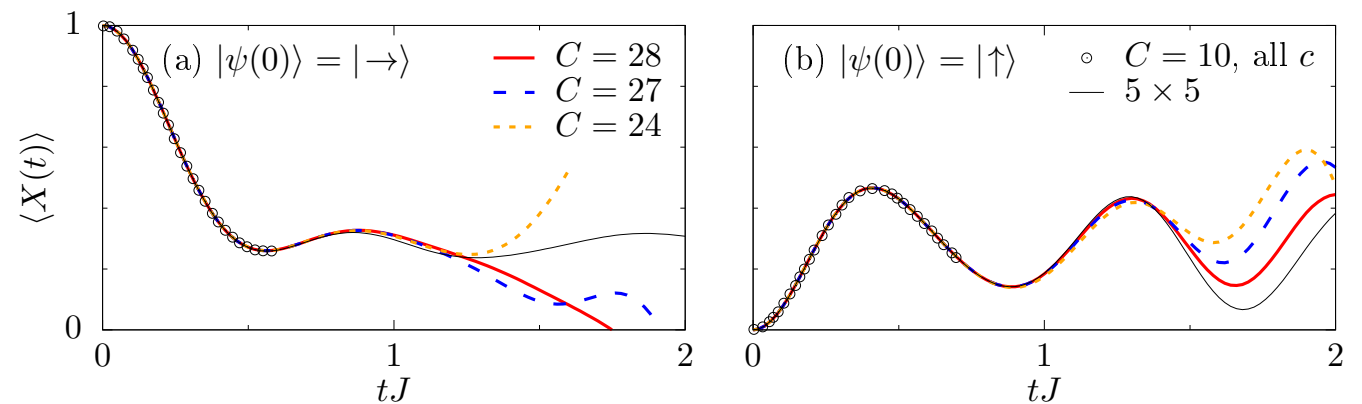
Figure 5. Dynamics of the transverse magnetization $\langle X(t) \rangle$ for a two-dimensional square lattice with transverse field $g = 1$, obtained by NLCE with rectangular clusters and expansion orders $C = 24, 27, 28$. The open circles are NLCE data digitized from Ref. [72], where all (also nonrectangular) cluster geometries with up to 10 lattice sites have been considered. In addition, we present data from a rectangle expansion up to $C = 10$ which, in comparison, converges to slightly shorter times than the full expansion. The dynamics for a 5×5 lattice with PBC is shown as well. The initial state is chosen as (a) $|\psi(0)\rangle = |\rightarrow\rangle$ and (b) $|\psi(0)\rangle = |\uparrow\rangle$.

for the two-dimensional lattice.) Importantly, Ref. [72] has considered all (also nonrectangular) cluster geometries in the expansion and has used full ED to evaluate the respective weights. Due to the computational bottlenecks of NLCEs discussed in Sec. III A, Ref. [72] was consequently limited to rather small clusters with up to 10 lattice sites. In Fig. 5, we find that our NLCE with solely rectangular clusters nicely reproduces the data from Ref. [72]. In particular, while the results of Ref. [72] are converged for times $tJ < 1$, the rectangular NLCE up to expansion order $C = 28$ (i.e. the largest clusters are of size 7×4, 14×2, 28×1) yields converged results on time scales which are approximately twice as long. This demonstration, that a NLCE restricted to rectangular cluster geometries can be better than a NLCE comprising all (possibly nonrectangular) clusters, is an important result of the present paper.

Let us add some comments on the convergence properties of the NLCE in Fig. 5. First, as an additional comparison between the rectangle expansion and the full expansion from Ref. [72], Figs. 5 (a) and (b) also show data obtained by the rectangle expansion with the lower expansion order $C = 10$. For this value of C, we find that the rectangle expansion is converged to slightly shorter times than the data from Ref. [72]. This is expected since, for a fixed value of C, the full expansion should always perform equally well or better compared to any restricted NLCE. However, let us stress once again the crucial advantage of the rectangle expansion that higher expansion orders can be included due to the reduced combinatorial costs. Secondly, we note that given the NLCE results up to expansion order $C = 28$ in Figs. 5 (a) and (b), the short-time dynamics for this value of the transverse field can apparently be accessed also by the direct simulation of a 5×5 lattice with PBC. This is similar to our previous findings for chains and ladders in Secs. IV A and IV B. Namely, depending on the parameter regime, NLCEs might not necessarily outperform a direct simulation of a finite system with PBC if the latter yields small finite-size effects. As shown in Appendix C, however, the advantage of the NLCE is more pronounced when one compares to direct simulations of systems with OBC instead.

Next, let us study quenches starting from the state $|\psi(0)\rangle = |\uparrow\rangle$ such that $\langle Z(0)\rangle = 1$ and $\langle X(0)\rangle = 0$, and consider a strong transverse field $g = 2.63g_c \approx 8$, i.e., a quench across the quantum critical point. Again, we consider clusters with up to 28 lattice sites in the NLCE. In Fig. 6 (a), we find that $\langle Z(t)\rangle$ displays pronounced oscillations with an amplitude that is weakly damped over time. Correspondingly, the transverse magnetization $\langle X(t)\rangle$ in Fig. 6 (b) exhibits damped oscillations as well (with a frequency that is twice as large). It is instructive to compare these NLCE data for the thermodynamic limit to a simulation of a 5×5 lattice with PBC. Specifically, one observes that for such a finite system and times $tJ \gtrsim 1$, the oscillations of $\langle Z(t)\rangle$ and $\langle X(t)\rangle$ die away rather quickly. This is in contrast to the NLCE

results for $L \to \infty$ which capture the persistent oscillations on a longer time scale. In addition, we compare our NLCE results for $\langle Z(t)\rangle$ in Fig. 6 (a) to recent data digitized from Ref. [56], which are computed by an artificial neural-network (ANN) approach for a 8×8 lattice. While the NLCE and ANN data agree nicely with each other for times $tJ < 1$, the NLCE remains converged also on longer time scales. In particular, the ANN data from Ref. [56] up to times $tJ \lesssim 1$ can be reproduced even by the smaller 5×5 lattice. Thus, for the parameter regime considered in Fig. 6, it appears that the NLCE can be better than the direct simulation of finite systems with PBC as well as the ANN approach from Ref. [56]. This is another important result of the present paper.

Finally, we also consider quenches starting from the state $|\psi(0)\rangle = |\rightarrow\rangle$. The values of the transverse field are chosen as $g = 0.1g_c, 1g_c, 2g_c$, which again allows us to compare to ANN data from Ref. [56], as well as to data from Ref. [52] based on infinite projected entangled pair states (iPEPS). For all values of g shown in Figs. 7 (a)-(c), we find a convincing agreement between the data from Refs. [52, 56] and our NLCE results up to expansion order $C = 28$, with convergence times that are rather similar for all three methods. In order to put the convergence times into perspective, it is again helpful to compare the NLCE data to a simulation of a finite 5×5 lattice with PBC. While finite-size effects appear to be less important for $g = 0.1g_c$ and $g = 2g_c$, we observe pronounced finite-size effects for $g = g_c$ already at short times $tJ \approx 0.5$ due to, e.g., the divergence of the relevant length scales at the quantum critical point. Importantly, the NLCE results for $g = g_c$ in Fig. 7 (b) remain converged up to times $tJ \approx 1.5$. One explanation for the advantage of NLCEs at the quantum critical point might be given by the fact that the expansion involves a variety of clusters with different ratios of width and height such that one can capture the dynamics on longer time and length scales. This is another central result of this paper. In this context, let us add that the inclusion of rectangles with different length ratios appears to be crucial to achieve a good convergence. For instance, we have checked that an expansion using solely square-shaped clusters ($1 \times 1, 2 \times 2, \ldots, 5 \times 5$) performs very poorly instead (not shown here).

V. CONCLUSION

To summarize, we have studied the nonequilibrium dynamics of the transverse and the longitudinal magnetization resulting from quantum quenches with fully polarized initial states in the transverse-field Ising model defined on different lattice geometries. To this end, we have relied on an efficient combination of numerical linked cluster expansions and a forward propagation of pure states via Chebyshev polynomials.

Depending on the geometry and the parameter regime under consideration, the quench dynamics has been
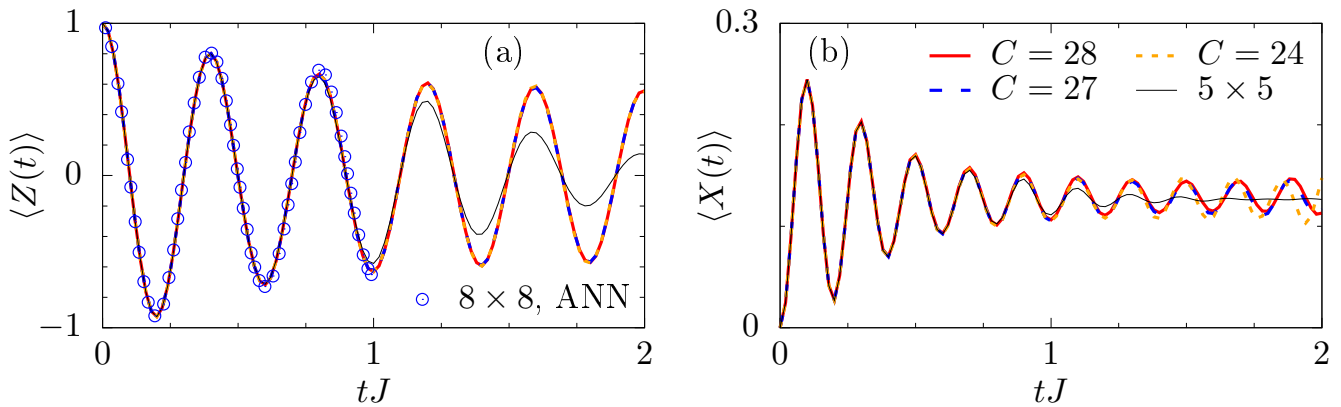
Figure 6. Dynamics of the (a) longitudinal magnetization $\langle Z(t) \rangle$ and (b) transverse magnetization $\langle X(t) \rangle$, resulting from the initial state $|\psi(0)\rangle = |\uparrow\rangle$ for a two-dimensional square lattice with $g = 2.63 g_c$. Data obtained by NLCE for expansion orders $C = 24, 27, 28$ are compared to a simulation of a 5×5 lattice with PBC. In (a), we additionally show digitized ANN data from Ref. [56] for a 8×8 lattice.
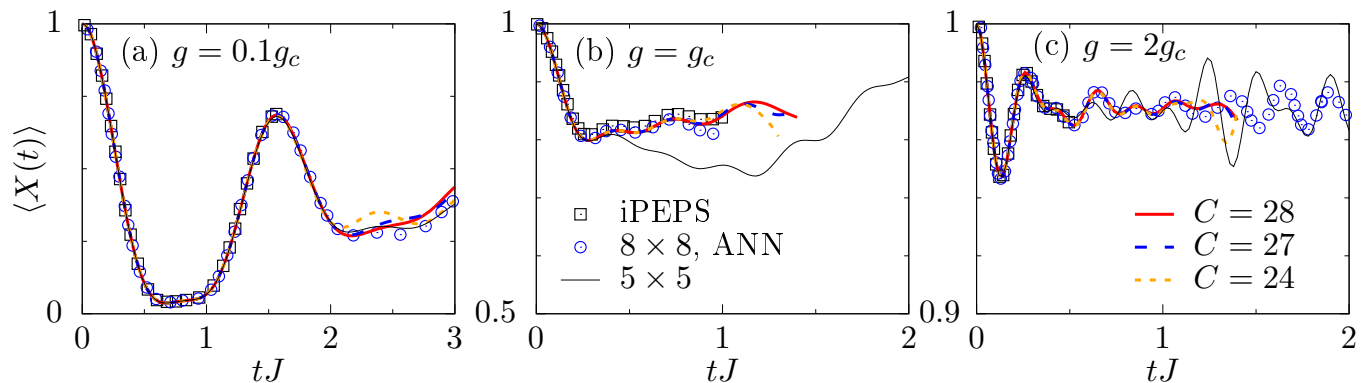

Figure 7. Dynamics of the transverse magnetization $\langle X(t) \rangle$ for two-dimensional lattices with initial state $|\psi(0)\rangle = |\rightarrow\rangle$ and transverse fields (a) $g = 0.1 g_c$, (b) $g = 1 g_c$, and (c) $g = 2 g_c$. Data obtained by NLCE for expansion orders $C = 24, 27, 28$ are compared to the simulation of a 5×5 lattice with PBC. Additionally, we show iPEPS data digitized from Ref. [52] and ANN data for a 10×10 lattice digitized from Ref. [56].

found to display a variety of different behaviors ranging from quick equilibration, over slower monotonous relaxation, to persistent (weakly damped) oscillations. As a main result, we have demonstrated that NLCEs comprising solely rectangular clusters provide a promising approach to study the dynamics of two-dimensional quantum many-body systems directly in the thermodynamic limit. While the organization of the NLCE becomes straightforward due to the simple cluster geometry, the memory efficient pure-state propagation made it possible to include clusters with up to 28 lattice sites. Especially, for quenches to the quantum critical point, where finite-size effects are typically strong, we have shown that NLCEs can yield converged results on time scales which compare favorably to direct simulations of finite systems with periodic boundary conditions (also in the case of chains or ladders). By comparing to existing data from the literature, we have demonstrated that the reachable time scales are also competitive to other state-of-the-art numerical methods. While NLCEs with rectangu-

lar clusters have been used before to obtain thermodynamic quantities [100] or entanglement entropies [68], the present paper unveils that such NLCEs also provide a powerful tool to study the real-time dynamics of quantum many-body systems.

A natural direction of future research is to further explore the capabilities of NLCEs to simulate quantum quench dynamics of two-dimensional systems in the thermodynamic limit. In this context, it might be promising to consider other building blocks for the expansion such as, e.g., clusters that consist of multiple corner-sharing 2×2 squares [66]. Moreover, it will be interesting to study other two-dimensional lattice geometries such as triangular or Kagome lattices with nonrectangular cluster shapes. One particular question in the field of quantum many-body dynamics where NLCEs might be able to contribute is the existence of many-body localization in higher dimensions. While the usage of NLCEs in disordered systems involves additional complications beyond our explanations in Sec. III A, NLCEs can yield results

directly in the thermodynamic limit which is especially important close to the potential transition between the thermal and the MBL regime. Although truly long times might still remain out of reach, the usage of supercomputing will be helpful to include higher expansion orders (up to $C \approx 40$ [76]), which improves the convergence of the NLCE even further.

Note added: After this paper was submitted, we became aware of the related work [101] which appeared in the same arXiv posting as our manuscript. While Ref. [101] also presents NLCE calculations for the dynamics of two-dimensional systems using an expansion in rectangles, its focus is on the application of NLCEs to disordered systems and inhomogeneous initial states. In addition, while Ref. [101] employs full ED to evaluate the contributions of the clusters, the present paper highlights the usefulness of efficient pure-state propagation methods to reach expansion orders beyond the range of full ED and to extend the convergence times of the NLCE.

Appendix A: Exact solution for the integrable chain

In the case of a chain geometry, the transverse-field Ising model (1) is a paradigmatic example of an integrable model and can be diagonalized by means of subsequent Jordan-Wigner, Fourier, and Bogoliubov transforms [60],

$$\mathcal{H} = \sum_k E_k \eta_k^\dagger \eta_k + \text{const.} , \qquad (A1)$$

$$E_k = 2J\sqrt{(g - \cos k)^2 + \sin^2 k} . \qquad (A2)$$

Since quantum quenches in the transverse-field Ising chain have been studied extensively before, and since the focus of this paper is on the numerical analysis of nonintegrable geometries, we here refrain from providing more details and refer to the large body of existing literature instead [89–96]. Given the notation of $\mathcal{H}$ in Eqs. (1) and (A1), as well as an initial state $|\psi(0)\rangle$ which is chosen as the groundstate of $\mathcal{H}$ for some transverse field g', the dynamics of the transverse magnetization $\langle X(t) \rangle$ for a quench $g' \to g$ is then given by [86–88, 90],

$$\langle X(t) \rangle = 2 \int_0^\pi \frac{dk}{2\pi} \frac{1}{E_k^2 E_k'} \qquad (A3)$$
$$\times \left[\epsilon_k(\epsilon_k \epsilon_k' + \gamma_k^2) + \gamma_k^2(\epsilon_k' - \epsilon_k)\cos(2E_k t) \right] ,$$

where we have used the abbreviations

$$\epsilon_k = 2J(g - \cos k) , \quad \gamma_k = 2J\sin k , \qquad (A4)$$

and E_k' and ϵ_k' are defined like their unprimed counterparts, but with $g \to g'$. In order to obtain the results shown in Fig. 2 of the main text, we have numerically evaluated the integral in Eq. (A3) either for $g' = 0$ ($|\psi(0)\rangle = |\uparrow\rangle$) or for $g' \to \infty$ ($|\psi(0)\rangle = |\rightarrow\rangle$).

Appendix B: Accuracy of the pure-state propagation

While we have already demonstrated that our numerical results agree very well with existing data, let us nevertheless discuss the accuracy of the Chebyshev-polynomial expansion which is used to evaluate the time evolution of the pure states $|\uparrow\rangle$ and $|\rightarrow\rangle$. To this end, Fig. 8, shows the dynamics of the transverse magnetization $\langle X(t) \rangle$ for a cluster of size $L_x \times L_y = 7 \times 3$ (with OBC), initial state $|\psi(0)\rangle = |\rightarrow\rangle$, and transverse field $g = g_c \approx 3.044$.

First, in Fig. 8 (a), we set the discrete time step to $\delta t J = 0.02$ and depict results for different expansion orders $M = 5, 10, 15, 20$ (curves). On the one hand, for small $M = 5$, we observe clearly unphysical results (e.g. $\langle X(t) \rangle > 1$), which can also be explained by the fact that the norm $\langle \psi(t)|\psi(t) \rangle$ (symbols) is not conserved over time for this choice of M. On the other hand, for $M = 10, 15, 20$, all curves for $\langle X(t) \rangle$ are perfectly on top of each other, i.e., convergence with respect to M has been reached, and $\langle \psi(t)|\psi(t) \rangle = 1$.

Next, Fig. 8 (b) shows results for a fixed expansion order $M = 15$ and varying time step $\delta t J = 0.01, 0.02, 0.05, 0.1$. We find that $\langle X(t) \rangle$ is practically independent of the time step for the three smallest values of $\delta t J$ used here. However, visible deviations occur in the case of the largest time step $\delta t J = 0.1$. While the required time step δt and expansion order M can certainly depend on the parameter regime under consideration, the typical choice used in the main text, i.e., $\delta t J = 0.02$ and $M = 15$, appears to yield very accurate results.

Appendix C: Additional results for lower expansion orders and systems with open boundary conditions

In Figs. 2 - 7 of the main text, we have compared the convergence of the NLCE to direct simulations of systems with periodic boundary conditions. However, since the clusters entering the NLCE are defined with open boundary conditions, it might be interesting to compare the convergence of the NLCE to direct simulations with OBC as well. Such a comparison is shown in Fig. 9 for the dynamics of the transverse magnetization $\langle X(t) \rangle$ in chains [panel (a)], ladders [panel (b)], and two-dimensional square lattices [panel (c)], with one exemplarily chosen transverse field g in each case. Specifically, the curves shown in Fig. 9 are complementary to
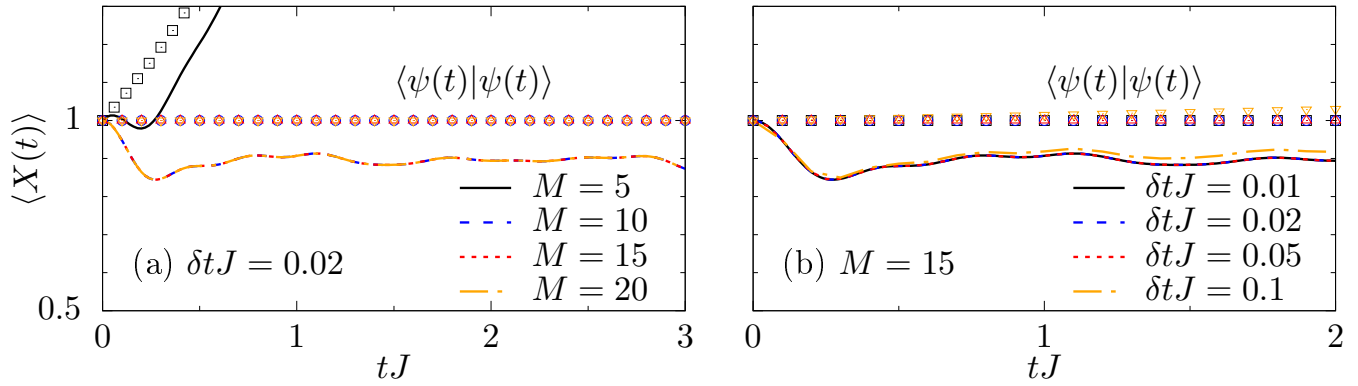
Figure 8. Dynamics of the transverse magnetization $\langle X(t) \rangle$ for a cluster of size $L_x \times L_y = 7 \times 3$ (with OBC), initial state $|\psi(0)\rangle = |\rightarrow\rangle$, and transverse field $g = 3.044$. The symbols indicate the norm $\langle\psi(t)|\psi(t)\rangle$. (a) Fixed time step $\delta t J = 0.02$ and varying expansion order M. (b) Fixed $M = 15$ and varying $\delta t J$.
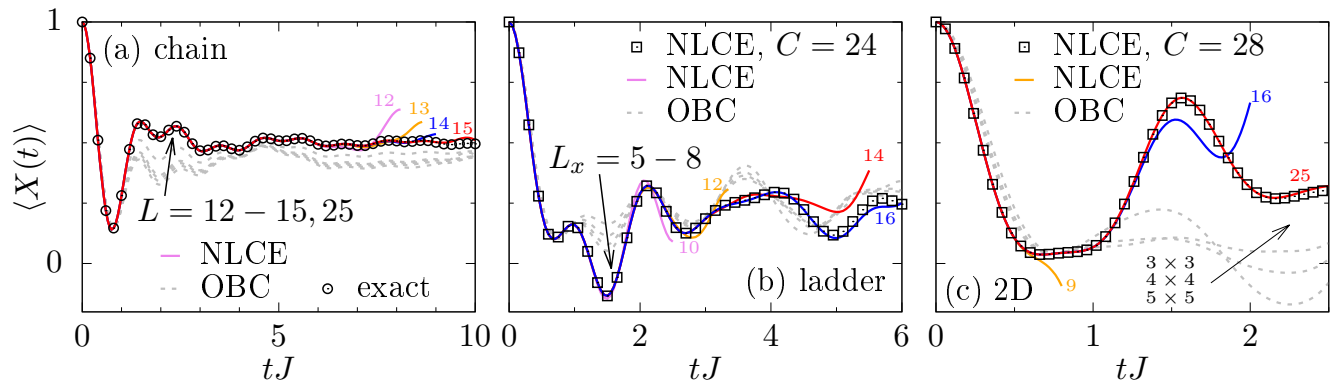

Figure 9. Dynamics of the transverse magnetization $\langle X(t) \rangle$ for quenches in (a) chains with $g = 0.5$, (b) two-leg ladders ($L = L_x \times 2$) with $g = 0.5$, and (c) two-dimensional lattices with $g = 0.1g_c$. The initial state is $|\psi(0)\rangle = |\rightarrow\rangle$. Results obtained by numerical linked cluster expansion for different expansion orders C (solid curves) are compared to direct simulations for systems with open boundary conditions (gray dashed curves). In all cases, we find that for a given expansion order C (or system size L) the NLCE yields converged results for significantly longer times than the corresponding direct simulation with OBC.

our earlier data in Figs. 2 (d), 4 (a), and 7 (a), as we now also include NLCE results for lower expansion orders. Moreover, to guarantee a fair comparison, Fig. 9 always shows curves for matching system sizes and expansion orders, i.e., $L = C$ (recall that the expansion order of the NLCE is defined as the largest cluster size involved in the expansion). Importantly, we find that the NLCE yields converged results on significantly longer time scales than the simulation of the finite system with OBC for all cases shown here. For instance, in the case of the chain [Fig. 9 (a)], expansion order $C = 15$ is already sufficient to yield converged results up to $tJ = 10$, whereas the direct simulation for a system with OBC fails to capture the correct long-time plateau even for the considerably larger system size $L = 25$. Similarly, in the case of the two-leg ladder [Fig. 9 (b)], the curves for finite systems with OBC converge only up to the rather short time $tJ \approx 1$, while the convergence of the NLCE quickly improves with increasing C. Especially for the two-dimensional case [Fig.

9 (c)], the simulations for the finite system with OBC even fail to describe the initial decay of $\langle X(t) \rangle$ correctly. Thus, we conclude that for a given expansion order C (or system size L) the NLCE performs considerably better than the corresponding direct simulation with OBC.

Appendix D: Eigenstate entanglement and spectral decomposition of initial states

Let us discuss some properties of the fully polarized initial states $|\uparrow\rangle$ and $|\rightarrow\rangle$. To this end, we first study the entanglement (von Neumann) entropy $S_{|n\rangle}$ of the eigenstates $|n\rangle$ of $\mathcal{H}$,

$$S_{|n\rangle} = -\text{Tr}[\rho_A \ln \rho_A] , \quad \rho_A = \text{Tr}_B \{|n\rangle\langle n|\} , \quad (D1)$$

where ρ_A is the reduced density matrix on a subsystem A, obtained by tracing over the degrees of freedom in the
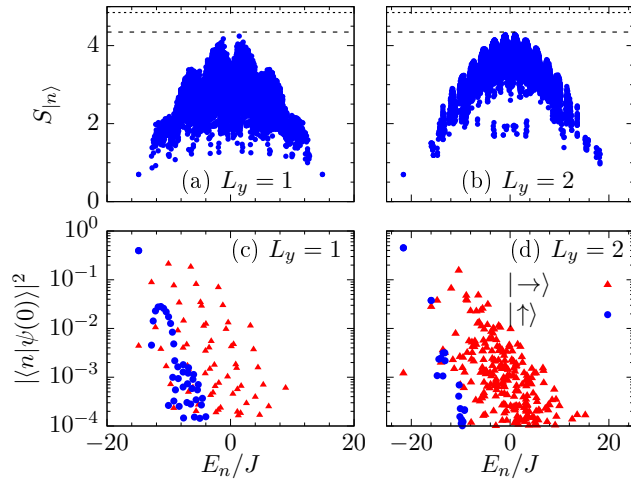
Figure 10. (a) and (b) Eigenstate entanglement entropy $S_{|n\rangle}$ of a chain and a two-leg ladder. The dashed line indicates the "Page value" for a random state [105], while the dotted line indicates the maximum entropy possible for the chosen bipartition. (c) and (d) Overlap of initial states $|\uparrow\rangle$ and $|\rightarrow\rangle$ with the eigenstates $|n\rangle$. We have $L = 14$, $g = 0.5$, and PBC in all cases.

complement B. In Figs. 10 (a) and (b), $S_{|n\rangle}$ is shown for a chain and a two-leg ladder respectively, numerically obtained by full exact diagonalization for $L = 14$ sites, transverse field $g = 0.5$, and periodic boundary conditions. In both cases, we have chosen A as one half of the system, i.e., the first 7 lattice sites in case of the chain, or the first three rungs and one site of the fourth rung in case of the ladder. On the one hand, for the integrable chain geometry in Fig. 10 (a), we find that $S_{|n\rangle}$ is comparatively small at the edges (consistent with the area-law entanglement scaling of ground states [102]), while weakly and strongly entangled states coexist in the bulk of the spectrum (see also Refs. [103, 104]). On the other hand, for the two-leg ladder in Fig. 10 (b), the fluctuations of $S_{|n\rangle}$

in the center of the spectrum are clearly smaller, i.e., the eigenstates are typically stronger entangled. This behavior of $S_{|n\rangle}$ can be interpreted as an indication of the transition from integrability to nonintegrability [104], by going from chains to ladders. In addition, we can identify a small number of eigenstates $|n\rangle$ with energy close to $E = 0$ in Fig. 10 (b), which exhibit a distinctly lower value of $S_{|n\rangle}$. This appears to be consistent with the recent proposal of quantum scars in transverse-field Ising ladders in Ref. [97].

Next, it is useful to study $S_{|n\rangle}$ in combination with the overlap between the initial states $|\psi(0)\rangle = |\uparrow\rangle, |\rightarrow\rangle$ and the eigenstates $|n\rangle$,

$$P_{|\psi\rangle} = \sum_{n=1}^{D} |\langle n|\psi(0)\rangle|^2 \delta(E - E_n) , \qquad \text{(D2)}$$

where E_n is the eigenvalue of $\mathcal{H}$ belonging to $|n\rangle$. As shown in Figs. 10 (c) and (d), this spectral distribution is narrow and peaked at the groundstate in the case of $|\uparrow\rangle$, while $P_{|\psi\rangle}$ is much broader for $|\rightarrow\rangle$, both for the chain and the ladder. Thus, a quench to $g = 0.5$ with $|\psi(0)\rangle = |\uparrow\rangle$, results in a dynamics which is strongly dominated by the groundstate with a significantly smaller admixture of excited states. Note that exactly for such a situation, i.e., a quantum many-body system with one macroscopically populated eigenstate, an analytical prediction for the temporal relaxation has been recently obtained in Ref. [106]. While this is beyond the scope of the present manuscript, it appears that quantum quenches in transverse-field Ising chains or ladders can be promising candidates to test such predictions.

Finally, as already pointed out in the main text, we note that the fully polarized initial states $|\uparrow\rangle$ and $|\rightarrow\rangle$ do not exhibit a distinguished overlap with the rare, weakly entangled eigenstates discussed in Fig. 10 (b). These potential quantum scars therefore do not play an essential role for the resulting quench dynamics.

[1] A. Polkovnikov, K. Sengupta, A. Silva, and M. Vengalattore, Rev. Mod. Phys. **83**, 863 (2011).

[2] J. Eisert, M. Friesdorf, and C. Gogolin, Nat. Phys. **11**, 124 (2015).

[3] B. Bertini, F. Heidrich-Meisner, C. Karrasch, T. Prosen, R. Steinigeweg, and M. Žnidarič, Rev. Mod. Phys. **93**, 025003 (2021).

[4] A. Mitra, Annu. Rev. Condens. Matter Phys. **9**, 245 (2018).

[5] J. Dziarmaga, Adv. Phys. **59**, 1063 (2010).

[6] P. Reimann, Nat. Commun. **7**, 10821 (2016).

[7] S. Erne, R. Bücker, T. Gasenzer, J. Berges, and J. Schmiedmayer, Nature **563**, 225 (2018).

[8] M. Prüfer, P. Kunkel, H. Strobel, S. Lannig, D. Linnemann, C.-M. Schmied, J. Berges, T. Gasenzer, and M. K. Oberthaler, Nature **563**, 217 (2018).

[9] J. Richter and R. Steinigeweg, Phys. Rev. E **99**, 012114 (2019).

[10] J. Richter, J. Gemmer, and R. Steinigeweg, Phys. Rev. E **99**, 050104(R) (2019).

[11] M. Dupont and J. E. Moore, Phys. Rev. B **101**, 121106(R) (2020).

[12] L. P. García-Pintos, N. Linden, A. S. L. Malabarba, A. J. Short, and A. Winter, Phys. Rev. X **7**, 031027 (2017).

[13] H. Wilming, T. R. de Oliveira, A. J. Short, and J. Eisert, in *Thermodynamics in the Quantum Regime* (Springer, Cham, 2018) pp. 435–455.

[14] Á. M. Alhambra, J. Riddell, and L. P. García-Pintos, Phys. Rev. Lett. **124**, 110605 (2020).

[15] L. D'Alessio, Y. Kafri, A. Polkovnikov, and M. Rigol, Adv. Phys. **65**, 239 (2016).

[16] F. Borgonovi, F. Izrailev, L. F. Santos, and V. Zelevinsky, Phys. Rep. **626**, 1 (2016).

[17] C. Gogolin and J. Eisert, Rep. Prog. Phys. **79**, 056001 (2016).

[18] J. M. Deutsch, Phys. Rev. A **43**, 2046 (1991).

[19] M. Srednicki, Phys. Rev. E **50**, 888 (1994).

[20] M. Rigol, V. Dunjko, and M. Olshanii, Nature **452**, 854 (2008).

[21] L. F. Santos and M. Rigol, Phys. Rev. E **82**, 031130 (2010).

[22] R. Steinigeweg, J. Herbrych, and P. Prelovšek, Phys. Rev. E **87**, 012118 (2013).

[23] W. Beugeling, R. Moessner, and M. Haque, Phys. Rev. E **89**, 042112 (2014).

[24] R. Mondaini, K. R. Fratus, M. Srednicki, and M. Rigol, Phys. Rev. E **93**, 032104 (2016).

[25] R. Mondaini and M. Rigol, Phys. Rev. E **96**, 012157 (2017).

[26] H. Kim, T. N. Ikeda, and D. A. Huse, Phys. Rev. E **90**, 052105 (2014).

[27] D. Jansen, J. Stolpp, L. Vidmar, and F. Heidrich-Meisner, Phys. Rev. B **99**, 155130 (2019).

[28] F. H. L. Essler and M. Fagotti, J. Stat. Mech. **2016**, 064002 (2016).

[29] E. T. Jaynes, Phys. Rev. **106**, 620 (1957).

[30] M. Rigol, V. Dunjko, V. Yurovsky, and M. Olshanii, Phys. Rev. Lett. **98**, 050405 (2007).

[31] L. Vidmar and M. Rigol, J. Stat. Mech. **2016**, 064007 (2016).

[32] R. M. Nandkishore and D. A. Huse, Annu. Rev. Condens. Matter Phys. **6**, 15 (2015).

[33] D. A. Abanin, E. Altman, I. Bloch, and M. Serbyn, Rev. Mod. Phys. **91**, 021001 (2019).

[34] N. Shiraishi and T. Mori, Phys. Rev. Lett. **119**, 030601 (2017).

[35] C. J. Turner, A. A. Michailidis, D. A. Abanin, M. Serbyn, and Z. Papić, Nat. Phys. **14**, 745 (2018).

[36] M. Schecter and T. Iadecola, Phys. Rev. Lett. **123**, 147201 (2019).

[37] T. Iadecola and M. Žnidarič, Phys. Rev. Lett. **123**, 036403 (2019).

[38] K. Lee, R. Melendrez, A. Pal, and H. J. Changlani, Phys. Rev. B **101**, 241111 (2020).

[39] V. Khemani, M. Hermele, and R. M. Nandkishore, Phys. Rev. B **101**, 174204 (2020).

[40] P. Sala, T. Rakovszky, R. Verresen, M. Knap, and F. Pollmann, Phys. Rev. X **10**, 011047 (2020).

[41] H. Aoki, N. Tsuji, M. Eckstein, M. Kollar, T. Oka, and P. Werner, Rev. Mod. Phys. **86**, 779 (2014).

[42] A. Nauts and R. E. Wyatt, Phys. Rev. Lett. **51**, 2238 (1983).

[43] M. W. Long, P. Prelovšek, S. El Shawish, J. Karadamoglou, and X. Zotos, Phys. Rev. B **68**, 235106 (2003).

[44] T. Heitmann, J. Richter, D. Schubert, and R. Steinigeweg, Z. Naturforsch. A **75**, 421 (2020).

[45] J. Wurtz, A. Polkovnikov, and D. Sels, Ann. Phys. (NY) **395**, 341 (2018).

[46] U. Schollwöck, Ann. Phys. (NY) **326**, 96 (2011).

[47] S. Paeckel, T. Köhler, A. Swoboda, S. R. Manmana, U. Schollwöck, and C. Hubig, Ann. Phys. (NY) **411**, 167998 (2019).

[48] M. P. Zaletel, R. S. K. Mong, C. Karrasch, J. E. Moore, and F. Pollmann, Phys. Rev. B **91**, 165112 (2015).

[49] A. J. A. James and R. M. Konik, Phys. Rev. B **92**, 161111 (2015).

[50] T. Hashizume, I. P. McCulloch, and J. C. Halimeh, arXiv:1811.09275.

[51] C. Hubig and J. I. Cirac, SciPost Phys. **6**, 031 (2019).

[52] P. Czarnik, J. Dziarmaga, and P. Corboz, Phys. Rev. B **99**, 035115 (2019).

[53] B. Kloss, D. Reichman, and Y. Bar Lev, SciPost Phys. **9**, 070 (2020).

[54] G. Carleo and M. Troyer, Science **355**, 602 (2017).

[55] M. Schmitt and M. Heyl, SciPost Phys. **4**, 013 (2018).

[56] M. Schmitt and M. Heyl, Phys. Rev. Lett. **125**, 100503 (2020).

[57] J.-y. Choi, S. Hild, J. Zeiher, P. Schauss, A. Rubio-Abadal, T. Yefsah, V. Khemani, D. A. Huse, I. Bloch, and C. Gross, Science **352**, 1547 (2016).

[58] E. Guardado-Sanchez, P. T. Brown, D. Mitra, T. Devakul, D. A. Huse, P. Schauß, and W. S. Bakr, Phys. Rev. X **8**, 21069 (2018).

[59] V. Lienhard, S. de Léséleuc, D. Barredo, T. Lahaye, A. Browaeys, M. Schuler, L.-P. Henry, and A. M. Läuchli, Phys. Rev. X **8**, 021070 (2018).

[60] P. Pfeuty, Ann. Phys. (NY) **57**, 79 (1970).

[61] B. Blaß and H. Rieger, Sci. Rep. **6**, 38185 (2016).

[62] H. W. J. Blöte and Y. Deng, Phys. Rev. E **66**, 066110 (2002).

[63] M. Rigol, T. Bryant, and R. R. P. Singh, Phys. Rev. Lett. **97**, 187202 (2006).

[64] M. Rigol, T. Bryant, and R. R. P. Singh, Phys. Rev. E **75**, 061118 (2007).

[65] D. Ixert, T. Tischler, and K. P. Schmidt, Phys. Rev. B **92**, 174422 (2015).

[66] K. Bhattaram and E. Khatami, Phys. Rev. E **100**, 013305 (2019).

[67] R. Schäfer, I. Hagymási, R. Moessner, and D. J. Luitz, Phys. Rev. B **102**, 054408 (2020).

[68] A. B. Kallin, K. Hyatt, R. R. P. Singh, and R. G. Melko, Phys. Rev. Lett. **110**, 135702 (2013).

[69] A. Biella, J. Jin, O. Viyuela, C. Ciuti, R. Fazio, and D. Rossini, Phys. Rev. B **97**, 035103 (2018).

[70] M. Rigol, Phys. Rev. Lett. **112**, 170601 (2014).

[71] B. Wouters, J. De Nardis, M. Brockmann, D. Fioretto, M. Rigol, and J.-S. Caux, Phys. Rev. Lett. **113**, 117202 (2014).

[72] I. G. White, B. Sundar, and K. R. A. Hazzard, arXiv:1710.07696.

[73] K. Mallayya and M. Rigol, Phys. Rev. E **95**, 033302 (2017).

[74] K. Mallayya and M. Rigol, Phys. Rev. Lett. **120**, 070603 (2018).

[75] J. Richter and R. Steinigeweg, Phys. Rev. B **99**, 094419 (2019).

[76] J. Richter, F. Jin, L. Knipschild, H. De Raedt, K. Michielsen, J. Gemmer, and R. Steinigeweg, Phys. Rev. E **101**, 062133 (2020).

[77] B. Tang, E. Khatami, and M. Rigol, Comput. Phys. Commun. **184**, 557 (2013).

[78] S. Dusuel, M. Kamfor, K. P. Schmidt, R. Thomale, and J. Vidal, Phys. Rev. B **81**, 064412 (2010).

[79] P. de Vries and H. De Raedt, Phys. Rev. B **47**, 7929 (1993).

[80] T. A. Elsayed and B. V. Fine, Phys. Rev. Lett. **110**, 070404 (2013).

[81] R. Steinigeweg, J. Gemmer, and W. Brenig, Phys. Rev. Lett. **112**, 120601 (2014).

[82] H. Tal-Ezer and R. Kosloff, J. Chem. Phys. **81**, 3967 (1984).

[83] V. V. Dobrovitski and H. A. De Raedt, Phys. Rev. E **67**, 056702 (2003).

[84] A. Weiße, G. Wellein, A. Alvermann, and H. Fehske, Rev. Mod. Phys. **78**, 275 (2006).

[85] H. Fehske, J. Schleede, G. Schubert, G. Wellein, V. S. Filinov, and A. R. Bishop, Phys. Lett. A **373**, 2182 (2009).

[86] E. Barouch, B. M. McCoy, and M. Dresden, Phys. Rev. A **2**, 1075 (1970).

[87] E. Barouch and B. M. McCoy, Phys. Rev. A **3**, 786 (1971).

[88] E. Barouch and B. M. McCoy, Phys. Rev. A **3**, 2137 (1971).

[89] F. Iglói and H. Rieger, Phys. Rev. Lett. **85**, 3233 (2000).

[90] K. Sengupta, S. Powell, and S. Sachdev, Phys. Rev. A **69**, 053616 (2004).

[91] D. Rossini, A. Silva, G. Mussardo, and G. E. Santoro, Phys. Rev. Lett. **102**, 127204 (2009).

[92] F. Iglói and H. Rieger, Phys. Rev. Lett. **106**, 035701 (2011).

[93] L. Foini, L. F. Cugliandolo, and A. Gambassi, Phys. Rev. B **84**, 212404 (2011).

[94] P. Calabrese, F. H. L. Essler, and M. Fagotti, Phys. Rev. Lett. **106**, 227203 (2011).

[95] P. Calabrese, F. H. L. Essler, and M. Fagotti, J. Stat. Mech. **2012**, P07016 (2012).

[96] P. Calabrese, F. H. L. Essler, and M. Fagotti, J. Stat. Mech. **2012**, P07022 (2012).

[97] B. van Voorden, J. Minář, and K. Schoutens, Phys. Rev. B **101**, 220305 (2020).

[98] J. Hafner, B. Blass, and H. Rieger, EPL (Europhys. Lett.) **116**, 60002 (2016).

[99] S. De Nicola, B. Doyon, and M. J. Bhaseen, J. Phys. A **52**, 05LT02 (2019).

[100] B. Bruognolo, Z. Zhu, S. R. White, and E. M. Stoudenmire, arXiv:1705.05578.

[101] J. Gan and K. R. A. Hazzard, Phys. Rev. A **102**, 013318 (2020).

[102] J. Eisert, M. Cramer, and M. B. Plenio, Rev. Mod. Phys. **82**, 277 (2010).

[103] V. Alba, M. Fagotti, and P. Calabrese, J. Stat. Mech. **2009**, P10020 (2009).

[104] W. Beugeling, A. Andreanov, and M. Haque, J. Stat. Mech. **2015**, P02002 (2015).

[105] D. N. Page, Phys. Rev. Lett. **71**, 1291 (1993).

[106] P. Reimann, B. N. Balz, J. Richter, and R. Steinigeweg, Phys. Rev. B **101**, 094302 (2020).

Preprint of Publication [P6]

[P6] Tjark Heitmann, Jonas Richter, Jochen Gemmer, and Robin Steinigeweg,
Nontrivial Damping of Quantum Many-Body Dynamics,
Journal reference: Phys. Rev. E **104**, 054145 (2021)
DOI: 10.1103/PhysRevE.104.054145
Preprint: `arXiv:2103.06646`

Nontrivial Damping of Quantum Many-Body Dynamics

Tjark Heitmann [iD],[1, *] Jonas Richter [iD],[2, †] Jochen Gemmer,[1, ‡] and Robin Steinigeweg [iD][1, §]

[1]*Department of Physics, University of Osnabrück, D-49069 Osnabrück, Germany*
[2]*Department of Physics and Astronomy, University College London, Gower Street, London WC1E 6BT, UK*

Understanding how the dynamics of a given quantum system with many degrees of freedom is altered by the presence of a generic perturbation is a notoriously difficult question. Recent works predict that, in the overwhelming majority of cases, the unperturbed dynamics is just damped by a simple function, e.g., exponentially as expected from Fermi's golden rule. While these predictions rely on random-matrix arguments and typicality, they can only be verified for a specific physical situation by comparing to the actual solution or measurement. Crucially, it also remains unclear how frequent and under which conditions counterexamples to the typical behavior occur. In this work, we discuss this question from the perspective of projection-operator techniques, where exponential damping of a density matrix occurs in the interaction picture but not *necessarily* in the Schrödinger picture. We show that a nontrivial damping in the Schrödinger picture can emerge if the dynamics in the unperturbed system possesses rich features, for instance due to the presence of strong interactions. This suggestion has consequences for the time dependence of correlation functions. We substantiate our theoretical arguments by large-scale numerical simulations of charge transport in the extended Fermi-Hubbard chain, where the nearest-neighbor interactions are treated as a perturbation to the integrable reference system.

I.   INTRODUCTION

Questions of equilibration and thermalization in isolated quantum systems have experienced a renaissance in recent years [1–3]. However, notwithstanding the significant progress that has been made [4], describing the precise dynamics of a given quantum many-body system still remains a very challenging task. "Universal" principles, which provide a faithful understanding of a wide class of models in various nonequilibrium situations, are therefore highly desirable [5–10]. A particularly successful strategy in this context has been the usage of random-matrix ensembles which mimic certain aspects of the full many-body problem [11]. Prominent examples include the eigenstate thermalization hypothesis [12–14], which asserts that the matrix structure of observables becomes essentially random in the eigenbasis of chaotic Hamiltonians [15–18], as well as random-circuit models [19–21], which have led to new insights into the emergence of hydrodynamics and information scrambling in isolated quantum systems.

A particularly intriguing and omnipresent question in physics is how the dynamics of a given quantum system is affected by the presence of a perturbation [12, 22–26], i.e., scenarios where the Hamiltonian $\mathcal{H}$ of the full system can be written as

$$\mathcal{H} = \mathcal{H}_0 + \varepsilon \mathcal{V} , \tag{1}$$

with $\mathcal{H}_0$ being an unperturbed reference system and ε denoting the strength of the perturbation $\mathcal{V}$. This includes,

e.g., the phenomenon of prethermalization [27–32], where $\mathcal{V}$ weakly breaks a conservation law of the (usually integrable) $\mathcal{H}_0$, and also the analysis of imperfect echo protocols [33, 34], where the respective Hamiltonians governing the forward and backward time evolutions are different. In an even broader context, the impact of perturbations also plays an important role for simulations on today's noisy intermediate-scale quantum devices [35], where $\mathcal{V}$ can be interpreted as the inevitable imperfections of elementary gates which alter the desired circuit [36].

Given a quantum system with many degrees of freedom, the impact of a perturbation can clearly be manifold. It is therefore quite remarkable that a series of recent works predict that, in the overwhelming majority of cases, the reference dynamics is just damped by a simple function [24, 25], e.g., exponentially as expected from Fermi's golden rule [26, 37, 38]. In essence, these works rely on random-matrix theory as $\mathcal{V}$ is modeled by (an ensemble of) random matrices with respect to the eigenstates of $\mathcal{H}_0$ [24], as well as on the concept of typicality [39–42], as a given perturbation is shown to behave very similar to the ensemble average. However, while these predictions were found to compare favorably to a variety of experimental and numerical examples [24], it yet remains unclear how frequent and under which conditions counterexamples to the typical behavior occur.

In this work, we discuss exactly this question from the perspective of projection-operator techniques, which are well established in the realm of open quantum systems [43]. In this way, we provide a fresh insight and show that, within these techniques and under mild assumptions, the "standard" case of exponential damping emerges for the density matrix in the interaction picture but not *necessarily* in the Schrödinger picture. We particularly suggest that a nontrivial damping in the Schrödinger picture can emerge if the dynamics in the unperturbed system possesses rich features. This sug-

---

* tjark.heitmann@uos.de
† j.richter@ucl.ac.uk
‡ jgemmer@uos.de
§ rsteinig@uos.de

gestion has consequences for the time dependence of correlation functions. It is substantiated by large-scale numerical simulations of charge transport in the extended Fermi-Hubbard chain, where the nearest-neighbor interactions are treated as a perturbation to the integrable reference system.

This paper is structured as follows. In Sec. II we first establish the setup by introducing an exemplary model and observable, and then turn to a description of our projection-operator approach and its implications on the relaxation dynamics in perturbed many-body quantum systems. We show illustrating numerical results in Sec. III and conclude in Sec. IV.

II.   SETUP AND PROJECTION-OPERATOR APPROACH

A.   Model and observable

Even though our analytical reasoning can be applied to arbitrary operators and Hamiltonians, we here consider for concreteness the dynamics of the particle current in the extended Fermi-Hubbard chain, which constitutes a physically relevant many-body quantum problem (see Refs. [44–46] and references therein). The Hamiltonian of this model reads $\mathcal{H} = \sum_{r=1}^{L} h_r$ and is a sum over L local terms

$$h_r = - t_{\mathrm{h}} \sum_{\sigma=\uparrow,\downarrow} (c_{r,\sigma}^{\dagger} c_{r+1,\sigma} + \mathrm{H.c.}) + U(n_{r,\uparrow} - \tfrac{1}{2})(n_{r,\downarrow} - \tfrac{1}{2})$$
$$+ U' \sum_{\sigma,\sigma'} (n_{r,\sigma} - \tfrac{1}{2})(n_{r+1,\sigma'} - \tfrac{1}{2}) , \quad (2)$$

where we assume periodic boundary conditions, i.e., we have $L+1 \equiv 1$. $c_{r,\sigma}^{\dagger}$ ($c_{r,\sigma}$) creates (annihilates) a fermion with spin σ at lattice site r and $n_{r,\sigma} = c_{r,\sigma}^{\dagger} c_{r,\sigma}$ is the occupation-number operator. t_{h} is the hopping matrix element and $U, U' > 0$ denote the strengths of the repulsive on-site and nearest-neighbor interactions, respectively. While the model is noninteracting for $U, U' = 0$, it in fact remains integrable in terms of the Bethe ansatz also for finite on-site interactions $U > 0$ [47]. In contrast, this integrability is broken for any $U' > 0$. Note that $\mathcal{H}$ preserves the number of each fermion species.

As an observable, we consider the particle current. It can be derived from a continuity equation and takes on the well-known form (see Refs. [44–46] and references therein) $\mathcal{J} = \sum_{r=1}^{L} j_r$,

$$j_r = -t_{\mathrm{h}} \sum_{\sigma=\uparrow,\downarrow} [(i\, c_{r,\sigma}^{\dagger} c_{r+1,\sigma} + \mathrm{H.c.})] . \quad (3)$$

While the particle current does not depend on U and U', its dynamics does. Only in the case $U = U' = 0$, we have $[\mathcal{J}, \mathcal{H}] = 0$. Generally, $\mathrm{tr}[\mathcal{J}] = 0$ and $\mathrm{tr}[\mathcal{J}^2] = DL t_{\mathrm{h}}^2/4$, where $D = 4^L$ is the dimension of the Hilbert space. In this paper, we will be particularly concerned with the

dynamics of current-current correlation functions. However, as already stated above, all that follows now carries over to other choices of observable and Hamiltonian.

B.   Projection-operator approach

To apply projection-operator techniques, we first decompose the full system $\mathcal{H}$ according to Eq. (1) into an unperturbed system $\mathcal{H}_0$ and a perturbation $\varepsilon \mathcal{V}$. For instance, for the Fermi-Hubbard chain (2), we will later consider two different reference systems $\mathcal{H}_0$, i.e., the non-interacting $\mathcal{H}_0 = \mathcal{H}(U = U' = 0)$ and the interacting integrable $\mathcal{H}_0 = \mathcal{H}(U \neq 0, U' = 0)$.

After this decomposition, we then define a projection superoperator $\mathcal{P}$, which projects a density matrix $\rho(t)$ at time t onto a set of relevant degrees of freedom. This set should at least include the identity and the observable of interest,

$$\mathcal{P}\,\rho(t) = \frac{1}{D} + \frac{C(t)}{\langle \mathcal{J}^2 \rangle}\, \mathcal{J} , \quad C(t) = \langle \mathcal{J}\rho(t) \rangle , \quad (4)$$

where $\langle \bullet \rangle = \mathrm{tr}[\bullet]/D$. Due to $\langle \mathcal{J} \rangle = 0$, $\mathcal{P}^2 = \mathcal{P}$. In this work, we are interested in the time-dependent part $C(t)$ of the projected density matrix. It is important to note that, using the projection in Eq. (4), $C(t)$ is not identical in the Schrödinger and interaction picture. Even though $C(t)$ is a coefficient and not an expectation value, it will turn out below that $C(t)$ can be expressed in terms of certain types of correlation functions. Importantly, throughout this paper, the notions of Schrödinger or interaction picture should be understood with respect to the dynamics of the density matrix. This wording should not be confused with the fact that expectation values of observables are the same in both pictures.

While taking into account more degrees of freedom is possible, this will not be necessary for our purposes. In particular, for initial conditions $\rho(0)$ in the span of 1 and $\mathcal{J}$, we further have $\mathcal{P}\rho(0) = \rho(0)$. From now on, we will focus on such kind of initial conditions, which also appear in the context of linear response theory [48] .

After having defined the projection superoperator (and the reference system), the so-called time-convolutionless (TCL) projection-operator technique routinely leads to a time-local differential equation for the evolution of $\mathcal{P}\rho_{\mathrm{I}}(t)$ in the interaction picture [43, 51],

$$\frac{\partial}{\partial t} \mathcal{P}\rho_{\mathrm{I}}(t) = \mathcal{G}(t)\,\mathcal{P}\rho_{\mathrm{I}}(t) + \mathcal{I}(t)\,(1-\mathcal{P})\,\rho(0) , \quad (5)$$

where $\rho_{\mathrm{I}}(t) = e^{i\mathcal{H}_0 t} e^{-i\mathcal{H}t} \rho(0) e^{i\mathcal{H}t} e^{-i\mathcal{H}_0 t}$. The term $\mathcal{I}(t)$, i.e., the inhomogeneity on the right hand side (r.h.s.) of Eq. (5), can be neglected, due to $(1-\mathcal{P})\,\rho(0) = 0$. The generator $\mathcal{G}(t)$ is given as a systematic series expansion in powers of ε. In many cases, just like in our case, odd orders vanish. Hence, the lowest order is the second order

and reads

$$\mathcal{G}_2(t) = \varepsilon^2 \int_0^t dt' \, \mathcal{P}\mathcal{L}(t)\mathcal{L}(t')\mathcal{P} \,, \qquad (6)$$

where the Liouvillian is given by $\mathcal{L}(t)\bullet = -i[\mathcal{V}_\mathrm{I}(t), \bullet]$ with $\mathcal{V}_\mathrm{I}(t) = e^{i\mathcal{H}_0 t} \mathcal{V}(0) e^{-i\mathcal{H}_0 t}$.

So far, we have invoked no significant assumption. The central assumption in the following will be a truncation to lowest order. The quality of such a truncation naturally depends on the perturbation strength ε, but also on the structure of the perturbation $\mathcal{V}$ and the degrees of freedom in the projection superoperator $\mathcal{P}$. Note, however, that a truncation to lowest order does not necessarily imply that we have to restrict ourselves to weak perturbations $\varepsilon \to 0$ and long times $t \to \infty$. In particular, a lowest-order truncation turns out to be reasonable in many situations [41]. While the quality can naturally be further improved by taking into account higher-order corrections [52], conditions for neglecting higher orders at rather large ε can be found in Ref. [52].

Now, we use a truncation to lowest order, as well as the simple mathematical facts that,

$$C(t) \propto \langle \mathcal{J}(t)\mathcal{J} \rangle \,, \quad C_\mathrm{I}(t) \propto \langle \mathcal{J}(t)\mathcal{J}_\mathrm{I}(t) \rangle \,, \qquad (7)$$

which relate the time-dependent part of the density matrix (in the Schrödinger or interaction picture) to a certain type of correlation function. (A derivation of this relation can be found in Appendix C.) In particular, within the TCL formalism, a rate equation can be obtained for $C_\mathrm{I}(t)$ in the interaction picture,

$$\frac{\partial}{\partial t}\langle \mathcal{J}(t)\mathcal{J}_\mathrm{I}(t) \rangle = -\varepsilon^2 \, \gamma_2(t) \, \langle \mathcal{J}(t)\mathcal{J}_\mathrm{I}(t) \rangle \,, \qquad (8)$$

where $\mathcal{J}(t) = e^{i\mathcal{H}t} \mathcal{J}(0) e^{-i\mathcal{H}t}$ and the time-dependent damping $\gamma_2(t)$ results from a time-integral over a kernel $k_2(t,t') = k_2(\tau = t - t')$,

$$\gamma_2(t) = \int_0^t d\tau \, k_2(\tau) \,, \; k_2(\tau) = \frac{\langle i[\mathcal{J}, \mathcal{V}_\mathrm{I}(\tau)]i[\mathcal{J}, \mathcal{V}_\mathrm{I}] \rangle}{\langle \mathcal{J}^2 \rangle} \,. \quad (9)$$

Apparently, if $k_2(\tau) \to 0$ for sufficiently long times, then we have $\gamma_2(t) \to$ const. at such time scales. We note that the kernel $k_2(\tau)$ can in principle be calculated analytically in the thermodynamic limit, if the reference system $\mathcal{H}_0$ is integrable. But often a numerical calculation of $k_2(\tau)$ in systems of finite size is sufficient [52].

The solution of rate equation (8) obviously is an exponential decay of the form

$$\frac{\langle \mathcal{J}(t)\mathcal{J}_\mathrm{I}(t) \rangle}{\langle \mathcal{J}^2 \rangle} = \exp\left[-\varepsilon^2 \int_0^t dt' \, \gamma_2(t') \right]. \qquad (10)$$

This solution reflects our central result: Within our TCL approach, the time-dependent part of the density matrix is damped exponentially in the interaction picture and not *necessarily* in the Schrödinger picture. Clearly,

both pictures must agree, if the observable $\mathcal{J}$ is preserved in the reference system $\mathcal{H}_0$, $[\mathcal{J}, \mathcal{H}_0] = 0$. For instance, for the particle current in the Fermi-Hubbard chain, this preservation is given in the noninteracting $\mathcal{H}_0 = \mathcal{H}(U = U' = 0)$. Therefore, both pictures can also be expected to be rather similar, whenever the dynamics of $\mathcal{J}_\mathrm{I}(t)$ is sufficiently slow compared to the dynamics of $\mathcal{J}(t)$. In the general situation, however, the two pictures are just not the same:

$$\frac{\langle \mathcal{J}(t)\mathcal{J} \rangle_{\varepsilon>0}}{\langle \mathcal{J}(t)\mathcal{J} \rangle_{\varepsilon=0}} \neq \frac{\langle \mathcal{J}(t)\mathcal{J}_\mathrm{I}(t) \rangle}{\langle \mathcal{J}^2 \rangle} \,. \qquad (11)$$

Hence, *a priori*, one cannot expect that the lowest-order prediction of an exponential decay in Eq. (10) simply carries over to the Schrödinger picture, and the relaxation dynamics of $\langle \mathcal{J}(t)\mathcal{J} \rangle_{\varepsilon>0}$ may exhibit nontrivial behavior that is distinct from typicality predictions in Refs. [24, 25]. For instance, as we demonstrate later, this difference is eye striking for the strongly interacting reference system $\mathcal{H}_0 = \mathcal{H}(U \gg t_\mathrm{h}, U' = 0)$. Note that Eq. (10) has also consequences for transport quantities.

III.   NUMERICAL ILLUSTRATION

Next, we illustrate our central result in numerical simulations after a description of the employed method.

A.   Method

To study system sizes larger than what is possible with full exact diagonalization (ED), we rely on the concept of dynamical quantum typicality (DQT) [39, 40, 42, 53] and obtain time-dependent autocorrelation functions from a single pure state $|\psi\rangle$, which is drawn at random from a high-dimensional Hilbert space. While this approach is by now well established for "standard" correlation functions such as $\langle \mathcal{J}(t)\mathcal{J} \rangle$ (see Refs. [54, 55] and references therein), the dynamics of correlation functions with a more complicated time dependence such as $\langle \mathcal{J}(t)\mathcal{J}_\mathrm{I}(t) \rangle$ can be obtained in a rather similar fashion. Specifically, we first introduce the two auxiliary pure states

$$|\phi(t)\rangle = e^{-i\mathcal{H}t} e^{i\mathcal{H}_0 t} |\psi\rangle \,, \qquad (12)$$
$$|\varphi(t)\rangle = e^{-i\mathcal{H}t} e^{i\mathcal{H}_0 t} \mathcal{J} |\psi\rangle \,, \qquad (13)$$

and then approximate the autocorrelation function and its time dependence as

$$\langle \mathcal{J}(t)\mathcal{J}_\mathrm{I}(t) \rangle = \frac{\langle \phi(t)| \mathcal{J} |\varphi(t)\rangle}{\langle \phi|\phi\rangle} + \mathcal{O}\left(\frac{1}{\sqrt{D}} \right), \qquad (14)$$

where the statistical error becomes negligibly small for system sizes studied here. Compared to the usual approximation of $\langle \mathcal{J}(t)\mathcal{J} \rangle$ [56, 57], the approximation of $\langle \mathcal{J}(t)\mathcal{J}_\mathrm{I}(t) \rangle$ is more costly from a numerical point of view, since at each point in time an additional backward prop-

agation with respect to the reference system $\mathcal{H}_0$ is required. However, this extra operation can still be carried out in large Hilbert spaces beyond the range of full ED, thereby reducing the impact of finite-size effects, see Appendix B for a detailed analysis of finite-size effects. In this paper, we treat systems with up to $L = 16$, where $D \approx 4.3 \times 10^9$, and the largest symmetry subspace has a dimension $\approx 10^7$. Note that a time evolution of the form (12) is also relevant for the stability of quantum motion with respect to a static perturbation [58].

B.   Results

Let us now turn to our actual numerical results for the two scenarios of a noninteracting and an interacting reference system.

1.   Noninteracting reference system

We start with a decomposition where the reference system is chosen to be noninteracting, $\mathcal{H}_0 = \mathcal{H}(U = U' = 0)$, such that Schrödinger and interaction picture are identical, $C(t) = C_I(t)$, due to $[\mathcal{J}, \mathcal{H}_0] = 0$. The role of the perturbation is then played by the particle-particle interaction terms. In Fig. 1, we summarize the decay of the current autocorrelation function $\langle \mathcal{J}(t)\mathcal{J} \rangle = \langle \mathcal{J}(t)\mathcal{J}_I(t) \rangle$ for a finite system of size $L = 16$ and interaction strengths $U/t_{\rm h} = U'/t_{\rm h} = \varepsilon \leq 4$. The decay is faster the larger ε, and an exponential relaxation for weak ε changes into a Gaussian type of relaxation for stronger ε. This overall behavior is in qualitative agreement with the lowest-order prediction of the TCL projection-operator technique in Eq. (10). Note that the Gaussian behavior is expected due to $\gamma_2(t) \propto t$ at small t, which become relevant for large ε [52].

To exclude that this agreement is accidental, we depict in Figs. 1(b) and 1(c) numerical results for the kernel $k_2(t)$ and rate $\gamma_2(t)$, as both given in Eq. (9), for different chain lengths $L \leq 16$. Apparently, $k_2(t)$ decays fast to zero, and the visible finite-size effects set in at time scales after this initial decay. As a consequence, the damping $\gamma_2(t)$ shows a mild dependence on system size and, in particular, a conclusion on the plateau value of $\gamma_2(t)$ for $L \to \infty$ is possible. Therefore, we can quantitatively evaluate the lowest-order prediction in Eq. (10) and compare to the direct numerics in Fig. 1 discussed before. We find that the agreement is remarkably good over a wide range of perturbation strengths ε, and small differences might be either related to residual finite-size effects or missing higher-order corrections. A detailed analysis of finite-size effects can be found in Appendix B. Thus, our TCL approach correctly captures the "standard" case of exponential damping of $\langle \mathcal{J}(t)\mathcal{J} \rangle$, in agreement with typicality and random-matrix considerations [24–26].
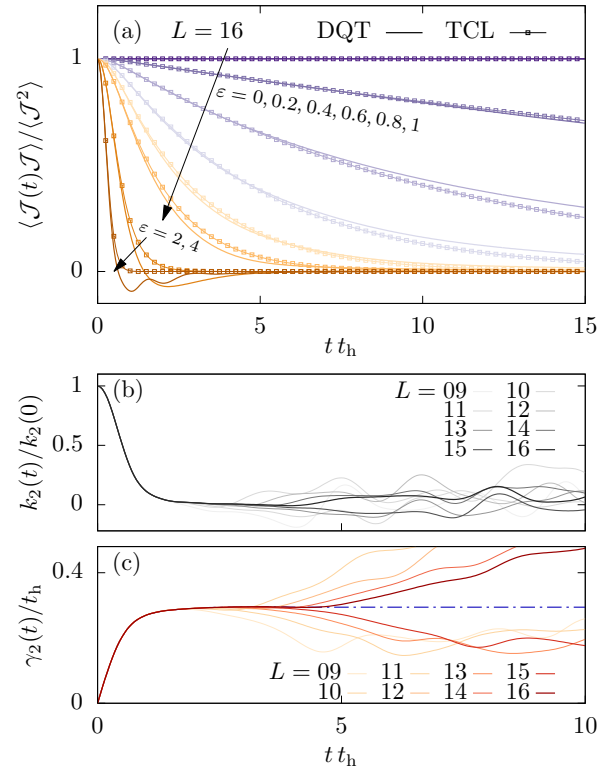

Figure 1.   (a) Decay of the current autocorrelation function $\langle \mathcal{J}(t)\mathcal{J} \rangle$ for the noninteracting $\mathcal{H}_0 = \mathcal{H}(U = U' = 0)$, which is perturbed by particle-particle interactions of various strengths $U/t_{\rm h} = U'/t_{\rm h} = \varepsilon \leq 4$. Numerical results from DQT in a finite system of size $L = 16$ are compared to the lowest-order prediction of the TCL projection-operator technique in Eq. (10). (b) Kernel $k_2(t)$ and (c) rate $\gamma_2(t)$, as both given in Eq. (9), for $L \leq 16$. Finite-size effects are mild and systematic. The expected plateau value of $\gamma_2(t)$ for $L \to \infty$ is indicated (dash-dotted line).

2.   Interacting reference system

Finally, and most importantly in the context of this paper, we turn to the decomposition $\mathcal{H} = \mathcal{H}_0 + \varepsilon\mathcal{V}$ with an interacting reference system, $\mathcal{H}_0 = \mathcal{H}(U \neq 0, U' = 0)$, where the Schrödinger and interaction picture are no longer the same, $C(t) \neq C_I(t)$, and the perturbation $\mathcal{V}$ is given by the nearest-neighbor interaction $U' > 0$. We decide to choose a large on-site interaction $U/t_{\rm h} = 16 \gg 1$, since the dynamics for such U is known to have rich features [59, 60]. However, the overall phenomenology emerges for smaller values of U as well, as can be seen in the additional data presented in Appendix A. As shown in Fig. 2(a) for a finite system size $L = 12$, $C(t) = \langle \mathcal{J}(t)\mathcal{J} \rangle$ in the Schrödinger picture exhibits oscillatory behavior, where the frequencies and zero crossings also vary with the strength $U'/t_{\rm h} = \varepsilon$ of the nearest-neighbor interaction. Hence, from visual inspection, it is clear that unperturbed and perturbed dynamics cannot be related by a simple damping function. Their nontriv-
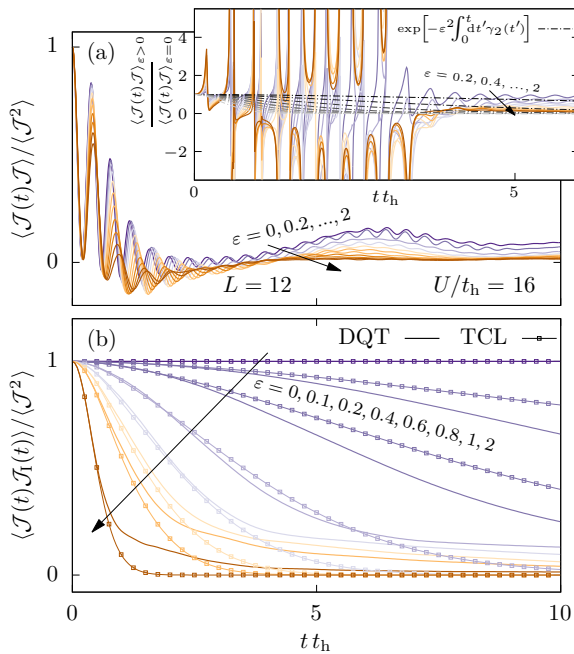
Figure 2. Decay of (a) $C(t) = \langle \mathcal{J}(t)\mathcal{J} \rangle$ and (b) $C_{\mathrm{I}}(t) = \langle \mathcal{J}(t)\mathcal{J}_{\mathrm{I}}(t) \rangle$ for the interacting $\mathcal{H}_0 = \mathcal{H}(U/t_{\mathrm{h}} = 16, U' = 0)$, which is perturbed in this case by nearest-neighbor particle-particle interactions of strength $U'/t_{\mathrm{h}} = \varepsilon \leq 2$. Numerical results from DQT are shown for a finite system of size $L = 12$ and in (b) additionally compared to the lowest-order prediction of the TCL projection-operator technique in Eq. (10). For the kernel $k_2(t)$ and rate $\gamma_2(t)$, see Fig. 5 in Appendix B. The inset in (a) shows the ratio between $\langle \mathcal{J}(t)\mathcal{J} \rangle_{\varepsilon > 0}$ (perturbed dynamics) and $\langle \mathcal{J}(t)\mathcal{J} \rangle_{\varepsilon = 0}$ (unperturbed dynamics) in the Schrödinger picture. This ratio is a nontrivial function and does not coincide with the damping in the interaction picture.

ial relation becomes even more obvious by plotting their ratio (see the inset of Fig. 2).

In the interaction picture, however, the situation turns out to be different. As shown in Fig. 2(b), the behavior of $C_{\mathrm{I}}(t) = \langle \mathcal{J}(t)\mathcal{J}_{\mathrm{I}}(t) \rangle$ is like the one in Fig. 1. It decays monotonously and changes from exponential to Gaussian type of relaxation as ε is increased, in qualitative agreement with the lowest-order prediction of the TCL projection-operator technique in Eq. (10). Furthermore, a quantitative comparison is also feasible, since the corresponding kernel $k_2(t)$ and rate $\gamma_2(t)$ are converged with respect to system size (see Fig. 5 in Appendix B), at least for the time scales depicted in Fig. 2(b). Apparently, the agreement is not as convincing as before and deviations set in for times $t\,t_{\mathrm{h}} \sim 4$. However, for such times, the direct numerics is known to still depend on system size (see, e.g., Refs. [59, 60] and Appendix B), and deviations might eventually disappear in the thermodynamic limit $L \to \infty$. We should also stress that the restriction by the finite-size time $t\,t_{\mathrm{h}} \sim 4$ does not allow us to study very weak perturbations $\varepsilon \ll 0.1$ in our numerical simulation, where the relaxation takes place on

a much longer time scale. How to numerically study the limit of very weak ε therefore remains an open problem.

In the specific context of currents, this result also has direct consequences for the transport behavior [61–63]; i.e., only in the interaction picture is the dynamics of the density matrix exponentially damped due to perturbations such that (i) the frequency dependence of the conductivity has a simple Lorentzian form and (ii) the dc conductivity σ_{dc} scales as $\sigma_{\mathrm{dc}} \propto 1/\varepsilon^2$. But for the dynamics of the density matrix in the Schrödinger picture, which is of actual interest, both (i) and (ii) cannot be expected (see also the corresponding data shown in Appendix D).

IV.   CONCLUSION

We have addressed the question of how the dynamics of a given quantum system is altered when a perturbation is switched on. We have shown that, within our analytical approach based on projection-operator techniques, the "standard" case of exponential damping occurs for the density matrix in the interaction picture but not *necessarily* in the Schrödinger picture. This key point we have illustrated explicitly in numerical simulations for charge transport in the strongly interacting extended Fermi-Hubbard chain, as a physically relevant many-body problem. Using this example, we have unveiled the emergence of nontrivial damping of current-current correlation functions, which is on the one hand not expected from typicality and random-matrix considerations and on the other hand demonstrates the complexity of quantum many-body systems out of equilibrium. While our numerics has focused on one specific example, our analytical reasoning suggests a similar behavior for other quantum systems. We expect that a nontrivial damping of relaxation dynamics in perturbed many-body quantum systems occurs most likely for cases where already the unperturbed dynamics possesses rich features. Thus, strongly interacting spin-1/2 XXZ chains or ladders [64–66] are natural candidates and promising future directions of research. However, we do not expect that integrability is a necessary condition. It would also be desirable to tackle the open problem of how to numerically study the limit of very weak perturbations.
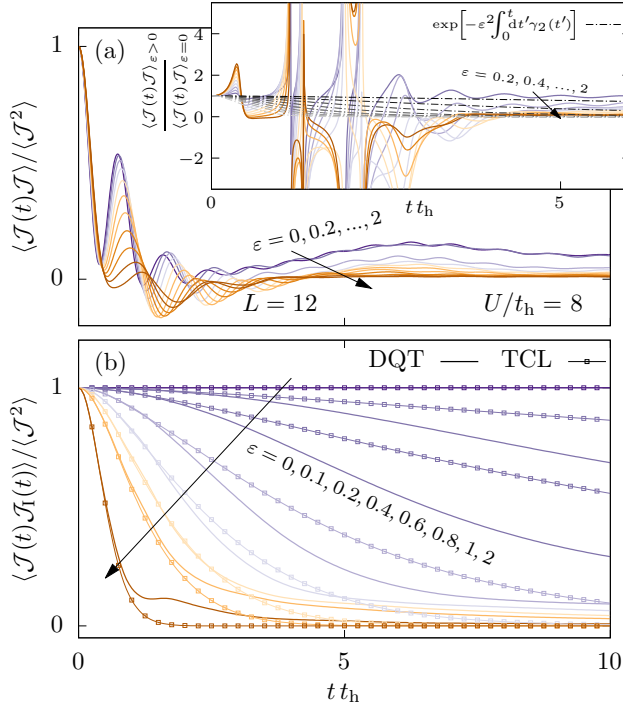
Figure 3. Similar data as depicted in Fig. 2, but now shown for the on-site interaction strength $U/t_{\rm h} = 8$.

Appendix A: Other values for the on-site interaction

Since we have focused in the main text on a strongly interacting reference system $\mathcal{H}_0 = \mathcal{H}(U/t_{\rm h} \gg 1, U' = 0)$ with a single on-site interaction strength $U/t_{\rm h} = 16$, we redo the calculation in Fig. 2 for another value of U. As shown in Fig. 3, the overall picture remains the same for $U/t_{\rm h} = 8$. Therefore, our numerical illustration is not fine-tuned with respect to U. Additionally, Fig. 4 shows similar data as Fig. 3(a) but for small interaction strengths $U/t_{\rm h} = 2$ and $U/t_{\rm h} = 1$. Naturally, with decreasing interaction strength U, we start to approach the noninteracting limit where $\mathcal{J}$ is conserved and the oscillations in the reference dynamics disappear. However, while the ratio $\langle \mathcal{J}(t)\mathcal{J}\rangle_{\varepsilon>0}/\langle \mathcal{J}(t)\mathcal{J}\rangle_{\varepsilon=0}$ assumes a more well-behaved shape, the relation between perturbed and unperturbed dynamics remains hardly reconcilable with exponential damping for $U/t_{\rm h} = 2$.

Appendix B: Finite-size scaling

1.   Interacting reference system

In the main text, we have mentioned in the context of Fig. 2 that the corresponding kernel $k_2(t)$ and the rate $\gamma_2(t)$ are converged with respect to system size for the relevant time scales. To support this, we depict in Fig. 5 the numerical results for $k_2(t)$ and $\gamma_2(t)$ for different system

sizes $L \leq 15$. We have also mentioned that finite-size effects for the strongly interacting case $U/t_{\rm h} = 16$ in Fig. 2 occur for times $t\, t_{\rm h} \sim 4$. Since we have shown curves for a single system size $L = 12$ there, we now illustrate in Fig. 6 these finite-size effects explicitly by depicting curves for different system sizes $L \leq 15$. We do so for $\mathcal{H}(U/t_{\rm h} = 16, U' = 0)$, which enters as $\mathcal{H}_0$ the interaction picture for all perturbations $U'/t_{\rm h} = \varepsilon > 0$.

2.   Noninteracting reference system

In the discussion of Fig. 1 in the main text, we have mentioned that small differences between direct DQT calculations and lowest-order TCL predictions of the current autocorrelation function $\langle \mathcal{J}(t)\mathcal{J}\rangle$ might in part be related to residual finite-size effects. To support this, we depict similar data for different system sizes and for two exemplary perturbation strengths $\varepsilon = 0.2$ and $\varepsilon = 0.6$ in Fig. 7. Numerical results from DQT for different system sizes $L \leq 16$ are shown and compared to the lowest-order prediction of the TCL projection operator technique in Eq. (10) of the main text. Here, we show three different curves (labeled as TCL₁₅, TCL₁₆, and TCL∞), corresponding to the rate $\gamma_2(t)$ obtained for the two largest numerically accessible chain lengths $L = 15, 16$ as well as its estimate for the thermodynamic limit $L \to \infty$, featuring a constant plateau for $t\, t_{\rm h} \gtrsim 4$ [see Fig. 1(c) of the main text]. For $\varepsilon = 0.2$ [Fig. 7(a)], the DQT curves for the largest system sizes are converged up to times $t\, t_{\rm h} \sim 5$ and coincide with all three TCL curves. For later times, both the DQT and the TCL results show mild finite-size effects, whereby the TCL∞ prediction appears to agree best with the scaling behavior of the DQT data. For $\varepsilon = 0.6$ [Fig. 7(b)], a very similar behavior is found in the comparison of the DQT and the TCL curves.

Complementary to the DQT and the TCL data, Fig. 7 also shows numerical results for $\langle \mathcal{J}(t)\mathcal{J}\rangle$ in the thermodynamic limit $L \to \infty$ as obtained by means of a numerical linked-cluster expansion (NLCE) (see, e.g., Refs. [67, 68] and below) for different expansion orders $c_{\rm max} \leq 15$. The NLCE results agree with the DQT and the TCL data at times $t\, t_{\rm h} \lesssim 5$ for both $\varepsilon = 0.2$ and $\varepsilon = 0.6$. Beyond times $t\, t_{\rm h} \sim 5$, the NLCE does not add much to the information on the thermodynamic limit for $\varepsilon = 0.2$. However, for $\varepsilon = 0.6$, the NLCE curves are converged just long enough to indicate that the TCL∞ prediction is most suitable to describe $\langle \mathcal{J}(t)\mathcal{J}\rangle$ in the thermodynamic limit.

a.   NLCE in a nutshell

In the framework of NLCE, the per-site value of the current autocorrelation function on an infinite chain can be expanded in terms of its respective weights W_c on all linked (sub-)clusters (i.e., open-boundary chains of
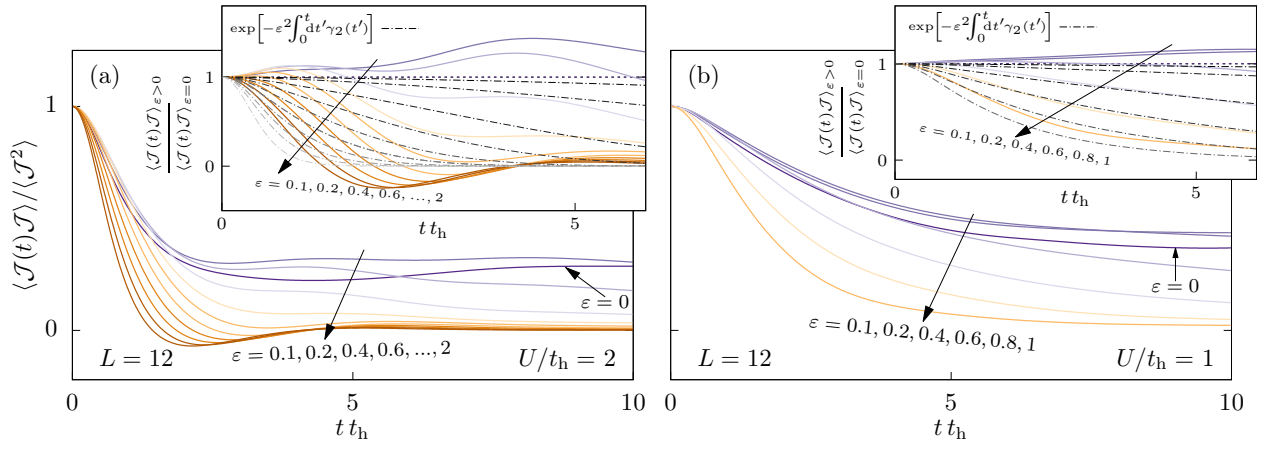
Figure 4. Similar data as depicted in Fig. 3(a), but now shown for smaller on-site interaction strengths (a) $U/t_h = 2$ and (b) $U/t_h = 1$.

different lengths c),

$$\langle \mathcal{J}(t)\mathcal{J}\rangle/L = \sum_c W_c(t) . \tag{B1}$$

For numerical calculations, the sum in Eq. (B1) naturally has to be truncated to the maximum accessible cluster size c_{max}. This, together with the inclusion-exclusion principle for the calculation of each weight, $W_c(t) = \langle \mathcal{J}(t)\mathcal{J}\rangle^{(c)} - \sum_{s \subset c} W_s(t)$, results in the very simple expression approximating Eq. (B1),

$$\sum_c^{c_{max}} W_c(t) = \langle \mathcal{J}(t)\mathcal{J}\rangle^{(c_{max})} - \langle \mathcal{J}(t)\mathcal{J}\rangle^{(c_{max}-1)} , \tag{B2}$$

which is reliable up to a certain maximum time, increasing with the maximum cluster size c_{max}. The $\langle \mathcal{J}(t)\mathcal{J}\rangle^{(c)}$ (evaluated on open-boundary chains of length c) are again obtained with DQT and additionally averaged over multiple random states in order to counteract the sensitivity of the difference in Eq. (B2) to small statistical errors.

Appendix C: Relation to correlation functions

To see that $\langle \mathcal{J}\mathcal{P}\rho_I(t)\rangle \propto \langle \mathcal{J}(t)\mathcal{J}_I(t)\rangle$, we first insert the definition of the projection superoperator $\mathcal{P}$ in $\langle \mathcal{J}\mathcal{P}\rho_I(t)\rangle$, which yields

$$\langle \mathcal{J}\mathcal{P}\rho_I(t)\rangle = \langle \mathcal{J}\Big(\frac{1}{D} + \frac{\langle \mathcal{J}\rho_I(t)\rangle}{\langle \mathcal{J}^2\rangle}\mathcal{J}\Big)\rangle . \tag{C1}$$
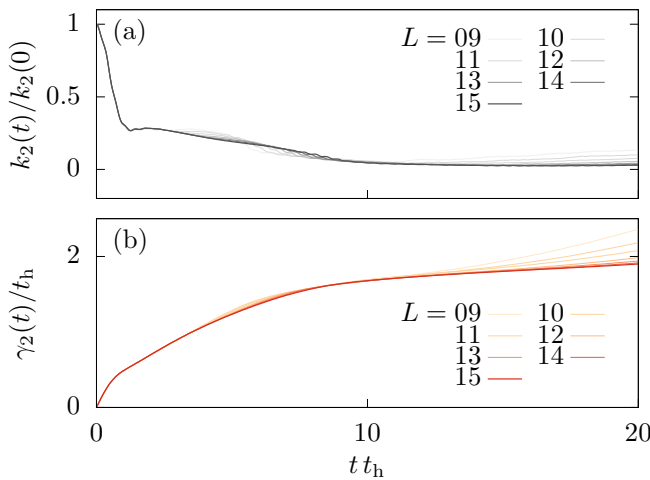

Figure 5. Second-order (a) kernel $k_2(t)$ and (b) damping $\gamma_2(t)$, as both given in Eq. (9) of the main text, for the interacting $\mathcal{H}_0 = \mathcal{H}(U/t_h = 16, U' = 0)$. Numerical results from DQT are shown for various chain lengths $L \leq 15$.
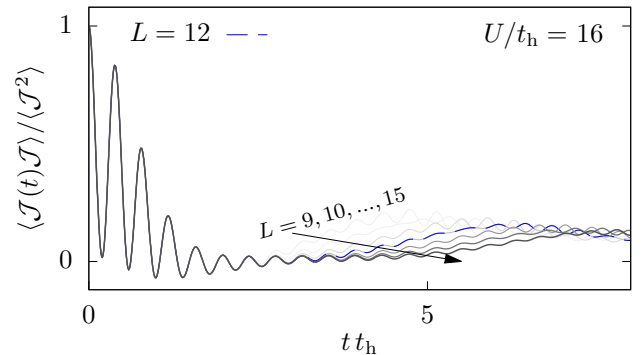

Figure 6. Time dependence of the current autocorrelation function $\langle \mathcal{J}(t)\mathcal{J}\rangle$ in the strongly interacting system $\mathcal{H}(U/t_h = 16, U' = 0)$, as obtained from DQT for different system sizes $L \leq 15$. For such L, data are converged up to times $t\,t_h \sim 4$. Similar data can be found in [60].
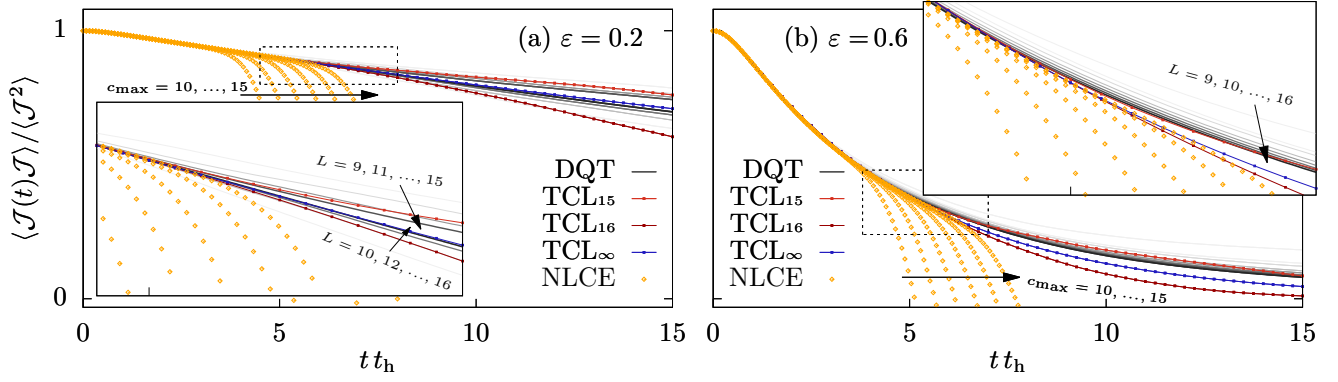
Figure 7. Time dependence of the current autocorrelation function $\langle \mathcal{J}(t)\mathcal{J} \rangle$ in the noninteracting system $\mathcal{H}_0 = \mathcal{H}(U = U' = 0)$, which is perturbed by interactions $U/t_{\mathrm{h}} = U'/t_{\mathrm{h}} = \varepsilon$ for two exemplary strengths (a) $\varepsilon = 0.2$ and (b) $\varepsilon = 0.6$. Numerical results from DQT are shown for different system sizes $L = 9, ..., 16$ and compared to the lowest-order prediction of the TCL projection-operator technique in Eq. (10) of the main text. For the TCL curves, different rates $\gamma_2(t)$ corresponding to finite system sizes $L = 15$ (TCL_{15}), $L = 16$ (TCL_{16}), as well as its estimate for $L \to \infty$ (TCL_∞) are used [cf. Fig. 1 (c) of the main text]. Additionally, NLCE data is shown for expansion orders $c_{\mathrm{max}} \leq 15$.

Since $\langle \mathcal{J} \rangle = 0$, performing the outer angles leads to

$$\langle \mathcal{J}\mathcal{P}\rho_{\mathrm{I}}(t) \rangle = \langle \mathcal{J}\rho_{\mathrm{I}}(t) \rangle . \qquad (C2)$$

We then insert the initial condition $\rho(0) \propto 1 + b\mathcal{J}$ and use the time dependence of a density matrix in the interaction picture, $\rho_{\mathrm{I}}(t) = e^{i\mathcal{H}_0 t} e^{-i\mathcal{H}t} \rho(0) e^{i\mathcal{H}t} e^{-i\mathcal{H}_0 t}$, to obtain

$$\langle \mathcal{J}\mathcal{P}\rho_{\mathrm{I}}(t) \rangle \propto \langle \mathcal{J}e^{i\mathcal{H}_0 t} e^{-i\mathcal{H}t} (1 + b\mathcal{J}) e^{i\mathcal{H}t} e^{-i\mathcal{H}_0 t} \rangle . \quad (C3)$$

Using $\langle \mathcal{J} \rangle = 0$ again, we thus get

$$\langle \mathcal{J}\mathcal{P}\rho_{\mathrm{I}}(t) \rangle \propto \langle \mathcal{J}e^{i\mathcal{H}_0 t} e^{-i\mathcal{H}t} \mathcal{J} e^{i\mathcal{H}t} e^{-i\mathcal{H}_0 t} \rangle , \qquad (C4)$$

which, after a cyclic permutation, reads

$$\langle \mathcal{J}\mathcal{P}\rho_{\mathrm{I}}(t) \rangle \propto \langle e^{-i\mathcal{H}t} \mathcal{J}e^{i\mathcal{H}t} e^{-i\mathcal{H}_0 t} \mathcal{J} e^{i\mathcal{H}_0 t} \rangle . \qquad (C5)$$

Denoting by $\mathcal{J}(t) = e^{i\mathcal{H}t} \mathcal{J} e^{-i\mathcal{H}t}$ and $\mathcal{J}_{\mathrm{I}}(t) = e^{i\mathcal{H}_0 t} \mathcal{J} e^{-i\mathcal{H}_0 t}$ the time evolution of an operator in the Heisenberg and interaction picture, respectively, we can write

$$\langle \mathcal{J}\mathcal{P}\rho_{\mathrm{I}}(t) \rangle \propto \langle \mathcal{J}(-t)\mathcal{J}_{\mathrm{I}}(-t) \rangle . \qquad (C6)$$

Due to $\mathcal{J}^\dagger = \mathcal{J}$, we can replace $t \to -t$ and end up with

$$\langle \mathcal{J}\mathcal{P}\rho_{\mathrm{I}}(t) \rangle \propto \langle \mathcal{J}(t)\mathcal{J}_{\mathrm{I}}(t) \rangle . \qquad (C7)$$

Appendix D: Conductivity

In Fig. 8, we show the frequency-dependent conductivity in the strongly interacting system $\mathcal{H}(U/t_{\mathrm{h}} = 16, U' = 0)$, perturbed by interactions $U'/t_{\mathrm{h}} = \varepsilon$. This conductivity is obtained by the Fourier transform of the current au-

tocorrelation functions depicted in Fig. 2(a) of the main text,

$$\sigma(\omega) = \int_{-t_{\mathrm{max}}}^{t_{\mathrm{max}}} \mathrm{d}t \, e^{-i\omega t} \frac{\langle \mathcal{J}(t)\mathcal{J} \rangle}{L} , \qquad (D1)$$

with a cutoff time $t_{\mathrm{max}} t_{\mathrm{h}} = 100$. The overall shape of the conductivity is incompatible with a simple Lorentzian form, while the freestanding shoulder shifts from higher to lower ω as the perturbation strength increases, attesting to the shift in the frequencies observed in the oscillatory behavior of the corresponding current autocorrelation functions. In addition, the spectral weight at small ω provides a rough estimate for the value of the dc conductivity σ_{dc}, which clearly does not scale as $\sigma_{\mathrm{dc}} \propto 1/\varepsilon^2$. For the detailed extraction of σ_{dc}, see Ref. [45].
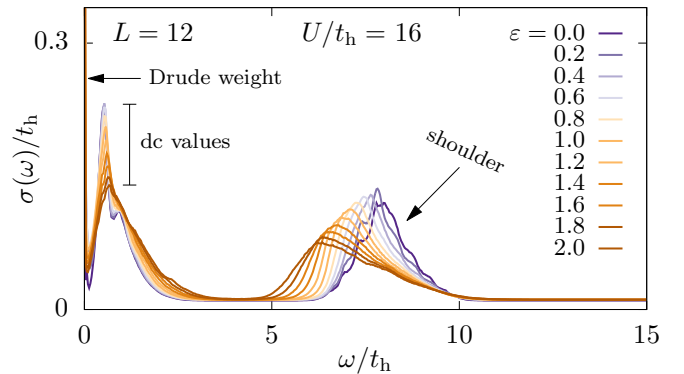

Figure 8. Frequency dependence of the conductivity $\sigma(\omega)$, as obtained by the Fourier transform (D1) of the current autocorrelation functions shown in Fig. 2(a) of the main text.

[1] L. D'Alessio, Y. Kafri, A. Polkovnikov, and M. Rigol, Adv. Phys. **65**, 239 (2016).
[2] F. Borgonovi, F. Izrailev, L. F. Santos, and V. Zelevinsky, Phys. Rep. **626**, 1 (2016).
[3] C. Gogolin and J. Eisert, Rep. Prog. Phys. **79**, 056001 (2016).
[4] S. Paeckel, T. Köhler, A. Swoboda, S. R. Manmana, U. Schollwöck, and C. Hubig, Ann. Phys. (NY) **411**, 167998 (2019).
[5] J. Dziarmaga, Adv. Phys. **59**, 1063 (2010).
[6] A. Polkovnikov, K. Sengupta, A. Silva, and M. Vengalattore, Rev. Mod. Phys. **83**, 863 (2011).
[7] S. Erne, R. Bücker, T. Gasenzer, J. Berges, and J. Schmiedmayer, Nature **563**, 225 (2018).
[8] M. Prüfer, P. Kunkel, H. Strobel, S. Lannig, D. Linnemann, C.-M. Schmied, J. Berges, T. Gasenzer, and M. K. Oberthaler, Nature **563**, 217 (2018).
[9] P. Reimann, B. N. Balz, J. Richter, and R. Steinigeweg, Phys. Rev. B **101**, 094302 (2020).
[10] Á. M. Alhambra, J. Riddell, and L. P. García-Pintos, Phys. Rev. Lett. **124**, 110605 (2020).
[11] T. A. Brody, J. Flores, J. B. French, P. A. Mello, A. Pandey, and S. S. M. Wong, Rev. Mod. Phys. **53**, 385 (1981).
[12] J. M. Deutsch, Phys. Rev. A **43**, 2046 (1991).
[13] M. Srednicki, Phys. Rev. E **50**, 888 (1994).
[14] M. Rigol, V. Dunjko, and M. Olshanii, Nature **452**, 854 (2008).
[15] I. M. Khaymovich, M. Haque, and P. A. McClarty, Phys. Rev. Lett. **122**, 070601 (2019).
[16] J. Richter, A. Dymarsky, R. Steinigeweg, and J. Gemmer, Phys. Rev. E **102**, 042127 (2020).
[17] C. Schönle, D. Jansen, F. Heidrich-Meisner, and L. Vidmar, Phys. Rev. B **103**, 235137 (2021).
[18] M. Brenes, S. Pappalardi, M. T. Mitchison, J. Goold, and A. Silva, Phys. Rev. E **104**, 034120 (2021).
[19] C. W. von Keyserlingk, T. Rakovszky, F. Pollmann, and S. L. Sondhi, Phys. Rev. X **8**, 021013 (2018).
[20] A. Nahum, S. Vijay, and J. Haah, Phys. Rev. X **8**, 021014 (2018).
[21] V. Khemani, A. Vishwanath, and D. A. Huse, Phys. Rev. X **8**, 031057 (2018).
[22] L. Knipschild and J. Gemmer, Phys. Rev. E **98**, 062103 (2018).
[23] C. Nation and D. Porras, Phys. Rev. E **99**, 052139 (2019).
[24] L. Dabelow and P. Reimann, Phys. Rev. Lett. **124**, 120602 (2020).
[25] L. Dabelow and P. Reimann, J. Stat. Mech. **2021**, 013106 (2021).
[26] J. Richter, F. Jin, L. Knipschild, H. De Raedt, K. Michielsen, J. Gemmer, and R. Steinigeweg, Phys. Rev. E **101**, 062133 (2020).
[27] J. Berges, S. Borsányi, and C. Wetterich, Phys. Rev. Lett. **93**, 142002 (2004).
[28] M. Moeckel and S. Kehrein, Phys. Rev. Lett. **100**, 175702 (2008).
[29] B. Bertini, F. H. L. Essler, S. Groha, and N. J. Robinson, Phys. Rev. Lett. **115**, 180601 (2015).
[30] T. Mori, T. N. Ikeda, E. Kaminishi, and M. Ueda, J. Phys. B **51**, 112001 (2018).
[31] P. Reimann and L. Dabelow, Phys. Rev. Lett. **122**, 080603 (2019).
[32] K. Mallayya, M. Rigol, and W. De Roeck, Phys. Rev. X **9**, 021027 (2019).
[33] M. Schmitt and S. Kehrein, Phys. Rev. B **98**, 180301(R) (2018).
[34] L. Dabelow and P. Reimann, Phys. Rev. Research **2**, 023216 (2020).
[35] J. Preskill, Quantum **2**, 79 (2018).
[36] F. Arute *et al.*, Nature **574**, 505 (2019).
[37] S. Genway, A. F. Ho, and D. K. K. Lee, Phys. Rev. Lett. **111**, 130408 (2013).
[38] M. A. Werner, C. P. Moca, Ö. Legeza, and G. Zaránd, Phys. Rev. B **102**, 155108 (2020).
[39] S. Popescu, A. J. Short, and A. Winter, Nat. Phys. **2**, 754 (2006).
[40] S. Goldstein, J. L. Lebowitz, R. Tumulka, and N. Zanghì, Phys. Rev. Lett. **96**, 050403 (2006).
[41] C. Bartsch, R. Steinigeweg, and J. Gemmer, Phys. Rev. E **77**, 011119 (2008).
[42] P. Reimann, Phys. Rev. E **97**, 062129 (2018).
[43] H.-P. Breuer and F. Petruccione, *The Theory of Open Quantum Systems* (Oxford University Press, 2007).
[44] X. Zotos and P. Prelovšek, in *Strong interactions in low dimensions* (Springer Netherlands, Dordrecht, 2004) Chap. 11, pp. 347–382.
[45] B. Bertini, F. Heidrich-Meisner, C. Karrasch, T. Prosen, R. Steinigeweg, and M. Žnidarič, Rev. Mod. Phys. **93**, 025003 (2021).
[46] V. B. Bulchandani, S. Gopalakrishnan, and E. Ilievski, J. Stat. Mech. **2021**, 084001 (2021).
[47] F. H. L. Essler, H. Frahm, F. Göhmann, A. Klümper, and V. E. Korepin, *The One-Dimensional Hubbard Model* (Cambridge University Press, 2005).
[48] A canonical density matrix $\rho \propto \exp[-\beta(\mathcal{H} - \lambda\mathcal{J}]$ with a sufficiently small inverse temperature β can be expanded as $\rho \propto 1 + \beta\lambda\mathcal{J} + \mathcal{O}(\lambda^2)$ [49, 50].
[49] R. Kubo, M. Toda, and N. Hashitsume, *Statistical Physics II*, 2nd ed., Springer Series in Solid-State Sciences, Vol. 31 (Springer Berlin Heidelberg, 1991).
[50] W. Brenig, *Statistical Theory of Heat* (Springer Berlin Heidelberg, 1989).
[51] S. Chaturvedi and F. Shibata, Z. Phys. B **35**, 297 (1979).
[52] R. Steinigeweg, Phys. Rev. E **84**, 011136 (2011).
[53] C. Bartsch and J. Gemmer, Phys. Rev. Lett. **102**, 110403 (2009).
[54] F. Jin, D. Willsch, M. Willsch, H. Lagemann, K. Michielsen, and H. De Raedt, J. Phys. Soc. Jpn. **90**, 012001 (2021).
[55] T. Heitmann, J. Richter, D. Schubert, and R. Steinigeweg, Z. Naturforsch. A **75**, 421 (2020).
[56] T. Iitaka and T. Ebisuzaki, Phys. Rev. Lett. **90**, 047203 (2003).
[57] T. A. Elsayed and B. V. Fine, Phys. Rev. Lett. **110**, 070404 (2013).
[58] T. Prosen and M. Žnidarič, J. Phys. A **35**, 1455 (2002).
[59] C. Karrasch, D. M. Kennes, and J. E. Moore, Phys. Rev. B **90**, 155104 (2014).
[60] F. Jin, R. Steinigeweg, F. Heidrich-Meisner, K. Michielsen, and H. De Raedt, Phys. Rev. B **92**, 205103 (2015).

[61] X. Zotos, Phys. Rev. Lett. **92**, 067202 (2004).

[62] P. Jung, R. W. Helmes, and A. Rosch, Phys. Rev. Lett. **96**, 067202 (2006).

[63] R. Steinigeweg, J. Herbrych, X. Zotos, and W. Brenig, Phys. Rev. Lett. **116**, 017202 (2016).

[64] C. Karrasch, J. E. Moore, and F. Heidrich-Meisner, Phys. Rev. B **89**, 075139 (2014).

[65] C. Karrasch, D. M. Kennes, and F. Heidrich-Meisner, Phys. Rev. B **91**, 115130 (2015).

[66] R. Steinigeweg, F. Heidrich-Meisner, J. Gemmer, K. Michielsen, and H. De Raedt, Phys. Rev. B **90**, 094417 (2014).

[67] M. Rigol, T. Bryant, and R. R. P. Singh, Phys. Rev. Lett. **97**, 187202 (2006).

[68] J. Richter and R. Steinigeweg, Phys. Rev. B **99**, 094419 (2019).